Grant Agreement No.: 226479

# SafeLand

Living with landslide risk in Europe: Assessment,
effects of global change, and risk management strategies

7th Framework Programme
Cooperation Theme 6 Environment (including climate change)
Sub-Activity 6.1.3 Natural Hazards

**Deliverable D3.9**

Methodology for predicting the changes in the landslide risk during the next 50
years at selected sites in Europe. Changing pattern of landslide risk in hotspot
and evolution trends in Europe according to global change scenarios.

Work Package 3.3 – Landslide hazard evolution in Europe and risk evolution in
selected "hotspot" areas

Deliverable/Work Package Leader: BRGM                    Revision: 0 – Final

April, 2012

| Rev. | Deliverable Responsible | Controlled by | Date |
|------|-------------------------|---------------|------|
| 0 | BRGM | ICG | 30 April 2012 |
| 1 | | | |
| 2 | | | |

# SUMMARY

Previous studies within Area 3 of the Safeland project developed and applied a method to estimate impacts of climate change (Deliverable D3.7) on the landslide hazard at local scale (Deliverable D3.8) in several "hot spots" in Europe . The first part of this deliverable focuses on the evolution of landslide risk at three European test sites during the next 50-70 years. The test sites are located in Norway, France and Scotland.

The French and Norwegian test sites have already been studied in the previous parts of Area 3. In particular, the landslide hazard evolution for the next 50 years for these two tests sites were assessed for the downscaled climate change scenarios developed in SafeLand. The site in Scotland, however, was introduced for the first time in this deliverable, and the climate change scenarios for this area were not assessed in other SafeLand work packages.

The second part of this deliverable presents some new avenues of research for a more precise assessment of future landslide risk evolution at local scale. Theoretical frameworks for assessing the impact of land cover changes on landslide hazard and the time evolution of vulnerability taking into consideration different corrosion processes are described in that section.

## Note about contributors

The following organisations contributed to the work described in this deliverable:

> **Lead partner responsible for the deliverable:**
> BRGM: Audrey Baills, Mélanie Fontaine, Audrey Hohmann, Rosalie Vandromme, Nicolas Desramaut

> **Partner responsible for quality control:**
> ICG: Farrokh Nadim

> **Other contributors:**
> AUTH: S. Fotopoulou, K. Pitilakis
> CRSA: A. Modaressi, S. Hemmati, F. Lopez-Caballero
> ICG: J.M. Cepeda, E. Syre
> TRL: M.G. Winter, B. Shearer

# CONTENTS

## Illustration Table

# Tables

# INTRODUCTION

The potential effect of climate change on landslide triggering varies depending on the type of landslides considered. For rainfall-induced landslides, the hazard evolution is tightly linked to the variation of precipitation threshold parameters in time. Other types of landslide may be impacted differently by climate change. For instance the main triggering parameter for rock falls is the frost and defrost cycles; but those cases were not developed in the work performed within the Area 3. Other thresholds related to change in land cover vegetation are developed in the methodology but could not be integrated in the test cases studies.

In the first part of the deliverbale, changes in landslides risk are assessed for three European test sites. Two of those test sites have already been studied in the previous parts of Area 3: French and Norwegian ones. There are parts of the study for WP 3.1, WP 3.2 and Deliverable 3.8 from WP 3.3 where the landslide hazard has been assessed for the next 50 years in order to fit with the climate change scenarios downscaling developed in WP 3.1. The last site in Scotland, has been introduced in the Area 3 for this unique deliverable. So the climate change scenarios for this area were not computed in SafeLand work packages. Thus the studied period is different for this site: the assessment of risk evolution was performed until 2080.

The second part of this deliverable presents some new avenues of research for a more precise assessment of future landslide risk evolution at local scale. Theoretical frameworks for assessing the impact of land cover changes on landslide hazard and the time evolution of vulnerability taking into consideration different corrosion processes are described in that section.

# FIRST PART – Prediction of landslides risk evolution in selected hotspots in Europe

# 1      RISK ASSESSMENT ON BARCELONNETTE SITE

The Barcelonnette site is a 350 km$^2$ zone, situated in the south of France in the department of Alpes-de-Haute-Provence. It is located in a mountainous area, reaching altitudes of approximately 3 100 m, with an average altitude of 1 100 m, and is crossed by the Ubaye River.

## 1.1     DATA

### 1.1.1   Hazard Data

The hazard assessment performed in SafeLand Deliverable D3.8 studied the evolution of the climate-induced landslide hazard in the next 50 years, regarding the source areas of landslides. They correspond to the unstable zones where landslides are likely to be initiated, but do not represent the total area affected by landslides. Since that methodology does not take into account the landslide runout, the landslide occurrence probability assessed in Deliverable 3.8 was not sufficient for risk assessment purposes. That is why we used the program BORA to assess the run-out distance for each area source defined previously. This tool developed by Sedan et al (2006) is written in Visual Basic 6 and interfaced with ArcGIS®. It provides the probability for a given point being reached by propagated landslides.

**BORA Program and its application to the site**

The main principle is that, at a given point A under an uphill instable point B, if the initiation and the run-out of landslides are assumed independent, the probability of the point A to be affected by the landslides initiated in B can be schematically expressed as:

*P (A affected by landslide initiated in B) =P (landslide is initiated in B) x P (landslide initiated in B reaches A)*

The BORA model (Figure 1 and Figure 2) is based on the following hypothesis:

- a sliding mass moves preferably along the steepest slope;

- the energy of a sliding mass has an upper limit;

- the energy of a sliding mass increases and decreases as a function of the slope;

- there is a probability of the sliding mass moving away from the steepest slope path (lateral dispersion).
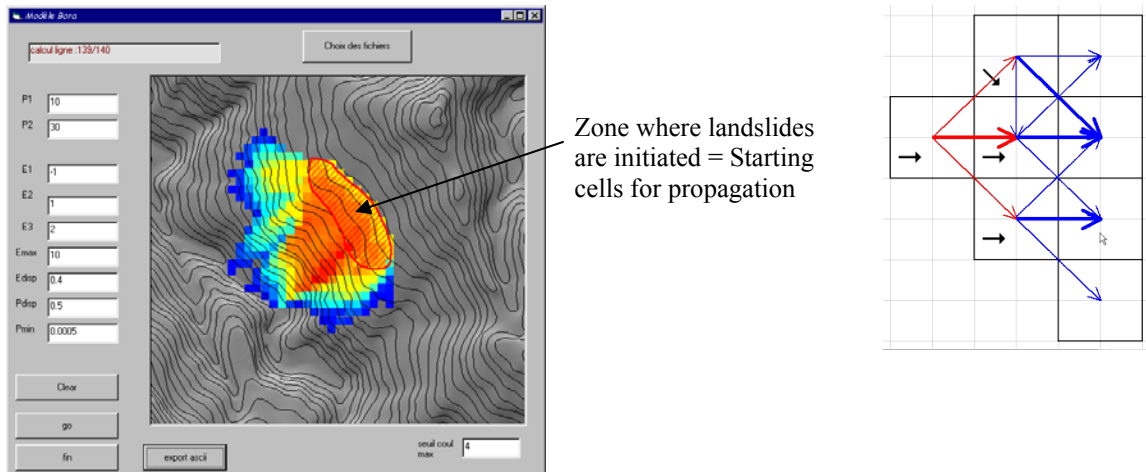
*Figure 1 Illustration of BORA method: Computation of the probability of being reached by propagated landslides*



With α: slope , E: Pseudo-Energy and P: Probability to be affected
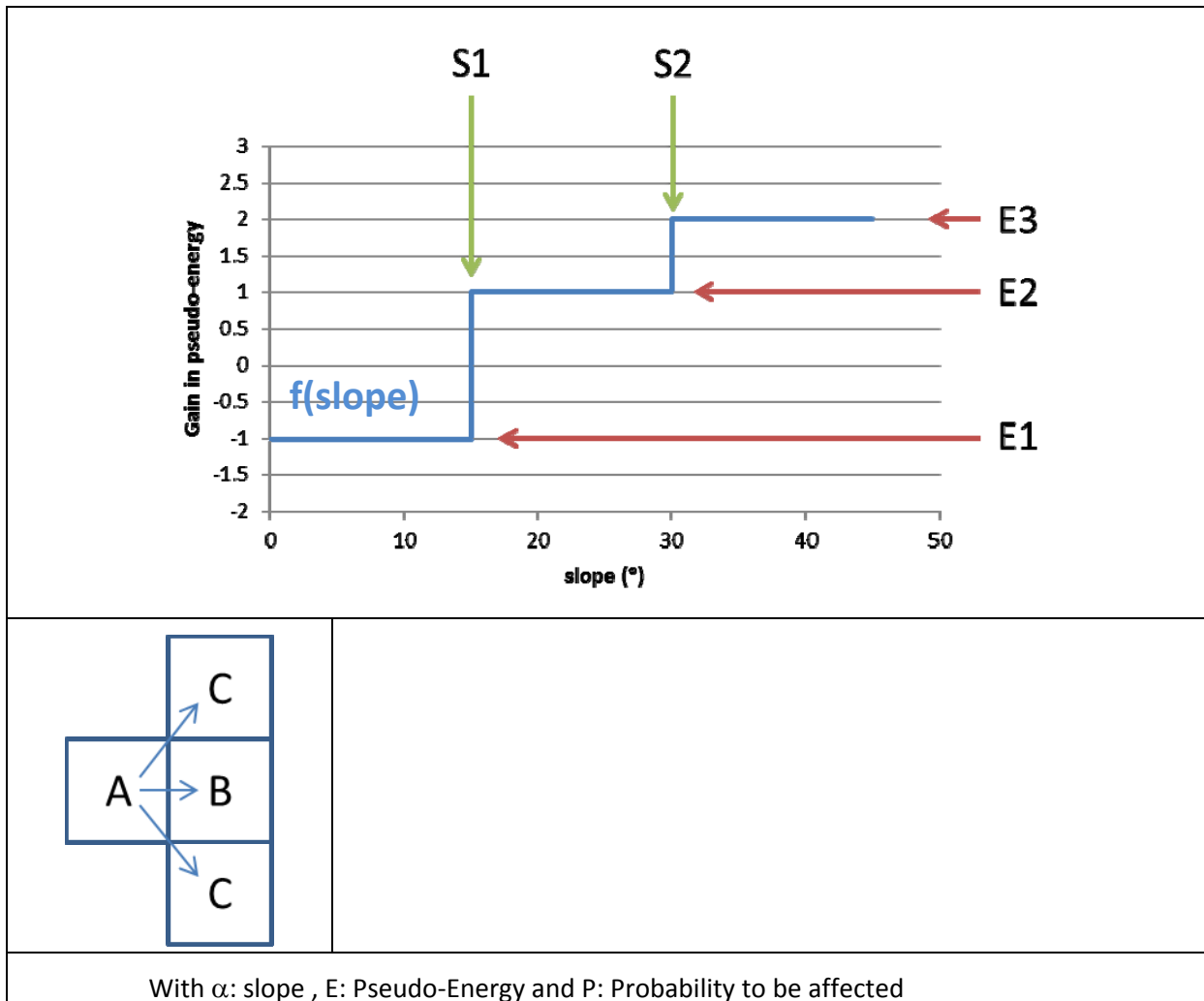
*Figure 2 Empirical laws used in BORA*

Empirical laws are used to characterize the traveling behaviour of sliding masses: the energy and the probability of lateral dispersion are defined as functions of the slope. These functions

can be different according to the types of landslides. The user must calibrate and define the parameters used in the formulations of these functions.

The input data are the following:

- the DEM;

- the map of landslides occurrence probability (which is the outcome of the stability analyses, done in the SafeLand Deliverable D3.8);

- the parameters related to the energy and the lateral dispersion of the sliding mass (estimated based on expert judgments and represented in Table 1).

Finally, in every cell, the total probability of being affected by landslides is computed, which results from the union of both the potential initiation of a landslide in this cell and the potential propagation of landslides initiated in other cells on this cell.

The output is a landslide hazard map on which every cell is associated with the overall probability of being affected by landslides and a relative indicator of pseudo-energy at this cell. This last indicator allows to somehow providing aggression factors which could be convoluted with vulnerability indexes to evaluate risks. It represents the residual kinetic energy.

For Barcelonnette site, the sets of parameters have been calibrated based on initial assumptions from the geotechnical parameters and on the landslides inventories, using, as inputs, the map of landslide occurrence probability obtained from observed meteorological data. The resulting values are listed in Table 1.

| S1 | S2 | E1 | E2 | E3 | Emax | Edisp |
|------|------|------|------|------|------|------|
| 15° | 30° | -1 | 0.5 | 1 | 2 | 0.8 |

*Table 1 BORA parameters calibrated for Barcelonnette site*

Maps of affected areas can then be computed for the past period (1983-2013) and the future one (2020-2050) based on the map of landslide occurrence probability evaluated in the Deliverable D3.8, with Climate change data as meteorological inputs. These maps were used as a basis for the risk assessment of the present deliverable and they are shown in the following                                                    figures                                                    (
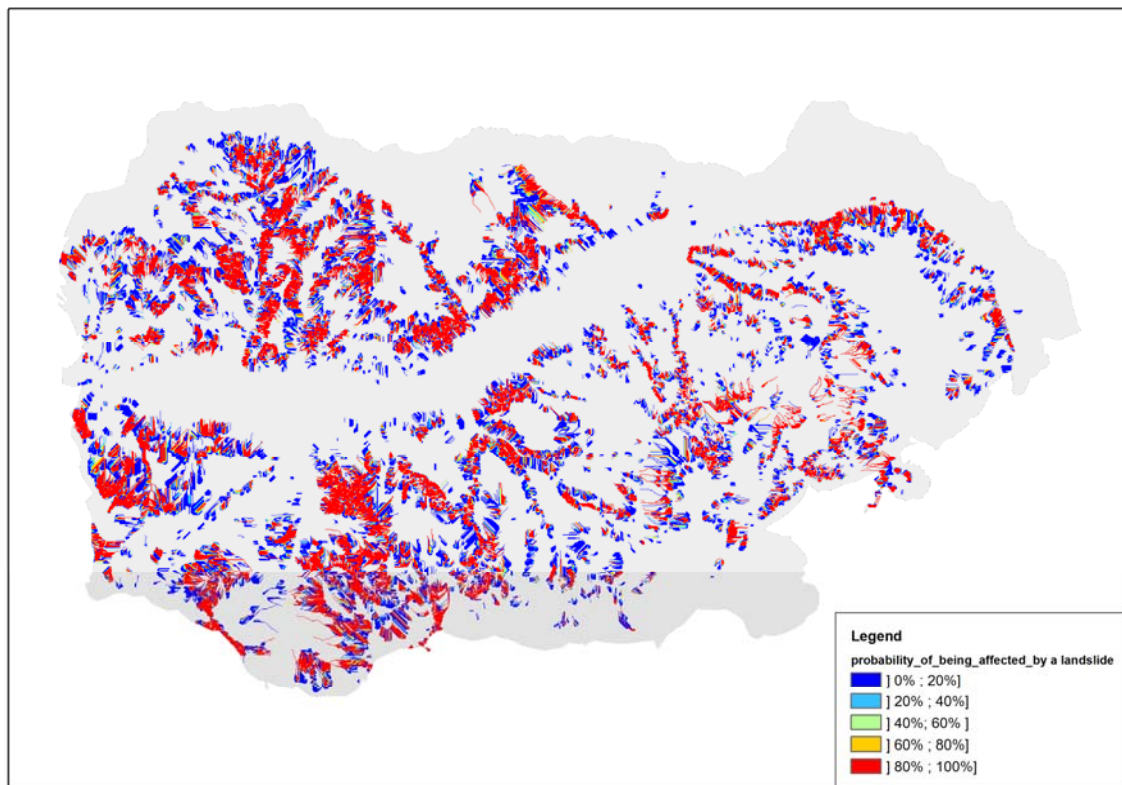
Figure 3 to Figure 6).
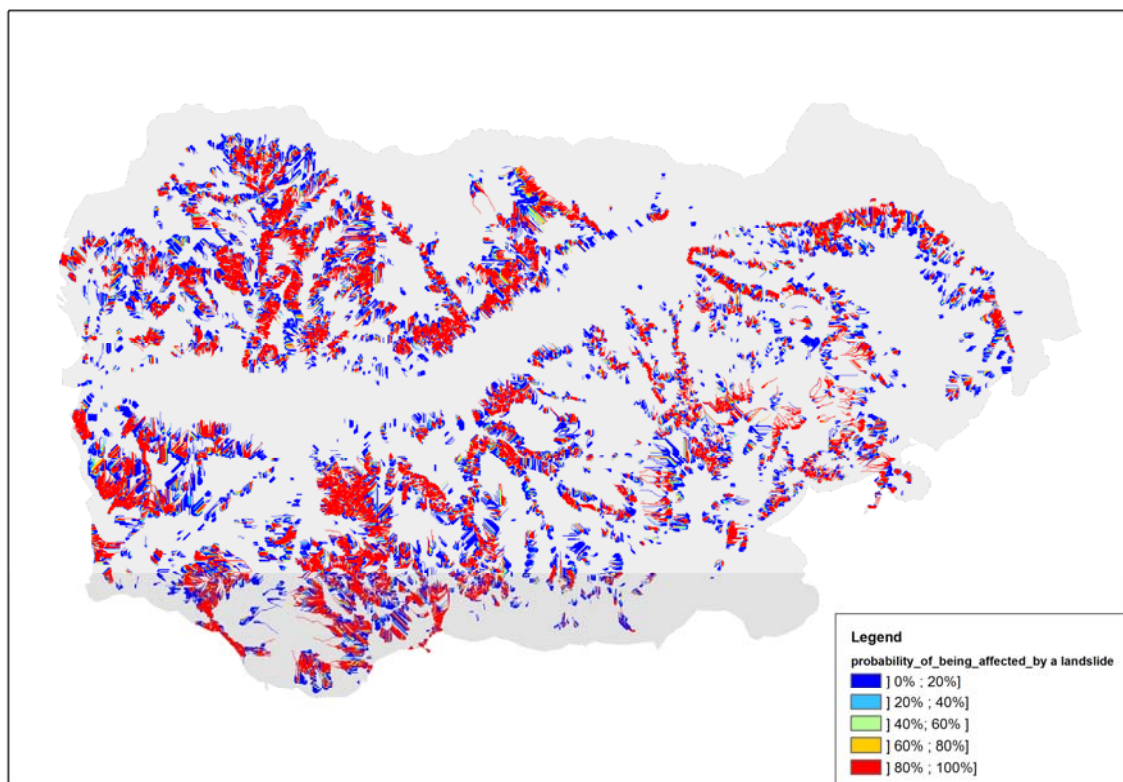


*Figure 3 Overall probability of being affected by a landslide in 2010*
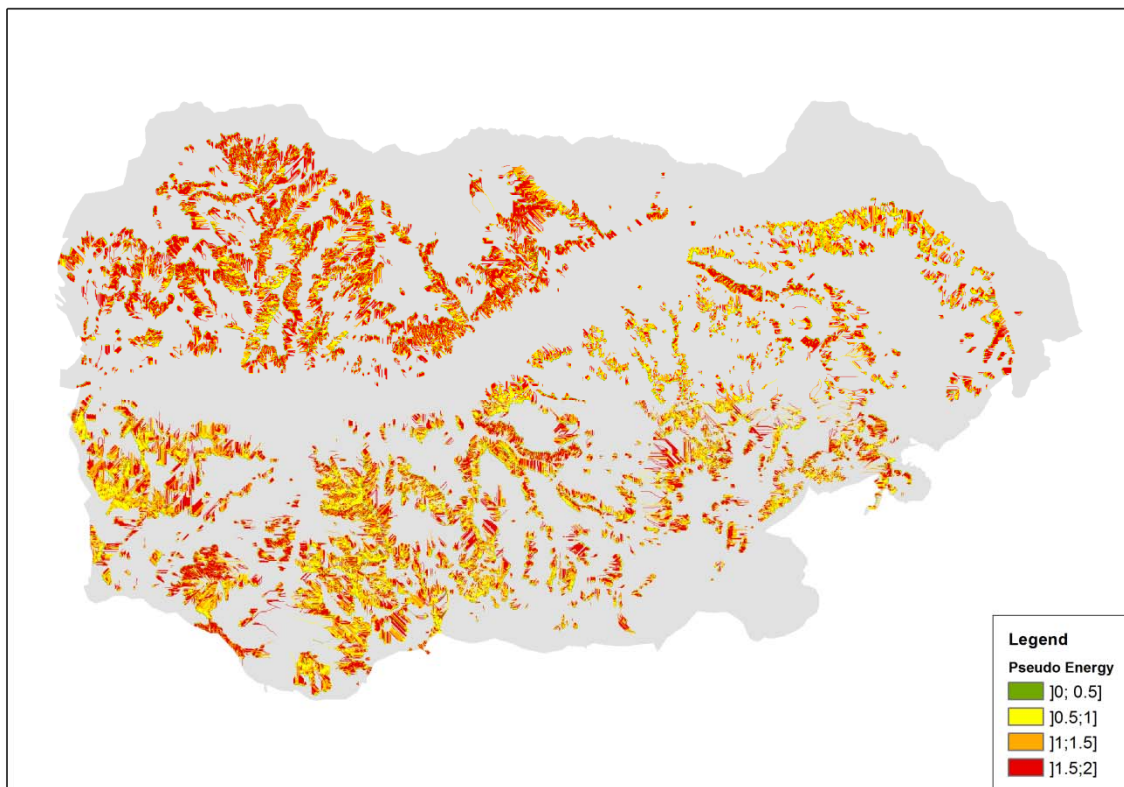
*Figure 4 Pseudo-energy of landslides in 2010*
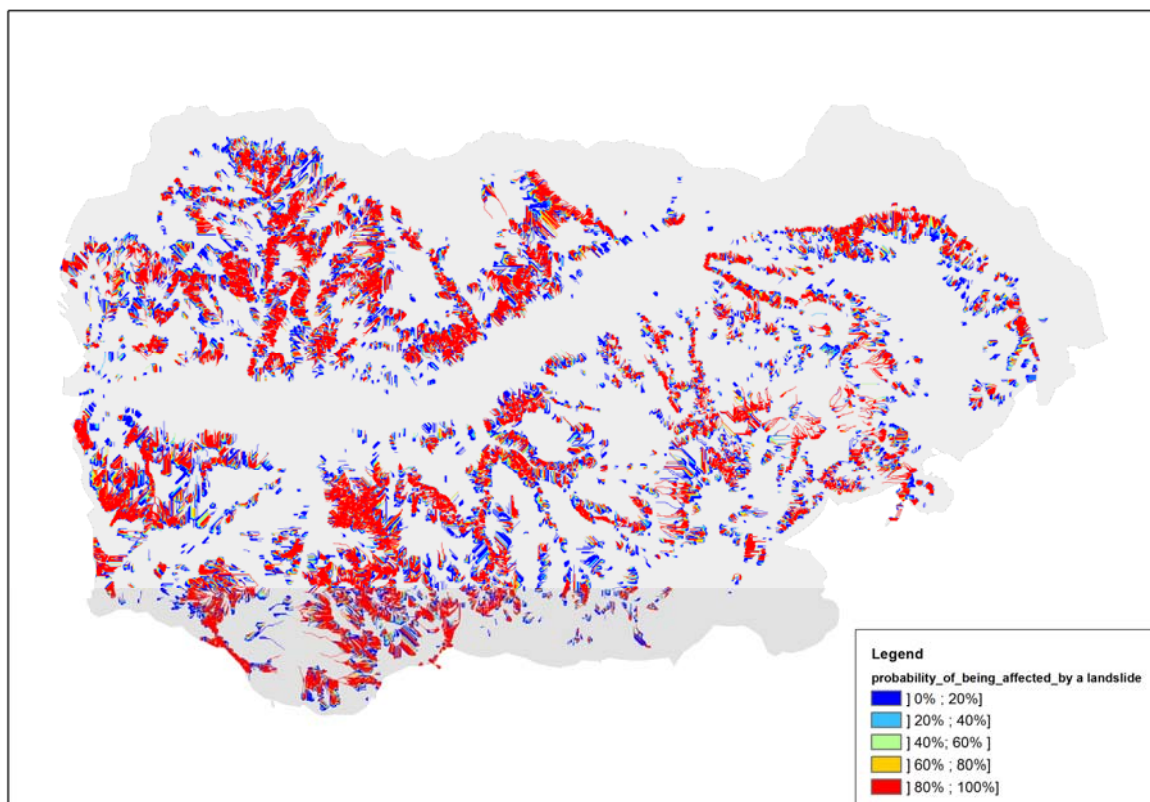


*Figure 5 Overall probability of being affected by a landslide in 2050*
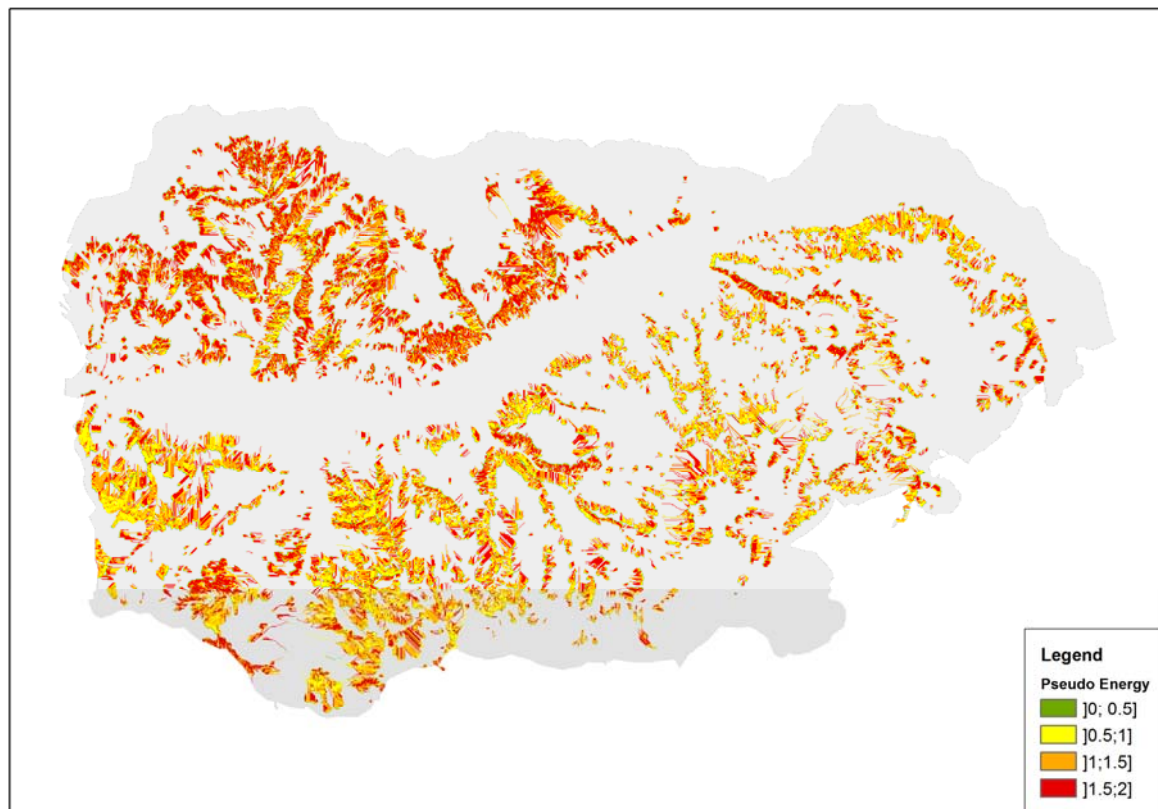
*Figure 6 Pseudo-energy of landslides in 2050*

### 1.1.2   Elements at risk

Aiming at comparing the evolution of the landslide risk in Barcelonnette from now to 2050, we decided to take into account several elements at risk:
- Roads: classified as main, secondary or minor roads and tracks;
- Buildings: since the future scenarios were not precise to that scale, they are not considered as units but as built-up areas;
- Population: census data provided the whole number of inhabitants per municipality, and then we linked this number to the built-up area of each municipality.

The overall area exposed was also considered while assessing the risk.

### 1.1.3   Vulnerability

In order to assess the landslide risk, we need to quantify vulnerability. Since the data were neither accurate nor complete on that topic (e.g. no vulnerability functions usable for masonry buildings), we decided to assess the assets' exposure more than the risk they were exposed to. Furthermore, thanks to the data provided by the BORA program, we used the overall landslide probability (including the propagation) and the pseudo- energy to obtain a sort of hazard susceptibility. It allowed us, in some degree, to go beyond the exposure in its narrow sense (whether it will be affected or not) and integrate a vulnerability concept (degree of damage due to an event). Therefore, in the following, exposure will include a part of vulnerability and will not only be the rough intersection of hazard maps and elements at stake.

## 1.1.4   2050 Data

We assumed that till 2050, no new roads will be constructed, since expansion of build-up areas is mainly focused on existing roads. That's why we analysed the same road network for current and future state. Nevertheless, we could consider an arbitrary "growing" factor for this network. If it is true that completely new roads are rarely built, some of the current ones are more often enlarged.

Concerning the built-up areas, the four scenarios used to predict the land cover changes are issued from Andrej MORAVEK's thesis "Modelling of land cover changes in the Barcelonnette basin, Alpes-de-Haute-Provence (France). The first scenario, named "Environmental protection", takes into account a very high environmental awareness leading to a very small increase of the built-up areas. The second scenario, named "Tourism progression", aims at providing more accommodations and services to tourists, and by the way, increasing the built-up areas. The third scenario, named "Agricultural recultivation", is mainly focused on the increase of agricultural activities even though since the tourism is slightly on rise, so are the built-up areas. The fourth scenario, named "Landslide hazard", is the "worst case". It takes into account many constraints that also contribute to degrading the terrain stability while increasing the proportion of built-up areas.

Risk can evolved depending on the construction of new buildings placing people in previously unoccupied areas or by more people living in the area. Since it may increase the risk, demographic changes also need to be integrated.
The data collected on demography in SafeLand Deliverable D3.6 was used as a basis for the quantification of inhabitants in the study area in 2050 as follows. The INSEE[1] provided useful information thanks to several censuses at national scale. The population surveys of seven municipalities surrounding Barcelonnette are available for six different dates (1968, 1975, 1982, 1990, 1999, and 2006). However these municipalities are quite small and the figures can be affected by single events. For example, the construction of a private housing estate or the closure of an important factory may significantly change the demographic pattern of the area. Consequently, it is impossible to estimate accurately how population will evolve in the relatively near future at this scale. This is confirmed by more global INSEE surveys, which only provide prospects at the department scale.

These prospective figures of the department population can be used to roughly estimate the population of the study area's municipalities in 2050, assuming that the population will represent the same fraction of the department population in 2006 and in 2050. This method is by no means perfect and its results depend on the year of the census data. Another prospective method, detailed in Deliverable D3.6 for 2030 prospection, could have been used to produce more reliable forecasts, and would have given maximum and minimum values for population figures. But when applied to 2050 forecasting, this method produces a very large range of values, much too large to be used. That is why we decided to stick to the first approach

---

mentioned and to apply to the seven municipalities' population a percentage +0.8% per year increase to obtain a prospective "2050 census".

## 1.2    METHODOLOGY AND RESULTS

### 1.2.1    Hazard Classes

First, we built "susceptibility matrices" by crossing pseudo-energy and the overall landslide probability. Considering that roads and buildings are not affected in the same way by landslides, we chose to define two different matrices for those two different elements at stake by attributing different weights to occurrence and energy:

1. Buildings: since the more the energy grows the more a landslide mass can have an impact, a higher weight has been attributed to energy than to occurrence probability;

2. Roads: this type of asset will react differently, traffic can be interrupted due to debris blocking the road (which can be easy to fix) or if the surface of the road itself is being washed away due a landslide initiating (which requires more time and money to re-build). For that type of asset, we decided to attribute the same weights to energy and occurrence probability, but also to consider separately the landslide occurrence probability, without propagation, to highlight the potential most impacted areas.

In order to obtain susceptibility matrices, we distributed into classes each range values of the maps provided by ALICE and BORA (probabilities and energy): class 1 to 5 for probabilities' maps (initiation and propagation) and class 10 to 50 for energy maps.

The crossing of these classes led to the definition of the following matrices (Table 2):

| Probability and energy classes | 1 | 2 | 3 | 4 | 5 |
|---|---|---|---|---|---|
| 10 | 0.1 | 0.1 | 0.1 | 0.3 | 0.5 |
| 20 | 0.3 | 0.4 | 0.5 | 0.6 | 0.7 |
| 30 | 0.5 | 0.6 | 0.7 | 0.8 | 0.9 |
| 40 | 0.6 | 0.7 | 0.8 | 0.9 | 1 |
| 50 | 0.8 | 0.9 | 1 | 1 | 1 |

| Probability and energy classes | 1 | 2 | 3 | 4 | 5 |
|---|---|---|---|---|---|
| 10 | 0.2 | 0.3 | 0.4 | 0.5 | 0.6 |
| 20 | 0.3 | 0.4 | 0.5 | 0.6 | 0.7 |
| 30 | 0.4 | 0.5 | 0.6 | 0.7 | 0.8 |
| 40 | 0.5 | 0.6 | 0.7 | 0.8 | 0.9 |
| 50 | 0.6 | 0.7 | 0.8 | 0.9 | 1 |

*Table 2 Landslide susceptibility matrices for buildings (on left) and roads (on right)*

These two matrices can also be expressed in terms of hazard classes as showed below (Table 3).

| Probability and energy classes | 1 | 2 | 3 | 4 | 5 |
|---|---|---|---|---|---|
| 10 | low | low | low | modest | medium |
| 20 | modest | modest | medium | medium | high |
| 30 | medium | medium | high | high | Very high |
| 40 | medium | high | high | Very high | Very high |
| 50 | high | Very high | Very high | Very high | Very high |

| Probability and energy classes | 1 | 2 | 3 | 4 | 5 |
|---|---|---|---|---|---|
| 10 | low | modest | modest | medium | medium |
| 20 | modest | modest | medium | medium | high |
| 30 | modest | medium | medium | high | high |
| 40 | medium | medium | high | high | Very high |
| 50 | medium | high | high | Very high | Very high |

*Table 3 Landslide hazard matrices for buildings (on left) and roads (on right)*

## 1.2.2  Road exposure

The roads network is distributed into main (18.55 km), secondary (80.45 km) or minor (104.44 km) roads and tracks (256.46 km).

Based on the crossing of the spatial distribution of the hazard classes defined previously and the road network, the percentage of each type of road exposed was evaluated in the study area. Two different exposures were calculated: the first one to direct ground instability, using the landslide occurrence probability data, generating bigger impacts and the second one to landslides (including propagation), using the overall landslide probability and pseudo-energy data.

The following maps and tables show the differences between those two approaches. Below each set of map, a table presents the representative susceptibility (which stands for the main level of hazard, in terms of linear kilometres) for each type of road, excluding the low class.

## Current state : Roads' exposure

**Landslides' occurence probability**
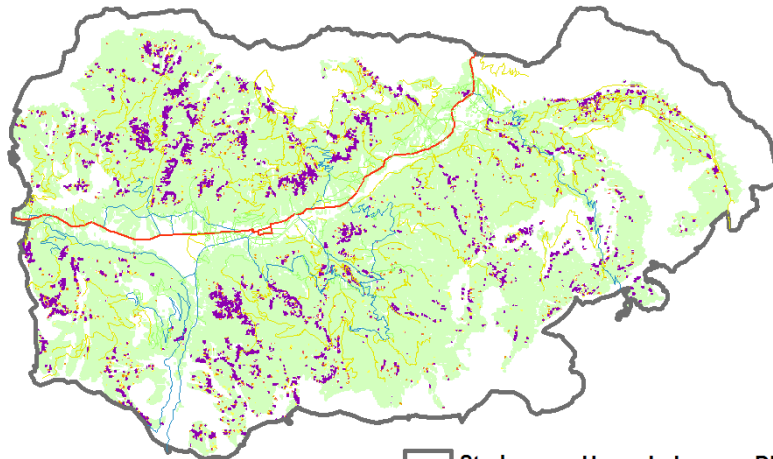
N

**Landslides' hazard**

Study area    **Hazard classes**    **DEM 10 m**
**Roads**                        0         High : 3030
— Main                           1
— Secondary                      2         Low : 1072
— Minor                          3
— Track                          4

1:100 000

0        3        6
|_____|_____| Km
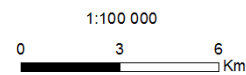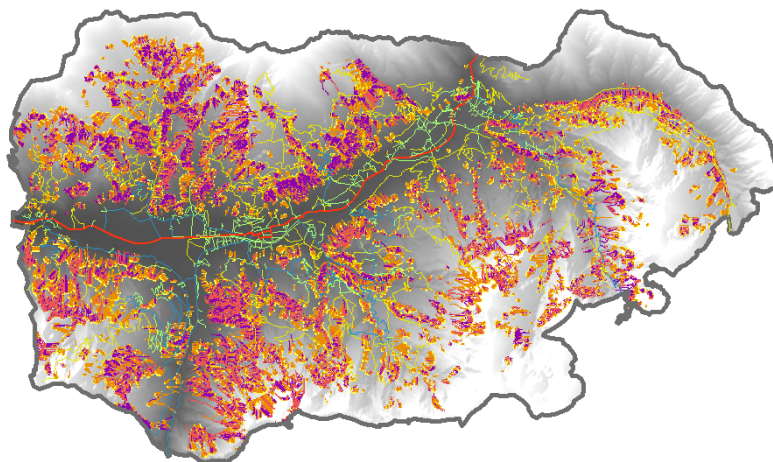
| | **Representative level of hazard** | |
|---|---|---|
| | OCCURRENCE PROBABILITY | HAZARD |
| **Main road** | null or low | modest |
| **Secondary road** | very high | medium |
| **Minor road** | medium | medium |
| **Track** | medium | medium |

2050 prediction : Roads' exposure
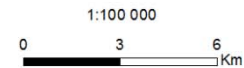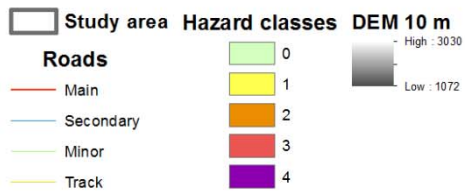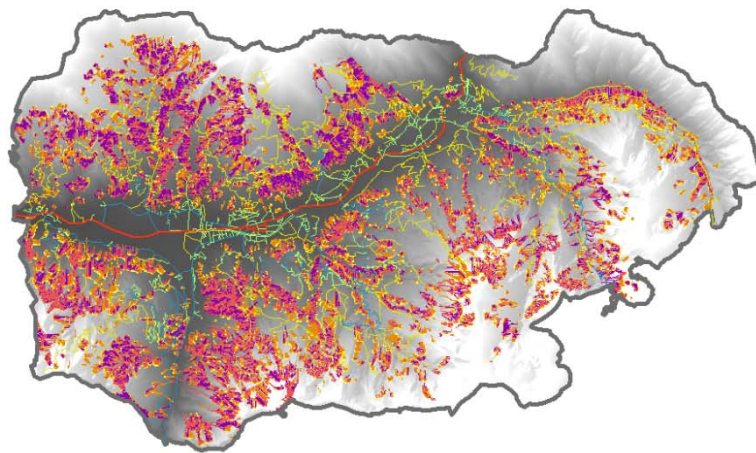
| | Representative level of hazard | |
|---|---|---|
| | OCCURRENCE PROBABILITY | HAZARD |
| **Main road** | modest | high |
| **Secondary road** | very high | medium |
| **Minor road** | modest | medium |
| **Track** | very high | medium |

We can already see that currently few roads are exposed to direct impacts whereas it is meant to increase in 2050, especially for tracks (mainly located uphill).
The following tables present the linear kilometers exposed to each type of hazard for each type of road.

| Hazard class ↓ | 2010 | | | | 2050 | | | | Ratio 2050 to 2010 | | | |
|---|---|---|---|---|---|---|---|---|---|---|---|---|
| | Main road | Secondary road | Minor road | Track | Main road | Secondary road | Minor road | Track | Main road | Secondary road | Minor road | Track |
| Modest | 0.08 | 2.73 | 2.17 | 12.99 | 0.08 | 2.14 | 1.81 | 10.46 | 1.00 | 0.78 | 0.83 | 0.80 |
| Medium | 0.03 | 7.86 | 4.19 | 31.14 | 0.02 | 6.00 | 3.94 | 25.11 | 0.61 | 0.76 | 0.94 | 0.81 |
| High | 0.08 | 4.22 | 0.73 | 19.89 | 0.09 | 5.84 | 1.19 | 23.94 | 1.13 | 1.39 | 1.64 | 1.20 |
| Very High | 0.00 | 2.83 | 0.41 | 12.20 | 0.00 | 3.39 | 0.62 | 15.92 | - | 1.20 | 1.50 | 1.30 |
| **Total →** | **0.19** | **17.64** | **7.51** | **76.22** | **0.18** | **17.37** | **7.56** | **75.42** | 0.99 | 0.98 | 1.01 | 0.99 |
| **% of total type linear** | **1.0** | **21.9** | **7.2** | **29.7** | **1.0** | **21.6** | **7.2** | **29.4** | - | - | - | - |
| **% of total network** | **0.2** | **4.8** | **1.6** | **6.5** | **0.2** | **4.7** | **1.6** | **6.4** | - | - | - | - |

*Table 4 Evolution of roads' overall exposure (in linear kilometres)*

If we consider the overall exposure of the roads' network, we can notice a few changes:
- For each type of road, the total amount of exposed kilometres remains the same in 2010 and in 2050;
- Roads exposed to modest and medium hazard are expected to experiment a decrease (green cells of the table) in the number of kilometers impacted whereas roads exposed to high and very high hazard are expected to experiment an increase (red cells of the table) in the number of kilometres impacted.

It is quite different if we consider only the landslides occurrence probability, which means that the roads exposed will be more severely impacted when effectively concerned. The Table 5 shows that there is an important increase expected in the rate of tracks impacted.
In this second table we notice that the total amount of exposed kilometres is expected to increase in 2050 with a much more important increase for tracks at very high risk.
Moreover, if we consider that part of the tracks and minor roads are expected to be enlarged and by the way considered as bigger assets, this conclusion may be a little disturbing.

| Hazard class ↓ | 2010 | | | | 2050 | | | | Ratio 2050 to 2010 | | | |
|---|---|---|---|---|---|---|---|---|---|---|---|---|
| | Main road | Secondary road | Minor road | Track | Main road | Secondary road | Minor road | Track | Main road | Secondary road | Minor road | Track |
| Modest | 0.00 | 0.60 | 0.15 | 0.15 | 0.05 | 1.04 | 0.42 | 4.96 | - | 1.74 | 2.73 | 32.43 |
| Medium | 0.00 | 0.34 | 0.20 | 0.20 | 0.00 | 0.48 | 0.28 | 2.63 | - | 1.43 | 1.40 | 13.28 |
| High | 0.00 | 0.19 | 0.06 | 0.06 | 0.00 | 0.26 | 0.03 | 0.90 | - | 1.36 | 0.51 | 14.67 |
| Very High | 0.00 | 1.96 | 0.14 | 0.14 | 0.00 | 2.19 | 0.19 | 10.49 | - | 1.11 | 1.35 | 73.84 |
| **Total →** | **0.00** | **3.09** | **0.55** | **0.55** | **0.05** | **3.97** | **0.92** | **18.97** | **-** | **1.28** | **1.66** | **34.25** |
| **% of total type linear** | **0.0** | **3.8** | **0.5** | **0.2** | **0.3** | **4.9** | **0.9** | **7.4** | | | | |
| **% of total type linear** | **0.0** | **0.8** | **0.1** | **0.0** | **0.1** | **1.1** | **0.2** | **1.6** | | | | |

*Table 5 Evolution of roads' exposure to landslides occurrence (in linear kilometres)*

### 1.2.3  Build-up areas and human exposure

The following maps present the spatial distribution of landslide hazards using the specific matrix developed previously for buildings (using the overall landslide probability and pseudo-energy data) and the built-up areas in the study area taken into account in 2010 and in 2050 (four different scenarios). The "2050 hazard" layer remains the same for all the four scenarios.

2050 prediction : Exposure of built-up areas
Scenario 2



2050 prediction : Exposure of built-up areas
Scenario 3
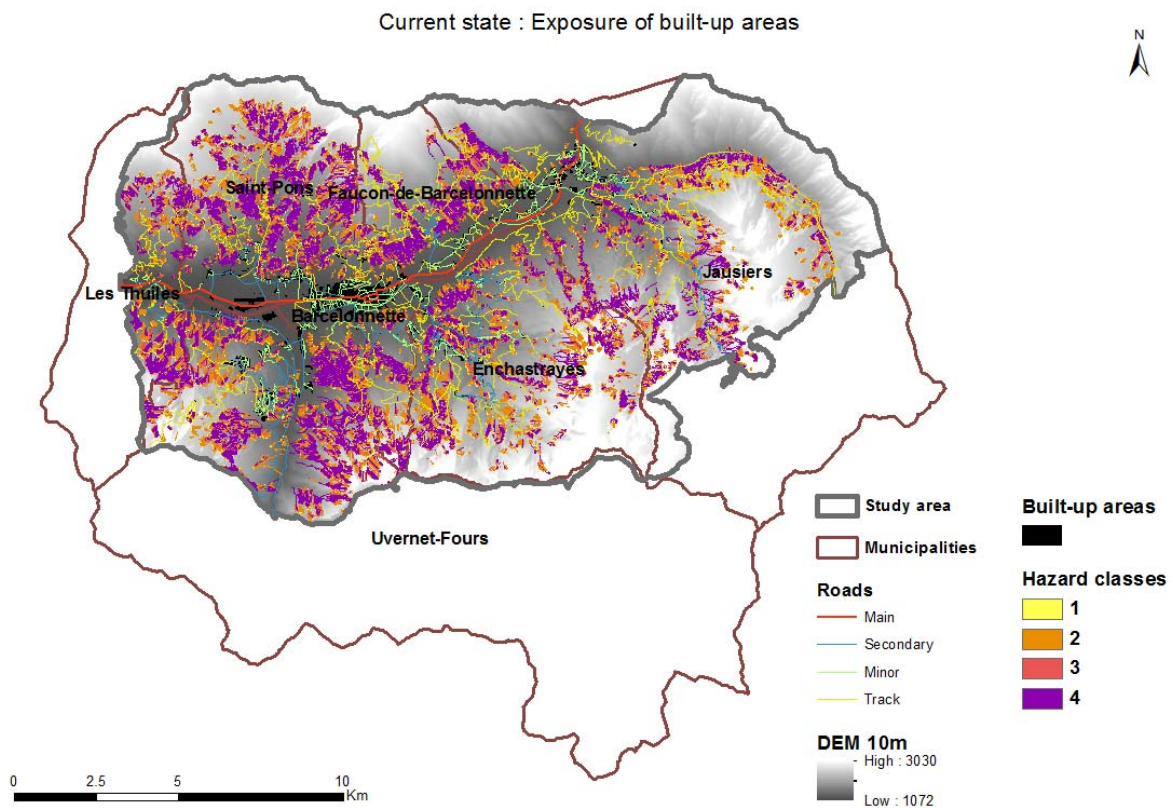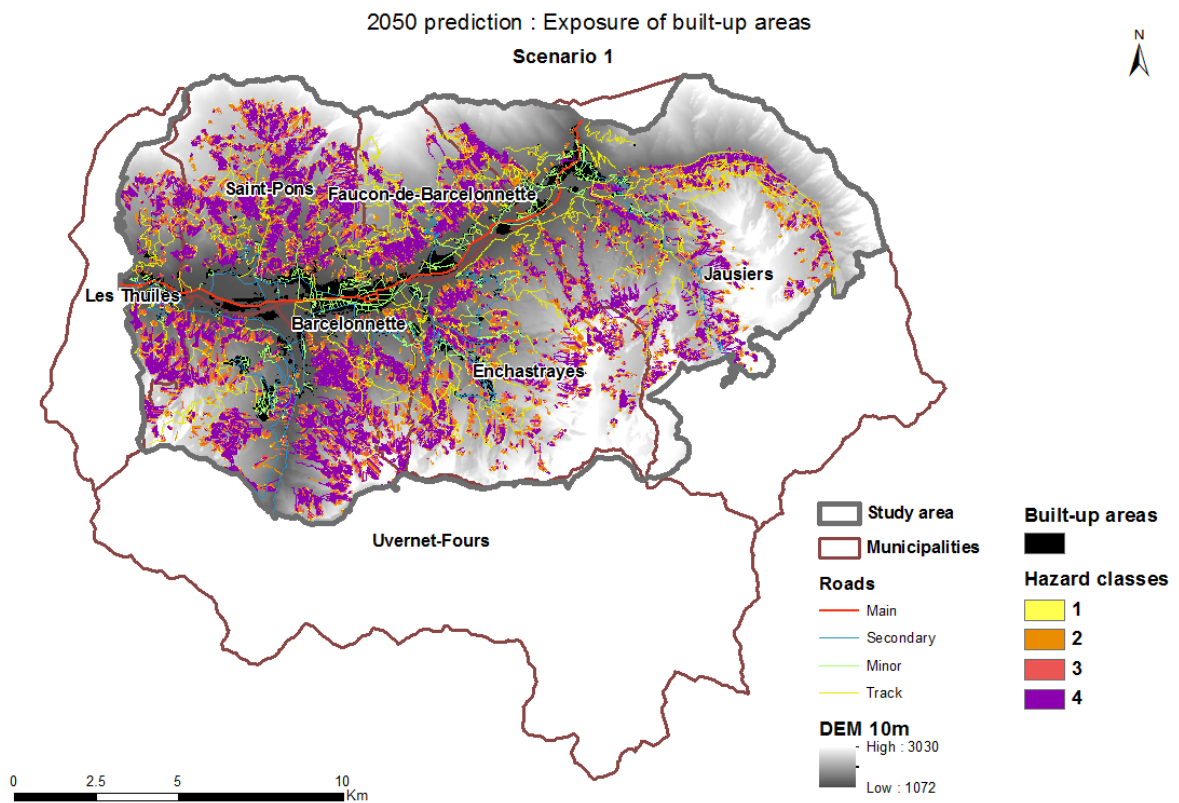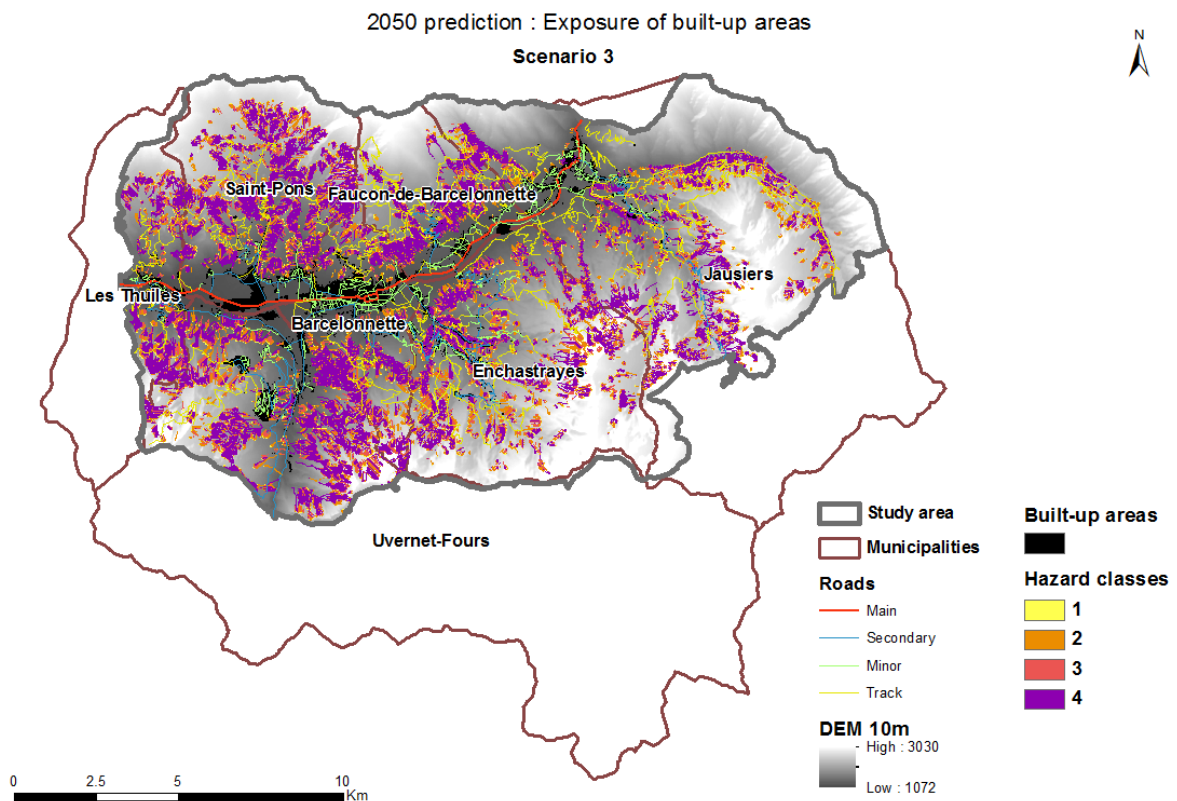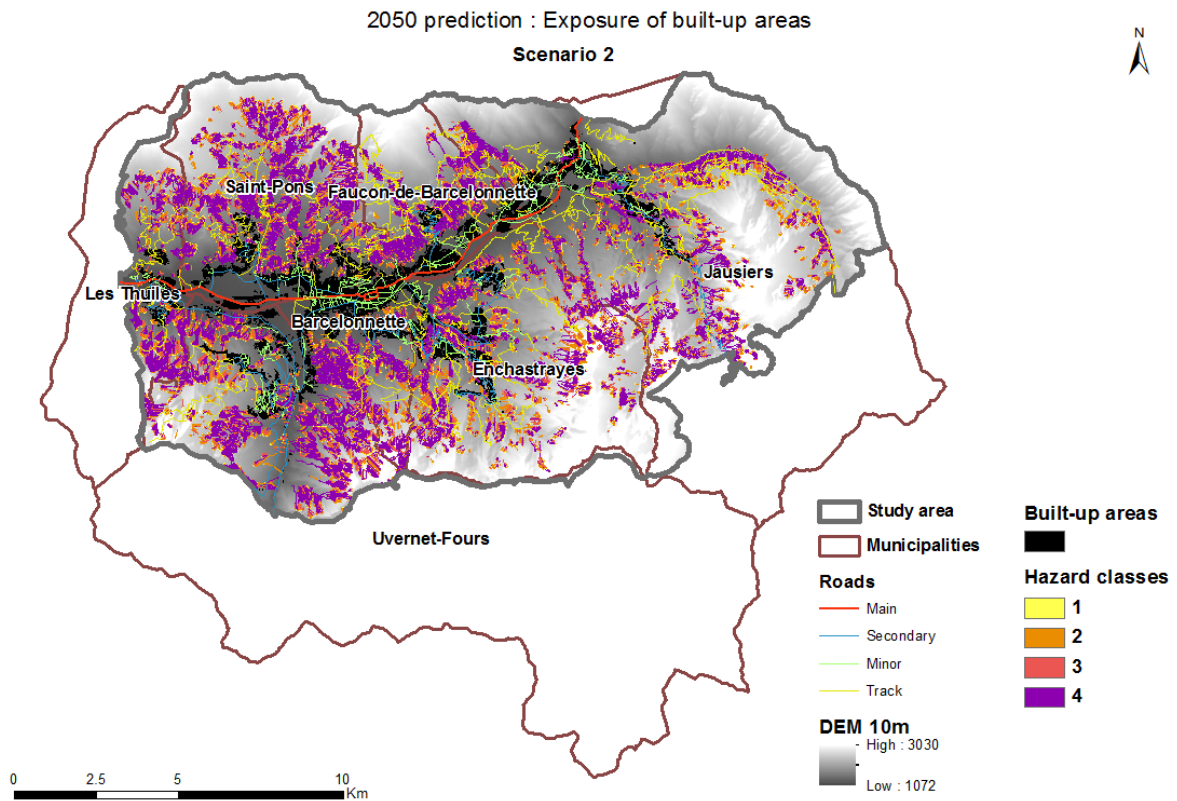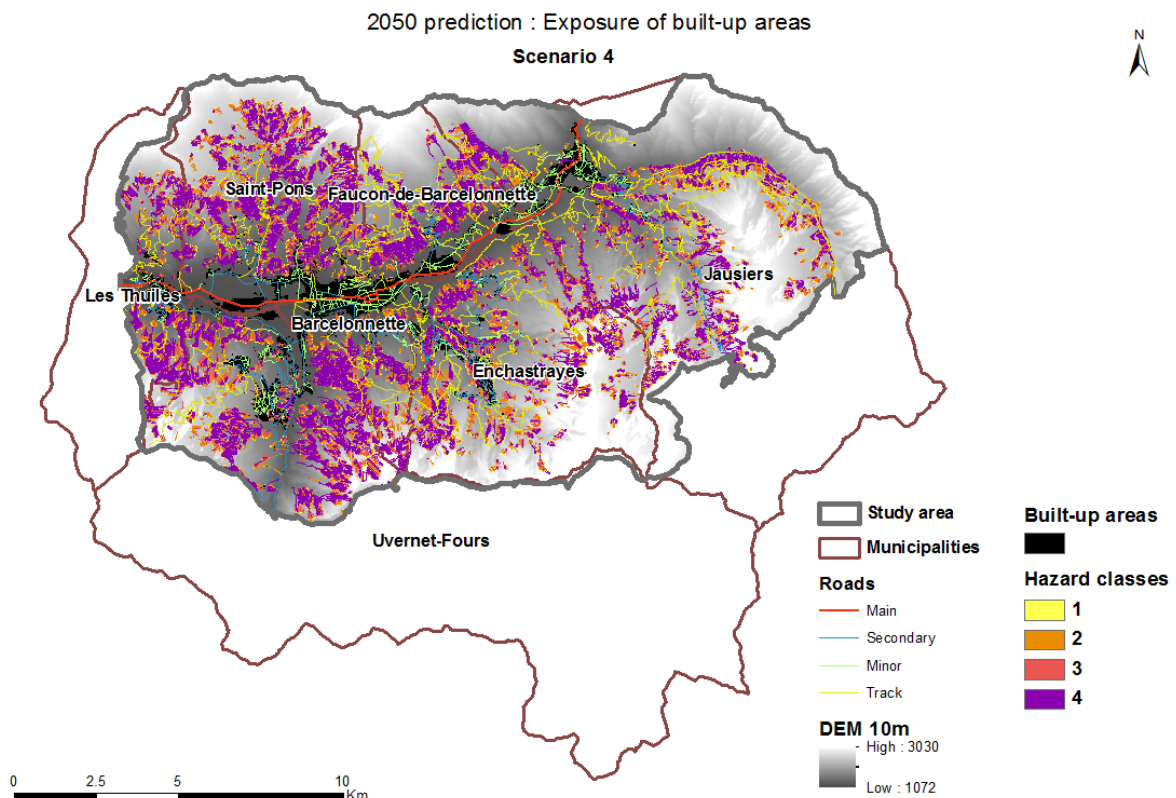
Changes are not obvious on these maps over the period 2010-2050. But in order to make some evolutions more readable, we led three different analysis on the basis of the crossing of the spatial distribution of the hazard classes defined previously and :

- the surface of the municipalities intersecting the study area: it allows to know for each class of hazard and municipality, the global surfaces impacted whatever the land-use;
- the built-up areas: it allows to focus the risk study to the urban assets independently from the population;
- the population: knowing the occupation rate of the previous buildings, a number of exposed inhabitants was calculated for each class of hazard.

The following tables (Table 6 to Table 9) show the evolution between 2010 and 2050 for those three approaches.

## Global surfaces' exposure:

The study area includes 7 municipalities, three of them being only partially intersected by our data: *Uvernet-Fours*, *Jausiers* and *Les Thuiles*.

| Municipality Name | Global Surface (ha) | Intersection with study area (%) | Studied surface (ha) |
|---|---|---|---|
| Uvernet-Fours | 13 572.20 | 23.71 | 3 217.93 |
| Saint-Pons | 3 206.94 | 100.00 | 3 206.94 |
| Les Thuiles | 3 268.63 | 38.62 | 1 262.26 |
| Faucon-de-Barcelonnette | 1 722.22 | 100.00 | 1 722.22 |
| Jausiers | 10 826.20 | 66.01 | 7 145.90 |
| Enchastrayes | 4 443.81 | 100.00 | 4 443.81 |
| Barcelonnette | 1 657.43 | 100.00 | 1 657.43 |

*Table 6 Surface (in ha) studied for each municipality*

For this analysis, the results will be the same for the four scenarios of future land-use planning, that is why only one figure is given for the 2050 exposure. The following tables present the overall surface (in ha) exposed to each type of hazard for each municipality.

| Hazard class ↓ | BARCELONNETTE | | | ENCHASTRAYES | | |
|---|---|---|---|---|---|---|
| | 2010 | 2050 | Ratio 2050 to 2010 | 2010 | 2050 | Ratio 2050 to 2010 |
| Modest | 26.91 | 27.03 | 1.00 | 82.49 | 80.75 | 0.98 |
| Medium | 193.39 | 128.82 | 0.67 | 510.72 | 332.91 | 0.65 |
| High | 64.20 | 93.04 | 1.45 | 180.02 | 253.93 | 1.41 |
| Very High | 239.96 | 274.12 | 1.14 | 488.37 | 584.75 | 1.20 |
| Total → | 524.46 | 523.01 | 1.00 | 1 261.60 | 1 252.34 | 0.99 |
| % of total studied surface | 31.64 | 31.56 | | 28.39 | 28.18 | |

*Table 7 Evolution of studied surface's overall exposure (in ha) for the municipalities of Barcelonnette and Enchastrayes*

| Hazard class ↓ | FAUCON | | | JAUSIERS | | |
|---|---|---|---|---|---|---|
| | 2010 | 2050 | Ratio 2050 to 2010 | 2010 | 2050 | Ratio 2050 to 2010 |
| Modest | 19.92 | 18.93 | 0.95 | 89.38 | 86.54 | 0.97 |
| Medium | 118.49 | 78.57 | 0.66 | 467.59 | 301.81 | 0.65 |
| High | 51.09 | 60.40 | 1.18 | 177.24 | 240.93 | 1.36 |
| Very High | 240.48 | 272.62 | 1.13 | 606.72 | 700.51 | 1.15 |
| Total → | 429.98 | 430.52 | 1.00 | 1 340.93 | 1 329.79 | 0.99 |
| % of total studied surface | 24.97 | 25.00 | | 18.77 | 18.61 | |

*Table 8 Evolution of studied surface's overall exposure (in ha) for the municipalities of Faucon and Jausiers*

| Hazard class ↓ | LES THUILES | | | SAINT-PONS | | | UVERNET-FOURS | | |
|---|---|---|---|---|---|---|---|---|---|
| | 2010 | 2050 | Ratio 2050 to 2010 | 2010 | 2050 | Ratio 2050 to 2010 | 2010 | 2050 | Ratio 2050 to 2010 |
| Modest | 23.80 | 23.76 | 1.00 | 66.55 | 65.38 | 0.98 | 52.40 | 51.42 | 0.98 |
| Medium | 147.62 | 87.87 | 0.60 | 349.35 | 219.89 | 0.63 | 402.78 | 239.86 | 0.60 |
| High | 62.23 | 84.06 | 1.35 | 149.83 | 190.04 | 1.27 | 158.94 | 219.72 | 1.38 |
| Very High | 227.65 | 264.31 | 1.16 | 648.53 | 740.17 | 1.14 | 609.18 | 708.62 | 1.16 |
| Total → | 461.30 | 460.00 | 1.00 | 1 214.26 | 1 215.48 | 1.00 | 1 223.30 | 1 219.62 | 1.00 |
| % of total studied surface | 36.55 | 36.44 | | 37.87 | 37.90 | | 38.02 | 37.90 | |

*Table 9 Evolution of studied surface's overall exposure (in ha) for the municipalities of Les Thuiles, Saint-Pons and Uvernet-Fours*

All the municipalities are approximately impacted in the same way if we only consider the global surface exposed: it is comprised between 20 and 40% of the overall surface studied. When looking at the distribution between the different classes of hazard, we can see that only a small percentage of the surface exposed is dealing with a modest hazard (4 to 7% depending on the municipalities) whereas the main part of the surface exposed is dealing with a very high hazard (38 for Enchastrayes to 56% for Faucon, depending on the municipalities). The remaining surfaces are exposed mainly to medium hazard, at least twice as much as to high hazard.

If we consider the overall exposure of the studied surface of the seven municipalities in 2010 and in 2050, we can notice a few changes:

- For each municipality, the global surface exposed (in ha) remains the same in 2010 and in 2050;
- For each municipality, the surface exposed to modest hazard is expected to remain quite the same in 2010 and 2050;
- For each municipality, the surface exposed to medium hazard is expected to experiment a decrease (green cells of the table) of about 30 to 40%;
- For each municipality, surfaces exposed to high and very high hazard are expected to experiment an increase (red cells of the table) of at least 15% for the very high hazard class. This increase is expected to be even more important for the high hazard class.

The Table 10 presents the representative susceptibility (which stands for the main level of hazard, in terms of areas) for each municipality, excluding the low class.

| | Representative level of hazard | |
|---|---|---|
| **Municipality Name** | **2010** | **2050** |
| Barcelonnette | very high | very high |
| Enchastrayes | medium | very high |
| Faucon | very high | very high |
| Jausiers | very high | very high |
| Les Thuiles | very high | very high |
| Saint-Pons | very high | very high |
| Uvernet-Fours | very high | very high |

*Table 10 Evolution of municipalities' representative level of hazard*

The representative level of hazard is not discriminant at this stage because of the areas considered: the overall surface exposed. The only municipality exposed to a representative medium hazard and not to a very high one is *Enchastrayes* in 2010. Due to the global trends detailed previously, this representative level is upgraded to very high in 2050. It is consistent with the hypothesis made previously during the use of Alice or Bora and for the elaboration of the susceptibility matrix.

**Built-up areas' exposure:**

On the study area, all 7 municipalities include built-up areas. That is the asset we are going to consider now. For the current state, the built-up areas are issued from 2 data bases (2009 and 2011) provided by the CNRS and can be considered to be quite accurate, except for *Les Thuiles*. The original data did not cover this municipality; therefore we decided to use the 2006 Corine Land Cover data to assess a rough built-up area. That is why the figure for *Les Thuiles* in 2010 is over estimated comparatively to the other municipalities' figures.

| | Built-up areas (sq. m) | | | | |
|---|---|---|---|---|---|
| **Municipality Name** | **2010** | **2050 Scenario 1** | **2050 Scenario 2** | **2050 Scenario 3** | **2050 Scenario 4** |
| Uvernet-Fours | 637 700 | 294 000 | 533 600 | 348 100 | 402 900 |
| Saint-Pons | 644 000 | 293 700 | 600 800 | 404 600 | 374 900 |
| Les Thuiles | 396 600 | 106 200 | 234 600 | 120 800 | 149 200 |
| Faucon-de-Barcelonnette | 244 400 | 239 900 | 526 200 | 175 000 | 275 500 |
| Jausiers | 839 900 | 439 700 | 861 900 | 390 500 | 481 700 |
| Enchastrayes | 469 900 | 266 000 | 674 500 | 232 400 | 327 700 |
| Barcelonnette | 1 704 400 | 627 200 | 1 065 200 | 584 900 | 730 100 |

*Table 11 Built-up areas (in sq. m) studied for each municipality*

For this analysis, the four scenarios of future land-use planning detailed previously are going to be considered, that's why four different figures are given for the 2050 built-up areas and below for the exposure.

The following tables (Table 12 to Table 18) present the built-up areas (in square meters) exposed to each type of hazard for each municipality.

| BARCELONNETTE Hazard class ↓ | 2010 | 2050 | | | | Ratio 2050 to 2010 | | | |
|---|---|---|---|---|---|---|---|---|---|
| | | Sc. 1 | Sc. 2 | Sc. 3 | Sc. 4 | Sc. 1 | Sc. 2 | Sc. 3 | Sc. 4 |
| Modest | 1 300 | 1 100 | 5 900 | 1 300 | 1 700 | 0.85 | 4.54 | 1.00 | 1.31 |
| Medium | 10 000 | 3 800 | 17 000 | 10 700 | 6 400 | 0.38 | 1.70 | 1.07 | 0.64 |
| High | 400 | 3 300 | 13 600 | 5 800 | 4 500 | 8.25 | 34.00 | 14.50 | 11.25 |
| Very High | 1 900 | 1 900 | 5 100 | 3 000 | 2 300 | 1.00 | 2.68 | 1.58 | 1.21 |
| Total → | 13 600 | 10 100 | 41 600 | 20 800 | 14 900 | 0.74 | 3.06 | 1.53 | 1.10 |
| % of global built-up areas | 0.80 | 1.61 | 3.91 | 3.56 | 2.04 | | | | |

*Table 12 Evolution of studied built-up areas' overall exposure (in sq. m) for the municipality of Barcelonnette*

| ENCHASTRAYES Hazard class ↓ | 2010 | 2050 | | | | Ratio 2050 to 2010 | | | |
|---|---|---|---|---|---|---|---|---|---|
| | | Sc. 1 | Sc. 2 | Sc. 3 | Sc. 4 | Sc. 1 | Sc. 2 | Sc. 3 | Sc. 4 |
| Modest | 15 400 | 5 800 | 13 700 | 4 500 | 7 200 | 0.38 | 0.89 | 0.29 | 0.47 |
| Medium | 34 600 | 10 700 | 27 600 | 15 200 | 16 600 | 0.31 | 0.80 | 0.44 | 0.48 |
| High | 2 100 | 3 000 | 14 500 | 6 300 | 7 300 | 1.43 | 6.90 | 3.00 | 3.48 |
| Very High | 1 200 | 5 300 | 37 400 | 18 000 | 13 200 | 4.42 | 31.17 | 15.00 | 11.00 |
| Total → | 53 300 | 24 800 | 93 200 | 44 000 | 44 300 | 0.47 | 1.75 | 0.83 | 0.83 |
| % of global built-up areas | 11.34 | 9.32 | 13.82 | 18.93 | 13.52 | | | | |

*Table 13 Evolution of studied built-up areas' overall exposure (in sq. m) for the municipality of Enchastrayes*

| FAUCON Hazard class ↓ | 2010 | 2050 | | | | Ratio 2050 to 2010 | | | |
|---|---|---|---|---|---|---|---|---|---|
| | | Sc. 1 | Sc. 2 | Sc. 3 | Sc. 4 | Sc. 1 | Sc. 2 | Sc. 3 | Sc. 4 |
| Modest | 200 | 300 | 1 600 | 600 | 1 000 | 1.50 | 8.00 | 3.00 | 5.00 |
| Medium | 1 400 | 700 | 5 700 | 1 100 | 1 000 | 0.50 | 4.07 | 0.79 | 0.71 |
| High | 200 | 500 | 4 900 | 900 | 1 800 | 2.50 | 24.50 | 4.50 | 9.00 |
| Very High | 400 | 200 | 5 900 | 1 600 | 2 500 | 0.50 | 14.75 | 4.00 | 6.25 |
| Total → | 2 200 | 1 700 | 18 100 | 4 200 | 6 300 | 0.77 | 8.23 | 1.91 | 2.86 |
| % of global built-up areas | 0.90 | 0.71 | 3.44 | 2.40 | 2.29 | | | | |

*Table 14 Evolution of studied built-up areas' overall exposure (in sq. m) for the municipality of Faucon*

| JAUSIERS Hazard class ↓ | 2010 | 2050 | | | | Ratio 2050 to 2010 | | | |
|---|---|---|---|---|---|---|---|---|---|
| | | Sc. 1 | Sc. 2 | Sc. 3 | Sc. 4 | Sc. 1 | Sc. 2 | Sc. 3 | Sc. 4 |
| Modest | 7 400 | 1 500 | 8 100 | 1 800 | 2 400 | 0.20 | 1.09 | 0.24 | 0.32 |
| Medium | 22 500 | 8 500 | 32 000 | 12 100 | 13 200 | 0.38 | 1.42 | 0.54 | 0.59 |
| High | 7 400 | 3 300 | 16 700 | 5 000 | 4 000 | 0.45 | 2.26 | 0.68 | 0.54 |
| Very High | 15 300 | 12 600 | 31 900 | 23 700 | 13 600 | 0.82 | 2.08 | 1.55 | 0.89 |
| Total → | 52 600 | 25 900 | 88 700 | 42 600 | 33 200 | 0.49 | 1.69 | 0.81 | 0.63 |
| % of global built-up areas | 6.26 | 5.89 | 10.29 | 10.91 | 6.89 | | | | |

*Table 15 Evolution of studied built-up areas' overall exposure (in sq. m) for the municipality of Jausiers*

| LES THUILES Hazard class ↓ | 2010 | 2050 | | | | Ratio 2050 to 2010 | | | |
|---|---|---|---|---|---|---|---|---|---|
| | | Sc. 1 | Sc. 2 | Sc. 3 | Sc. 4 | Sc. 1 | Sc. 2 | Sc. 3 | Sc. 4 |
| Modest | 6 700 | 1 300 | 2 800 | 600 | 1 700 | 0.19 | 0.42 | 0.09 | 0.25 |
| Medium | 28 100 | 6 900 | 18 500 | 7 200 | 12 200 | 0.25 | 0.66 | 0.26 | 0.43 |
| High | 3 800 | 1 300 | 9 800 | 1 700 | 3 300 | 0.34 | 2.58 | 0.45 | 0.87 |
| Very High | 400 | 600 | 3 300 | 1 100 | 3 100 | 1.50 | 8.25 | 2.75 | 7.75 |
| Total → | 39 000 | 10 100 | 34 400 | 10 600 | 20 300 | 0.26 | 0.88 | 0.27 | 0.52 |
| % of global built-up areas | 9.83 | 9.51 | 14.66 | 8.77 | 13.61 | | | | |

*Table 16 Evolution of studied built-up areas' overall exposure (in sq. m) for the municipality of Les Thuiles*

| SAINT-PONS Hazard class ↓ | 2010 | 2050 | | | | Ratio 2050 to 2010 | | | |
|---|---|---|---|---|---|---|---|---|---|
| | | Sc. 1 | Sc. 2 | Sc. 3 | Sc. 4 | Sc. 1 | Sc. 2 | Sc. 3 | Sc. 4 |
| Modest | 200 | 300 | 2 200 | 1 100 | 600 | 1.50 | 11.00 | 5.50 | 3.00 |
| Medium | 8 900 | 4 400 | 13 000 | 5 000 | 7 600 | 0.49 | 1.46 | 0.56 | 0.85 |
| High | 300 | 300 | 4 300 | 1 400 | 2 100 | 1.00 | 14.33 | 4.67 | 7.00 |
| Very High | 2 800 | 2 200 | 11 600 | 6 400 | 6 700 | 0.79 | 4.14 | 2.29 | 2.39 |
| Total → | 12 200 | 7 200 | 31 100 | 13 900 | 17 000 | 0.59 | 2.55 | 1.14 | 1.39 |
| % of global built-up areas | 1.89 | 2.45 | 5.18 | 3.44 | 4.53 | | | | |

*Table 17 Evolution of studied built-up areas' overall exposure (in sq. m) for the municipality of Saint-Pons*

| UVERNET-FOURS Hazard class ↓ | 2010 | 2050 | | | | Ratio 2050 to 2010 | | | |
|---|---|---|---|---|---|---|---|---|---|
| | | Sc. 1 | Sc. 2 | Sc. 3 | Sc. 4 | Sc. 1 | Sc. 2 | Sc. 3 | Sc. 4 |
| Modest | 6 500 | 5 000 | 7 900 | 5 800 | 7 400 | 0.77 | 1.22 | 0.89 | 1.14 |
| Medium | 15 600 | 7 200 | 22 600 | 10 000 | 16 400 | 0.46 | 1.45 | 0.64 | 1.05 |
| High | 2 200 | 4 000 | 9 300 | 5 900 | 9 300 | 1.82 | 4.23 | 2.68 | 4.23 |
| Very High | 3 200 | 3 500 | 12 600 | 9 200 | 14 000 | 1.09 | 3.94 | 2.88 | 4.38 |
| Total → | 27 500 | 19 700 | 52 400 | 30 900 | 47 100 | 0.72 | 1.91 | 1.12 | 1.71 |
| % of global built-up areas | 4.31 | 6.70 | 9.82 | 8.88 | 11.69 | | | | |

*Table 18 Evolution of studied built-up areas' overall exposure (in sq. m) for the municipality of Uvernet-Fours*

Depending on the municipality and the 2050 scenario considered, there is no global trend to the evolution of built-up areas' exposure between 2010 and 2050. Currently, the most exposed municipalities, in terms of percentage of built-up areas, are *Enchastrayes* (11% of the built-up areas exposed), *Jausiers* (6% of the built-up areas exposed) and *Les Thuiles* (10% of the built-up areas exposed). Some evolution trends can then be defined, one scenario at a time:

- Scenario 1: the global built-up area exposed is expected to decrease, more or less depending on the municipality, in 2050. Thus, areas exposed to high and / or very high hazard are expected to experiment an increase in particular for *Barcelonnette*, *Enchastrayes*, *Faucon*, *Les Thuiles* and *Uvernet-Fours*. *Enchastrayes* (9% of the built-up areas exposed), *Jausiers* (6% of the built-up areas exposed) and *Les Thuiles* (9% of the built-up areas exposed) remain the most exposed municipalities in terms of percentage of built-up areas, but *Uvernet-Fours* is joining them with almost 7% of the built-up areas exposed;

- Scenario 2: Apart from *Les Thuiles* (not particularly relevant due to the rough assessment of the built-up areas in 2010), the global built-up area exposed is expected to increase, more or less depending on the municipality, in 2050. It is worth noticing that in *Barcelonnette*, *Enchastrayes*, *Faucon* and to a lesser extent in *Saint-Pons*, the areas exposed to high and / or very high hazard are expected to experiment a huge increase (up to 30% in the first two municipalities). *Enchastrayes* (14% of the built-up areas exposed), *Jausiers* (10% of the built-up areas exposed) and *Les Thuiles* (15% of the built-up areas exposed) remain the most exposed municipalities in terms of percentage of built-up areas, but *Uvernet-Fours* is joining them with almost 10% of the built-up areas exposed. It is globally the worst scenario in terms of increasing the exposed built-up areas for all the municipalities;

- Scenario 3: depending on the municipalities considered, the global built-up area exposed is expected to experiment in 2050 a slight increase or decrease, from -40%

(*Jausiers*) to +40% (*Saint-Pons*) or even +70% (*Uvernet-Fours*). The global increase expected is much more important for *Faucon*. Due to the assessment of the 2010 built-up areas, *Les Thuiles* is a particular case not taken into account here. There is no global pattern obvious in the evolution of the hazard classes' distribution. For example, the areas exposed to high hazard in *Barcelonnette*, *Faucon* and *Saint-Pons* or to very high hazard in *Enchastrayes* are expected to experiment huge increases whereas the areas exposed to medium hazard are expected to globally experiment decreases in all the municipalities. Meanwhile in *Saint-Pons*, the areas exposed to medium hazard are the only ones to expect a decrease in 2050. *Enchastrayes* (19% of the built-up areas exposed), *Jausiers* (11% of the built-up areas exposed) and *Les Thuiles* (9% of the built-up areas exposed) remain the most exposed municipalities in terms of percentage of built-up areas, but *Uvernet-Fours* is still joining them with almost 9% of the built-up areas exposed;

- Scenario 4: depending on the municipalities considered, the global built-up area exposed is expected to experiment in 2050 a slight increase or decrease, from -20% (*Enchastrayes*, *Jausiers*) to +50% (*Barcelonnette*) or even +90% (*Faucon*). Due to the assessment of the 2010 built-up areas, *Les Thuiles* is a particular case not taken into account here. There is no global pattern obvious in the evolution of the hazard classes' distribution. For example, the areas exposed to very high hazard in *Enchastrayes* are expected to experiment a huge increase whereas the areas exposed to modest and medium hazard are expected to experiment a decrease. *Enchastrayes* (13.5% of the built-up areas exposed), *Jausiers* (7% of the built-up areas exposed) and *Les Thuiles* (14% of the built-up areas exposed) remain the most exposed municipalities in terms of percentage of built-up areas, but *Uvernet-Fours* is still joining them with almost 12% of the built-up areas exposed.

Moreover, we can also highlight some risk patterns per municipality whatever the scenario considered:

- *Barcelonnette*: The percentage of built-up areas exposed and more particularly the areas exposed to high hazard are expected to experiment an increase in 2050;
- *Enchastrayes*: The percentage of built-up areas exposed is mainly going to increase (except for scenario 1) and more particularly the areas exposed to high and even more to very high hazard are expected to experiment an increase in 2050 whereas the areas exposed to modest and medium hazard are expected to experiment a decrease;
- *Faucon*: The percentage of built-up areas exposed is mainly going to increase (except for scenario 1) and more particularly the areas exposed to modest, high and very high hazard are expected to experiment an increase in 2050 whereas the areas exposed to medium hazard are most likely to experiment a decrease;
- *Jausiers*: The percentage of built-up areas exposed is mainly going to increase (except for scenario 1). Except for scenario 2, the areas exposed are expected to decrease;

- *Saint-Pons*: The percentage of built-up areas exposed and more particularly the areas exposed to modest and to high hazard are expected to experiment an increase in 2050 whereas the areas exposed to medium hazard are expected to experiment a decrease (except for scenario 2);
- *Uvernet-Fours*: The percentage of built-up areas exposed and more particularly the areas exposed to high and very high hazard are expected to experiment an increase in 2050 whereas the areas exposed to modest and medium hazard are mostly expected to experiment a decrease (except for scenario 2).

The following table presents the representative susceptibility (which stands for the main level of hazard, in terms of areas) for each municipality, excluding the low class.

| Municipality Name | Representative level of hazard | | | | |
|---|---|---|---|---|---|
| | 2010 | 2050 Scenario 1 | 2050 Scenario 2 | 2050 Scenario 3 | 2050 Scenario 4 |
| Barcelonnette | medium | medium | medium | medium | medium |
| Enchastrayes | medium | medium | very high | very high | medium |
| Faucon | medium | medium | very high | very high | very high |
| Jausiers | medium | very high | medium | very high | very high |
| Les Thuiles | medium | medium | medium | medium | medium |
| Saint-Pons | medium | medium | medium | very high | medium |
| Uvernet-Fours | medium | medium | medium | medium | medium |

*Table 19 Evolution of municipalities' representative level of hazard for built-up areas*

If the representative hazard level for the area was very high when considering the whole study, it is only medium when considering only the built-up areas. This approach allows to "moderating" the risk according to a type of asset (buildings). The above table shows us that in few cases the representative hazard level skips from medium to very high. *Jausiers* and *Faucon* are particularly concerned three scenarios out four increasing their classification.

### Population's exposure:

Using the INSEE last census, we know the total population in each municipality of the study area in 2008.
Moreover we used spatial gridded data for the three municipalities partially out of the study area in order to rule out inhabitants living outside the study area. That led us to cut out *Uvernet-Fours*'s population from 50 people and *Les Thuiles*'s population from 13 people, which gives us the following figures for 2008.
As mentioned previously, we used a global trend (departmental scale) to assess the population in the seven municipalities of the study area in 2050: the following figures are obtained by applying the 2008 population a percentage of +0.8% per year to obtain the 2050 prospective.

| Municipality Name | Population | |
| --- | --- | --- |
| | 2008 census | 2050 prospective |
| Uvernet-Fours | 587.00 | 814 |
| Saint-Pons | 720.00 | 998 |
| Les Thuiles | 367.00 | 509 |
| Faucon-de-Barcelonnette | 305.00 | 423 |
| Jausiers | 1 068.00 | 1 481 |
| Enchastrayes | 427.00 | 592 |
| Barcelonnette | 2 735.00 | 3 792 |

*Table 20 Population in the study area for each municipality*

In order to assess the population exposure on the study area, we need to know the spatial distribution of inhabitants. Since the data are not precise enough to define detailed distribution rules, we assumed that the exposed population is limited to urban areas only and took into account the built-up areas evaluated in order to assess a "population density". That is the asset we are going to consider now, on the basis of the analysis previously realized.

| Municipality Name | Population density in built-up areas (inhabitants per sq. km) | | | | |
| --- | --- | --- | --- | --- | --- |
| | 2010 | 2050 Scenario 1 | 2050 Scenario 2 | 2050 Scenario 3 | 2050 Scenario 4 |
| Uvernet-Fours | 920.50 | 2768.04 | 1525.12 | 2337.85 | 2019.87 |
| Saint-Pons | 1118.01 | 3398.68 | 1661.44 | 2467.11 | 2662.56 |
| Les Thuiles | 925.37 | 4790.97 | 2168.80 | 4211.93 | 3410.19 |
| Faucon-de-Barcelonnette | 1247.95 | 1762.59 | 803.58 | 2416.26 | 1534.83 |
| Jausiers | 1271.58 | 3367.41 | 1717.89 | 3791.68 | 3073.81 |
| Enchastrayes | 908.70 | 2225.50 | 877.66 | 2547.26 | 1806.48 |
| Barcelonnette | 1604.67 | 6045.51 | 3559.66 | 6482.72 | 5193.46 |

*Table 21 Population density in the study area for each municipality*

The following tables present the population exposed (in number of inhabitants) to each type of hazard for each municipality.

| BARCELONNETTE | 2010 | 2050 | | | | Ratio 2050 to 2010 | | | |
|---|---|---|---|---|---|---|---|---|---|
| Hazard class ↓ | | Sc. 1 | Sc. 2 | Sc. 3 | Sc. 4 | Sc. 1 | Sc. 2 | Sc. 3 | Sc. 4 |
| Modest | 2 | 7 | 21 | 8 | 9 | 3.19 | 10.07 | 4.04 | 4.23 |
| Medium | 16 | 23 | 61 | 69 | 33 | 1.43 | 3.77 | 4.32 | 2.07 |
| High | 1 | 20 | 48 | 38 | 23 | 31.08 | 75.42 | 58.58 | 36.41 |
| Very High | 3 | 11 | 18 | 19 | 12 | 3.77 | 5.95 | 6.38 | 3.92 |
| Total → | 22 | 61 | 148 | 135 | 77 | 2.80 | 6.79 | 6.18 | 3.55 |
| % of global population | 0.80 | 1.61 | 3.91 | 3.56 | 2.04 | | | | |

*Table 22 Evolution of population exposure (in number of inhabitants) for the municipality of Barcelonnette*

| ENCHASTRAYES | 2010 | 2050 | | | | Ratio 2050 to 2010 | | | |
|---|---|---|---|---|---|---|---|---|---|
| Hazard class ↓ | | Sc. 1 | Sc. 2 | Sc. 3 | Sc. 4 | Sc. 1 | Sc. 2 | Sc. 3 | Sc. 4 |
| Modest | 14 | 13 | 12 | 11 | 13 | 0.92 | 0.86 | 0.82 | 0.93 |
| Medium | 31 | 24 | 24 | 39 | 30 | 0.76 | 0.77 | 1.23 | 0.95 |
| High | 2 | 7 | 13 | 16 | 13 | 3.50 | 6.67 | 8.41 | 6.91 |
| Very High | 1 | 12 | 33 | 46 | 24 | 10.82 | 30.10 | 42.05 | 21.87 |
| Total → | 48 | 55 | 82 | 112 | 80 | 1.14 | 1.69 | 2.31 | 1.65 |
| % of global population | 11.34 | 9.32 | 13.82 | 18.93 | 13.52 | | | | |

*Table 23 Evolution of population exposure (in number of inhabitants) for the municipality of Enchastrayes*

| FAUCON | 2010 | 2050 | | | | Ratio 2050 to 2010 | | | |
|---|---|---|---|---|---|---|---|---|---|
| Hazard class ↓ | | Sc. 1 | Sc. 2 | Sc. 3 | Sc. 4 | Sc. 1 | Sc. 2 | Sc. 3 | Sc. 4 |
| Modest | 0 | 1 | 1 | 1 | 2 | 2.12 | 5.15 | 5.81 | 6.15 |
| Medium | 2 | 1 | 5 | 3 | 2 | 0.71 | 2.62 | 1.52 | 0.88 |
| High | 0 | 1 | 4 | 2 | 3 | 3.53 | 15.78 | 8.71 | 11.07 |
| Very High | 0 | 0 | 5 | 4 | 4 | 0.71 | 9.50 | 7.74 | 7.69 |
| Total → | 3 | 3 | 15 | 10 | 10 | 1.09 | 5.30 | 3.70 | 3.52 |
| % of global population | 0.90 | 0.71 | 3.44 | 2.40 | 2.29 | | | | |

*Table 24 Evolution of population exposure (in number of inhabitants) for the municipality of Faucon*

| JAUSIERS Hazard class ↓ | 2010 | 2050 | | | | Ratio 2050 to 2010 | | | |
|---|---|---|---|---|---|---|---|---|---|
| | | Sc. 1 | Sc. 2 | Sc. 3 | Sc. 4 | Sc. 1 | Sc. 2 | Sc. 3 | Sc. 4 |
| Modest | 9 | 5 | 14 | 7 | 7 | 0.54 | 1.48 | 0.73 | 0.78 |
| Medium | 29 | 29 | 55 | 46 | 41 | 1.00 | 1.92 | 1.60 | 1.42 |
| High | 9 | 11 | 29 | 19 | 12 | 1.18 | 3.05 | 2.01 | 1.31 |
| Very High | 19 | 42 | 55 | 90 | 42 | 2.18 | 2.82 | 4.62 | 2.15 |
| Total → | 67 | 87 | 152 | 162 | 102 | 1.30 | 2.28 | 2.41 | 1.53 |
| % of global population | 6.26 | 5.89 | 10.29 | 10.91 | 6.89 | | | | |

*Table 25 Evolution of population exposure (in number of inhabitants) for the municipality of Jausiers*

| LES THUILES Hazard class ↓ | 2010 | 2050 | | | | Ratio 2050 to 2010 | | | |
|---|---|---|---|---|---|---|---|---|---|
| | | Sc. 1 | Sc. 2 | Sc. 3 | Sc. 4 | Sc. 1 | Sc. 2 | Sc. 3 | Sc. 4 |
| Modest | 6 | 6 | 6 | 3 | 6 | 1.00 | 0.98 | 0.41 | 0.94 |
| Medium | 26 | 33 | 40 | 30 | 42 | 1.27 | 1.54 | 1.17 | 1.60 |
| High | 4 | 6 | 21 | 7 | 11 | 1.77 | 6.04 | 2.04 | 3.20 |
| Very High | 0 | 3 | 7 | 5 | 11 | 7.77 | 19.34 | 12.52 | 28.56 |
| Total → | 36 | 48 | 75 | 45 | 69 | 1.34 | 2.07 | 1.24 | 1.92 |
| % of global population | 9.83 | 9.51 | 14.66 | 8.77 | 13.61 | | | | |

*Table 26 Evolution of population exposure (in number of inhabitants) for the municipality of Les Thuiles*

| SAINT-PONS Hazard class ↓ | 2010 | 2050 | | | | Ratio 2050 to 2010 | | | |
|---|---|---|---|---|---|---|---|---|---|
| | | Sc. 1 | Sc. 2 | Sc. 3 | Sc. 4 | Sc. 1 | Sc. 2 | Sc. 3 | Sc. 4 |
| Modest | 0 | 1 | 4 | 3 | 2 | 4.56 | 16.35 | 12.14 | 7.14 |
| Medium | 10 | 15 | 22 | 12 | 20 | 1.50 | 2.17 | 1.24 | 2.03 |
| High | 0 | 1 | 7 | 3 | 6 | 3.04 | 21.30 | 10.30 | 16.67 |
| Very High | 3 | 7 | 19 | 16 | 18 | 2.39 | 6.16 | 5.04 | 5.70 |
| Total → | 14 | 24 | 52 | 34 | 45 | 1.79 | 3.79 | 2.51 | 3.32 |
| % of global population | 1.89 | 2.45 | 5.18 | 3.44 | 4.53 | | | | |

*Table 27 Evolution of population exposure (in number of inhabitants) for the municipality of Saint-Pons*

| UVERNET-FOURS Hazard class ↓ | 2010 | 2050 | | | | Ratio 2050 to 2010 | | | |
|---|---|---|---|---|---|---|---|---|---|
| | | Sc. 1 | Sc. 2 | Sc. 3 | Sc. 4 | Sc. 1 | Sc. 2 | Sc. 3 | Sc. 4 |
| Modest | 6 | 14 | 12 | 14 | 15 | 2.31 | 2.01 | 2.27 | 2.50 |
| Medium | 14 | 20 | 34 | 23 | 33 | 1.39 | 2.40 | 1.63 | 2.31 |
| High | 2 | 11 | 14 | 14 | 19 | 5.47 | 7.00 | 6.81 | 9.28 |
| Very High | 3 | 10 | 19 | 22 | 28 | 3.29 | 6.52 | 7.30 | 9.60 |
| Total → | 25 | 55 | 80 | 72 | 95 | 2.15 | 3.16 | 2.85 | 3.76 |
| % of global population | 4.31 | 6.70 | 9.82 | 8.88 | 11.69 | | | | |

*Table 28 Evolution of population exposure (in number of inhabitants) for the municipality of Uvernet-Fours*

All the municipalities are approximately impacted in the same way if we consider the global number of inhabitants exposed: whatever the 2050 scenario taken into account, it is expected to experiment an increase, up to four or five times the 2010 figure for some cases and the inhabitants concerned are mainly exposed to medium hazard.

When looking at the distribution between the different classes of hazard, we can see that there are fewer differences than in the other two analyses.  In *Barcelonnette*, *Saint-Pons* and *Uvernet-Fours*, all the figures are expected to experiment an increase. The municipality of *Faucon* follows approximately the same trend (only slight decreases are being spotted for Scenario 1 -medium and very high hazard- and Scenario 4 –medium hazard). For *Les Thuiles*, all the classes will impact more inhabitants, except for the modest hazard class. It is approximately the same pattern in *Jausiers*, except for the Scenario 2, where the number of people exposed to modest hazard is expected to increase of about 50%. For *Enchastrayes,* high and very high hazards will impact more inhabitants, whereas modest and medium hazards will impact fewer inhabitants, except for the Scenario 3, where the number of people exposed to medium hazard is expected to increase of about 23%.

As with the previous analysis, the number of inhabitants exposed to high hazard in *Barcelonnette, Faucon* and *Saint-Pons* and to very high hazard in *Enchastrayes* and *Les Thuiles* are expected to highly increase.

This analysis allows integrating the evolution of the demography in addition to the one of the land-use and can be quite useful to highlight some hot spots to be considered for future urban plans.

Finally we could have presented the representative susceptibility (which stands for the main level of hazard, in terms of number of inhabitants exposed) for each municipality, excluding the low class, but it was not really relevant. Since this last analysis has been made on the built-up areas' analysis basis, the representative levels for population are influenced by our previous results. All the municipalities are classified as medium hazard in 2010 and *Jausiers* and *Faucon* are particularly concerned by an increasing of their classification to very high hazard.

## 1.3    CONCLUSION FOR BARCELONNETTE SITE

Regarding the case study in Barcelonnette, the changes in exposure to landslides over the period of analysis (2010 to 2050) are different depending on the assets considered.

For the roads network, changes are as follows:
- Roads exposed to modest and medium hazard are expected to experiment a decrease in the number of kilometres impacted whereas roads exposed to high and very high hazard are expected to experiment an increase in the number of the kilometres impacted;
- If we consider only the landslides' occurrence probability, the total amount of exposed kilometres is expected to experiment an increase and especially for the tracks at very high risk.

For the overall territory exposure, changes are the following ones:
- 20 to 40% of the studied territory of each municipality are concerned by landslides hazard, mostly by a very high one;
- For each municipality, surfaces exposed to modest hazard are expected to remain the same whereas surfaces exposed to medium hazard are expected to experiment a decrease of about 30 to 40%;
- For each municipality, surfaces exposed to high and very high hazard are expected to experiment an increase of at least 15% for the very high hazard class and even more important for the high hazard class (due to the decrease of the impact of the medium hazard).

For the built-up areas' exposure the evolution pattern is the following:
- The most exposed municipalities in terms of percentage of built-up areas are *Enchastrayes*, *Jausiers* and *Les Thuiles* in 2010. They remain the most exposed in 2050 in addition to *Uvernet-Fours*;
- In 2010, the representative hazard level for all the municipalities studied is medium whereas in 2050 this level is expected to be upgraded to a very high level for some municipalities (*Enchastrayes*, *Faucon*, *Jausiers*, *Saint-Pons*), depending on the scenario considered.

Finally, for population changes are as follows:
- The total number of inhabitants exposed to landslides is expected to increase in 2050;
- As a percentage of total population, the exposed population increases up to more than 10% between 2010 and 2050;
- In *Barcelonnette*, *Faucon* and *Saint-Pons*, the number of inhabitants exposed to high hazard is expected to highly increase as well as the number of inhabitants exposed to very high hazard in *Enchastrayes* and *Les Thuiles*;

The increment in exposed population is due to a combination of increase in both hazard and population associated to urban expansion.

# 2   NEDRE ROMERIKE TEST SITE, NORWAY

## 2.1   METHODOLOGY

The model used by ICG for the risk assessment in the Norwegian case study is an adaptation of the model presented by Nadim et al. (2006) and used in SafeLand D2.10, D3.7 and D3.8. The elements of the model are presented in Figure 7.
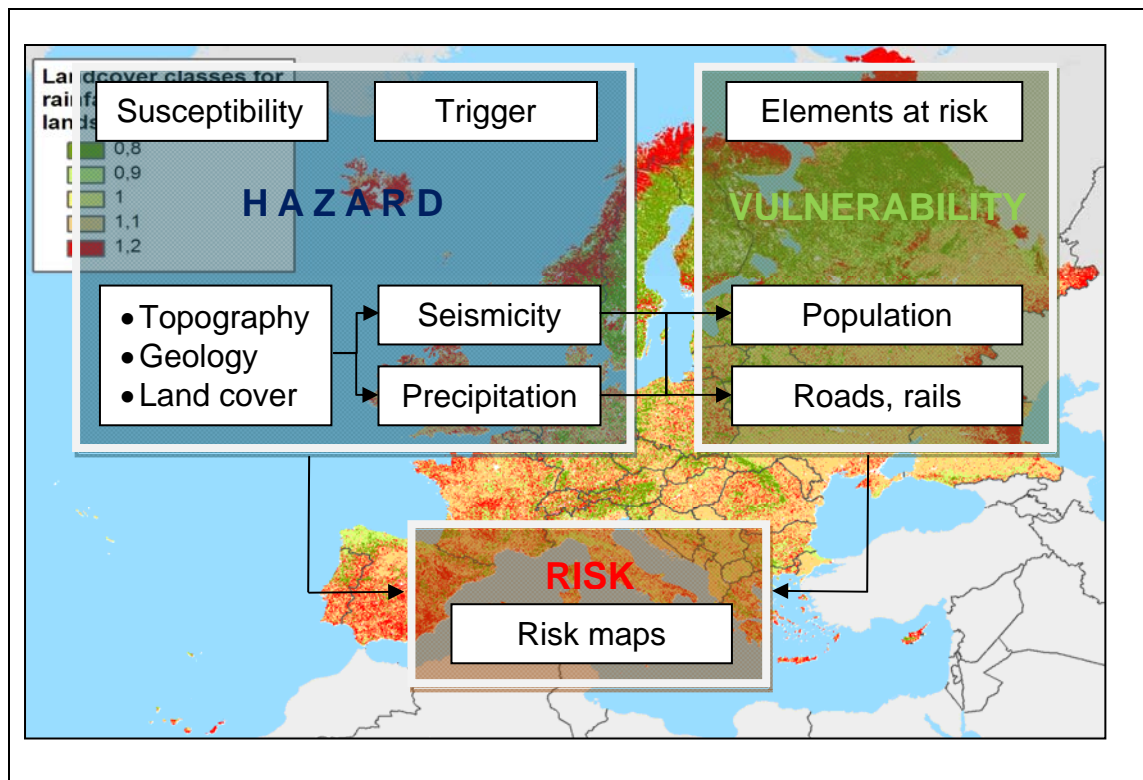


*Figure 7 Schematic approach for landslide hazard and risk evaluation*

The assessment of landslide hazard is performed as a combination of susceptibility and triggering factors using the following expression:

$$H_r = (S_r \times S_l \times S_v) \times T_p$$

*(Equation 1)*

where $H_r$ is the landslide hazard index for rainfall-induced landslides, $S_r$ is the slope factor within a selected grid, $S_l$ is lithological (or geological) conditions factor, $S_v$ is the vegetation cover or land use factor, and $T_p$ is the precipitation factor. This model was used for assessment of landslide hazard in SafeLand deliverable D3.8 in the study area of Nedre Romerike. The results of that evaluation are used here for assessment of landslide risk.

Following the procedure presented in NGI (2004; 2009), the percentage of population exposed can be correlated to the values of the landslide hazard index. For precipitation-induced landslides, NGI (2004; 2009) fitted the correlation to a function $y = a(x^b)$, where a = $7.307 \times 10^{-5}$ and b = 2. This function is shown in Figure 8.
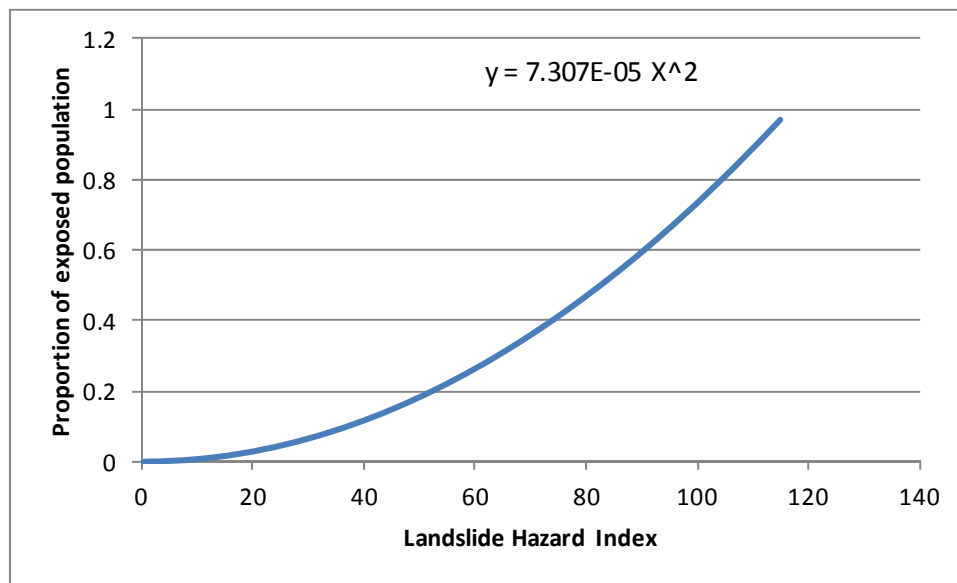
*Figure 8 Correlation between landslide hazard index and proportion of exposed population. Redrawn from NGI (2004; 2009)*

Then, the exposed population *PhExp* is evaluated in a single pixel using the following equation:

$$PhExp = a\,H^2\,POP \qquad \text{(Equation 2)}$$

where a is a fitted value obtained using global data in NGI (2004; 2009) equal to $7.307 \times 10^{-5}$, H is the landslide hazard index (in the present case, the result of the assessment in D3.8), and POP is the total population in a pixel.

In the present study, the exposed population is used as a proxy for risk.

## 2.2    Data and softaware

The processing of the ICG model was achieved by combining Matlab scripts for statistical analyses of the data (in particular for the evaluation of the precipitation triggering factor, see SafeLand D3.8 for details) and models prepared in ArcGIS for all computations directly involving all the spatial datasets.

The source for the land cover index $S_v$ was the CORINE Land Cover (CLC) database. This is a seamless European land cover vector database which was completed by the Norwegian Forest and Landscape Institute in 2008. The current distribution of land cover is shown in Figure 9.
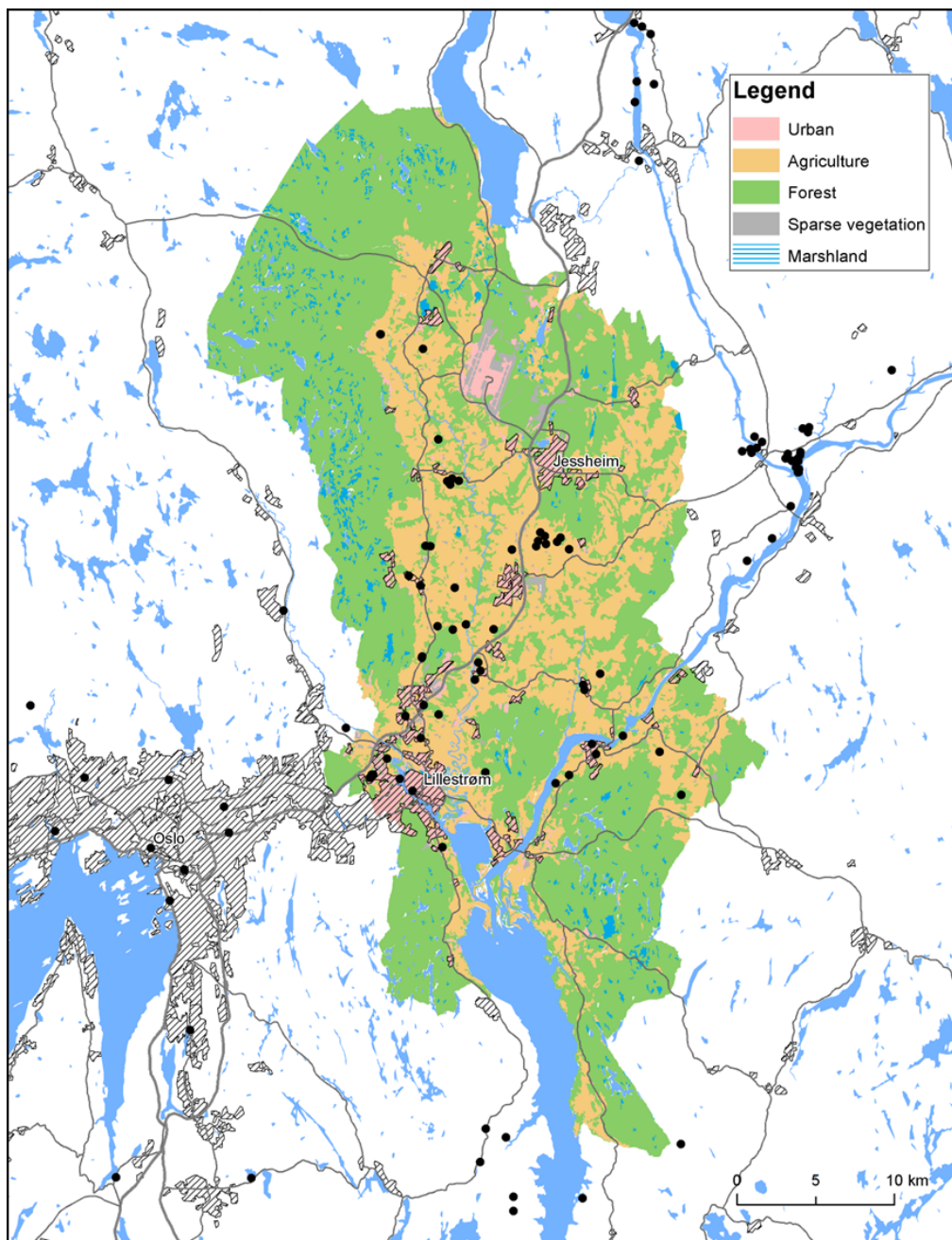
*Figure 9 Land cover map of the study area as of 2010 based on the CORINE Land Cover database. Black circle markers are landslides from the Norwegian inventory of landslides*

*The land cover was projected up to the year 2090 based on the current land cover dataset. The population of the region is expected to increase by 50% by 2040, resulting in a substantial growth of urban land covers. Plans from the Akershus County to which all municipalities belong indicate that a majority of this growth is expected in central towns, described as tie-point for communication. Though not a single list of tie-points exists yet, assumptions were made that the tie-points will be the largest of the existing towns. Smaller towns and villages will most likely see smaller changes. For this study, the urban growth was therefore modelled for the largest urban areas. For each 20-year period, these urban areas were expanded by a certain distance. Urban growth was limited by excluding water features. In addition, the urban area representing Oslo Airport was kept constant, even though an expansion is expected around 2030-2040. The model was calibrated versus expected area of the urban growth and versus plans for urban development of Skedsmo municipality for 2050. The spatial*

*distribution of land cover evolution over the period 2010 to 2090 is presented in Figure 10 and the evolution of changes for*
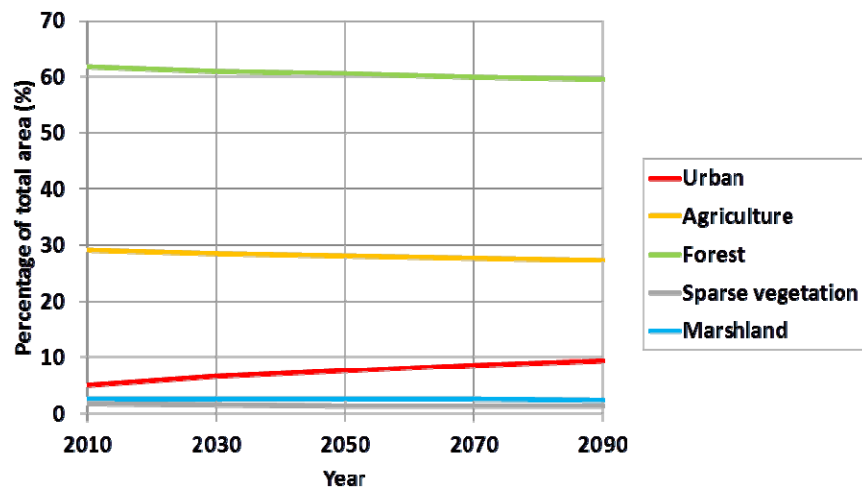


*each class is shown in*

Figure 11.
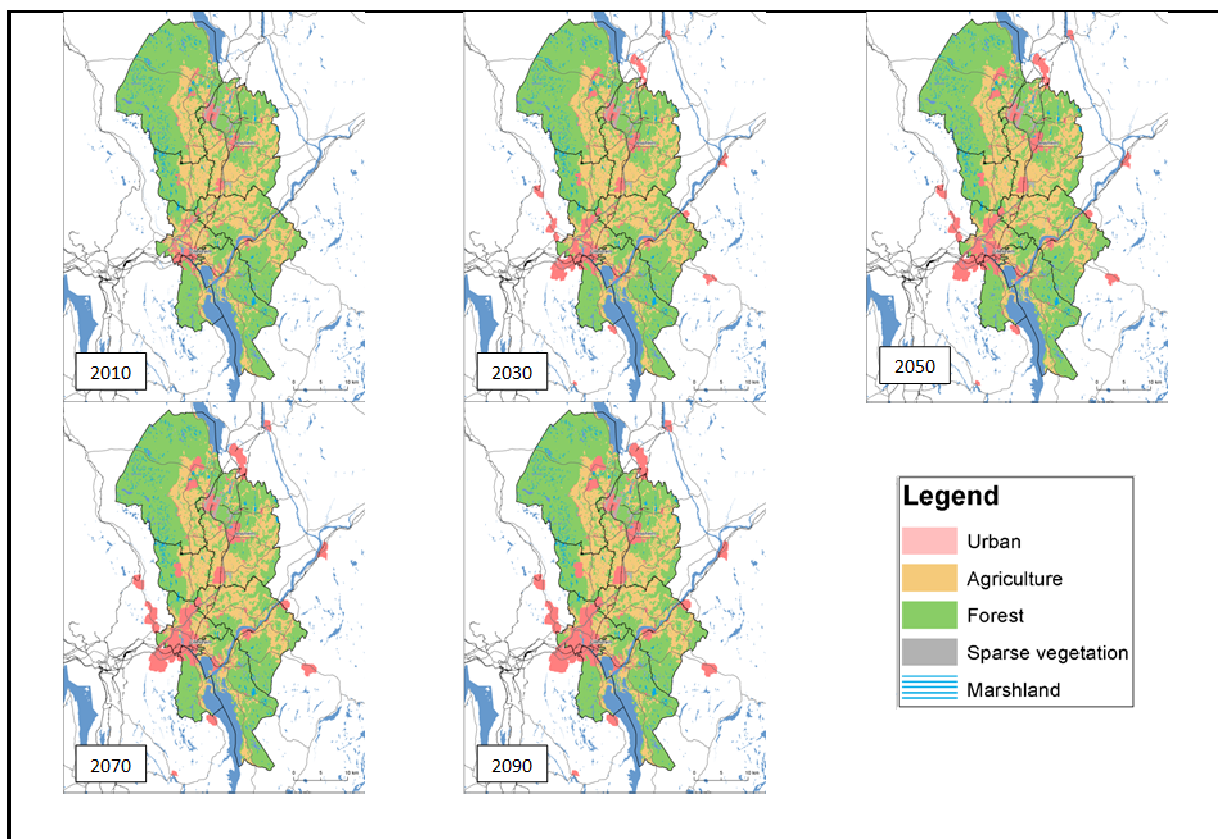


*Figure 10 Land cover evolution within the period 2010-2090 in the study area*

The Nedre Romerike area included in this study comprises the following municipalities which are part of the county of Akershus: Fet, Gjerdrum, Nannestad, Rælingen, Skedsmo, Sørum and Ullensaker. This region lies to the East of Oslo, the capital of Norway. The total population in 2010 was about 160 000+ habitants, which constitutes more than 30% of the total population of Oslo suburbs. In addition to the urban areas, Nedre Romerike includes

important industrial and agricultural areas. Land use plans from authorities consider urban expansion for the next 100 years. The study area is widely covered with marine deposits (clayey soils), and many slopes with marginal safety. The main triggering factors for landslides are human activity (anthropic) and precipitation. The study area is shown within the black square in Figure 12.
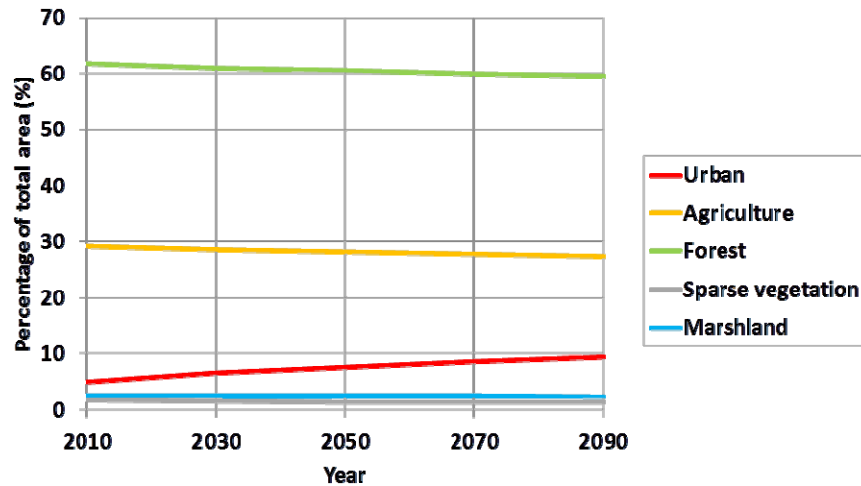


*Figure 11 Evolution in changes on land cover classes over the period 2010-2090*
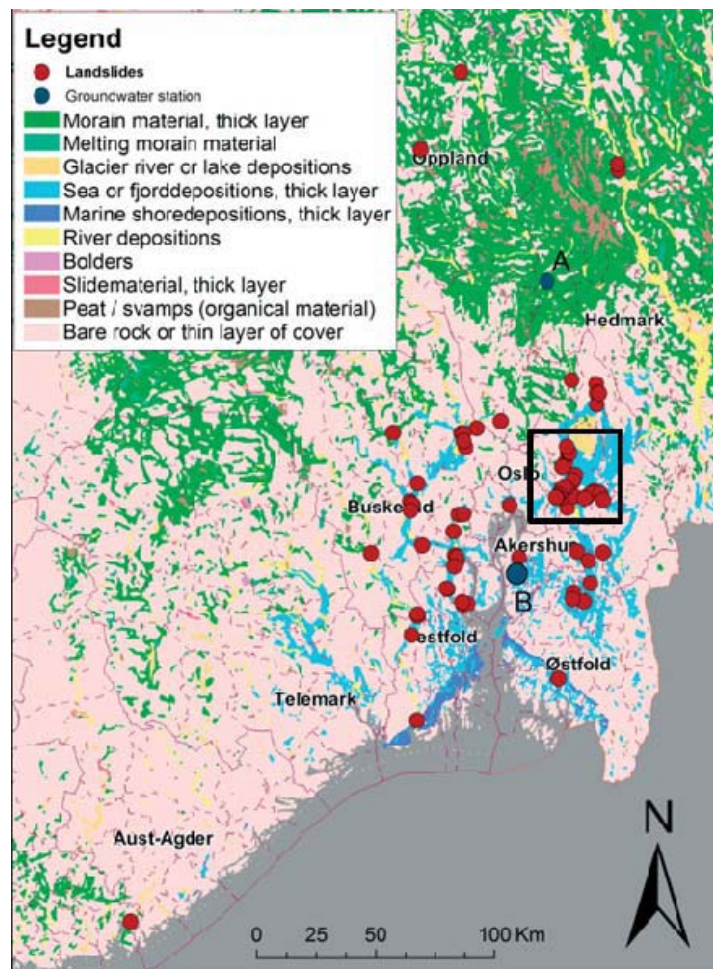
*Figure 12 Nedre Romerike area (black square) comprising the study area for the Norwegian case in the present deliverable. Adapted from Jaedicke and Kleven (2008).*

The hazard assessment performed in SafeLand Deliverable D3.8 was used as a basis for the risk assessment of the present deliverable. The results of the hazard analyses in D3.8 follow.

The spatial distribution of hazard due to precipitation induced landslides is presented in Figure 13. Changes from negligible to very low hazard are visible in the north west of the study area. Elsewhere changes are not clearly evidenced except for the moderate level that appears to the north in the 2050 scenario.

| 2010 | 2030 | 2050 |
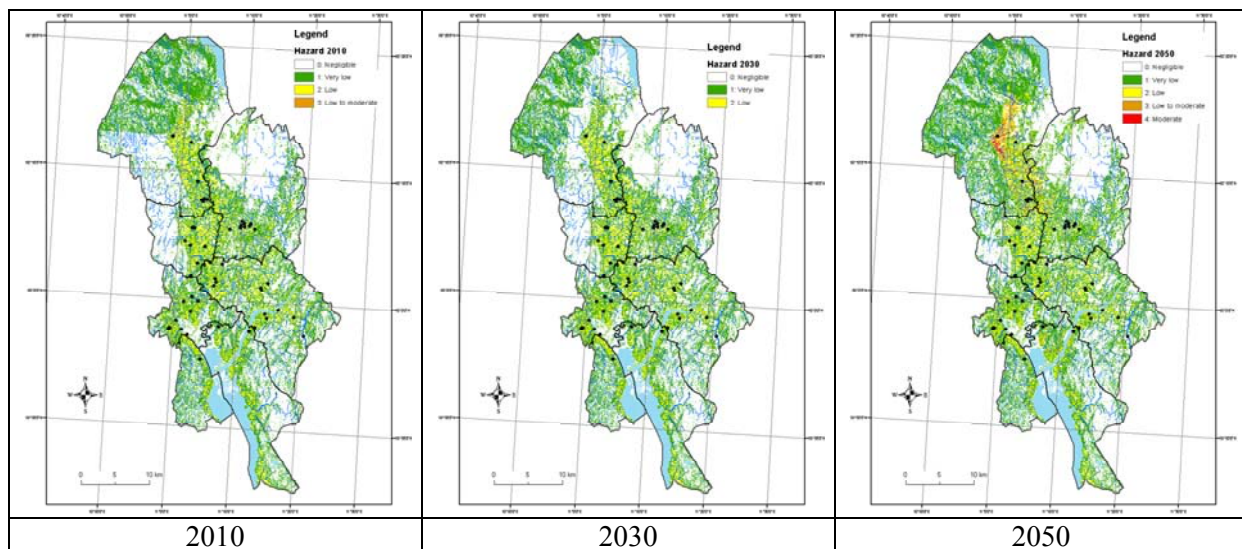
*Figure 13 Spatial distribution of hazard classes due to precipitation induced landslides in the study area*

The evolution of the spatial extent of each hazard class over the three scenarios is presented in Figure 14. The negligible class is reduced by about 5% when comparing 2010 and 2050. Most of the reduction is due to an increase in the very low class. The low, low to moderate and moderate classes increase in less than 2% over the whole period considered in the analysis.
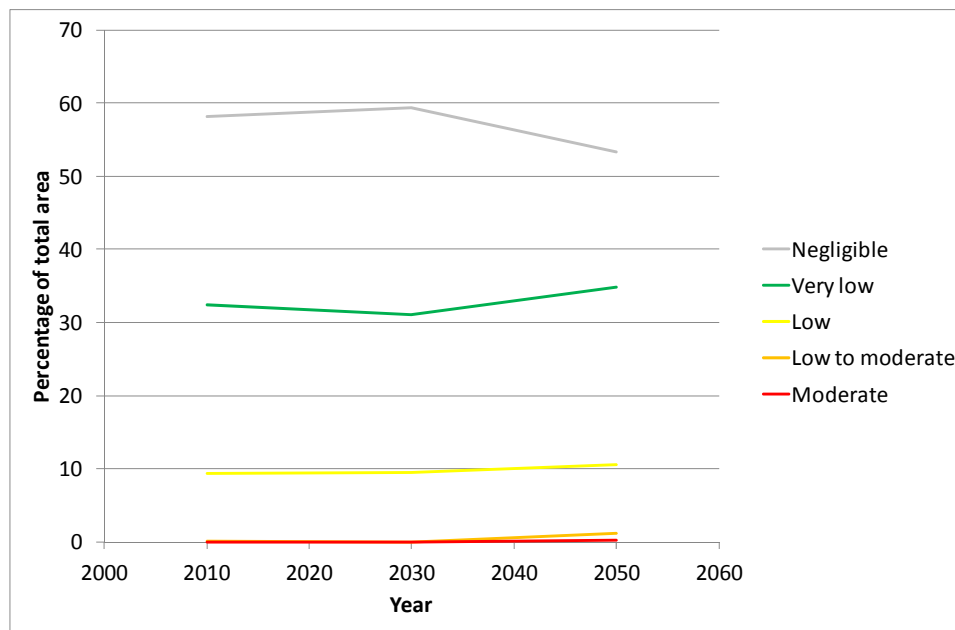


*Figure 14 Evolution of hazard classes as a percentage of the total area over the period considered in the assessment. This corresponds to the scenarios of spatial distribution presented in Figure 13*

Based on equation (2) and on the spatial distribution of the hazard classes, the percentage of population exposed was evaluated in the study area over the period of analysis (2010-2050) assuming that the exposed population is limited to urban areas only and that the population density is constant over the period of analysis. A conservative estimate of the exposed population was evaluated by using the upper-bound hazard index within each hazard class.

The spatial distribution of percentage of exposed population for each scenario is shown in Figure 15.
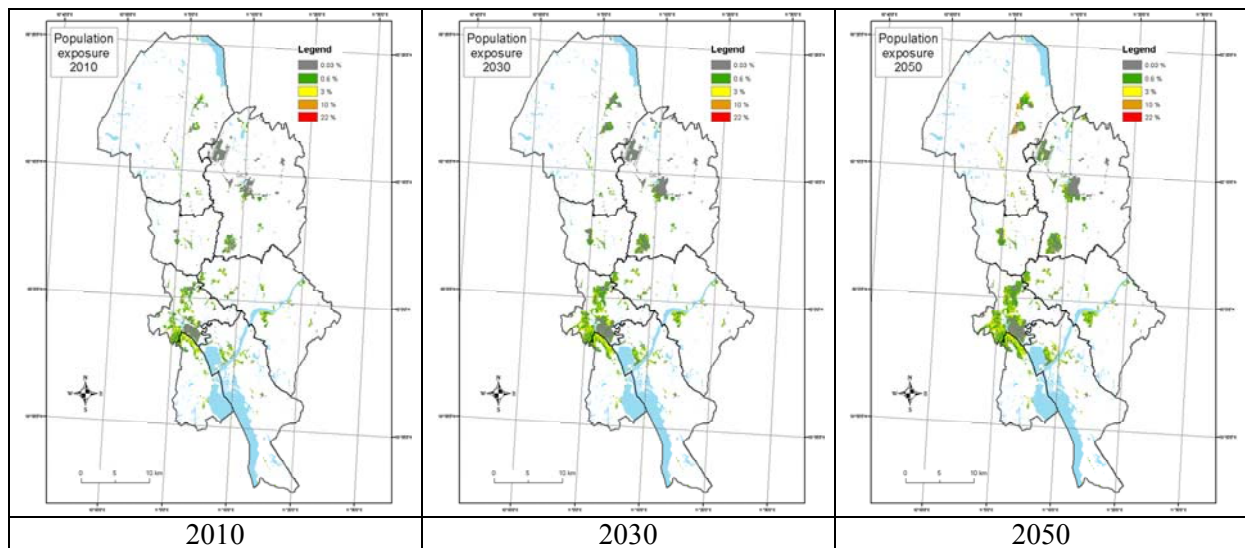


| 2010 | 2030 | 2050 |

*Figure 15 Spatial distribution of percentage of exposed population over the three scenarios in 2010, 2030 and 2050*

The exposed population in the areas with the different hazard classes is shown in Table 29.

*Table 29 Number of people exposed in Nedre Romerike in each hazard class over the analysed scenarios*

| Hazard class ↓ | 2010 | 2030 | 2050 | Ratio 2050 to 2010 |
|---|---|---|---|---|
| Negligible | 19 | 23 | 23 | 1.21 |
| Very low | 301 | 392 | 486 | 1.61 |
| Low | 661 | 953 | 1266 | 1.92 |
| Low to moderate | 22 | 0 | 236 | 10.73 |
| Moderate | 0 | 0 | 82 | - |
| **Total →** | 1003 | 1368 | 2093 | 2.09 |
| **% of total population** | 0.74 | 0.78 | 1.04 | - |

## 2.3    RESULTS

Regarding the case study in Nedre Romerike, the changes in population exposure over the period of analysis (2010 to 2050) is as follows:

- In areas with negligible hazard, the exposed population increases in 20%.
- Areas with very low and low hazard are expected to experiment increments in exposed population in the range 60-90%.
- Zones with low to moderate hazard level are estimated to increase the total exposed population in about ~ 1000%.
- The total number of persons exposed to landslides is expected to increase in 200%.
- As a percentage of total population, the exposed population increases from 0.7% to 1% between 2010 and 2050.
- The increment in exposed population is due to a combination of increase in both hazard and population associated to urban expansion.

# 3    A SCOTTISH PERSPECTIVE

With respect to landslides, the UK is clearly a relatively low risk environment (e.g. Gibson et al. In Press; Winter & Bromhead, 2011) in which fatalities due to landsliding are rare and the impacts are largely of a socio-economic nature. Notwithstanding this there is a strong academic tradition in the area (e.g. Bromhead et al., 2012) and when events do take place the profile generated is usually substantial and involves both the media and politicians, as well as the general public (Winter et al., 2007).

Against this background it is perhaps unsurprising that a strong interest has been expressed in the effects of climate change primarily upon landslide hazard frequency and magnitude, but also on landslide risk. The CLIFFS network (http://cliffs.lboro.ac.uk/), funded by EPSRC and organised by Loughborough University (Dixon et al., 2006) both responded to, and generated interest in, the issues surrounding the impact of climate change on landslides in the UK.

This network included a number of seminars in the UK and drawing on the associated presentations, and also on a related Session convened at the European Geoscience Union (EGU) Congress in 2008, a number of papers on the subject were commissioned to form a Thematic Issue of the *Quarterly Journal of Engineering Geology and Hydrogeology* (*QJEGH*) on 'Land-Use and Climate Change Impacts of Landslides' (Winter et al., 2010a). Contributions focussing on Italy (Polemio & Petrucci, 2010; Wasowski et al., 2010), Canada (Guthrie et al., 2010) and Asia (Petley, 2010) were included, while the remaining papers were UK-focussed and covered engineered infrastructure slopes (Clarke et al., 2010; Loveridge et al., 2010), the effects of debris flow on infrastructure (Winter et al., 2010b) and on the urban landslide complex at the Ventnor Undercliff on the Isle of Wight (Moore et al., 2010). In addition, Dijkstra and Dixon (2010) present an overview of the indicators of climate change that could be derived from the UKCIP02 climate changes forecasts that were then available (Hulme et al., 2002).

The UKCIP02 forecasts were extant at the time of the UK-based work described in the above paragraph. The main message from UKCIP02 included increased average annual temperatures with important regional and seasonal variations, wetter winters and drier summers (leading to potentially large reductions in end-of-summer soil moisture conditions), and more frequent storm rainfall (especially in the winter).

The UKCIP02 forecasts represented an advance in the description of the future UK climate compared to the scenarios published by UKCIP in 1998. The former were based on new global emissions scenarios published in 2000 by the Intergovernmental Panel on Climate Change (IPCC) in their Special Report on Emissions Scenarios, based on a series of climate modelling experiments completed by the Hadley Centre using their most recently developed models. The scenarios describe four alternative emissions scenarios for the UK named, respectively, Low Emissions, Medium-Low Emissions, Medium-High Emissions and High Emissions.

These scenarios were extensively used in the UK (Dixon et al., 2006; Galbraith et al., 2005; Winter et al., 2005; 2008; 2009a) for precisely the purposes intended. However, it was frequently noted, not least within the CLIFFS network, that the inability to undertake

probabilistic assessments was a major obstacle to a greater understanding of the detailed likely effects of climate change on slope instability.

The most recent UKCP09 climate change forecasts (Jenkins et al., 2009) for the UK address precisely this limitation and give probabilistic estimations of climate change for three (High, Medium and Low) emissions scenarios.

This report considers the UKCIP02 and UKCP09 climate change forecasts, as they relate to landslide potential, and the associated recent trends in Scotland's rainfall climate. It then reconciles the outcomes with a view of likely future landslide hazard trends and presents a picture of potential future landslide risk in Scotland.

## 3.1    RAINFALL PATTERNS AND LANDSLIDES

Landslides are frequently cited as being caused by rainfall and the link between high intensity-short duration, storm rainfall and debris flows has been documented in Japan (Fukuoka, 1980), New Zealand (Selby, 1976) and Brazil (Jones, 1973) amongst other places. However, the potential influence of longer term, antecedent rainfall prior to storm events is clear from the events experienced in Scotland in August 2004 (Winter et al., 2007).

In a study based in the Santa Cruz Mountains of California, Wieczorek (1987) noted that no debris flows were triggered until 280mm of seasonal rain fell, thus clearly acknowledging the importance of antecedent rainfall, a factor that has also been recognised in studies in Southern California (Campbell, 1975), New Zealand (Eyles, 1979) and Alaska (Sidle and Swanson, 1982). Wieczorek (1987) also noted that for high permeability soils, such as those found in Hong Kong (e.g. Ko, 2005), the period of antecedent rainfall may be short or that the necessary antecedent rainfall may even be supplied by the early part of the storm event itself. In this context it is important to appreciate that both low intensity-long duration (antecedent) rainfall and high intensity-short duration (storm) rainfall may contribute to the conditions resulting in instability.

Many studies have also included back analyses of rainfall records to define specific rainfall threshold levels that lead to conditions likely to cause landslides. These include, for example, Australia, Hong Kong, Italy, Jamaica, Nepal, Norway, Singapore, Slovenia, Switzerland, UK and the USA. Many authors of such studies state that their methodologies either could be, or will be, used for actively forecasting conditions likely to lead to landslides, but relatively few report such practical implementation and use of their work (Winter et al., 2009a). The back analyses use a wide range of methodologies; however, these are dominated by intensity-duration analyses (e.g. Ahmad, 2003; Aleotti, 2004; Caine, 1980; Flentje & Chowdury, 2006; Hurlimann, et al., 2003) which appears to be a viable and well-established methodology. Further details are given by Winter et al. (2009a) and a wider-ranging review of rainfall thresholds is presented by Anon (2007).

## 3.2    SCOTLAND'S CLIMATE

The causal link between manmade emissions of greenhouse gases, increases in the global temperature anomaly and climate change, which may or may not manifest as higher

temperatures at any given location, are now well-established and have become part of the body of mainstream thinking (e.g. Hill *et al*., 2007). Climate change is thus increasingly seen as a scientific fact; occasionally a dissenting voice may be heard but such disputes are increasingly focused upon the scale of such changes and on the most appropriate actions to be taken in terms of mitigation and adaptation (e.g. Bellamy & Barrett, 2007).

There is perhaps a tendency to focus upon the future climate change issues at the expense of the wealth of information captured within current weather patterns and recent climate trends. In this section these three closely related threads of information – history, recent trends and future change – are brought together to provide a more holistic view of climate patterns as they relate to landslides.

### 3.2.1   Scotland's rainfall climate

The climate of Scotland in terms of its rainfall may be very broadly divided into the relatively dry east and the relatively wet west (Figure 16), where almost twice as much rain falls, on average, each year. Figure 16 shows data for the United Kingdom in its entirety. The trend towards greater rainfall in the more westerly parts is broadly maintained throughout, with the possible exception of the south-east of Northern Ireland. However, what is also important to note is that the areas subject to high rainfall are much smaller in the southern part of Great Britain (England and Wales) than in Scotland in the north.

Data presented by the Met Office[2] (Anon, 1989) indicates that in the lowland regions in the east of Scotland overall annual rainfall levels are relatively low, being broadly comparable with drier parts of England. While rainfall generally peaks in the summer months of July and August in the east, the monthly average rainfall data for Edinburgh (Figure 17), which is broadly representative of the east and one of the driest locations in Scotland, indicates that in the main the monthly variations in rainfall are relatively slight. Edinburgh may not be well known for debris flow events but (McAdam, 1993) reports that in 1744 a cloud burst resulted in the erosion of, and associated flow from, the gulley below the summit of Arthur's Seat known today as the Gutted Haddie. This feature remains clearly visible. More recently evidence of debris flow has been examined in the nearby Pentland Hills, although it should be noted that orographic effects will come into play here and that winter rainfall levels may well be higher than those for July/August (Winter et al., 2010b).

In the wetter west, maximum rainfall levels are reached during the period September to January (e.g. Tiree in Figure 17). Perhaps most marked is the variation in the monthly averages with the driest month of May receiving, on average, around half of the rainfall experienced in the wettest month of October. Although rainfall levels in the west are relatively low in August, they do increase from a low point in May. It is worth noting that while Tiree shows rainfall levels significantly in excess of those for Edinburgh and Pitlochry (1,106mm on average per annum compared to 626mm and 824mm respectively) other locations in the west of Scotland experience significantly more rainfall: e.g. Inverary Castle with around 2,036mm of rainfall on average per annum (Figure 17).

---

[2] The UK government agency responsible for weather forecasting, and climate modelling and research.

The central area, as represented by Pitlochry in Figure 17, has what might best be described as a mix of the rainfall characteristics of the 'east' and the 'west'. The rainfall peak is both lower and shorter (December and January) than in the west, but there are also small sub-peaks in August and October.
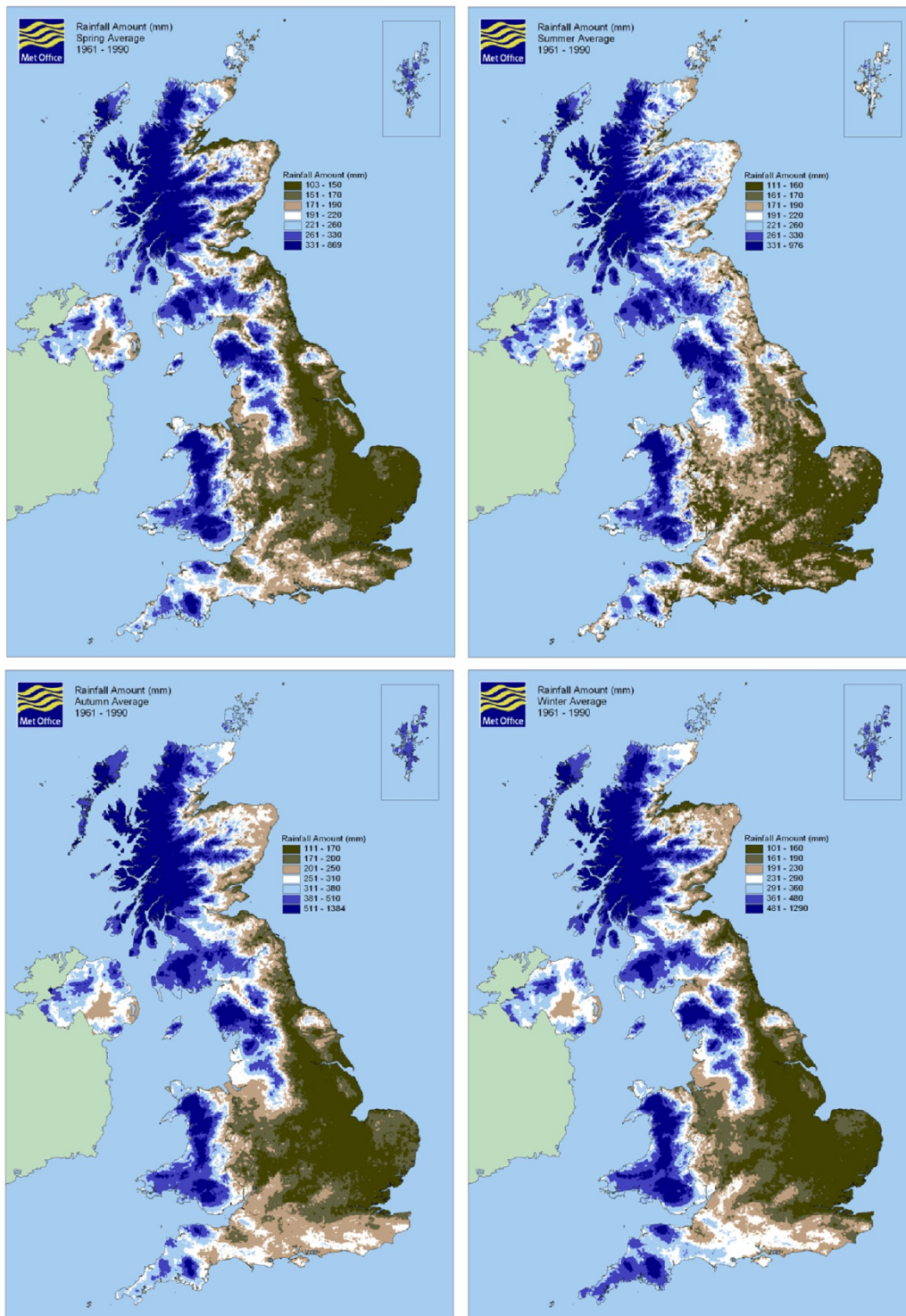


*Figure 16 UK Met Office 30-year monthly average rainfall data (1961 to 1990) for Spring (top left), Summer (top right), Autumn (bottom left) and Winter (bottom right) (images courtesy of the Met Office).*

Such average values mask large annual variations. Data presented by Barnett et al. (2006a; 2006b) indicate that the annual average rainfall for the west of Scotland varies between around 1,200mm and 2,100mm for the period 1914 to 2004, equivalent figures for the east of Scotland indicate an equivalent range of between around 770mm and 1,450mm (Figure 18). Such figures themselves can, of course, mask significant areal variations.
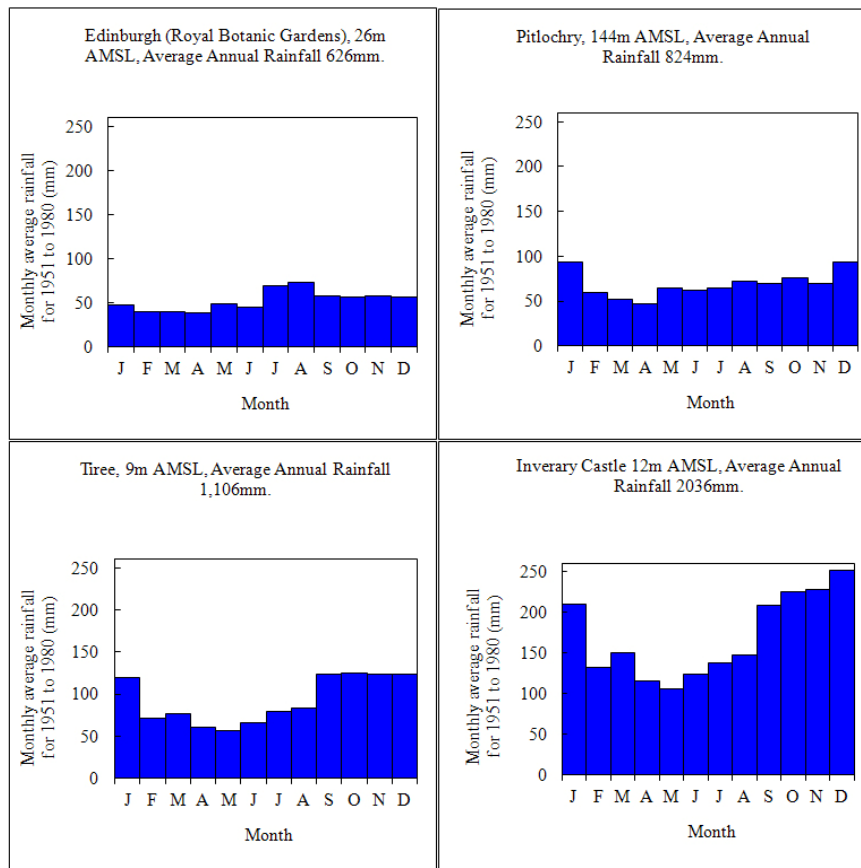


*Figure 17 Average rainfall patterns for selected locations in Scotland, based upon 30-year 1951 to 1980 averages from Anon (1989).*
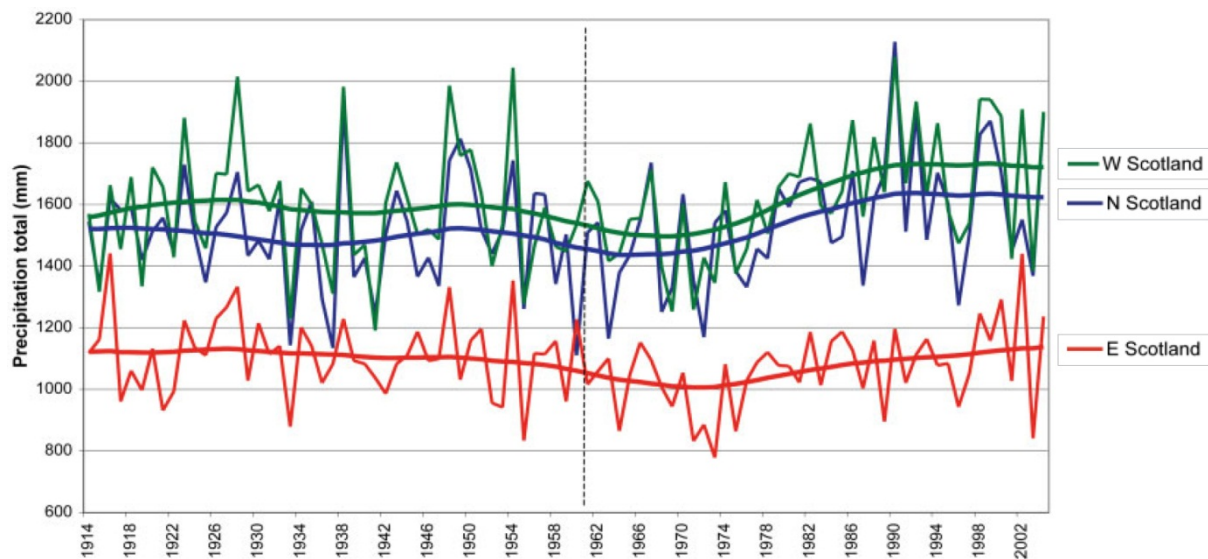
*Figure 18 Annual precipitation totals for Scottish regions from 1914 to 2004, with smoothed curves to show a running average (from Barnett et al., 2006a).*

Additionally, the majority of weather monitoring stations, including rainfall gauges, is inevitably located in generally more accessible low-lying areas. While developments in remote sensing have seen an increase in the number of observing sites in the more remote areas it remains the case that the station network is sparser in mountainous areas (McGregor & MacDougall, 2009). It is also the case that the network of observation stations is designed to meet general uses and climate (synoptic) monitoring requirements. Rainfall amounts in the higher elevation, mountain areas are usually greater due to orographic effects, albeit that the accumulations are likely to be generally higher on the westward-facing, windward, side of Scottish mountain ranges than on the eastward-facing, leeward, side where rain shadow effects may come into play. In broad terms these orographic effects are borne out at the macro scale for Scotland, and the UK as a whole, in Figure 16.  However, scenarios in both the west and the east indicate that the soil may be undergoing a transition from a dry to a wetter state at or around August and that in the period October/November to January the soil is likely to be in a wet, if not saturated, state and that rainfall continues to be at relatively high levels. This indicates an increased potential for debris flow and other forms of landslide activity during these periods.

Clearly, the soil water conditions necessary for debris flows may be generated by long periods of rainfall or by shorter intense storms. It is however widely accepted that Scottish debris flow events are usually preceded by both extended periods of (antecedent) rainfall and intense storms (Winter et al., 2009a) and it should be acknowledged that two landslide seasons are typically considered to prevail in Scotland: Summer, July and August; and Winter, (October) November to January (Winter et al., 2005).

## 3.2.2   Recent trends

It is instructive to consider not only the predictions for future climate change but also what trends may be observed in the climate of the recent past. Work by Barnett et al. (2006a; 2006b) describes trends in climate across Scotland during the last century. The figures

presented (for 1914 to 2004) indicate a broad, but small, increase in the running annual average rainfall for the north and, particularly, the west of Scotland while figures for the east of Scotland are broadly stable (Figure 18).

The conclusions that can be drawn from the work are variable and to a large extent depend upon the geographical area that is considered and the associated time period. Barnett et al. (2006a; 2006b) consider two time periods: 1914 to 2004 and 1961 to 2004. The data for the shorter period appears to be affected by a dip in overall average rainfall levels during the 1960s and 1970s and the associated recovery to previous levels and greater (Figure 18). As a result the changes found are greater for the shorter period than they are for the longer period (Table 30).

The data from the shorter (1961 to 2004) period shows a clear upward trend in both winter and annual precipitation while there is no clear trend for the spring, summer and autumn periods. For the longer period the statistical certainty inherent in the data is less and only two clear trends are apparent: a reduction in summer precipitation in East Scotland and an increase in spring precipitation in West Scotland.

Notwithstanding those trends that can be supported at the 95% statistical confidence level, the data more generally point to greater increases in annual precipitation in the winter and annual precipitation levels, particularly in the North and West of Scotland. Changes in summer precipitation show no clear trend in the 1961 to 2004 period but show a likely reduction for the longer 1914 to 2004 period. Certainly if a single long-term summary point is sought it would be that the trend in annual precipitation is either to remain roughly constant or to increase slightly while the changes within the annual period are generally reflective of increased winter precipitation, particularly in the West and North, and decreased summer precipitation, particularly in the North and East (Figure 19).

*Table 30 Percentage changes in average precipitation totals from 1961 to 2004 and 1914 to 2004. The values in bold indicate those changes that are considered to be part of a measurable trend at the 95% statistical confidence level (from Barnett et al., 2006a).*

|  | 1914 to 2004 | | | | 1961 to 2004 | | | |
|---|---|---|---|---|---|---|---|---|
|  | North Scotland | East Scotland | West Scotland | Scotland | North Scotland | East Scotland | West Scotland | Scotland |
| Spring | 13.9 | 6.1 | **22.0** | 14.3 | 16.2 | 9.4 | 17.3 | 14.8 |
| Summer | -12.7 | **-18.9** | -7.5 | -12.7 | -7.0 | 0.2 | 7.3 | -0.6 |
| Autumn | 13.6 | 0.7 | 15.6 | 11.1 | 5.3 | 22.2 | 5.9 | 9.1 |
| Winter | 20.9 | -0.8 | 9.0 | 11.6 | **69.9** | **36.5** | **61.3** | **58.3** |
| Annual | 9.6 | -3.5 | 9.5 | 6.2 | **21.0** | **18.4** | **22.3** | **21.1** |

Increases in the number of days of heavy rain (>10mm) are perhaps slightly more clear cut (Figure 20 and Figure 21, Figure 64; Table 31) showing a trend of increasing heavy rainfall in winter, particularly in North and West Scotland which have seen increase of more than eight days. In the other seasons the changes are too small to detect a trend. The spatial patterns of change are broadly similar to those for total rainfall with a strong east-west gradient in the winter months (Figure 21). It is also clear that the years in which the annual rainfall is highest (Figure 18) are also those with the highest number of days that experience heavy rain (Figure 20).

*Table 31 Changes in days of heavy rain (equal to or more than 10mm), in days, from 1961 to 2004. The values in bold indicate those changes that are considered to be part of a measurable trend at the 95% statistical confidence level (from Barnett et al., 2006a).*

|        | North Scotland | East Scotland | West Scotland | Scotland |
|--------|----------------|---------------|---------------|----------|
| Spring | 1.8            | 1.0           | 1.6           | 1.5      |
| Summer | -1.4           | -0.5          | 0.9           | -0.4     |
| Autumn | -0.2           | 2.3           | 0.1           | 0.7      |
| Winter | **8.3**        | **3.5**       | **8.2**       | **6.7**  |
| Annual | **8.2**        | **6.2**       | **10.6**      | **8.3**  |

Barnett et al. (2006a; 2006b) also report on the change in the number of consecutive dry days from 1961 and 2004, concluding that there had been very little change and that there is no obvious long-term trend in this index for this period.

The trends isolated by Barnett et al. (2006a; 2006b) are reinforced by other workers including Marsh (1996) who observed the increasing trend towards wetter winters and drier summers, with rainfall totals increasing, particularly in the north and west of the UK. Foster et al. (1997) note the marked differences between the annual rainfall trends in the west and east of Scotland over the period 1861 to 1994, with the west appearing to become significantly wetter and the east remaining much the same. In addition, Osbourn et al. (2000) found evidence that the intensity distribution of daily precipitation across Scotland had changed over the period 1961 to 1995; the majority of weather stations examined showed a general shift from light to medium intensity events to greater intensity events in winter, and to a lesser extent in the spring and autumn; the reverse was found to be true in the summer (Galbraith et al., 2005).

Barnett et al.'s (2006a; 2006b) data suggest pan-Scotland annual average temperature increases of around 0.5$^{\circ}$C (1914 to 2004) and around 1.0$^{\circ}$C (1961 to 2004). This apparent anomaly is explained by a dip in the temperature trend, centred on the 1970s, similar to that for precipitation (Figure 18).
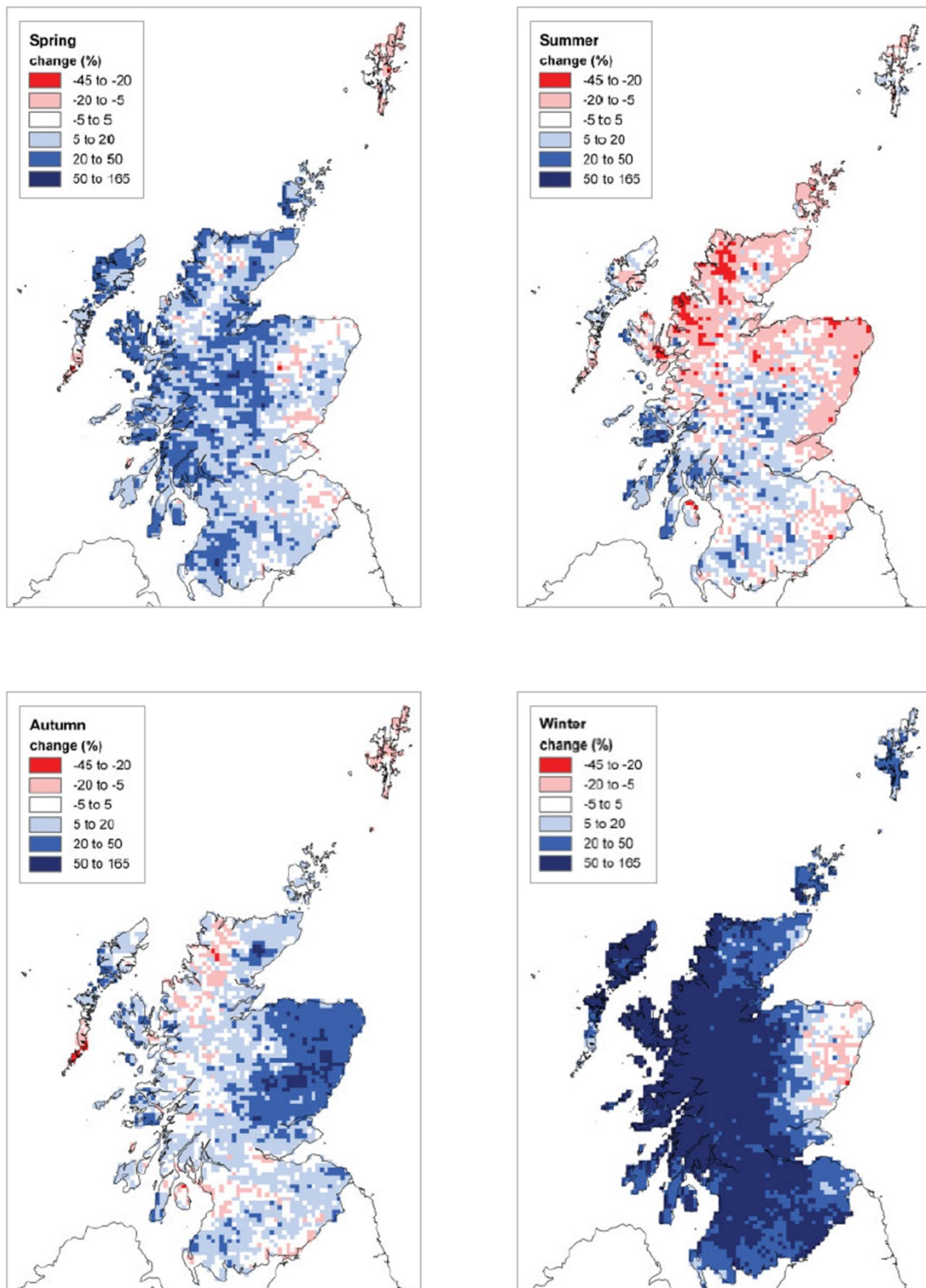
*Figure 19 Patterns of percentage change in precipitation totals between 1961 and 2004 for each season (from Barnett et al., 2006a).*
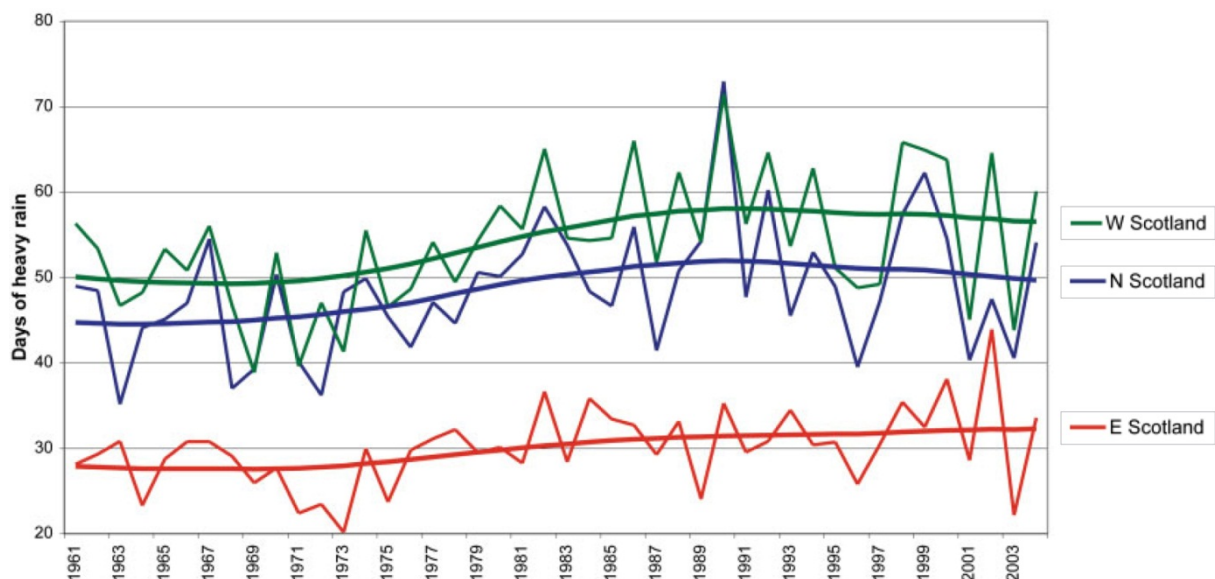
*Figure 20 Days of heavy rain (equal to or more than 10mm) for Scottish regions from 1961 to 2004, with smoothed curves to show a running average (from Barnett et al., 2006a).*

### 3.2.3   Potential climate change: UKCIP02

The UKCIP02 (UK Climate Impacts Programme) report considered three periods: the 2020s, the 2050s and the 2080s and four alternative emissions climates namely Low Emissions, Medium-Low Emissions, Medium-High Emissions and High Emissions (Hulme *et al*., 2002).

In general terms the scenarios for Scotland show little predicted change in annual mean precipitation over the next few decades, with any change being within the range that can be attributed to natural variability. However, Galbraith et al. (2005) note that even by the 2020s a distinct seasonal pattern could be discerned, even in the low emissions scenario. While little significant change was predicted for the spring or autumn precipitation amounts, changes were found to be likely for the winter and summer. Winter precipitation was predicted to increase by between 10% and 15% for the Low and High emissions scenarios in the eastern regions, with changes elsewhere being within the range of that which can be accounted for by natural variability (Figure 22).

In the summer decreases in the average precipitation are predicted to be widespread with only the far northwest seeing little change. By the 2020s Galbraith et al. (2005) indicate that the High emissions scenario implies that the decreases are likely to be greatest in the south east of Scotland and could be a much as 20% less than present day modelled levels.

Year-on-year, or inter-annual, variability in precipitation is also predicted to change (Galbraith et al., 2005). Although results were presented in the UKCIP02 outputs only for the 2080s the results are generally taken as being indicative of the type of change that is likely to be experienced in the 2020s on a proportional basis. Increased variability in precipitation in eastern Scotland is anticipated during the winter months, whilst the variability is likely to decrease over much of the rest of the country, particularly the south, during summer. It was also noted by Galbraith et al. (2005) that natural variability was likely to continue to dominate any climate change-related trend in the long term average over the next few decades. Thus, while winters may well become increasingly wet compared to the present there may also be

periods of below average rainfall. It is of course also important to recognise that average changes may mask the important effects of variability.
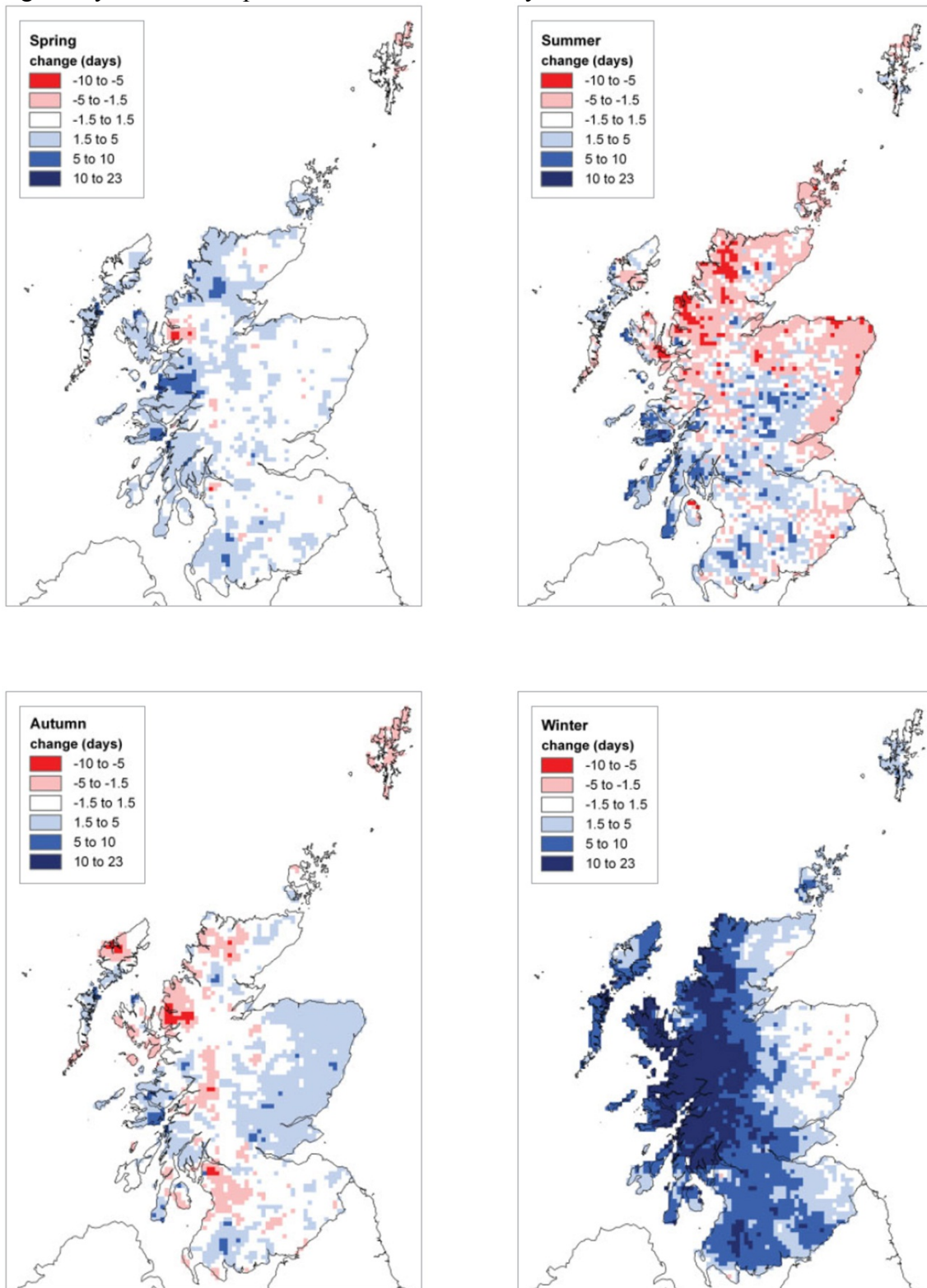


*Figure 21 Patterns of percentage change in the number of days with heavy rain (equal to or more than 10mm) between 1961 and 2004 for each season (from Barnett et al., 2006a).*
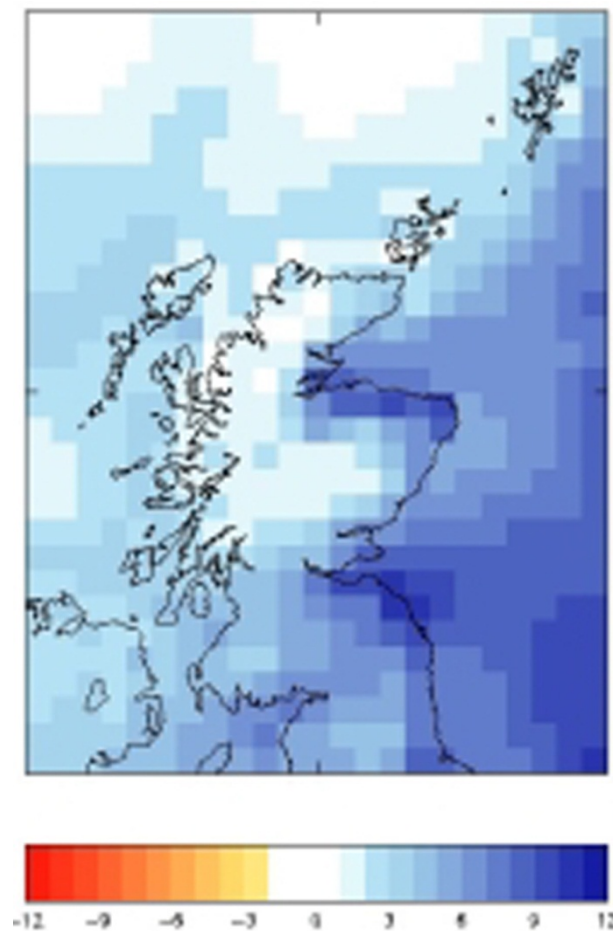
*Figure 22 Winter (December to February) percentage precipitation change by the 2020s for the Medium-High emissions scenario (25km BIC grid). Source: Met Office (from Galbraith et al. (2005).*

Figure 23 shows the UKCIP02 results for the increase in the magnitude of the two-year return period event which illustrates the general pattern of a decrease in the summer and increase in the winter with little change in the spring and autumn.

However one point of great importance when considering debris flow is that the climate models are generally considered not to be able to resolve localised convective storm activity. These types of storms are believed to be at least partially responsible for triggering the events of August 2004 in Scotland for example (Winter et al. 2005; 2006; 2009a), and climate data may not give a full picture of the relationship between precipitation and landslides. Furthermore, it is important to note that climate models generally predict averages and that the error limits can be substantial.

Predicted changes in the number of 'intense' rainfall days (defined as the uppermost 10% of total seasonal rainfall) generally indicate a net increase of less than one day per annum by the 2080s, with slightly fewer intense wet days in the summer and more in the winter, particularly in south-west Scotland (Figure 24).

Galbraith et al. 2005 summarise the predicted trends in storm event rainfall for short return periods by suggesting that by 2080 the design storm event rainfall depth will have increased by between 10% and 30% (or by between 4% and 13% by the 2020s). The most intense

winter rainfall may on average increase by slightly more whereas the spring and autumn are likely to have increased by slightly less. In addition summer rainfall depths are predicted to decrease by 0% to 10%. In broad terms the predicted changes in 'storminess' broadly follow the recent trends reported by Barnett et al. (2006a).
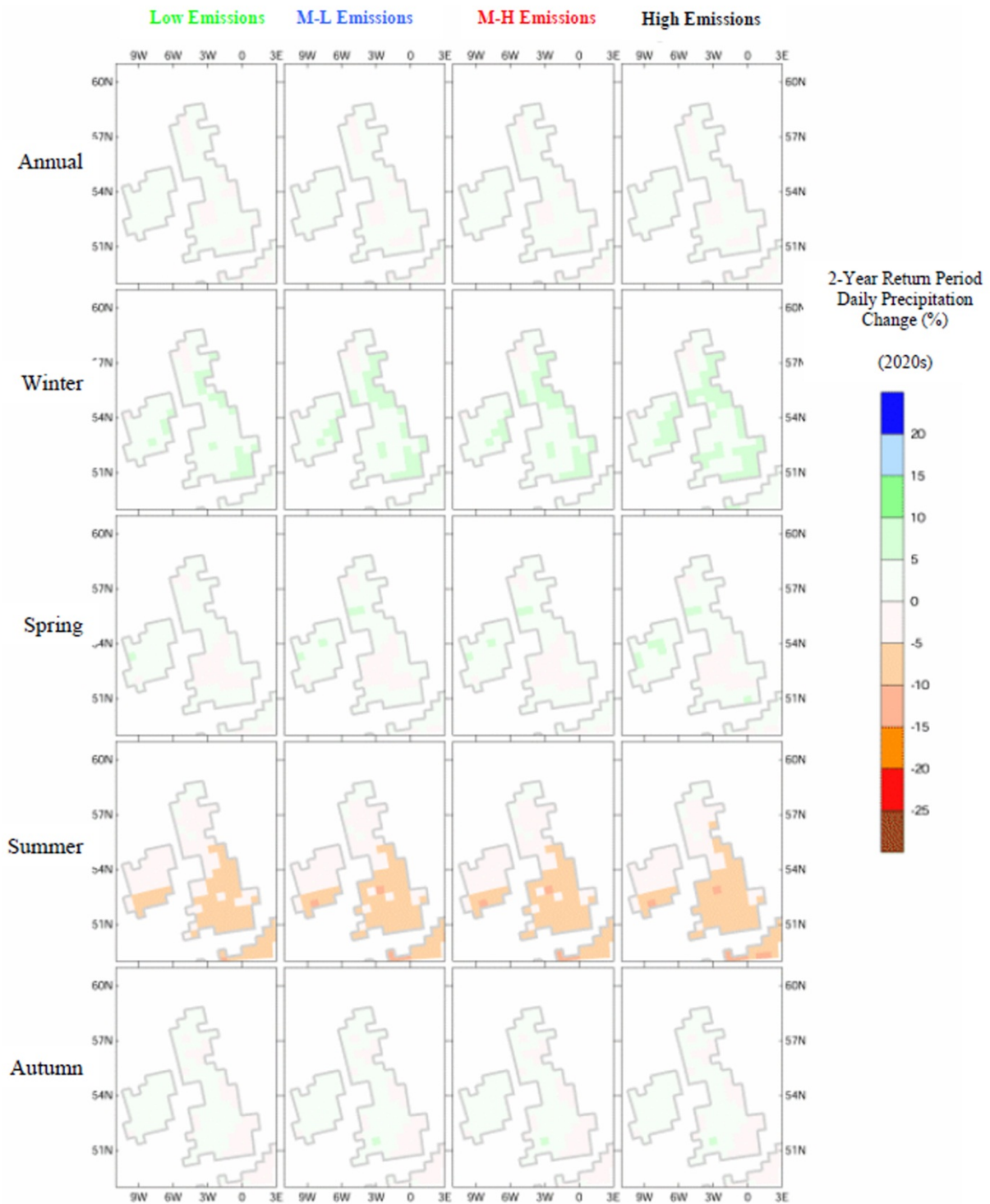


*Figure 23 Two-year return period daily precipitation percentage change by the 2020s for each UKCIP02 emissions scenario and season. Source: Hulme et al. (2002) (from Galbraith et al. 2005).*

The UKCIP02 report also considered that soil moisture and average soil moisture is likely to increase in the winter and decrease during the summer. However, the winter increases are lower than might be expected simply from the increased precipitation levels. As higher temperatures and reductions in relative humidity mean that evaporation will increase.
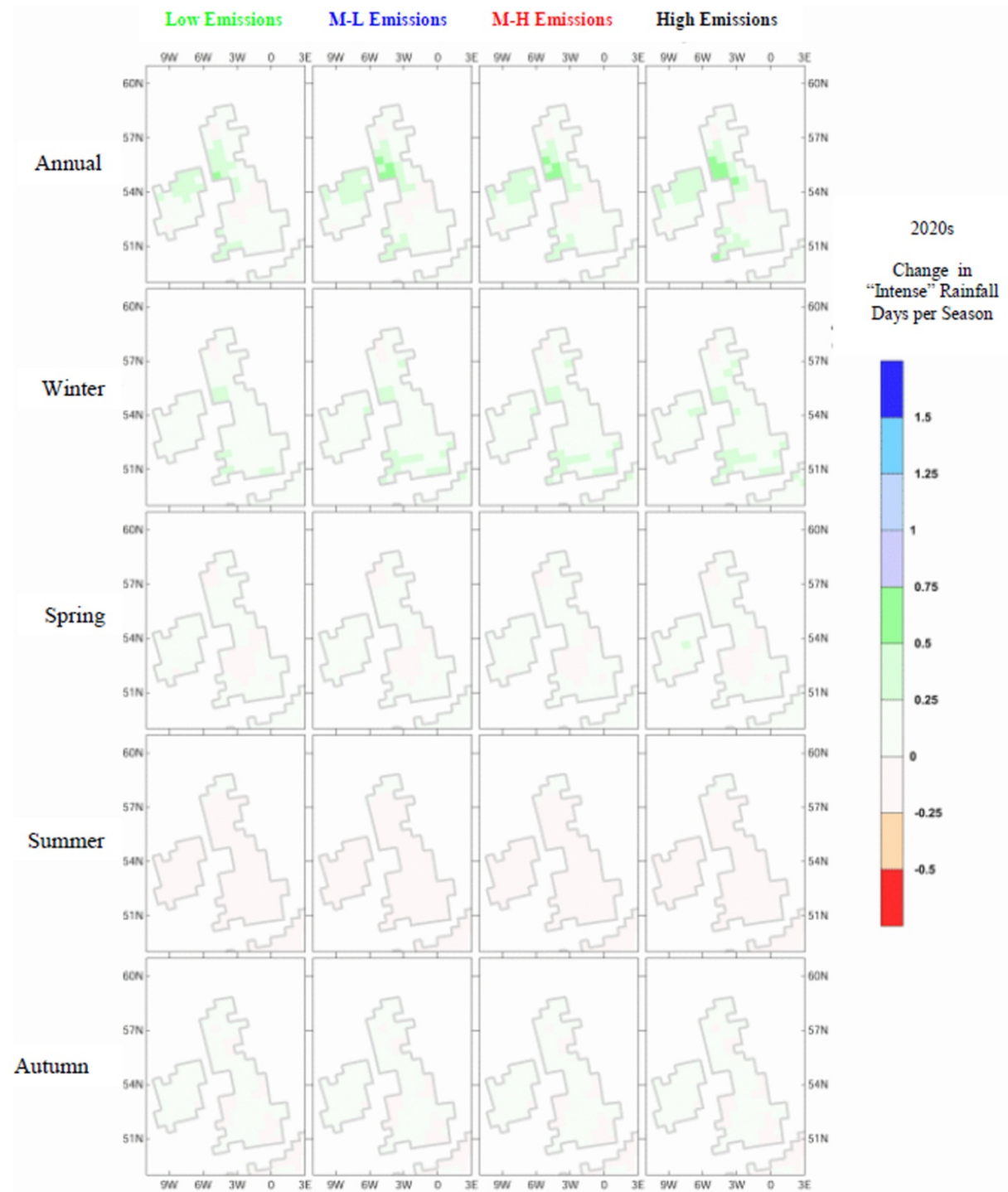


*Figure 24 Changes in 'intense' rainfall days per season by the 2020s for each UKCIP02 emissions scenario and season. Source: Hulme et al. (2002) (from Galbraith et al. 2005).*

It is predicted that by the 2080s the average soil moisture content will increase by between 3% and 5% in the winter and be between 10% and 30% lower in the summer and autumn. Using linear scaling, by the 2020s it is predicted that the average soil moisture content will be between 0% and 2% higher during the winter and between 3% and 8% lower during the summer and autumn.

UKCIP02 data (Galbraith et al., 2005) suggests that increases in daily annual temperature will rise by up to 1°C in the next few decades in Scotland for all emissions scenarios. The daily minimum and maximum temperatures are predicted to increase by the same order of magnitude. The growing season is also predicted to increase, from 150 days in the north of Scotland to 200±20 days by the 2080s and to 172±10 days by the 2020s.

### 3.2.4  Potential climate change: UKCP09

UKCP09 gives climate change projections for a number of climate variables over seven 30-year overlapping time periods, at a resolution of 25km (for administrative regions and river basins). This is the first UK set of predictions to attach probabilities to different levels of future climate change. These probabilities represent the relative degree to which each climate outcome is supported by the evidence currently available (Anon. 2011a). While UKCIP02 considered four scenarios (High, Medium-High, Medium-Low and Low) the UKCP09 scenarios consider three (High, Medium and Low).

The pertinent headline predictions for the 2080s, relative to a 1961-1990, for the Medium emissions scenario at the UK level were summarised by Jenkins et al. (2009) as follows:

- Changes in summer mean temperatures are greatest in parts of southern England (up to 4.2°C at the 50% probability level (2.2 to 6.8°C for the 10 and 90% probability levels, respectively)) and least in the Scottish Islands (just over 2.5°C (1.2 to 4.1°C)).

- Estimates of annual precipitation show relatively little change at the 50% probability level. Changes range from -16% at the 10% probability level to +14% at the 90% probability level, with no simple pattern.

- Changes in winter precipitation of up to +33% (+9 to +70%) are reported for the west of the UK, while decreases of a few percent (-11 to +7%) are reported in parts of the Scottish highlands.

- Changes in summer precipitation down to around -40% (-65 to -6%) are seen in parts of the far south of England. While changes close to zero (-8 to +10%) are seen over parts of northern Scotland.

- Changes in the wettest winter day range from zero (-12 to +13%) in parts of Scotland to +25% (+7 to +56%) in parts of England.

- Changes in the wettest summer day range from -12% (-38 to +9%) in parts of southern England to +12% (-1 to +51%) in parts of Scotland.

Clearly different time periods and emissions scenarios must be studied in order to obtain a higher resolution relative to a specific issue at a specific location. Indeed, Figure 25 considers the case of winter mean precipitation for Glasgow resulting from the High emissions scenario. The picture is, as clearly articulated in the diagram, one of wetter winters. However, the detailed picture is somewhat more complex and by the 2080s the upper estimate (at the 90%

probability level) suggests that the increase could be up to almost 50% greater than the baseline, while the lower estimate (10% probability) suggests that the increase is likely to be around 10%. The central estimate (50% probability) suggests that this increase is likely to lie in the range 20% to 30%.

Clearly this picture will be yet more complex if one then considers the potential effects of the Medium and Low emissions scenarios becoming manifest in the intervening period, most likely extending the range of potential mean winter precipitation increase downwards, perhaps suggesting a possible range of between close to zero and almost 50%.
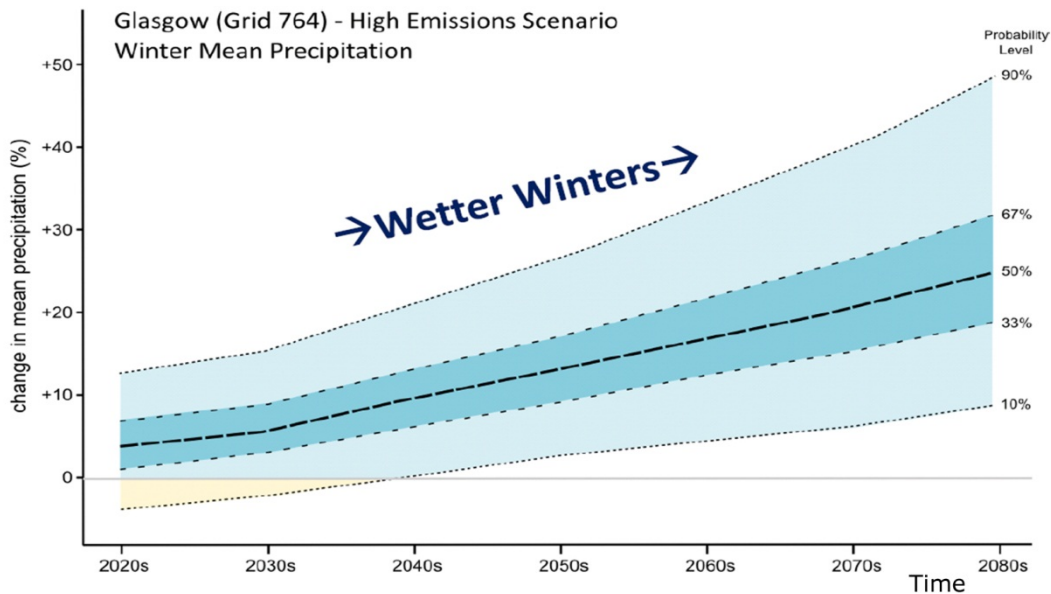


*Figure 25 Predicted changes in winter mean precipitation for Glasgow resulting from the High emissions scenario (from a presentation by J Hagg, SCCIP based on UKCP09 data).*

This concept is taken a step further (Walking-the-Talk, 2011). They observed that the three emissions scenarios presented broadly similar results up until the 2050s, before starting to diverge as the 2080s were approached, and that this was a reasonable timescale for the type of infrastructure that they were considering (rural footpaths). Accordingly the 2050s were selected as the central point for the work and the relationship between emissions scenarios and predicted climate change laid-out as follows:

| Emissions Scenario | Predicted Change by the 2050s | | |
|---|---|---|---|
| | 10% probability | 50% probability | 90% probability |
| High | | | Upper Limit |
| Medium | | Central Estimate | |
| Low | Lower Limit | | |

This rather elegant approach has the considerable benefit of somewhat simplifying the rather complex options implicit within a probability-based prediction of this nature. The predicted changes in precipitation for the 2050s are set-out in

Table 32. Certainly the figures for winter precipitation in West Scotland are broadly consistent with those for Glasgow in the 2080s (Figure 25).

Table 32 Predicted changes to seasonal mean precipitation by the 2050s (from Walking-the-Talk, 2011).

|  | Mean winter precipitation (%) | | | Mean summer precipitation (%) | | |
|---|---|---|---|---|---|---|
|  | Lower Limit | Central Estimate | Upper Limit | Lower Limit | Central Estimate | Upper Limit |
| North Scotland | -1 | +13 | +26 | -20 | -10 | +3 |
| East Scotland | +2 | +10 | +20 | -26 | -12 | +2 |
| West Scotland | -1 | +15 | +31 | -25 | -12 | +2 |

A more conventional approach is taken by Anon. (2011a) and also, as the work relates to the strategic road network, the period centred on the 2080s is considered. Notwithstanding this, where data as opposed to maps are presented, the equivalent Lower Limit, Central Estimate and Upper Limit estimates can be extracted from their work to provide a degree of comparison between the 2050s and the 2080s. Unfortunately Anon. (2011a) present only figures for annual mean precipitation and only confirm the previously noted trends and predictions that annual changes will be relatively small, albeit that the Upper Limit predictions almost reach 15%.

Table 33 Predicted changes to annual mean precipitation by the 2080s (from Anon., 2011a).

|  | Annual mean precipitation (%) | | |
|---|---|---|---|
|  | Lower Limit | Central Estimate | Upper Limit |
| North Scotland (Aviemore) | -3.5 | -0.9 | +3.8 |
| East Scotland (Dundee) | -2.2 | +1.4 | +10.6 |
| West Scotland (Glasgow) | -7.6 | -0.4 | +14.6 |
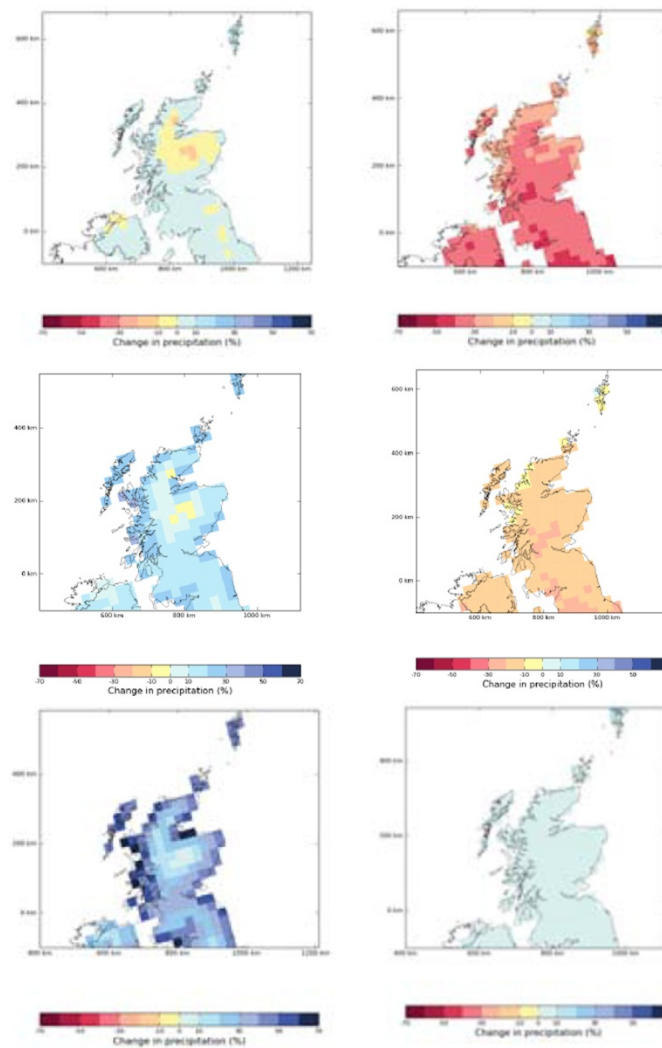
*Figure 26  Percentage change (-70% to +70%) winter (left) and summer (right) precipitation for the 2080s emissions scenario at the 10% probability (top), 50% probability (middle) and 90% probability (bottom) (from Anon., 2011a). (Note that the quality of this figure is dictated by that of the original.)*

It is important to note that despite the relative uniformity of winter mean precipitation increases across Scotland the actual magnitude of the changes will follow a rather steep gradient from east to west as suggest by Figure 16. As is pointed out by Anon. (2011a), a 10% increase in rainfall at Dundee (200mm for December to February), in the east, corresponds to an increase of 20mm while at Fort William (800mm for December to February), in the west, the same percentage increase corresponds to an additional 80mm.

Both Anon. (2011a) and Walking-the-Talk (2011) go on to discuss precipitation intensity. The latter consider the precipitation on the wettest day in winter and summer (Figure 27), demonstrating that in the winter for the Lower Limit and Central Estimate the change is less than ±10% across most of the country. However, for the Upper limit the increase is of the order of 30% to 40% in coastal areas. In the summer the change could range from 10% to 20% less in the lower limit prediction to 10% to 20% greater in the upper limit prediction.
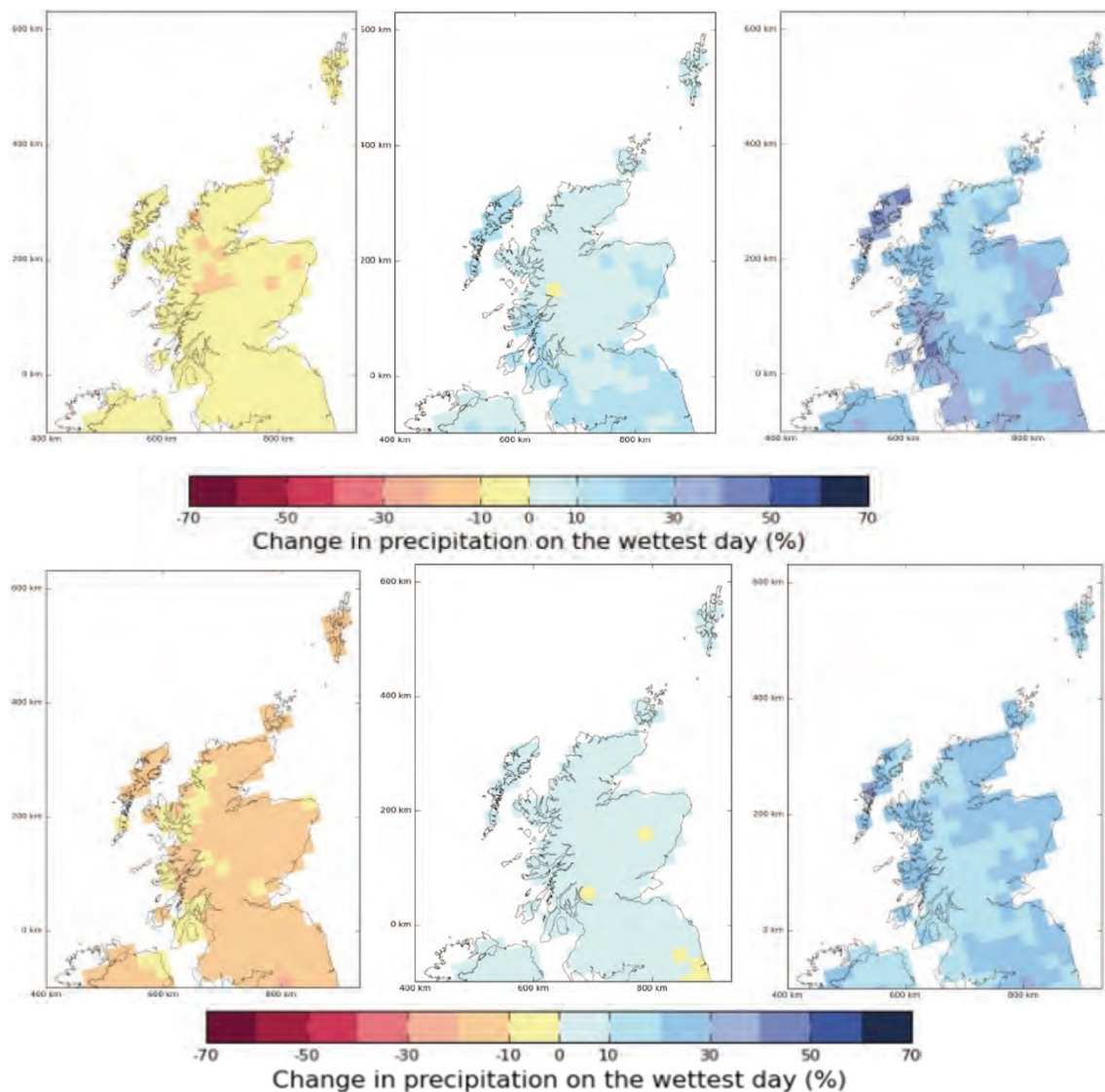
*Figure 27 Percentage change in the precipitation in the wettest day in winter (top) and summer (bottom) for the 2050s. Lower Limit (left), Central Estimate (middle) and Upper Limit (right) (from Walking-the-Talk, 2011).*

Further analysis for extreme weather events (greater than 30mm in 24 hours) in the 2050s demonstrated that intense rainfall events are more frequent for the higher emissions scenario, especially for the west of Scotland in which area the largest events are expected to be experienced in the winter. Extreme events were also found to be more likely further north (Walking-the-Talk, 2011).

A somewhat different approach, involving the estimation of 10-year return period daily one-day rainfall depths, is taken to the issue of intense rainfall events by Anon. (2011a). The estimations were made using the UKCP09 weather generator and were undertaken for the 2080s as well as the 2020s and the baseline period of 1961 to 1990. The latter allowed a comparison between the estimated and 'observed' taken from the Flood Estimation Handbook (Institute of Hydrology, 1999) depth-duration-frequency rainfall statistics (Table 34).

*Table 34 10-year return period daily rainfall depths (in mm) derived from the UKCP09 weather generator for the baseline, 2020s and 2080s periods for the medium emissions scenario and for the 10%, 50% and 90% probability levels. The observed values provide the currently accepted value based on the analysis of real observed data.*

| | Observed | Baseline 1961 to 1990 | | | 2080s Medium | | | 2020s Medium | | |
|---|---|---|---|---|---|---|---|---|---|---|
| | | 10% | 50% | 90% | 10% | 50% | 90% | 10% | 50% | 90% |
| Glasgow (W) | 47.4 | 42.0 | 47.6 | 52.7 | 50.4 | 59.8 | 72.0 | 46.7 | 54.1 | 61.8 |
| Aviemore (N) | 48.9 | 44.1 | 49.9 | 56.7 | 48.3 | 58.2 | 72.7 | 47.5 | 53.1 | 67.7 |
| Dundee (E) | 48.9 | 41.1 | 47.4 | 54.8 | 50.9 | 61.3 | 77.9 | 44.2 | 54.1 | 64.0 |

The simulated baseline value from the weather generator compare well with the observed values, especially, as might be anticipated, at the 50% probability level, giving confidence in the ability of the weather generator to make coherent predictions. Clearly the potential increases in rainfall depth are significant as set out in Table 35 and Table 36 for Lower Limit, Central Estimate and Upper Limit for the 2080s and 2020s respectively.

*Table 35 Predicted percentage changes in rainfall depth from the baseline condition (Table 34) for Lower Limit, Central Estimate and Upper Limit scenarios for 10-year and 2-year return periods for the 2080s.*

| | Change for 2080s 10-year Return | | | Change for 2080s 2-year Return | | |
|---|---|---|---|---|---|---|
| | Lower Limit | Central Estimate | Upper Limit | Lower Limit | Central Estimate | Upper Limit |
| Glasgow (W) | -3 | +29 | +72 | -3 | +21 | +49 |
| Aviemore (N) | -8 | +20 | +75 | -7 | +12 | +30 |
| Dundee (E) | +5 | +31 | +72 | 0 | +19 | +44 |

*Table 36 Predicted percentage changes in rainfall depth from the baseline condition (Table 34) for Lower Limit, Central Estimate and Upper Limit scenarios for 10-year and 2-year return periods for the 2020s.*

| | Change for 2020s 10-year Return | | | Change for 2020s 2-year Return | | |
|---|---|---|---|---|---|---|
| | Lower Limit | Central Estimate | Upper Limit | Lower Limit | Central Estimate | Upper Limit |
| Glasgow (W) | -10 | +14 | +47 | -2 | +8 | +13 |
| Aviemore (N) | -11 | +9 | +44 | -10 | +4 | +26 |
| Dundee (E) | -12 | +16 | +45 | -5 | +5 | +26 |

Although lower limit predictions are generally negative, most of the data suggest that rainfall depths will increase in the future. Interestingly, the longer return period (more intense rainfall) events show the greater increase. This might be taken to indicate that higher magnitude events will become even greater and that there is thus a general propensity for storms or greater intensity which are, of course, intrinsically linked with the triggering of landslides.

Finally, temperature is an important variable in that it has a strong influence on evapotranspiration and the duration of the growing season. Data from Walking-the-Talk (2011) in table20 suggest that both mean winter and mean summer temperatures will increase by the 2050s regardless of the emissions/probability scenario considered. The increases are broadly similar across the whole of the relatively small land mass of Scotland and are greater for the summer period than they are for the winter period. The data presented also suggest increases to the winter (+0.6$^{\circ}$C to +4.3 $^{\circ}$C) and summer maximum temperatures (+0.9$^{\circ}$C to +6.4 $^{\circ}$C).

*Table 37 Predicted changes to seasonal mean temperatures by the 2050s (from Walking-the-Talk, 2011).*

|  | Mean winter precipitation (%) | | | Mean summer precipitation (%) | | |
|---|---|---|---|---|---|---|
|  | Lower Limit | Central Estimate | Upper Limit | Lower Limit | Central Estimate | Upper Limit |
| North Scotland | +0.6 | +1.7 | +3.0 | +0.9 | +2.0 | +3.9 |
| East Scotland | +0.6 | +1.7 | +3.1 | +1.0 | +2.3 | +4.5 |
| West Scotland | +0.8 | +1.9 | +3.3 | +1.0 | +2.4 | +4.4 |

Similar conclusions can be drawn from the less detailed datasets presented by (Anon., 2011a).

### 3.2.5  Summary

The historical trend data (Section 3.2.3) and the UKCIP02 (Section 3.2.4) data both suggest that the mean winter rainfall will increase and that the summer mean rainfall will decrease, while the annual mean rainfall will remain broadly comparable with present levels.

Rainfall intensity is clearly an important issue for landslides and the most articulate data set is that derived from UKCP09, which suggests that not only will intense rainfall increase in severity but that the effect will be more pronounced for higher magnitude events and that there is thus a general propensity for storms or greater intensity which are, of course, intrinsically linked with the triggering of landslides. It should, of course, be noted that the prediction of high intensity rainfall (weather) events is neither the purpose of climate models nor are such models best-suited to such activities.

Importantly, all of the data sets suggest increases in the temperature, described as daily mean, annual mean or minima or maxima.

The change from the rather deterministic data sets provided by UKCIP02 to the probabilistic data sets of UKCP09 is interesting. The overall picture presented by UKCP09 could be validly described as both more complex than that provided by UKCIP02 but also as having a greater granularity or resolution. Certainly the more recent model provides a more useful data set and the simplification of the emissions scenario-probability matrix proposed by Walking-the-Talk (2011) to give lower limit, central estimate and upper limit scenarios is very helpful and has been used in Section 3.4 where possible.


### 3.3  CHANGING HAZARD

Changes in the factors discussed in the foregoing sections coupled with increased potential evapotranspiration (particularly in the summer) and a longer growing season (leading to increased root uptake) are expected to substantially affect soil moisture. The UKCIP02 model that deals with soil moisture predicts a 10% to 30% decrease in soil moisture in summer/autumn and a 3% to 5% increase in winter. The winter figures reflect the fact that soils can only contain a finite amount of water and most Scottish soils are already close to saturation in the winter.

The soils that form the slopes subject to debris flow comprise a wide range of materials, albeit that periglacial, glacial, and post-glacial processes dominate their formation and subsequent modification. In terms of the composition of debris flow the particle sizes may range from

coarse granular (including boulders) to fine cohesive with most sizes between potentially represented (e.g. McMillan et al., 2005); certainly the characteristics of the materials involved in the August 2004 events support this diverse view (Winter et al., 2006). Both Winter et al. (2009a) and Milne et al. (2009) acknowledge the importance of water-bearing soils, particularly peat, located on high, relatively flat ground as trigger materials for gulley-constrained debris flows. The materials that are later eroded, entrained and transported to form the body of the flow may be of entirely different characteristics; often coarser-grained materials from morainic and related features are critical to the development of such flows.

Increased rainfall during the winter months seems likely to increase the prevalence of landsliding in Scotland. This is particularly so when considered in the context of the likelihood of more intense rainfall events. Events such as that illustrated in Figure 13 are amongst those typical of winter events in Scotland.

The reduced soil moisture, as a result of both predicted temperature increases and rainfall decreases, during the summer and autumn may mean that the short-term stability of some slopes, particularly those formed from granular materials, may be enhanced by suction pressures. Soils under high levels of suction are, however, vulnerable to rapid inundation (Toll, 2001), and a consequent reduction in the stabilising suction pressures, under precisely the conditions that tend to be created by short duration, localised summer storms. In addition, non-granular soils may form low permeability crusts during extended dry periods as a result of desiccation. Providing that these do not experience excessive cracking due to shrinkage, then runoff to areas of vulnerable granular deposits may be increased. However, the formation of drying cracks could lead to the rapid development of instabilities in soil deposits, potentially creating conditions for the formation of debris flows. The complicating factors are that climate models are not best at resolving storm events and the precise nature of the localised failure mechanisms that will lead to the initiation of an individual debris flow. The measurement of soil suction is unlikely to provide a practical and reliable means of debris flow forecast.

While peat soils may not be overly vulnerable to the effects of drying and soil suction the association between with rainfall and sliding in peat deposits is well-founded (e.g. Boylan et al., 2008; Dykes et al., 2008; Long & Boylan, 2008, 2011; Nichol et al., 2007, 2008; Winter et al, 2009b; Dykes & Jennings, 2010a, 2011). Peat soils are well-recognised as sources of trigger events for debris flows in Scotland and their importance to the overall debris flow process has been widely recognised (e.g. Winter et al., 2009a).

Vegetation will also be affected by climate change. Lower overall levels and changed patterns of rainfall might be expected to increase the pressure on vegetation and thus to reduce its beneficial effect upon slope stability. Additionally, extended periods of exceptionally dry weather could potentially lead to wildfires and associated debris flow such as those described by Cannon *et al*. (2008). This seems less likely to be a factor in the relatively wet climate of Scotland and it seems more likely that an extension to the growing season will predominate in terms of the effects of vegetation. However, the possibility of vegetation desiccation cannot be dismissed during prolonged summer dry spells.
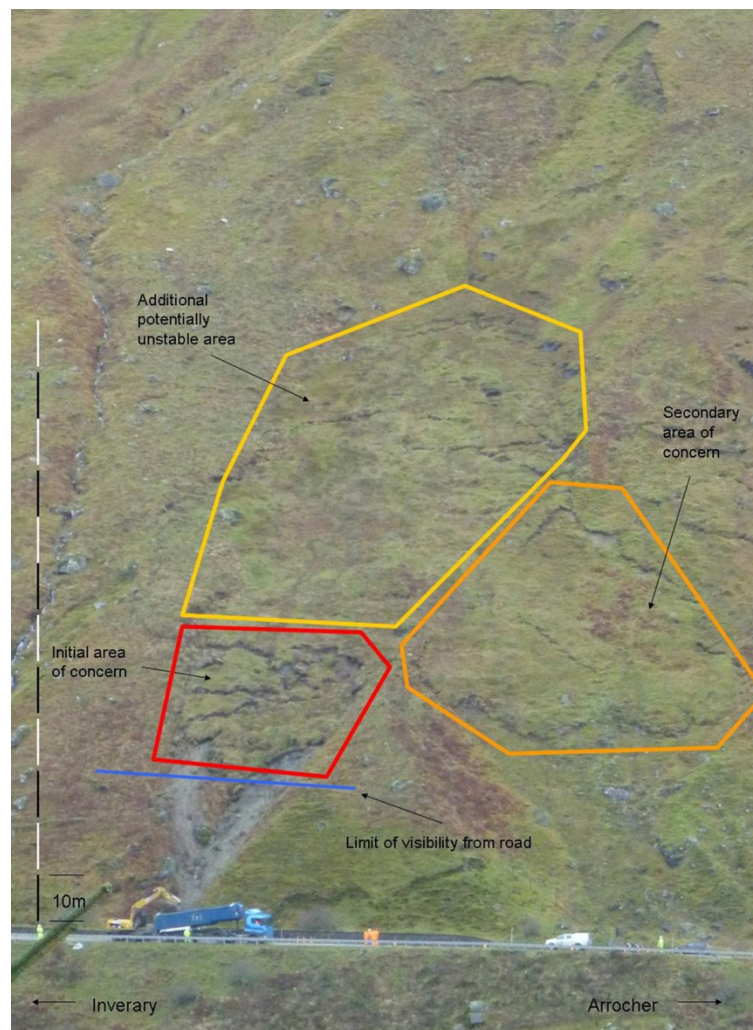
*Figure 28 A83 Rest and be Thankful debris flow event of 1 December 2011. View from the opposite side of Glen Croe showing further potential failures including the subsequent movement of the 'secondary area of concern' (outlined in orange) of 22 February 2012.*

The issue of soil suction perhaps bears further inspection. That rainfall can cause landslides was vividly demonstrated in February 2005 when catastrophic landslides occurred following intense storms on the western seaboard of North America. Property destruction and loss of life resulted from various landslides. Over approximately a seven-month period, the Malibu area of California received over 585mm (23 inches) of cumulative precipitation. Then in February 2005 an additional 228mm (9 inches) fell over four days, after which time the landsides occurred (Geoslope, 2005).

Analyses by Geoslope, replicating the rainfall conditions experienced in California and British Columbia in February 2005 yielded some interesting results. The analysis confirmed that a typical model slope remained stable for seven months during which 585mm of cumulative rainfall fell but became unstable after a further 228mm fell during four days. Typically the failure could not be attributed to increased positive pore water pressures as the failure surface did not penetrate below the water table. Geoslope attributed the failure to decreases in suction. This type of behaviour corresponds well with that predicted from

unsaturated soil mechanics theory (Wheeler et al., 2003) and the broad style of this type of failure mechanism is supported by experiment (Springman et al., 2003).

On balance the predicted changes in climate seem to suggest the potential for greater landslide activity in terms of both frequency and magnitude in Scotland, certainly during the winter months. A rather more complex picture emerges for the summer months but one possible outcome is that the frequency of events may decrease but that the magnitude of those that do occur may increase.

## 3.4    CHANGING RISK

In Scotland landslides are, by far, most common in more remote mountainous, rural areas with *relatively* little vulnerability to buildings and static human populations. Clearly there are exceptions as illustrated in Figure 29, but these are generally located in areas that are unlikely to be subject to future urban development to any great extent, not least as the available land is extremely limited. It is recognised, however, that some form of planning control at such sites might be beneficial in terms of ensuring that the risk level is not exacerbated. This seems unlikely to happen in a systematic manner, but it does seem equally unlikely that extensive redevelopment would be condoned by the planning authorities.



*Figure 29 Urban landslide at Bervie Braes, Stonehaven, on the north-east coast of Scotland (February 2010). The landslides at Bervie Braes occur on a raised sea cliff.*

Perhaps the greatest hazards coincide with, primarily, road, but also rail, links between rural communities. Typically such roads carry 5,000 to 6,000 vehicles per day (all vehicles two-way, 24 hour AADF – Annual Average Daily Flow) as is the case for the A83 (Figure 30) and the A85, while the more substantial A9 (Figure 31) carries around 13,500 vehicles per day. These figures are for the most highly-trafficked month of the year for each of the roads, either July or August. Minimum flows occur in either January or February and are roughly half those of the maxima. The figures reflect the importance of tourism and related seasonal industries to Scotland's economy.

The three most important administrative regions in Scotland with respect to landslides, as they affect roads, are the Argyll and Bute, Highland, and Perth and Kinross council areas. Traffic figures for these areas as well as for Scotland as a whole are given in Table 38 and Figure 32 for the period 1995 to 2010 and for trunk roads, such as those discussed above, local roads and all roads. Whilst it is clear that there is traffic growth over this period the scale of the trends are not overly apparent; plotting the growth in traffic normalised to the 1995 figures (Table 39 and Figure 33) makes these trends much more apparent. In general the trend is for growth of between around 10% (1.1 times 1995 levels) and 26% (1.26 times) over the 15 year period since 1995, including a noticeable dip from 2008 onwards which seems most likely to be associated with the global economic downturn. The dip centred around 2000 and 2001 is less well-resolved for Scotland as a whole and may be associated with data sampling, collection and analysis at the local authority level.



*Figure 30 Debris flow at A83 Rest and be Thankful (January 2007).*

*Figure 31 Debris flow at A9 north of Dunkeld (August 2004).*

*Table 38 Traffic on trunk (strategic), local authority and all roads by selected areas1 (in million vehicle kilometres) (data from Anon. 2006; 2011b).*

| Area | 1995 | 1996 | 1997 | 1998 | 1999 | 2000 | 2001 | 2002 | 2003 | 2004 | 2005 | 2006 | 2007 | 2008 | 2009 | 2010 |
|------|------|------|------|------|------|------|------|------|------|------|------|------|------|------|------|------|
| **Argyll and Bute** | | | | | | | | | | | | | | | | |
| Trunk Roads (T) | 319 | 331 | 338 | 336 | 336 | 321 | 322 | 349 | 344 | 353 | 344 | 360 | 358 | 356 | 359 | 352 |
| Local Authority Roads (L) | 447 | 458 | 465 | 468 | 479 | 474 | 478 | 515 | 527 | 526 | 515 | 551 | 552 | 548 | 541 | 532 |
| All Roads (All) | 766 | 789 | 803 | 804 | 815 | 795 | 800 | 864 | 871 | 879 | 858 | 911 | 910 | 904 | 900 | 884 |
| **Highland** | | | | | | | | | | | | | | | | |
| Trunk Roads (T) | 1,270 | 1,317 | 1,347 | 1,350 | 1,375 | 1,346 | 1,391 | 1,465 | 1,476 | 1,464 | 1,468 | 1,503 | 1,525 | 1,519 | 1,556 | 1,530 |
| Local Authority Roads (L) | 891 | 910 | 925 | 931 | 946 | 941 | 950 | 985 | 1,001 | 1,012 | 1,022 | 1,053 | 1,070 | 1,078 | 1,067 | 1,055 |
| All Roads (All) | 2,161 | 2,227 | 2,272 | 2,281 | 2,321 | 2,286 | 2,341 | 2,449 | 2,477 | 2,477 | 2,490 | 2,556 | 2,595 | 2,597 | 2,623 | 2,586 |
| **Perth and Kinross** | | | | | | | | | | | | | | | | |
| Trunk Roads (T) | 1,151 | 1,202 | 1,251 | 1,273 | 1,244 | 1,232 | 1,308 | 1,339 | 1,296 | 1,336 | 1,345 | 1,381 | 1,379 | 1,345 | 1,332 | 1,299 |
| Local Authority Roads (L) | 832 | 849 | 861 | 868 | 885 | 849 | 845 | 896 | 927 | 931 | 928 | 960 | 972 | 958 | 960 | 945 |
| All Roads (All) | 1,983 | 2,051 | 2,112 | 2,141 | 2,129 | 2,081 | 2,153 | 2,235 | 2,223 | 2,267 | 2,273 | 2,340 | 2,351 | 2,303 | 2,292 | 2,244 |
| **Scotland** | | | | | | | | | | | | | | | | |
| Trunk Roads (T) | 12,892 | 13,477 | 13,960 | 14,252 | 14,463 | 14,333 | 14,710 | 15,335 | 15,599 | 15,976 | 15,906 | 16,375 | 16,548 | 16,504 | 16,546 | 16,222 |
| Local Authority Roads (L) | 23,844 | 24,301 | 24,621 | 24,917 | 25,307 | 25,228 | 25,354 | 26,200 | 26,439 | 26,729 | 26,811 | 27,745 | 28,118 | 27,966 | 27,673 | 27,266 |
| All Roads (All) | 36,736 | 37,778 | 38,581 | 39,169 | 39,770 | 39,561 | 40,064 | 41,535 | 42,038 | 42,705 | 42,717 | 44,120 | 44,666 | 44,470 | 44,219 | 43,488 |

[1] These estimates are not National Statistics. They provide only a rough estimate of the likely total volume of traffic on roads in each area.
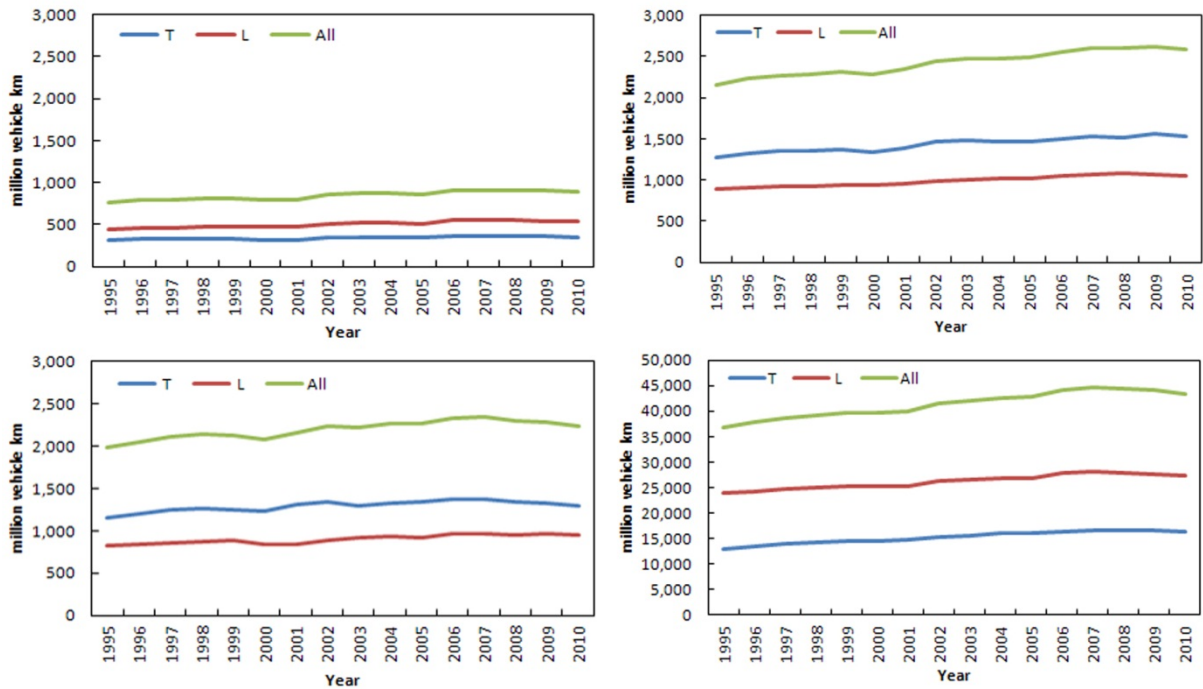
*Figure 32 Traffic figures for Argyll and Bute (top left), Highland (top right), Perth and Kinross (bottom left), and Scotland (bottom right) for trunk roads (T), local roads (L) and all roads (All).*

*Table 39 Normalised traffic data (from Table 9) on trunk (strategic), local authority and all roads by selected areas (in million vehicle kilometres).*

| Area | 1995 | 1996 | 1997 | 1998 | 1999 | 2000 | 2001 | 2002 | 2003 | 2004 | 2005 | 2006 | 2007 | 2008 | 2009 | 2010 |
|---|---|---|---|---|---|---|---|---|---|---|---|---|---|---|---|---|
| **Argyll and Bute** | | | | | | | | | | | | | | | | |
| Trunk Roads (T) | 1 | 1.038 | 1.060 | 1.053 | 1.053 | 1.006 | 1.009 | 1.094 | 1.078 | 1.107 | 1.078 | 1.129 | 1.122 | 1.116 | 1.125 | 1.103 |
| Local Authority Roads (L) | 1 | 1.025 | 1.040 | 1.047 | 1.072 | 1.060 | 1.069 | 1.152 | 1.179 | 1.177 | 1.152 | 1.233 | 1.235 | 1.226 | 1.210 | 1.190 |
| All Roads (All) | 1 | 1.030 | 1.048 | 1.050 | 1.064 | 1.038 | 1.044 | 1.128 | 1.137 | 1.148 | 1.120 | 1.189 | 1.188 | 1.180 | 1.175 | 1.154 |
| **Highland** | | | | | | | | | | | | | | | | |
| Trunk Roads (T) | 1 | 1.037 | 1.061 | 1.063 | 1.083 | 1.060 | 1.095 | 1.154 | 1.162 | 1.153 | 1.156 | 1.183 | 1.201 | 1.196 | 1.225 | 1.205 |
| Local Authority Roads (L) | 1 | 1.021 | 1.038 | 1.045 | 1.062 | 1.056 | 1.066 | 1.105 | 1.123 | 1.136 | 1.147 | 1.182 | 1.201 | 1.210 | 1.198 | 1.184 |
| All Roads (All) | 1 | 1.031 | 1.051 | 1.056 | 1.074 | 1.058 | 1.083 | 1.133 | 1.146 | 1.146 | 1.152 | 1.183 | 1.201 | 1.202 | 1.214 | 1.197 |
| **Perth and Kinross** | | | | | | | | | | | | | | | | |
| Trunk Roads (T) | 1 | 1.044 | 1.087 | 1.106 | 1.081 | 1.070 | 1.136 | 1.163 | 1.126 | 1.161 | 1.169 | 1.200 | 1.198 | 1.169 | 1.157 | 1.129 |
| Local Authority Roads (L) | 1 | 1.020 | 1.035 | 1.043 | 1.064 | 1.020 | 1.016 | 1.077 | 1.114 | 1.119 | 1.115 | 1.154 | 1.168 | 1.151 | 1.154 | 1.136 |
| All Roads (All) | 1 | 1.034 | 1.065 | 1.080 | 1.074 | 1.049 | 1.086 | 1.127 | 1.121 | 1.143 | 1.146 | 1.180 | 1.186 | 1.161 | 1.156 | 1.132 |
| **Scotland** | | | | | | | | | | | | | | | | |
| Trunk Roads (T) | 1 | 1.045 | 1.083 | 1.105 | 1.122 | 1.112 | 1.141 | 1.189 | 1.210 | 1.239 | 1.234 | 1.270 | 1.284 | 1.280 | 1.283 | 1.258 |
| Local Authority Roads (L) | 1 | 1.019 | 1.033 | 1.045 | 1.061 | 1.058 | 1.063 | 1.099 | 1.109 | 1.121 | 1.124 | 1.164 | 1.179 | 1.173 | 1.161 | 1.144 |
| All Roads (All) | 1 | 1.028 | 1.050 | 1.066 | 1.083 | 1.077 | 1.091 | 1.131 | 1.144 | 1.162 | 1.163 | 1.201 | 1.216 | 1.211 | 1.204 | 1.184 |
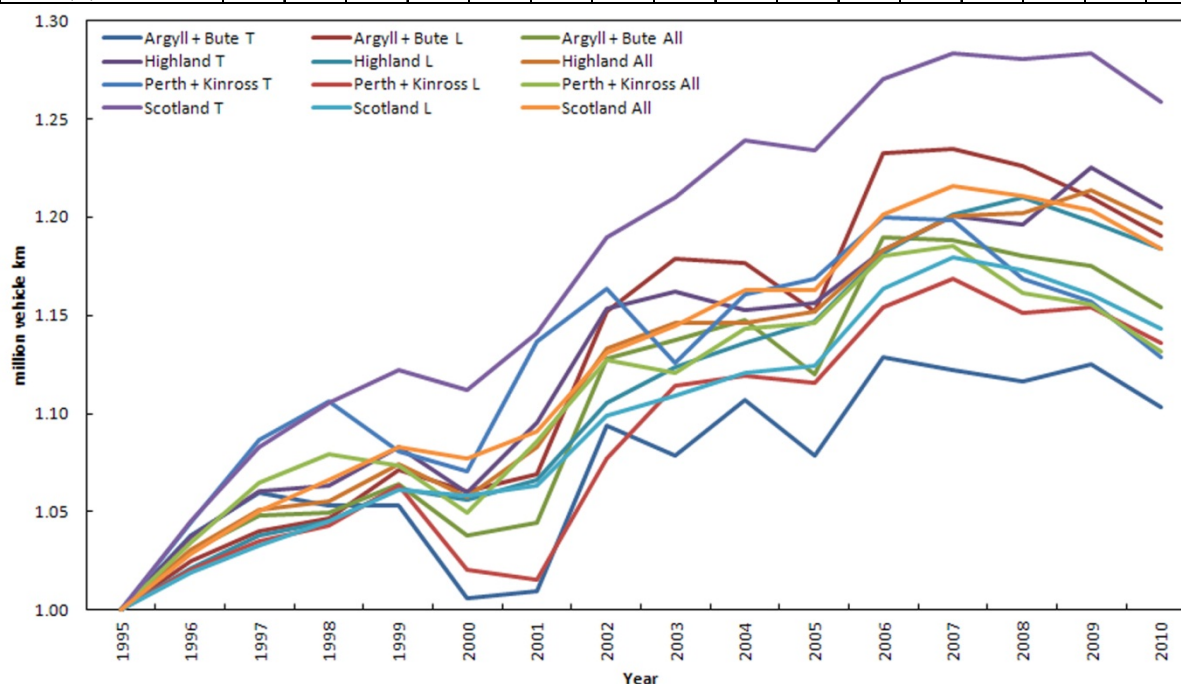


*Figure 33 Normalised traffic figures for Argyll and Bute, Highland, Perth and Kinross, and Scotland for trunk roads (T), local roads (L) and all roads (All).*

While it is by no means clear that these trends will continue it is instructive to consider what the change would be relative to 1995 levels in 2020, 2050 and 2080 if that were to be the case and these are as follows:

    2020: between 1.17 and 1.43 times 1995 levels.
    2050: between 1.38 and 1.95 times 1995 levels.
    2080: between 1.59 and 2.46 times 1995 levels.

Similarly, taking the figures for 2010 as the baseline then the corresponding increases are

    2020: between 1.07 and 1.17 times 2010 levels.
    2050: between 1.28 and 1.69 times 2010 levels.
    2080: between 1.48 and 2.21 times 2010 levels.

It must be clear that there is no suggestion that these levels of growth are likely to be sustained. Indeed current thinking (Clement, 2012, Personal Communication) suggests that

current traffic growth forecasts are likely to be somewhat lower than has been the case in the past. It must also be acknowledged that traffic growth will be affected not only by the ongoing economic situation but also by such factors as changing land use patterns and trends for people to move to less populated areas. These are factors that are likely to be affected by improved, developing and changing communications technology – the infrastructure for which may itself be at risk from landslide events. Predicting the patterns of change in land use, for example, is fraught with difficulty let alone forecasting the effects of such change and the 70 years between the present and 2080 hold the potential for sweeping technological innovation that may radically change the way in which people live and work.

However, and making the rather contentious leap from these annual estimates to daily traffic, based on the growth from 2010 onwards the traffic for roads such as the A83 and A85 could be between 5,500 vehicles per day and 7,000 vehicles per day by 2020, between 6,500 vehicles per day and 10,000 vehicles per day by 2050, and between 7,500 vehicles per day and 13,000 vehicles per day by 2080. Similarly, traffic levels on the A9 could range between 14,500 vehicles per day and 16,000 vehicles per day by 2020, between 17,000 vehicles per day and 23,000 vehicles per day by 2050, and between 20,000 vehicles per day and 30,000 vehicles per day by 2080.

It seems likely that the longer term estimates are least likely to be accurate, but even accepting much lower figures it does seem likely that growth in traffic is likely to be quite substantial.

However, increased traffic must be equated to increased numbers of road users and it thus seems likely that the level of exposure to landslides may well increase. Taken together with the potential for increased hazard levels set out in Section 4 an increase in the risks associated with landslides seems likely.

Notwithstanding the above, the Scottish Government's plan[1] to upgrade the A9 to dual-carriageway between Perth and Inverness by 2025, which includes much of the length potentially affected by landslides, has the potential to make some significant changes to the risk profile. First average speeds are likely to be higher and there is the potential for constraints on traffic growth to be less if such a route is provided. Set against this is the likelihood of the creation of an alignment with longer sightlines, affording greater opportunity for avoidance of debris on the road. Perhaps most significantly such a project offers the opportunity to assess the route in terms of landslide hazard and to avoid the areas that are likely to create the largest risks. This approach was embedded into the recommendations made by Winter et al. (2009a) and seems likely to be adopted as and when the planned upgrade goes ahead. This approach seems most likely to reduce the risk by reducing the hazard. The approach to hazard reduction may be by means of protection of the elements at risk, remediation of the hazard itself, or removal of the elements at risk to a location of lesser hazard (realignment and/or re-routing) (Winter, In Press) or, more likely, some combination of these approaches.

---

[1] http://www.scotland.gov.uk/News/Releases/2011/12/06104509.

In similar fashion, the Scottish Government recently announced a study[2] to consider options for the A83, including the Rest and be Thankful landslide site, in order identify and examine options to reduce *inter alia* landslide risk. The intention of the study is to examine and cost options for hazard, and consequently risk, reduction including protection, remediation and removal as outlined above.

Certainly the main factors associated with climate change seem most likely to increase the hazards associated with landslides in Scotland and in general it seems reasonable to assume that the associated risks will increase also. However, there are some factors that limit the potential scale of such risk increases. These include that many of the most active landslide areas are remote and unlikely to be subject to urban development. Indeed, the highest risks are generally posed to the transport infrastructure network in particular, but not limited to, the road network. This network connects remote rural communities to social and economic opportunities including education, employment and services such as health and it would be difficult to overstate their importance. Indeed, some of the roads provide the only transport link into and out of some communities (see Winter et al., 2009a).

While increased landsliding seems likely to increase the risks attendant upon the road network and its users, actions such as the A9 upgrade and the A83 study described in the foregoing paragraphs will go some considerable distance to limiting and, in some cases, removing that risk. These upgrade actions are very much in line with the potential increase in traffic levels.

The potential for greater hazards must be carefully considered in terms of the magnitude and frequency of events. If climate change increases the frequency of events to the extent that the throughput of debris in a given area exceeds the rate of the geomorphological process that form the debris then the magnitude and/or frequency of events may decrease to an extent that the risk is reduced. Notwithstanding this, it may well be that while individual high activity sites are affected in this manner the effects of climate change may develop new higher activity areas that pose elevated risks. The macro picture of the geomorphological processes and their effects upon hazard (magnitude and frequency) and risk are undoubtedly complex and resilience will need to continue to be incorporated into both the infrastructure and also the professionals who design, build, operate and maintain the infrastructure and the other specialists who advise them.

## 3.5   SUMMARY

In broad terms the available climate change forecasts present a picture that tends to suggest that landslide frequency and magnitude will increase in Scotland in the future, at least in the winter months. The picture for the summer months is considerably more complex, but one likely outcome is that the while the frequency of events will decrease their magnitude when they do occur may increase.

---

[2] http://www.transportscotland.gov.uk/news/A83-Investigation.

The primary landslide risks relate to transport infrastructure, albeit by no means exclusively. This is not anticipated to change radically in the future. At first sight it seems likely that landslide risks to transport infrastructure will increase. While there is considerable uncertainty regarding the level of traffic growth and thus the increase in the exposure of road users to such risks, traffic is expected to grow and the associated exposure to increase.

Set against this are major activities such as the planned upgrade of the A9 to dual-carriageway and the major study to identify and examine options to reduce *inter alia* landslide risk. Indeed, it is worth considering that should traffic levels grow substantially then the infrastructure will cease to be viable in its current form; if limits on access to the network are not to be introduced then major upgrades will become necessary affording the opportunity to address landslide hazards and risks from the outset.

Of course the complex interplay between changing land use and the effects of emerging technology on work patterns will change the way in which society addresses such infrastructure and may also introduce new infrastructure that may itself be at risk from landslide hazards.

# Second Part - Methodology development

# 4      LAND COVER CHANGES AND IMPACT ON HAZARD

Rainfall infiltration into unsaturated soil affects the slope stability due to the reduction of unsaturated soil suction. The matric suction reduction depth can be determined as a function of hydro-mechanical parameters of soil, initial soil water content and inclination of the slope independent of infiltration rate and soil permeability. The interest of this study is to predict the potential depth of slope sliding by only knowing the initial soil water content and soil hydro-mechanical parameters. The positive effect of canopy due to evapotranspiration also can be supposed to be limited to the potential depth of slope sliding. In this study the only effect of canopy is supposed to reduce the soil water content and to increase the soil shear resistant by increasing the soil suction. However the modification of intensity of precipitation due to the forest canopies could prevent sliding in some instances and other effect of canopy is to prevent the soil erosion due to runoff water flow on soil surface.

This part concerns the study of slope failure triggered by rainfall and specifically the impact of vegetation on such a risk. It is well known that rainfall infiltration has two effects that trigger slope failure. On one hand, the weight of the hydrated soil increases and on the other hand it reduces matric suction in soil which in turn results in the reduction of the soil shear strength.   Vegetation has some positive roles in improving the slopes stability. Vegetation provides protection against wind erosion, raindrop impact, and erosion surface water flow. It reduces the surface water runoff and also rainfall infiltration rate because of interception and reinforces the soils by roots (Coppin and Richards, 1990). The water uptake by plant roots increases suction increasing stability.

Different types of soil movement are usually possible as presented in Table 40. Although many types of mass movements are included in the general term "landslide", the more restrictive use of the term refers only to mass movements, where there is a distinct zone of weakness that separates the slide material from more stable underlying material. The two major types of slides are rotational slides and translational slides. In this work the transitional earth slides are studied. In the transitional landslides, mass moves along a roughly planar surface with little rotation or backward tilting (Figure 34). A block slide also is a translational slide in which the moving mass consists of a single unit or a few closely related units that move down slope as a relatively coherent mass (Figure 35).

*Table 40 Types of landslides. Abbreviated version of Varnes' classification of slope movements (Varnes, 1978)*

| TYPE OF MOVEMENT | | BEDROCK | TYPE OF MATERIAL | |
|---|---|---|---|---|
| | | | ENGINEERING SOILS | |
| | | | Predominantly coarse | Predominantly fine |
| FALLS | | Rock fall | Debris fall | Earth fall |
| TOPPLES | | Rock topple | Debris topple | Earth topple |
| SLIDES | ROTATIONAL | Rock slide | Debris slide | Earth slide |
| | TRANSLATIONAL | | | |
| LATERAL SPREADS | | Rock spread | Debris spread | Earth spread |
| FLOWS | | Rock flow | Debris flow | Earth flow |
| | | (deep creep) | (soil creep) | |
| COMPLEX | | Combination of two or more principal types of movement | | |
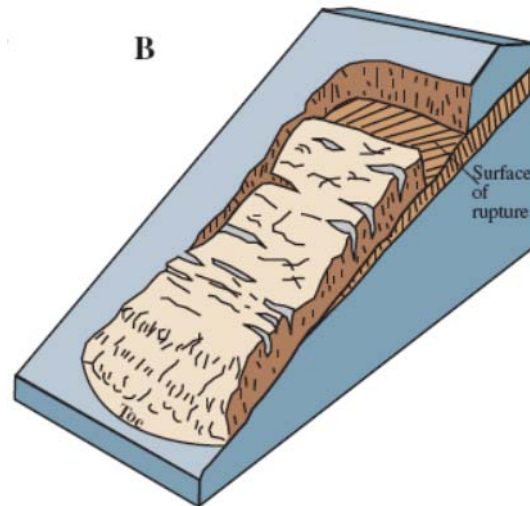
*Figure 34 Translational earth slide (factsheet ...)*
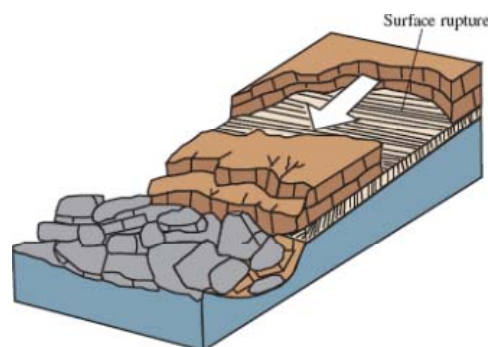


*Figure 35 Block slide (factsheet ...)*

The evaluation of the stability is usually performed through the estimation of a safety factor taking into account the soil resistance and the applied forces. We limit this report to the effect of gravitation forces. Therefore only the weight of the soil massif including the water present in the pores is applied.

## 4.1    HYDRO-MECHANICAL PROPERTIES

To model the mechanical behaviour of a saturated soil, the Terzaghi's effective stress tensor (Terzaghi 1967) that applies only to the skeleton is commonly used (A. Modaressi 2001,2011):

$$\underline{\underline{\sigma}} = \underline{\underline{\sigma}}' + p_w \underline{\underline{I}}$$

Where :

- $\underline{\underline{\sigma}}$ is the Cauchy total stress tensor;

- $\underline{\underline{\sigma}}'$ is the Cauchy effective stress tensor;

- $p_w$ is the pore pressure in the fluid;

- $\underline{\underline{I}}$ is the second order unit tensor.

Biot [BIO 41, BIO 57] proposed the following relation generalizing Terzaghi's postulate to materials with compressible solid phase:

$$\underline{\underline{\sigma}} = \underline{\underline{\sigma}}' + \alpha \, p_w \underline{\underline{I}}$$

$\alpha$ depends on the contrast between the stiffness of the material constituting the matrix (Ks) and that of the skeleton (K). This coefficient may vary between zero and one $\left(\alpha = 1 - \frac{K}{K_s}\right)$. It is obvious that the behaviour of unsaturated soil is dependent on both stresses and suction. However, the debate on whether to use one or the other of the stress tensors is still open.

The approaches used fall into two families. In the first and oldest one, our attempt is to proceed as in saturated soils. The problem then is how to define the effective stress tensor. Under this approach, we question only partially Terzaghi's postulate.

With $\underline{\underline{\sigma}}^*$ Cauchy net stress tensor and $p_g$ the gas phase pressure, it is assumed that the decomposition of stress tensor in the form:

$$\underline{\underline{\sigma}}^* = \underline{\underline{\sigma}} - p_g \underline{\underline{I}} = \underline{\underline{\sigma}}' + \underline{\underline{\sigma}}_f$$

is still valid. $\underline{\underline{\sigma}}_f$ represents the portion of stresses taken up by the fluid. In the case of an unsaturated soil, we can distinguish several possible formulations of $\underline{\underline{\sigma}}_f$ : the traditional formulation is to define $\underline{\underline{\sigma}}_f$ in a form close to the saturated case of the type:

$$\underline{\underline{\sigma}}_f = \overline{p}\underline{\underline{I}}$$

where p represents the total pressure of the fluid in the media. According to the mixture theory:

$$\overline{p} = S_w p_w + S_a p_a$$

where Si and pi represent the degree of saturation and the pressure of phase i (w: water, a: air) respectively. Generally, this first approach is amended by the introduction of an additional factor, function of Sw called the Skempton coefficient and obtained experimentally so that:

$$\underline{\underline{\sigma}}_f = B(S_w)p_w\underline{\underline{I}}$$

Again, it is common to improve this approach by introducing experimental coefficients. The coefficient most frequently used is that of Bishop [BIS 54]:

$$\underline{\underline{\sigma}}_f = p_a \underline{\underline{I}} - \chi(S_w) P_c \underline{\underline{I}}$$

*Equation 1*

where Pc = pa − pw is the suction. The simplest formulation of the Bishop's coefficient is:

$$\chi(S_w) = S_w$$

*Equation 2*

Experience has shown that the parameter $\chi$ depends on the stress path and soil properties.

Currently, models of increasing complexity can reproduce the behaviour of unsaturated soils. These models take into account different aspects of observed behaviour and can be used over a long period of the structure's lifetime, if not all of it. We can divide the research on the mechanical behaviour of unsaturated soils into three parts: that of the definition of effective stress, of volume change and the collapse phenomenon, and finally, of shear strength.

Based on work conducted by J. Biarez and JM Fleureau and the microstructural model composed of particles [TAI 94], we can introduce the concept of generalized effective stress into unsaturated soils. A capillary stress can be defined, so that the effective stress becomes:

$$\underline{\underline{\sigma}}' = \underline{\underline{\sigma}} + p_a \underline{\underline{I}} - \underline{\underline{\sigma}}_c$$

where

$\underline{\underline{\sigma}}_c$ is a function of capillary pressure as well as the density and grain-size of the material. The choice of formulation in generalized effective stresses provides a natural transition between the dry state, un-saturated and saturated. The capillary stress, depending on the geometry of pores, is not necessarily spherical. However, for the sake of simplicity and lack of an experimentally validated model, only the spherical part of this tensor is considered and we assume that:

$$\underline{\underline{\sigma}}_c = \pi_c \underline{\underline{I}}$$

It can be noted that for practical reasons and with respect to the level of approximation necessary for the present problem, the choice of Equation 1 and Equation 2 for the estimation of capillary pressure seems to be adequate. In Figure Moreover, the soil-water characteristic curve which relates the suction and the degree of saturation as presented in Figure 37 illustrates.
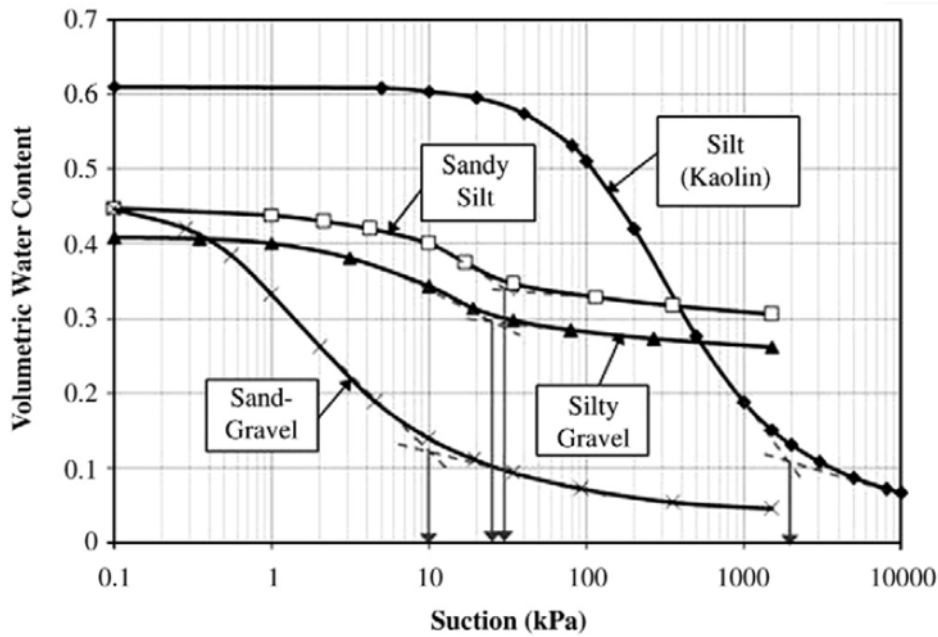
*Figure 36 Soil-Water characteristic curves after Lee et al. 2009*
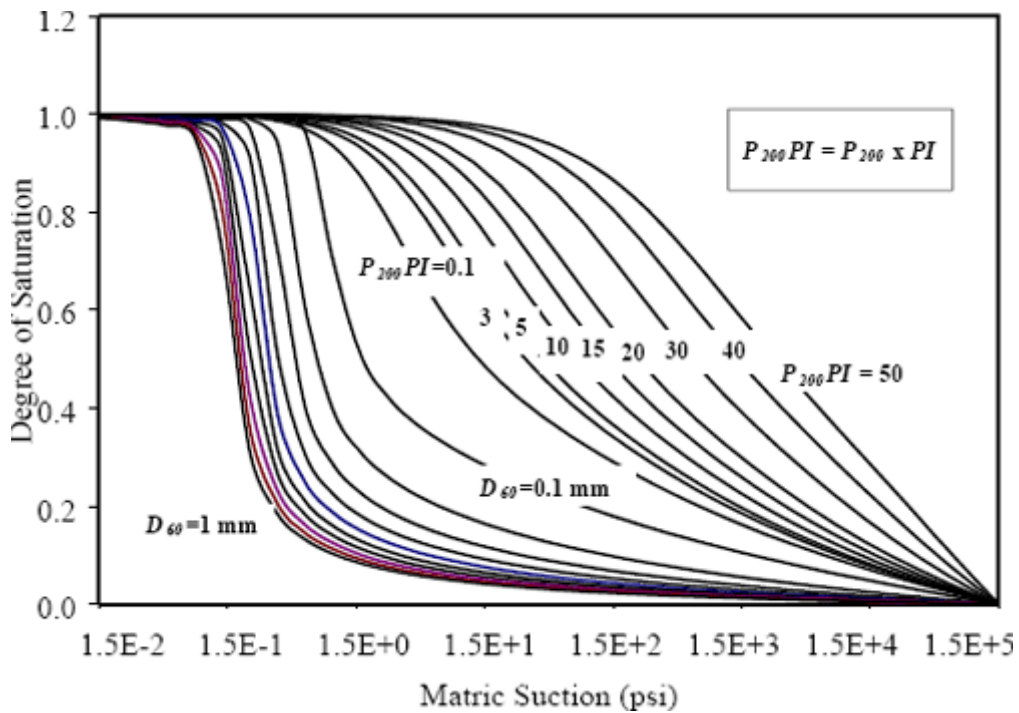


*Figure 37 Soil water characteristic curves (NCHRP 1-37A, 2004)*

The deduction made from the intrinsic curves obtained for unsaturated samples shows that, for a given density and particle-size, the variation of capillary stress as a function of capillary pressure reaches a plateau for high values of capillary pressure. We also impose continuity between the pore pressure and capillary stress at the limit of saturated and unsaturated domains.

This condition deduced from the results with a high degree of saturation allows us to use a single framework to model saturated and unsaturated geomaterials. Indeed, the same modelling tools can be used for analysing actual cases where the state of the *in-situ* material varies with hydrological and hydro-climatical conditions.

The choice of formulation in generalised effective stresses provides a natural transition between the dry state, un-saturated and saturated. Therefore, the Coulomb's failure criterion can be applied using the generalized effective stress criterion.

$$\tau_{max} = \sigma'_n \, tg \, \varphi' - C'$$

Where $\sigma'_n$ is the normal generalized effective stress and $\varphi'$ is the friction angle. It should be noted that by using this generalized effective stress, the effect of apparent cohesion in unsaturated soils due to suction is implicitly taken into account. Therefore, it is not necessary to take into account any cohesion terms unless other phenomena are present. For example, cementation and calcification introduce cohesion to the soil. As far as vegetation is considered, it may increase the soil shear strength due to two mechanisms. One is the mechanical effect of the roots which may reinforce the soil by their structure. The other is due to the water uptake which modifies the suction in the soil and therefore modifies the soil strength.

## 4.2    EFFECT OF VEGETATION

Due to Greenwood and Norris (2004), the main engineering influences of vegetation are:
- additional effective cohesion due to the vegetation
- increase in weight of slice due to the vegetation
- tensile reinforcement force by the roots present on the base of each slice
- wind force
- changes in undrained soil strength due to moisture removal by the vegetation
- changes in pore water pressure

The values of the effective cohesion introduced due to vegetation were measured by direct in-situ shear tests back analysis or from root density and vertical root model equations. Values vary from 1-25 $\left( kN/m^2 \right)$ depending on type of soil and vegetation (Norris and Greenwood, 2006) are given. Table 41 provides values of $c'_v$ for a variety of vegetation types. It should be noted that after the same authors, the reliable effect of the cohesion due to vegetation is limited to the shallow depths as root distribution is mainly concentrated within 1 m of ground surface. Moreover in the deeper parts of soils the positive role of suction on the factor of security decreases. The weight of plants and the wind forces transferred to the soil through them, should be considered as negative Vegetation may have negative drawbacks too as its weight may increase the

| Source | Vegetation, soil type and location | Root cohesion $c'_v$ (kN/m²) |
|---|---|---|
| **Grass and Shrubs** | | |
| Wu[1] (1984) | Sphagnum moss (*Sphagnum cymbifolium*), Alaska, USA | 3.5 – 7.0 |
| Barker in Hewlett *et al.*† (1987) | Boulder clay fill (dam embankment) under grass in concrete block reinforced cellular spillways, Jackhouse Reservoir, UK | 3.0 – 5.0 |
| Buchanan & Savigny* (1990) | Understorey vegetation (*Alnus, Tsuga, Carex, Polystichum*), glacial till soils, Washington, USA | 1.6 – 2.1 |
| Gray § (1995) | Reed fiber (*Phragmites communis*) in uniform sands, laboratory | 40.7 |
| Tobias † (1995) | *Alopecurus geniculatus*, forage meadow, Zurich, Switzerland | 9.0 |
| Tobias† (1995) | *Agrostis stolonifera*, forage meadow, Zurich, Switzerland | 4.8 – 5.2 |
| Tobias† (1995) | Mixed pioneer grasses (*Festuca pratensis, Festuca rubra, Poa pratensis*), alpine, Reschenpass, Switzerland | 13.4 |
| Tobias† (1995) | *Poa pratensis* (monoculture), Switzerland | 7.5 |
| Tobias† (1995) | Mixed grasses (*Lolium multiflorum, Agrostis stolonifera, Poa annua*), forage meadow, Zurich, Switzerland | -0.6 – 2.9 |
| Cazzuffi *et al.* § (2006) | Elygrass (*Elytrigia elongata*), Eragrass (*Eragrostis curvala*), Pangrass (*Panicum virgatum*), Vetiver (*Vetiveria zizanioides*), clayey-sandy soil of Plio-Pleistocene age, Altomonto, S. Italy | 10.0, 2.0, 4.0, 15.0 |
| Norris† (2005b) | Mixed grasses on London Clay embankment, M25, England | ~10.0 |
| van Beek *et al.* † (2005) | Natural understory vegetation (*Ulex parviflorus, Crataegus monogyna, Brachypodium* var.) on hill slopes, Almudaina, Spain | 0.5 – 6.3 |
| van Beek *et al.* † (2005) | *Vetiveria zizanoides*, terraced hill slope, Almudaina, Spain | 7.5 |
| **Deciduous and Coniferous trees** | | |
| Endo & Tsuruta † (1969) | Silt loam soils under alder (*Alnus*), nursery, Japan | 2.0 – 12.0 |
| O'Loughlin & Ziemer † (1982) | Beech (*Fagus* sp.), forest-soil, New Zealand | 6.6 |
| Riestenberg & Sovonick-Dunford * (1983) | Bouldery, silty clay colluvium under sugar maple (*Acer saccharum*) forest, Ohio, USA | 5.7 |
| Schmidt *et al.* ‡ (2001) | Industrial deciduous forest, colluvial soil (sandy loam), Oregon, USA | 6.8 – 23.2 |
| Swanston* (1970) | Mountain till soils under hemlock (*Tsuga mertensiana*) and spruce (*Picea sitchensis*), Alaska, USA | 3.4 – 4.4 |
| O'Loughlin* (1974) | Mountain till soils under conifers (*Pseudotsuga menziesii*), British Columbia, Canada | 1.0 – 3.0 |
| Ziemer & Swanston ‡§ (1977) | Sitka spruce (*Picea sitchensis*) - western hemlock (*Tsuga heterophylla*), Alaska, USA | 3.5 – 6.0 |
| Burroughs & Thomas* (1977) | Mountain and hill soils under coastal Douglas-fir and Rocky Mountain Douglas-fir (*Pseudotsuga menziesii*), West Oregon and Idaho, USA | 3.0 – 17.5 |
| Wu *et al.* ‡ (1979) | Mountain till soils under cedar (*Thuja plicata*), hemlock (*Tsuga mertensiana*) and spruce (*Picea sitchensis*), Alaska, USA | 5.9 |
| Ziemer † (1981) | Lodgepole pine (*Pinus contorta*), coastal sands, California, USA | 3.0 – 21.0 |
| Waldron & Dakessian*(1981) | Yellow pine (*Pinus ponderosa*) seedlings grown in small containers of clay loam. | 5.0 |
| Gray & Megahan‡ (1981) | Sandy loam soils under Ponderosa pine (*Pinus ponderosa*), Douglas-fir (*Pseudotsuga menziesii*) and Engelmann spruce (*Picea engelmannii*), Idaho,USA | ~ 10.3 |
| O'Loughlin *et al.* † (1982) | Shallow stony loam till soils under mixed evergreen forests, New Zealand | 3.3 |
| Waldron *et al.* † (1983) | Yellow pine (*Pinus ponderosa*) (54 months), laboratory | 3.7 – 6.4 |
| Wu ‡ (1984) | Hemlock (*Tsuga* sp.), Sitka spruce (*Picea sitchensis*) and yellow cedar (*Thuja occidentalis*), Alaska, USA | 5.6 – 12.6 |
| Abe & Iwamoto † (1986) | *Cryptomeria japonica* (sugi) on loamy sand (Kanto loam), Ibaraki Prefecture, Japan | 1.0 – 5.0 |
| Buchanan & Savigny * (1990) | Hemlock (*Tsuga* sp.), Douglas fir (*Pseudotsuga*), cedar (*Thuja*), glacial till soils, Washington, USA | 2.5 – 3.0 |
| Gray § (1995) | *Pinus contorta* on coastal sand | 2.3 |
| Schmidt *et al.* ‡ (2001) | Natural coniferous forest, colluvial soil (sandy loam), Oregon | 25.6 – 94.3 |
| van Beek *et al.* † (2005) | *Pinus halepensis*, hill slopes, Almudaina, Spain | -0.4 – 18.2 |

*Table 41 Values of for grasses, shrubs and trees as determined by field, laboratory tests, and mathematical models (Norris and Greenwood, 2006)*

As it can be noticed, vegetation has both positive and negative effects. In this report, we focus our work on the change in suction and its consequences on the slope stability.

As recalled previously, there is a strong coupling between the mechanical properties of an unsaturated soil and its hydric state. Therefore it is necessary to take into account the suction profile when analysing the stability of a slope.

## 4.3    STABILITY ANALYSIS

Let's consider the general configuration presented in Figure 38, where an infinite slope is illustrated.  The water table is positioned at the depth of $H_w$ while the depth of influence of the vegetation roots is $H_r$. Therefore, the pore water pressure profile below this level both in saturated and unsaturated zones is hydrostatically distributed. However, this distribution may be modified due to the existence of plant roots and the water uptake.
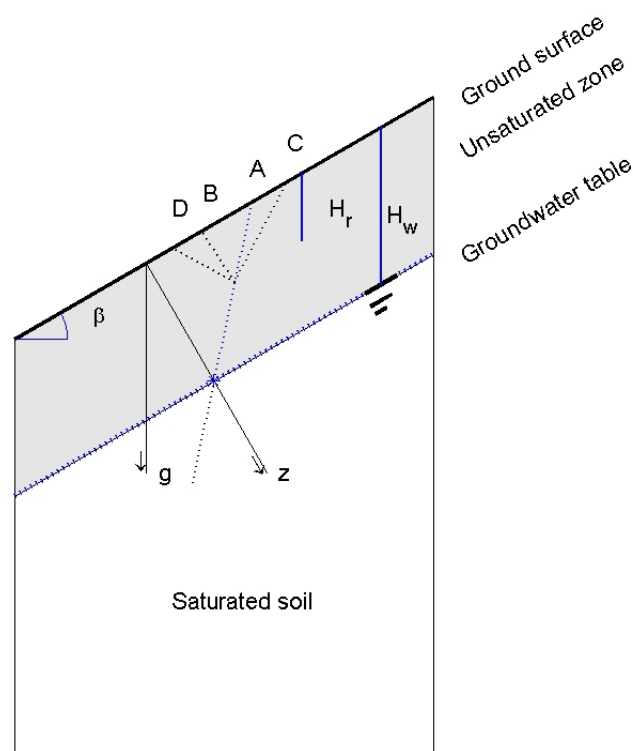


*Figure 38 Infinite slope model*

As it is illustrated, four cases of pore water pressure distribution may be encountered:
Case A: Hydrostatical distribution
Case B: Suction distribution is uniform as the minimum possible suction which depends on the soil type is encountered
Case C: Due to water uptake the suction in the soil is less than the hydraostatical condition
Case D: Infiltration has taken place reducing the suction. This may occur after rainfall.

At time t, at a given depth z (Figure 38), the safety factor may be written as:

$$F(z,t) = \frac{\tau_{max}(z,t)}{\tau(z,t)}$$

Where $\tau$ is the shear stress to which the soil is submitted given by:

$$\tau(z,t) = \int_0^z \rho(z,t) \cdot g \cdot \sin\beta \cdot dz$$

Where $z = H_w \cdot \cos\beta$ at the ground water level.

The specific mass of the massif depends on the soil's porosity $n$ and its degree of saturation with water $S_w$:

$$\rho = \rho_s \cdot (1-n) + S_w \cdot \rho_w \cdot n$$

Where $\rho_w$ and $\rho_s$ are the specific mass of the water and solid grains respectively.

As mentioned before, soil-water characteristic curves provide the relation between the suction and the degree of saturation. Therefore, in order to evaluate the hydric state, it is necessary to study the water infiltration in the soil. Once the pore water pressure distribution profile available, the weight and resistance of the soil maybe computed and the factor of safety evaluated.

## 4.4    WATER INFILTRATION IN PARTIALLY SATURATED SOIL

The mathematical expression governing the phenomenon of unsteady flow of water in soils can be found by combining the Darcy equation and the equation of continuity:

$$\frac{d(\rho_w\theta)}{dt} = -\nabla(\rho_w K \nabla H) + f \tag{1}$$

Where $\theta$ is volumetric water content ($\theta = S_r \cdot n$), $K$ is the hydraulic conductivity (permeability) of soil as a function of soil degree of saturation and $\nabla H$ is the gradient of the hydraulic head $H$. $f$ is a source/sink term which can be related to the water uptake of vegetation roots. The equation (1) given as a function of $\theta$ and $H$, can be expressed as a function of water pressure $p_w$ and degree of saturation $S_r$ after some mathematical operations:

$$\frac{d(\rho_w\theta)}{dp_w}\frac{dp_w}{dt} = -\nabla\left(\rho_w K \nabla\left(\frac{p_w}{\rho g} + z\right)\right) + f \tag{2}$$

$$\left(\frac{nS_r}{\rho_w}\frac{d\rho_w}{dp_w} + n\frac{dS_r}{dp_w}\right)\frac{dp_w}{dt} = -\nabla\left(\frac{K}{\rho_w g}\nabla(p_w + z\rho_w g)\right) + f \tag{3}$$

$$\left(\frac{nS_r}{\rho_w}\frac{d\rho_w}{dp_w} + n\frac{dS_r}{dp_w}\right)\frac{dp_w}{dt} = -\nabla\left(\frac{K}{\rho_w g}\nabla(p_w) + K\right) + f \tag{4}$$

$$-f + \left( \frac{nS_r}{\rho_w}\beta + n\frac{dS_r}{dp_w} \right)\frac{dp_w}{dt} + \nabla \left( \frac{K}{\rho_w g}\nabla(p_w) + K \right) = 0 \qquad (5)$$

Where $\beta = \dfrac{d\rho_w}{dp_w}$ is the water compressibility and $g$ is the gravity acceleration. The final form

of equation (2) can be presented by:

$$-f + \left( nS_r g\beta + n\rho_w g\frac{dS_r}{dp_w} \right)\frac{dp_w}{dt} + \nabla \left( K\nabla(p_w) + K\rho_w g \right) = 0 \qquad (6)$$

In unsaturated soil, the water permeability is a function of suction or/and degree of saturation. The relation commonly used is:

$$K = k_s.k_r(S_r)$$

Where $k_s$ is the saturated permeability depending only on the pore distribution and $k_r$ is a coefficient varying from one to zero, when the material's degree of saturation moves from one to the residual saturation :

$$k_r(S_r) = \left( \frac{S_r - s_{res}}{1 - s_{res}} \right)^3,$$

$g = 9.81(m/s^2)$, $\rho_w = 1000(kg/m^3)$, $\beta = 9.38*10^{-8}$. $p_w$ is negative at the unsaturated zone and is positive in saturated zone.

Several soil-water characteristic curves (SWWC) have been proposed in the literature such as those proposed by Brooks and Corey (1966) or van Genuchten (1980). In this study we use the one proposed by van Genuchten (1980):

$$S_r(p_w) = s_{res} + \frac{1 - s_{res}}{\left( 1 + \left( \frac{\alpha_s p_w}{\rho_w g} \right)^{n_s} \right)^{m_s}} \qquad (7)$$

and consequently:

$$\begin{cases} \dfrac{dS_r}{dp_w} = \dfrac{\alpha_s m_s n_s}{\rho_w g} \dfrac{s_{res}-1}{\left(\left(\dfrac{\alpha_s p_w}{\rho_w g}\right)^{n_s}+1\right)^{m_s+1}} \left(\dfrac{\alpha_s p_w}{\rho_w g}\right)^{n_s-1} & \text{if } \ p_w < 0 \\[4ex] \dfrac{dS_r}{dp_w} = 0 \ \ \text{if} \ \ p_w \geq 0 \end{cases} \tag{8}$$

The boundary conditions are expressed in terms of imposed flux or hydraulic head on the two partitions of the boundary such that:

$H(x,t) = H^*$          for $x$ in $\Gamma_H$

$-K \cdot \Delta H \cdot e_n = \varphi^*$      for $x$ in $\Gamma_\varphi$

As the problem is a non-linear and transitory, the initial conditions are necessary and play an important role. The initial pore water distribution may be chosen to express the four cases described above and in Figure 38 which may be themselves obtained by a sequence of computations with varying boundary conditions. They can be a combination of different conditions. For example, at the top layers, the pore pressure (suction) may be known through the knowledge of the water content using relation (9), and at deeper layers a hydrostatical distribution may be assumed. Therefore, the knowledge of the initial water content or pore pressure forms a major step in the analysis of the slope stability due to rainfall performed by a transient infiltration computation.

Before performing the parametric study of the transient seepage, the computations were validated on a variety of cases by comparing the obtained results with those given by an analytical solution developed by Wu and Zhang (2009). It happens that the analytical solution is given for specific forms of SWWC and permeability functions. In this analytical solution the soil permeability of unsaturated soil is presented as Gardner (1958):

$$K = \begin{cases} k_s & -\psi_{ae} \leq u \leq 0 \\ k_s e^{\alpha \psi_{ae}} e^{\alpha p_w} & u \leq -\psi_{ae} \end{cases} \tag{9}$$

Where $\alpha$ is a desaturation coefficient and $\psi_{ae}$ is the air-entry value. $u$ is the suction. The relationship between the volumetric water content and the soil suction may be described by the Boltzman model:

$$\theta(p_w) = \begin{cases} \theta_s & -\psi_{ae} \leq u \leq 0 \\ \theta_s e^{\alpha \psi_{ae}} e^{\alpha p_w} & u \leq -\psi_{ae} \end{cases} \tag{10}$$

Based on the relationship between the volumetric water content and the degree of saturation:

$$S_r\left(p_w\right) = \begin{cases} 1 & -\psi_{ae} \leq u \leq 0 \\ e^{\alpha\psi_{ae}}e^{\alpha p_w} & u \leq -\psi_{ae} \end{cases} \qquad (11)$$

In Figure 39, the evolution of pore pressure profiles obtained numerically for three different rainfall intensities are compared to those given by the analytical solution. As it can be noted, the comparison is very satisfactory.
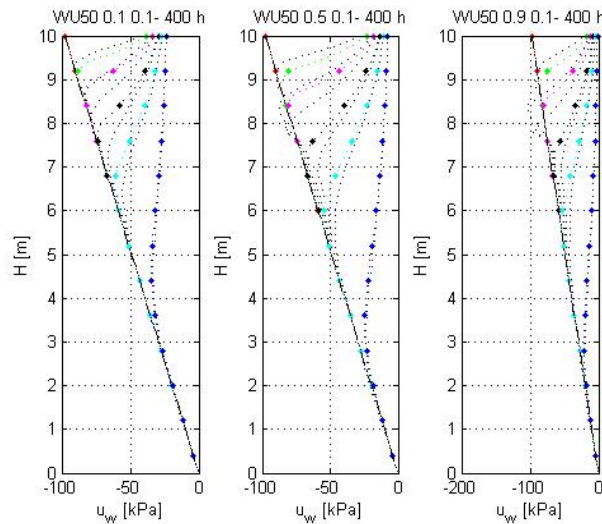


*Figure 39 Validation of computed pore water pressure by comparison to an analytical solution*

Moreover, the comparison of the effect of the SWWC curve and therefore the storage term showed that the van Genuchten relation results in sharper saturation fronts (Figure 40). However, the advance rate of this front in the two models is very close. According to this observation a simplified model was developed to compute the evolution of the saturation depth with time. This model is based on the assumption that the saturation front advances when the soil mass above is totally saturated. Therefore, knowing the initial saturation profile, the evolution of the saturated zone depth can be computed as a function of the rainfall intensity:

$$\int dm \, dt = \int I_r \, dt = \int_0^t \int_0^{zs} \rho_w \, d\theta \, dz \, dt = \rho_w \, n \int_0^t \int_0^{zs} dS \, dz \, dt$$

This can be written in the following discretized form:

$$M(t) = I_r \sum dt = I_r \cdot N.dt = \rho_w \, n \sum_{t \, dt} dt \sum_i (1 - S_i(z_i, 0)) \Delta z_i$$

Where $\Delta z_i$ represents the thickness of successive layers which are reached by the saturation front one after the other. N is the number of time steps. If N is chosen so that in one time step the front advances of 1 m, the evolution of the saturation front as a function of saturated permeability can be given:

$$Zs = \sum_i \Delta z_{i=} I_r. \, N \, dt = \rho_w \, n \, ( \, \sum_i \, (1 - S_i(z_i, 0))). \, N.dt$$
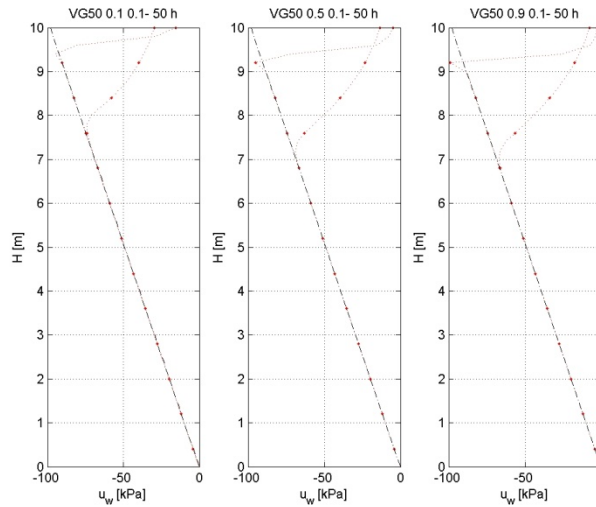


*Figure 40 Effect of rainfall intensity on the transient infiltration profiles for two different storage capacities  (Gardner and van Genuchten relations for SWCC and unsaturated permeability term)*

## 4.5    ROOT WATER UPTAKE EFFECT

The macroscopic approach is adopted in this work. The water uptake by tree roots is represented by sink terms distributed on root zone elements which will give a negative term for $f$ in equations (3-8). The integration of the sink term $S$ on the root volume is assumed to be equal to actual transpiration by the tree $T_r$.

$$T_r = \int_{V_{root}} S \, dV \qquad\qquad (12)$$

Root water uptake and consequently transpiration by trees decrease with increasing soil suction or reduction in soil water content. $S$ reaches its maximal value $S_{max}$ when the available water in the soil is more than water demand, i.e. there is no water restriction. In the agronomy this water restriction is usually called the "water stress". When the available water is less than the water demand, $S$ reduces with reduction in soil water content or increasing soil suction $\psi$. The sink term $S$ is given by the following relation, originally proposed by Feddes et al. ( 1978).

$$S = \alpha(\psi) S_{max} \qquad\qquad (13)$$

where $\alpha(\psi)$ is called the reduction function. The existing expressions of this function are mostly like the one presented in Figure 41. The reduction function $\alpha$ is expressed here as a function of the soil suction $\psi$ as done also by Feddes et al.(1978 ). Alternative variables like pressure head may also be used for this function. The reduction function presented in Figure 41 is characterized by different points: field capacity, maximum soil water deficit, permanent

wilting point. The following definitions are taken from British Columbia water conservation factsheet. It should be noted that the soil water content can be represented also by an equivalent soil suction or pressure head depending on the used equations.
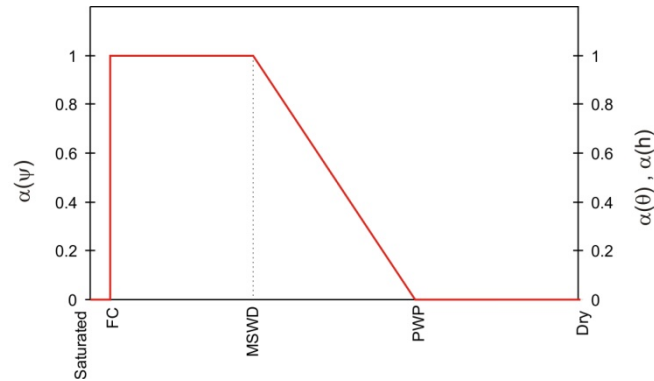


*Figure 41 Reduction function* $\alpha(\psi)$

- Field capacity (FC)

The soil water content where all free water has been drained form the soil through gravity. Sandy soils may drain within a few hours but fine textured soils such as clay may take a few days to drain. Proper irrigation brings soil moisture up to filed capacity.

- Maximum soil water deficit (MSWD)

Only a portion of the available water is easily used by the crop. The maximum soil water deficit is the amount of water stored in the plant's root zone that is readily available to the plant.

- Permanent wilting point (PWP)

The soil moisture content at which the plant will wilt and die. While there still may be water in the soil, but the plant is not able to extract sufficient water from the soil to meet its needs.

- Plant available soil moisture (PAW)

Available soil moisture is defined by the difference between the amount of water in the soil at field capacity and the amount at the permanent wilting point.

The maximum value of sink term $S_{max}$ can be presented as a function of root density distribution and potential transpiration $T_p$ distribution.

$$S_{max} = G(\beta)F(T_p) \tag{14}$$

where $G(\beta)$ is a function of root density distribution which should satisfy the following condition:

$$\int_{V_{root}} G(\beta)dV = 1 \tag{15}$$

The simplest form of $G(\beta)$ is the uniform density distribution proposed by Feddes *et al.* (1978 ). In this study the distribution function used by Landsberg *et al.* (1999 ) and Indraratna *et al.* ( 2006) is used:

$$G(\beta) = \frac{\tanh(k_3\beta)}{\int_{V_{root}} \tanh(k_3\beta)} \tag{16}$$

where

$$\beta(r,z) = \beta_{max} \exp\left(-k_1|z - z*| - k_2|r - r*|\right) \tag{17}$$

$\beta_{max}$ is the maximum root density and $k_1$, $k_2$ and $k_3$ are empirical coefficients that depend on soil and vegetation type.

The potential transpiration $T_p$ is the maximum continual loss of water by transpiration, at a given temperature, given a sufficient supply of water. The potential transpiration is considered to be distributed uniformly within the root zone in most of the existing models in the literature. In this work referring to the model proposed by Nimah and Hanks (1973 ) and used by Indraratna *et al.* (2006 ), a linear distribution with depth for potential transpiration is considered:

$$F(T_p) = \frac{T_P\left(1 + k_4(z_r - z)\right)}{\int_{V_{root}} G(\beta)\left(1 + k_4(z_r - z)\right)dV} \tag{18}$$

where $k_4$ is an empirical coefficient.

The presented framework of root water uptake has been used by Hemmati (2009) for numerical modeling of root water uptake effect on soil settlement.

## 4.6    DEFINITION OF THE PARAMETRIC ANALYSIS

In order to study the role of land cover changes on the slope stability due to rainfall, a large parametric study has been performed in which different soil types, climatic conditions and rainfall intensities as described below have been analyses.

- Climate conditions

    The climate conditions represent several issues. On one hand, they control the rainfall characteristics (amplitude, frequency, duration, ...), but on the other hand they control the water table, the soil water content and possible flows. This latter has been taken into account through the various initial conditions studied while the first one concerns the different rainfall scenarios studied.

- As both long duration-low intensity and short duration-high intensity rainfalls may trigger slope failure, in order to capture all possibilities different rainfall intensities have been used.
- As no runoff is taken into account in the model, the maximum rainfall intensity infiltrated into the soil is its saturated permeability. Therefore:
- Ir = Constant rainfall intensity [0.1 0.5 0.9]*$k_r$
- Four different water table depths, have been considered:
  Water table  [-8 -6 -4 -2 ] m
- At the 2m top layer, the initial water content depends on the evapotranspiration by the vegetation.

- Soil type

  - The soil types covered in this study vary from sandy-gravel to silty soil with a factor of 1000 between their saturated permeabilities:
  - Kr = [$10^{-5}$, $10^{-6}$, $10^{-7}$, $10^{-8}$ ]m/s.
  - As the dimension and distribution of the pores control the storage capacity of the soil three distinct seepage characteristic curve (SWCC), using the van Genuchten model have been chosen.
  - vanGenuchten $\alpha_S$ = [0.3, 1.25, 2.2]
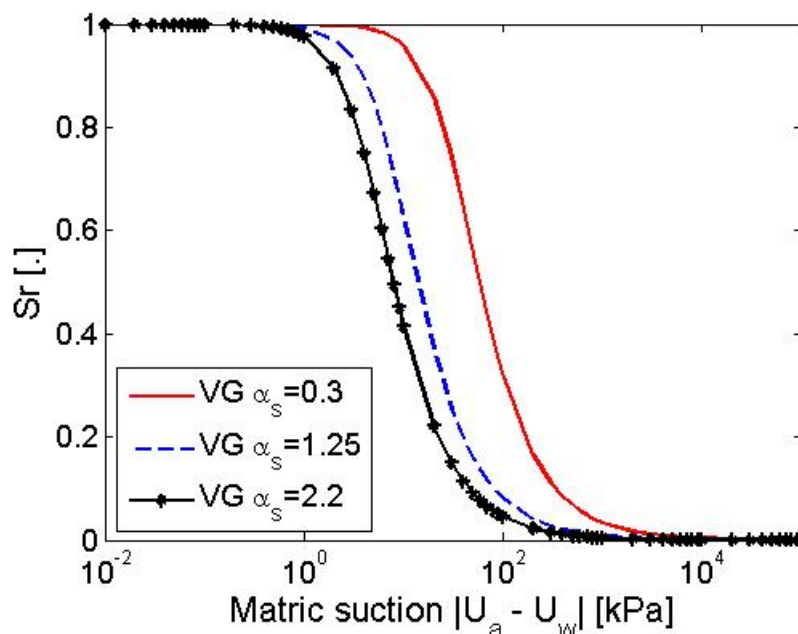


*Figure 42 Water retention curves of studied slopes*

- Vegetation

  The vegetation is characterised by the root density, potential of transpiration and climate conditions which condition the water content or/and suction in the soil.

In order to illustrate the possible changes in the soil water content or/and suction and the possible depths of influence, an example is illustrated in Figure 43. A 10m deep soil layer with a slope of 22° is considered with the following parameters:

- $Ks = 10^{-8}$ m./s,

- Van Genuchten $\alpha = 0.3$

- Transpiration:  5mm/day.

*Table 42 Root density distribution function*

| z | β(z) | G(β) | |
|---|---|---|---|
| 0 | 0.168 | 0.0146 | |
| 0.5 | 25 | 0.970 | |
| 1 | 0.168 | 0.0146 | |
| 1.5 | $1.135 \ 10^{-3}$ | $9.874 \ 10^{-5}$ | |
| 2 | $7.677 \ 10^{-6}$ | $6.679 \ 10^{-5}$ | $\Sigma \ G(\beta)=1$ |

In Figure 44 and Figure 45 the profiles of the suction and degree of saturation after one month of transpiration are given respectively. The evapotranspiration results in an increase of 300 kPa for the suction and the degree of saturation reduces to 10%.

Based on such computations, the depth of influence of the change in suction has been estimated and applied in the parametric studies performed for the evaluation of the slope stability charts.
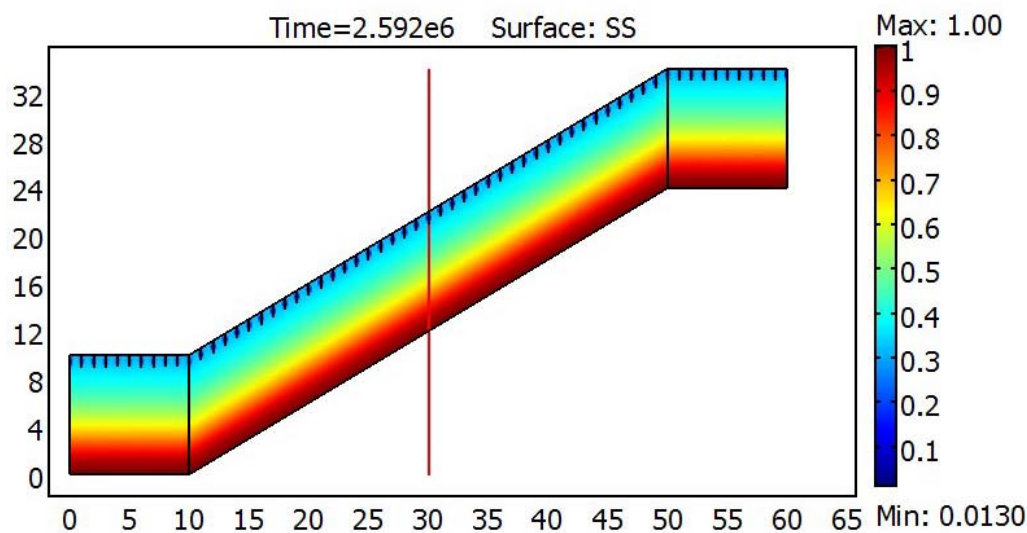


*Figure 43 The degree of saturation distribution and geometry of the site subjected to one month of evapo-transpiration*
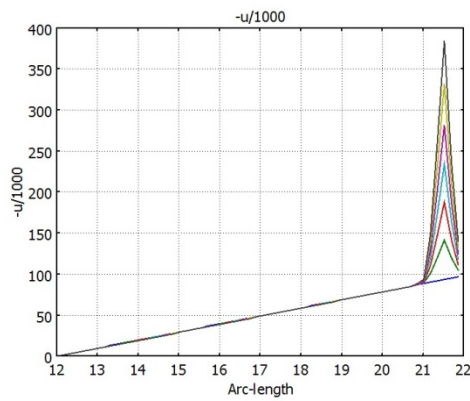
*Figure 44 Profile of suction at the middle of the slope*          *Figure 45 Profile of suction at the middle of the slope*
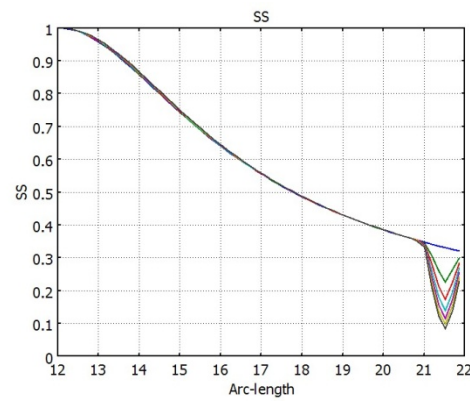
Based on these analyses, it was decided to limit the depth of influence of the vegetation to 2m. Three configurations are considered with different initial water contents at the upper 2m layer in which the suction increases up to 300kPa.
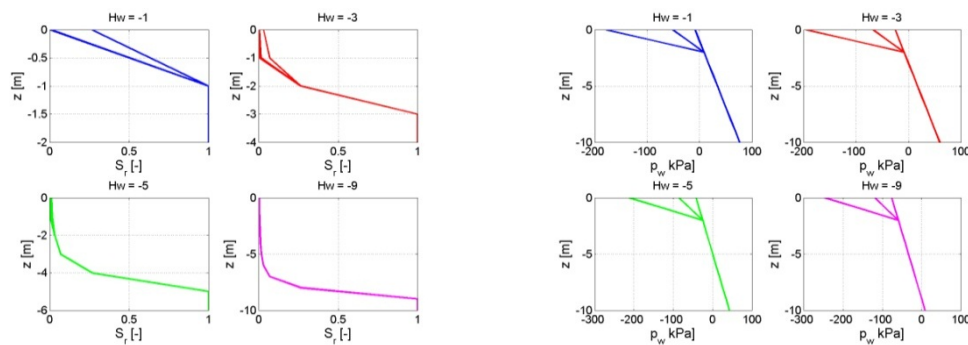


*Figure 46 The initial profiles of pore water pressure and degree of saturation considered in this study to take into account the effect of root uptake*

## 4.7    DEPTH OF NON-SATURATION CONTROLLED INSTABILITY

Before starting the transient seepage parametric analyses, as we aim to study the effect of vegetation which modifies the suction in the soil, it is interesting to identify cases which are concerned with such stability analyses. As we are interested in studying the effect of infiltration or evapotranspiration on slope stability in partially saturated soils, only the slopes that are not stable in saturated condition are studied. For example if in the saturated condition the soil friction angle is higher than soil slope angle, the factor of safety will be always greater than 1. The slope sliding is assumed to be due to infiltration from soil surface and sliding zone is considered to be above and sufficiently far from the water table. Different water retention curves and different internal friction angles for different slope angle are studied. Used water retention curves are presented in Figure 37.

For the smaller values of $\alpha$, the hydraulic properties of soil is closer to the clayey soils. Three values of friction angle are studied: 20° (Table 43), 25° (Table 44) and 30° (Table 45). As we are interested to study the instability due to saturation, we study the cases that are stable only

in unsaturated state. For example for the soil with friction angle supposed to be 20°, the slope angles 21°,23°,25° and 27° are studied that all of them are instable in saturated case.

For each soil friction angle one table of results is presented in which the first column is for $\alpha = 0.3$, the second one for $\alpha = 1.25$ and the third one for $\alpha = 2.2$.

It is assumed that the study is performed on an initially stable slope in which the factor of safety will decrease by increase of water content (reduction of soil suction).

$\alpha = 0.3$                          $\alpha = 1.25$

$\theta = 21°$



$\theta = 23°$



$\theta = 25°$



$\theta = 27°$
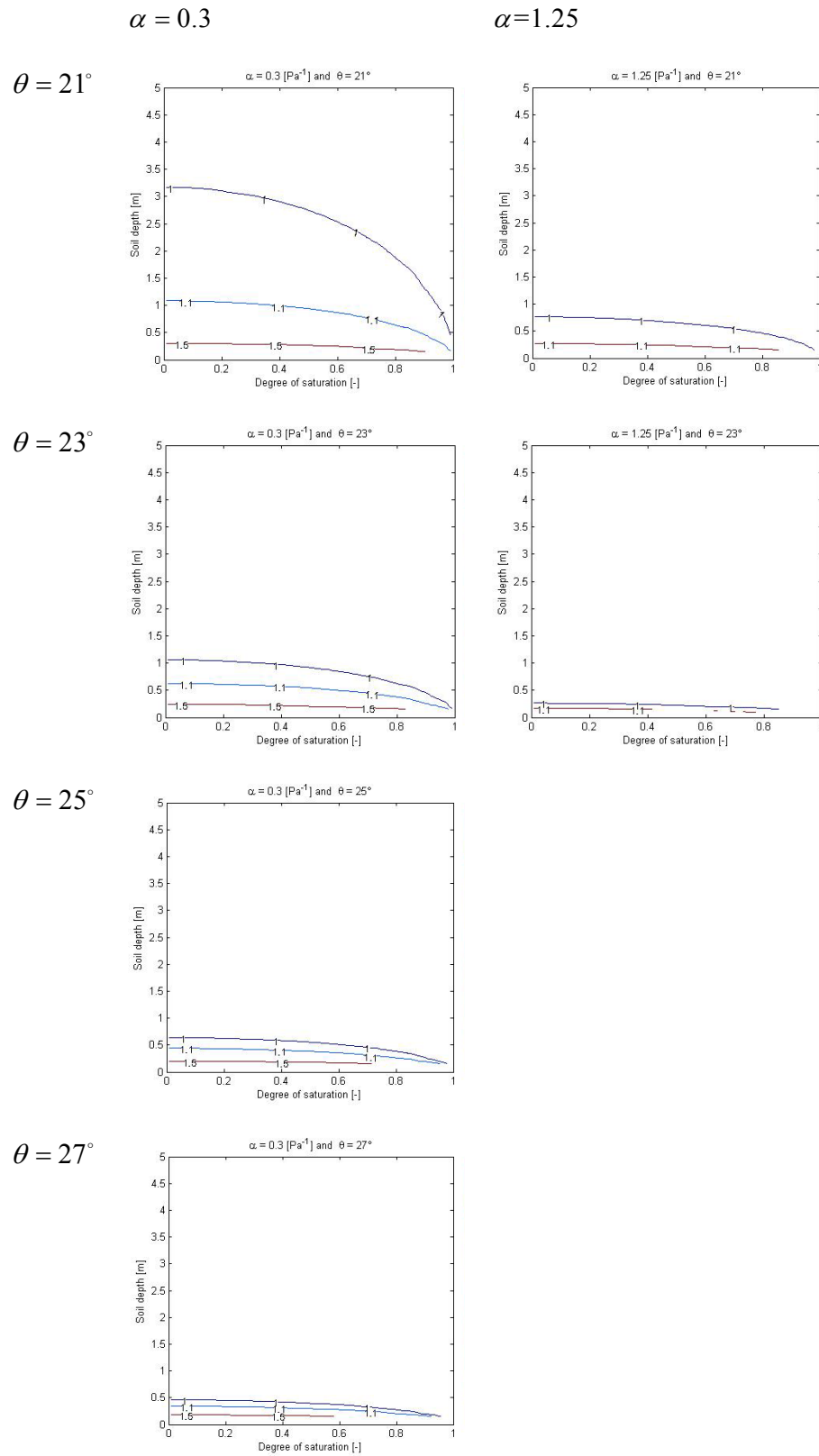
$\alpha = 2.2$

$\theta = 21°$
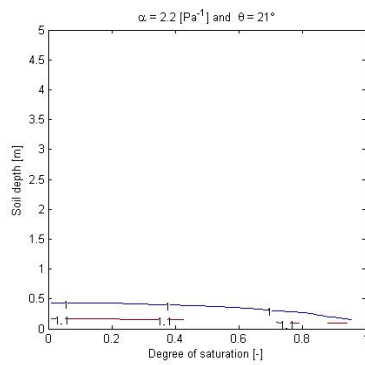


*Table 43 Variation of influence depth of soil instability as a function of degree of saturation for $\phi = 20°$*

$\alpha = 0.3$                                    $\alpha = 1.25$

$\theta = 26°$
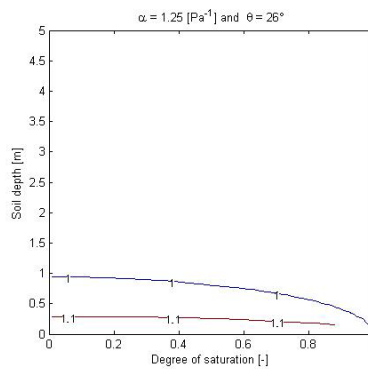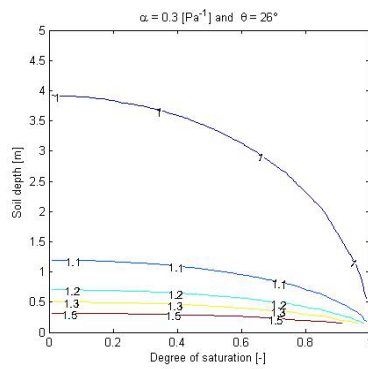


$\theta = 28°$
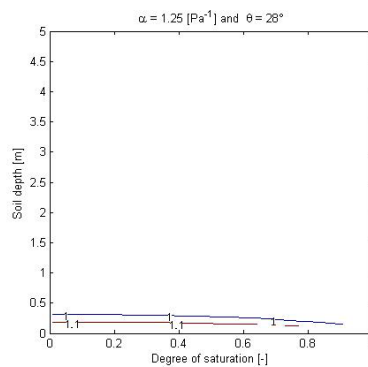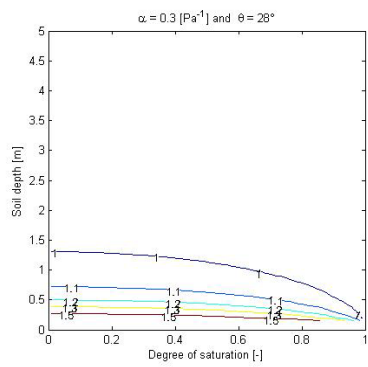
$\theta = 30°$
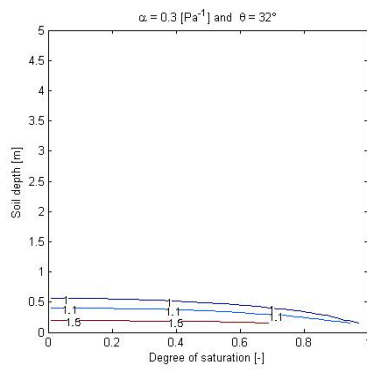


$\theta = 32°$
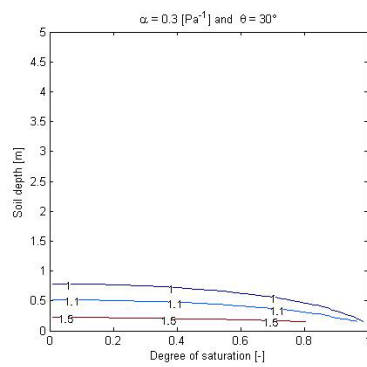


$\alpha = 2.2$

$\theta = 26°$
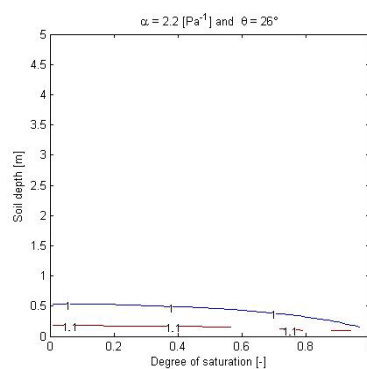


*Table 44 Variation of influenced depth of soil instability as a function of degree of saturation for $\varphi = 25°$*

$\alpha = 0.3$                                                    $\alpha = 1.25$

$\theta = 31°$



$\theta = 33°$



$\theta = 35°$



$\theta = 37°$
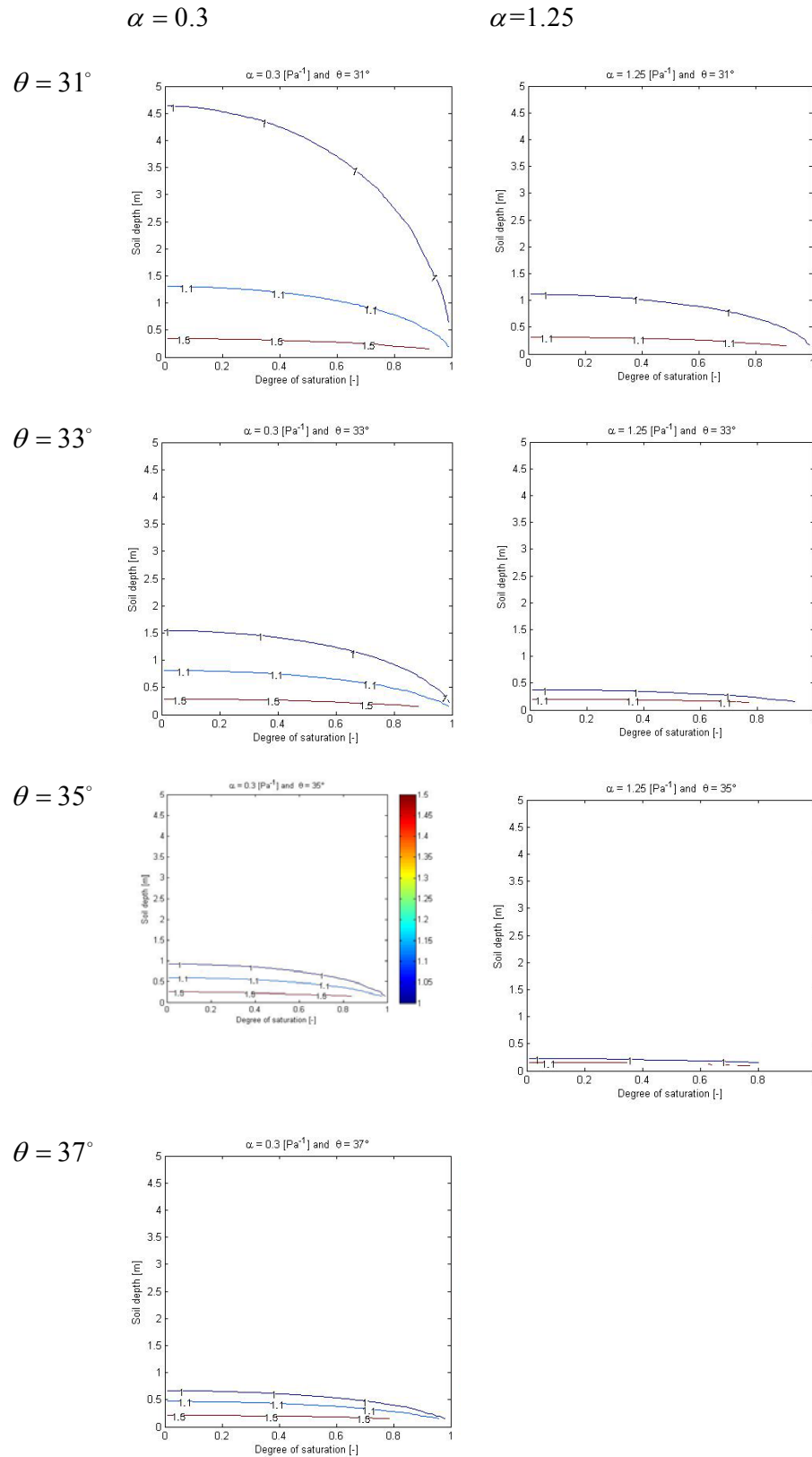
$$\alpha = 2.2$$

$$\theta = 31°$$
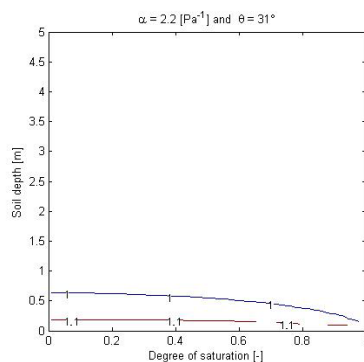


*Table 45 Variation of influenced depth of soil instability as a function of degree of saturation for $\phi = 30°$*

As can be seen, for different values of friction angle $\phi$, the variation of factor of safety due to increase of water content (reduction in soil suction) is limited to the first meter of depth. For the soils with water retention curves near the case $\alpha = 0.3$ (for smaller values of $\alpha$) the role of degree of saturation becomes more and more important and the depth of instability zone due to increase of degree of saturations reduced. For example, for example if a 3 meters thick soil layer with $\phi = 25°$ and $\alpha = 0.3$ for a slope angle of $\theta = 26°$ is stable up to $S_r = 60\%$, if the rainfall continues, a slope sliding can be occurred.

As the results show, the unsaturated soils sensibility to the slope sliding due to water infiltration can be classified as a function of soil water retention curves. For larger values of $\alpha$ the other mechanisms of sliding must be studied.

## 4.8    TRANSIENT ANALYSES

In Figure 47 the evolution of the saturation front is given. On the same figure, on the top right picture, the evolution of the safety factor 'ϕ=30°) with depth is given for different values of ground slope varying from 10° to 35° (right to the left with an increment of 5°). It can be noted, that according to this figure, because of the presence of water, the instable state (F=1) may be obtained for slopes with an angle less than the friction angle of the soil.
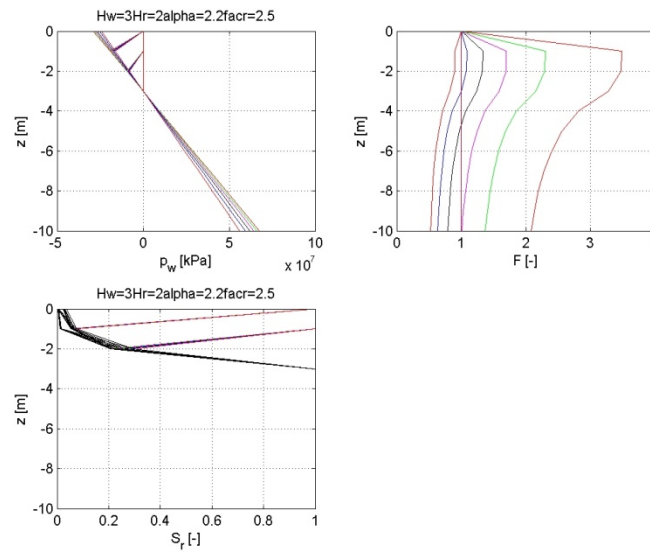
*Figure 47 profiles of saturation front in the simplified model*

As mentioned before, the role of vegetation is taken into account by modification of the initial water content of the soil in the upper layers. Therefore, three different saturation profiles with two of them diverting from the hydrostatical condition for the top layers were considered (Figure 45).
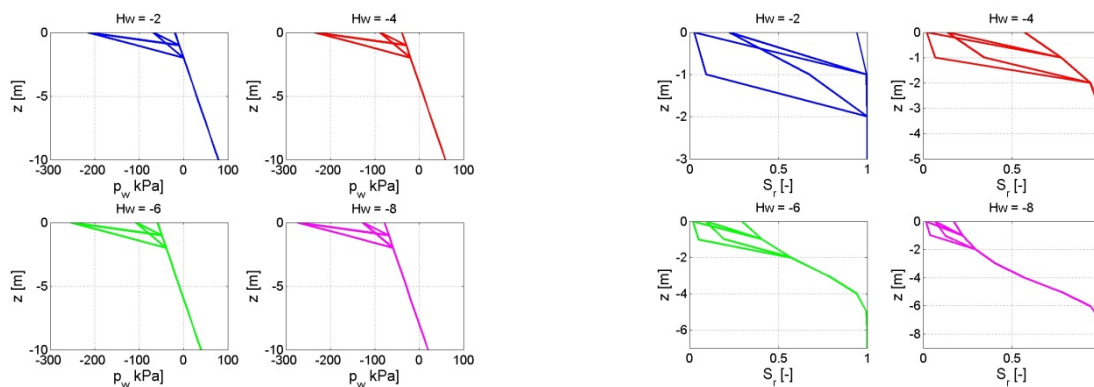


*Figure 48 Initial pore water pressure and degree of saturation profiles taking into account the root uptake*

It is very important to study the evolution of the safety factor with time when the water content in the soil increases due to rainfall. Firstly, the evolution of the safety factor with the advance of the saturation front is studied. In Figure 54, this evolution is illustrated for the cases where the water table is at 2m, 4m, 6m and 8m depth and three initial water content profiles.
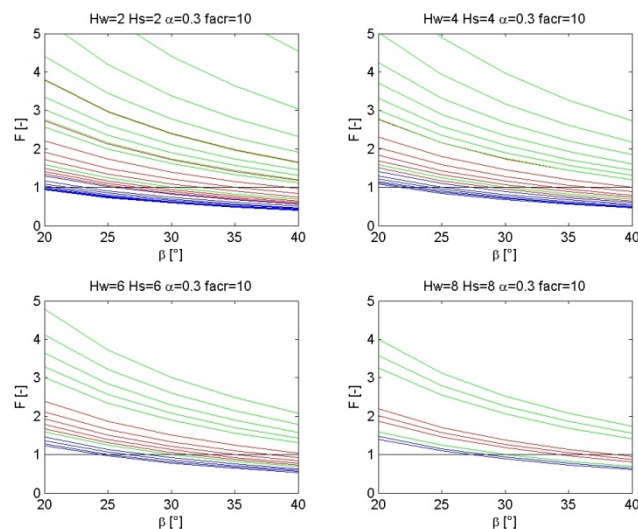
*Figure 49 Evolution of safety factor with the advance of saturation front for different slope angles*

*Blue: hydrostatic initial pore pressure*
*Red: moderated vegetation uptake*
*Green: arid zone*

In order to have an idea of the time the slope becomes unstable (F=1), contours of time for the saturation front to reach a given depth in the slope are drown on the same Figure as the contours of the points where F=1 and this for different slope angles. The intersection of the time contours and the F=1 ones, gives the position and time of failure. This is illustrated in Figure 50, Figure 51 and Figure 52. The time scale is normalized by the permeability.  Let's comment Figure 50 and describe the presented cases. Here, the water table is at Hw=-4m and van Genuchten's $\alpha$ is 0.3.  In Figure 50(a), where the initial pore pressure is hydrostatic, the profile is unstable at the depth of 2m for a slope of 30° and this depth decreases when the slope angle $\beta$ increases. The first horizontal green line corresponds to the unstable points when the saturation front reaches the depth of 0.2 m. We can see that if the slope is 45°, the time is 0.001 units, while for 43, 40, 37, .. we have 0.0012, 0.0015, 0.0018 ....

In Figure 50 (b), another initial state has been applied. This state corresponds to an increase of 30KPa in the suction of the top layer. The same failure scenarios happens but for longer durations of rainfall. For a slope of 35°, the layer at 0.2m fails at 0.446 time units and it is 0.225 for the 45° slope.  For the case C, where the suction of the top layer increases to 200 kPa a duration of 0.264 time units is necessary. The contours of the retard in time of failure for these cases are given in Figure 50(d) and Figure 50(e). The higher the slope, or the higher the suction at the top layer, the higher this difference in durations.

The same type of results may be obtained for other types of configurations. Some other examples are given in Figure 51 and Figure 52.

Such graphics can be obtained with the simplified model and integrated in risk analysis tools.

*Case A: Hydrostatic pore pressure   Case B: Moderate evapotranspiration    Case C: High evapotranspiration*
*distribution*
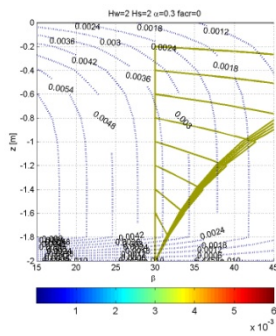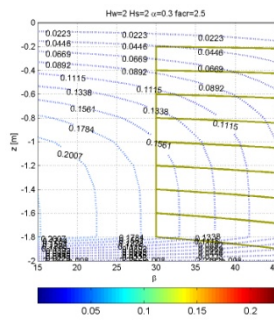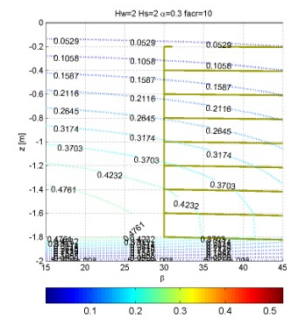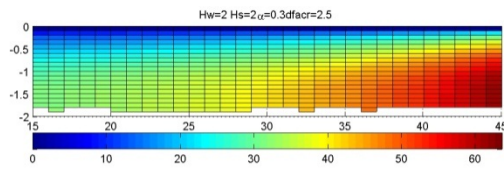


*(a)*



*(b)*



*(c)*



*Difference of time to failure between cases A and B*

*(d)*

*Difference of time to failure between cases A and C*

*(e)*



*Figure 50 Evolution of instability with time for Hw=-2m; α = 0.3*
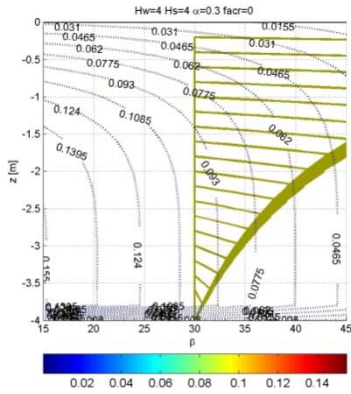
Hydrostatic pore pressure distribution    Moderate evapotranspiration    High evapotranspiration
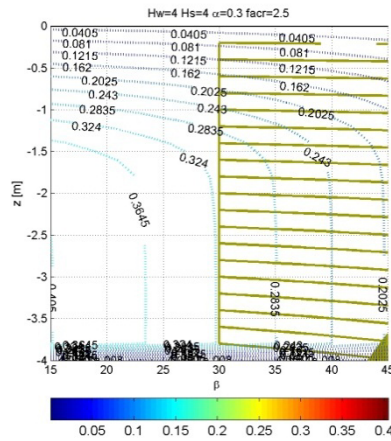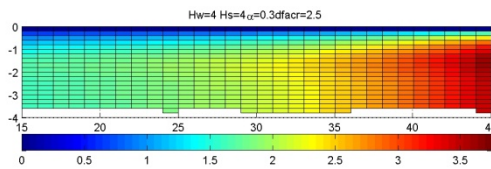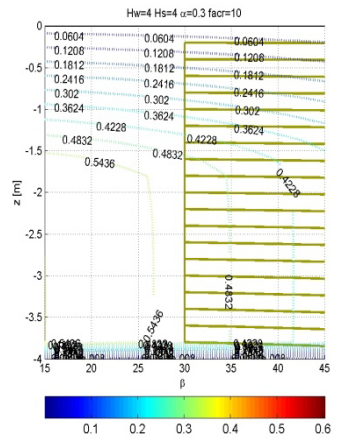
Difference of time to failure between cases A and B
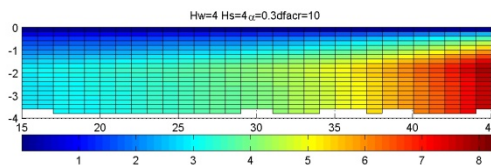
Difference of time to failure between cases A and C

*Figure 51 Evolution of instability with time for Hw=-4m; α = 0.3*
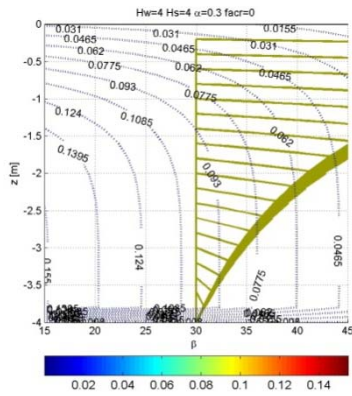
Hydrostatic pore pressure distribution     Moderate evapotranspiration     High evapotranspiration
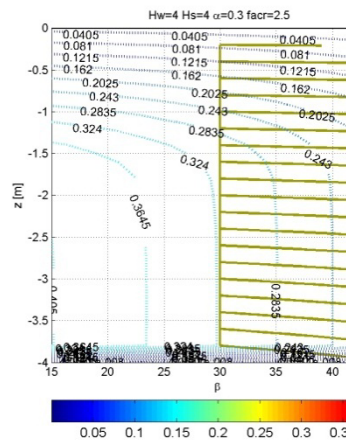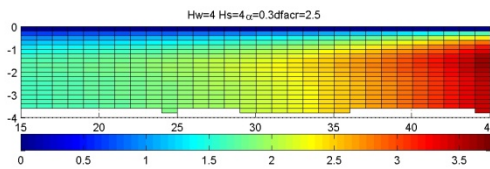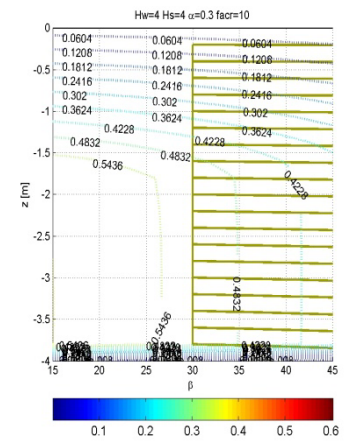


Difference of time to failure between cases A and B
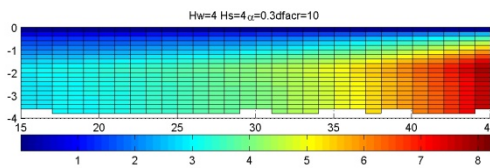
Difference of time to failure between cases A and C

*Figure 52 Evolution of instability with time for Hw=-4m; α = 0.3*

Case    A:   Hydrostatic   pore   Case          B:        Moderate   Case C: High evapotranspiration
pressure distribution                  evapotranspiration



(a)                                        (b)                                        (c)
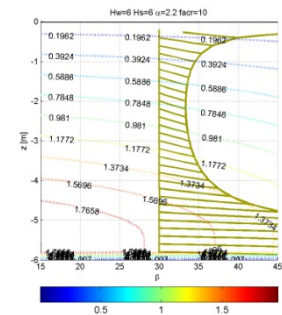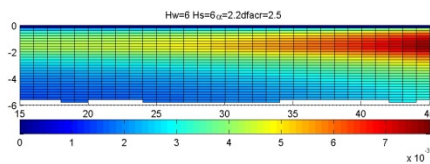


*Difference of time to failure between cases A and B*

*(d)*
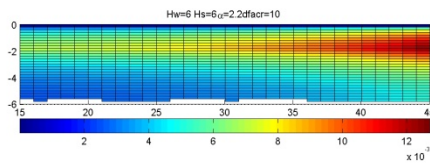
*Difference of time to failure between cases A and C*

*(e)*

*Figure 53 Evolution of instability with time for Hw=-6m; $\alpha$ = 2.2*

## 4.9     CONCLUSIONS

The influence of the suction change due to vegetation/canopy on the factor of safety is studied and based on the results obtained by transient infiltration computations, a methodology to obtain simplified and rapid estimations of possible unstable slopes and the moment of their failure is given. The approach considers only the influence of the root water uptake caused by evapotranspiration and other phenomenon due to the presence of vegetation is not taken into account. This methodology in which uncertainties can easily be integrated could be adapted for the estimation of failure probabilities because of its rapidity of execution.

# 5       EVOLUTION OF VULNERABILITY

The assessment of future landslide risk depends on the evaluation of landslide hazard and the vulnerability of exposed structures which both change with time. The real, non-stationary vulnerability modelling of structures due to landslides may be significantly affected by aging considerations, anthropogenic actions, cumulative damage from past landslide events and retrofitting measures.

With the above in mind, the present work aims at the development of an efficient analytical methodology to assess the evolution of building vulnerability with time exposed to the landslide hazard. In particular, the aging of typical RC buildings is considered by including probabilistic models of corrosion deterioration of the RC elements within the vulnerability modelling framework. Two potential adverse corrosion scenarios are examined: chloride and carbonation induced corrosion of the steel reinforcement. An application of the proposed methodology to reference low rise RC buildings exposed to seismically induced landslide hazard considering the effect of reinforcement corrosion is provided. Both buildings with stiff and flexible foundation system are examined. Non-linear static time history analyses of the buildings are performed using a fibre-based finite element code. The distribution for the corrosion initiation time is assessed through Monte Carlo simulation using appropriate probabilistic models for the carbonation and the chloride induced corrosion. Then, the loss of area of steel over time due to corrosion of the RC elements is modelled as a reduction in longitudinal reinforcing bar cross-sectional area in the fibre section model. Time dependent structural limit states are defined in terms of steel material strain. Fragility curves/surfaces are derived for different points in time as a function of Peak Horizontal Ground Acceleration PHGA at the seismic bedrock or permanent co-seismic ground displacement PGD at the slope area for both chloride and carbonation induced deterioration scenarios.

## 5.1     ENVIRONMENTAL DETERIORATION OF RC STRUCTURES

### 5.1.1   Corrosion of reinforcement

The strength of the components of any structural system in general is a time dependent property which may decrease in resistance along the structure's service life. Potential reasons for structural strength degradation can be attributed to multiple factors such as corrosion, erosion, other forms of chemical deterioration and fatigue (Melchers and Frangopol 2008). Among these, reinforcement corrosion is undoubtedly, one of the most important causes of deterioration of reinforced concrete in Europe and worldwide. Theoretically corrosion of the reinforcement should not occur as the reinforcement is supposedly well protected by the concrete cover and the alkalinity of the last. Non-carbonated concrete has a high alkalinity (pH=13) that is a result of the presence of sodium, potassium and calcium hydroxides produced during the hydration of the cement. In this alkaline environment an oxide layer is formed on the steel surface, the so called "passive film" that prevents the corrosion of the reinforcement. However, there are two processes that may break down this passive film: the ingress of chlorides and carbon dioxide.
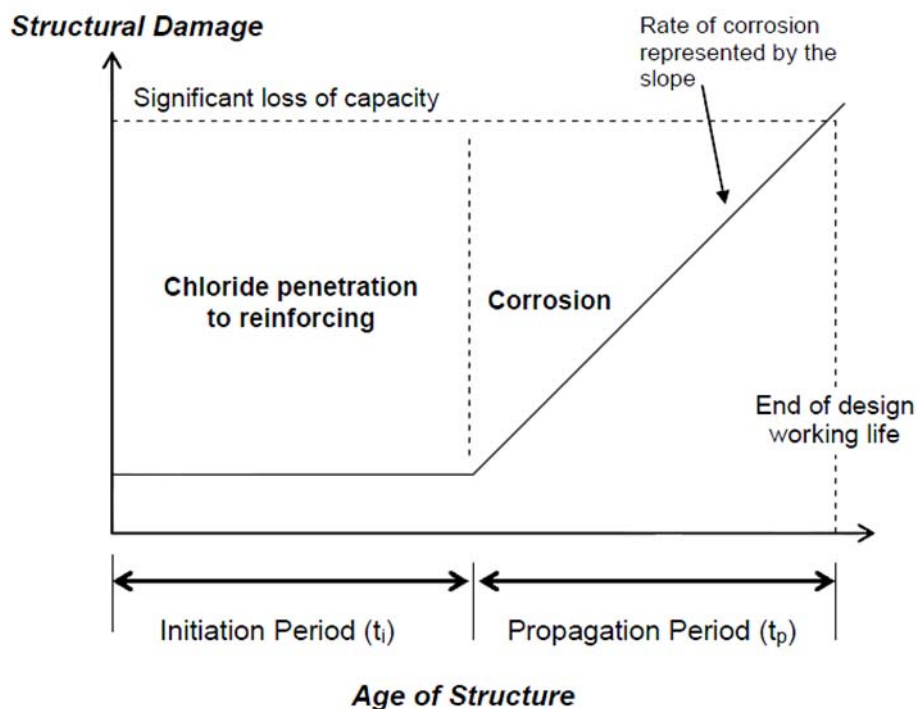
*Figure 54 Schematic illustration of the evolution of the reinforced concrete corrosion*

The amount of structural damage due to corrosion of steel reinforcement as a function of the age of the structure can be expressed through a bilinear model as schematically illustrated in Figure 54. Deterioration caused by reinforcement corrosion is normally divided into two main time periods, the initiation period (ti) and the propagation period (tp). The initiation period is defined as the time until the reinforcement becomes depassivated either by the presence of chloride salts or by carbonation. As soon as the concrete at the depth of the reinforcement is carbonated or contains a critical amount of free chlorides the reinforcement becomes depassivated and corrosion may occur. This limit state defines the beginning of the propagation period. During the propagation period the reinforcement is corroding, which may lead to deterioration of the concrete as well. Expansive corrosion products provoke cracks along the reinforcement, and subsequently, spalling of the concrete cover may occur. Finally, the loss of cross section of the reinforcement may lead to reduction of the load bearing capacity.

### 5.1.2   Carbonation-induced corrosion

#### *5.1.2.1 Mechanism*

Concrete carbonation induces a decrease of the pH of the pore solution, which leads to dissolving the protective layer (Figure 55). Then the corrosion of the reinforcement starts only if the reinforcing steel has significant electrical potential difference along with the presence of sufficient moisture and oxygen. Concrete carbonation is a complex physico-chemical process that develops in two distinct regions: the anode, where the passive layer is destroyed and the steel dissolved; and the cathode, where hydroxide ions are formed due to the combination of oxygen, water and the electrons coming from the anode. It includes the diffusion of $CO_2$ into

the gas phase of the concrete pores and its reaction with the calcium hydroxyl $Ca(OH)_2$. As the high pH of uncarbonated concrete is mainly due to the presence of $Ca(OH)_2$, it is clear that the consumption of this species will lead to a pH drop, which can attain a value of 9 when the reaction is completed. In this environment, the oxide layer that protected the reinforcement bars is attacked and corrosion starts. In practice, $CO_2$ penetrates into the concrete mass by diffusion from the surface layer. Thus a carbonation front appears that moves into the structure (Figure 56).
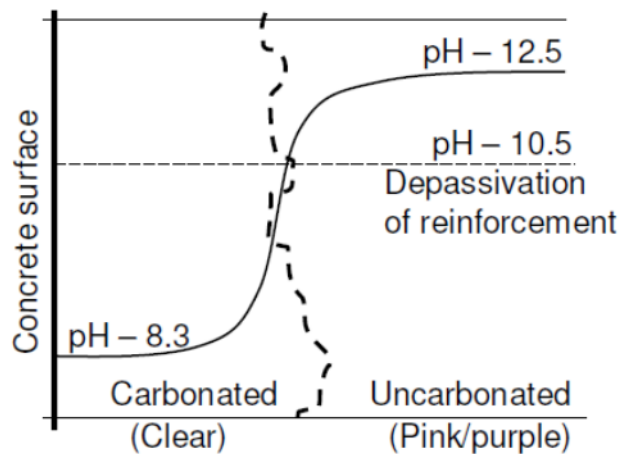


*Figure 55 Carbonation in concrete (Beushausen and Alexander, 2010)*
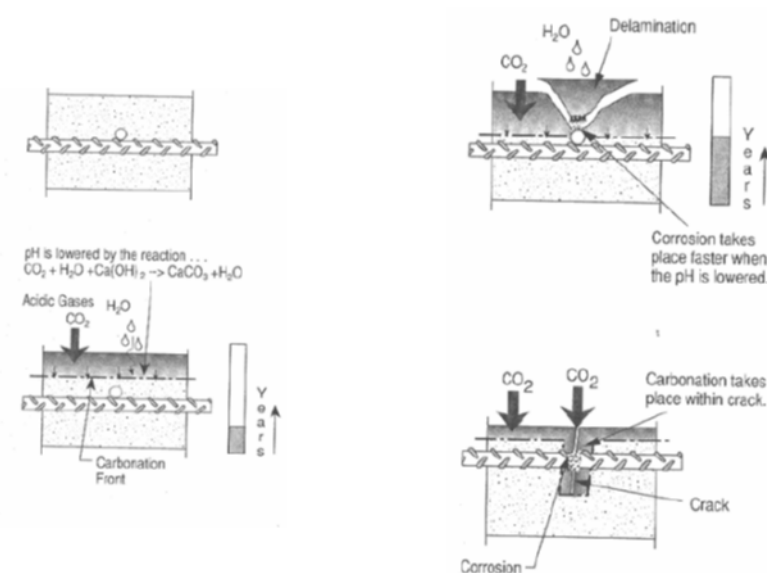


*Figure 56 Carbonation induced corrosion (Beushausen and Alexander, 2010)*

### 5.1.2.2 Probabilistic modelling of carbonation induced corrosion initiation

Several methods have been proposed to model corrosion due to carbonation (e.g. Sudret et al. 2007; Peng and Stewart, 2008; Marques and Costa, 2010 etc.). The probabilistic model for

computing the carbonation depth xc proposed by FIB- CEB Task Group 5.6 (2006) is adopted. The model has been developed within the research project DuraCrete and slightly revised in the research project DARTS, each project was funded by the European Union. It is based on diffusion as the prevailing transport mechanism within the concrete (Fick's 1st law of diffusion) assuming that the diffusion coefficient for carbon dioxide through the material is a constant material property.

$$x_c(t) = \sqrt{2 \cdot k_e \cdot k_c \cdot (k_t \cdot R_{ACC,0}^{-1} + \dot{a}_t) \cdot C_s} \cdot \sqrt{t} \cdot W(t) \qquad \text{(Equation 3)}$$

Where

xc(t): carbonation depth at the time t [mm]
t: time [years]
ke: environmental function [-]
kc: execution transfer parameter [-]
kt: regression parameter [-]
RACC,0-1: inverse effective carbonation resistance of concrete [(mm2/years)/(kg/m3)]
at: error term,
CS: CO2-concentration [kg/m3]
W(t): weather function [-]

It is supposed that corrosion immediately starts when carbonation has attained the rebar. Denoting by a (mm) the concrete cover, the time necessary for corrosion to start, called corrosion initiation time, is given as:

$$T_{init} = \left( \frac{2 \cdot k_e \cdot k_c \cdot (k_t \cdot R_{ACC,0}^{-1} + \dot{a}_t) \cdot C_s}{a^2} \cdot t_0^{2 \cdot w} \right)^{\left( \frac{1}{2 \cdot w - 1} \right)} \qquad \text{(Equation 4)}$$

The environmental function ke takes account of the influence of the humidity level on the diffusion coefficient and hence on the carbonation resistance of the concrete. The reference

$$k_e = \left( \frac{1 - \left( \frac{RH_{real}}{100} \right)^{f_c}}{1 - \left( \frac{RH_{ref}}{100} \right)^{f_c}} \right)^{g_c}$$

climate is T= +20°C/ 65% RH. It can be described by means of (Equation 5).

$$k_e = \left( \frac{1 - \left( \frac{RH_{real}}{100} \right)^{f_c}}{1 - \left( \frac{RH_{ref}}{100} \right)^{f_c}} \right)^{g_c} \qquad \text{(Equation 5)}$$

Where
>    RHreal: weather nearest station data (daily mean value: 0 % < RH < 100 %)
>    $RH_{ref}$ [%]: constant parameter, value: 65
>    ge [-]: constant parameter, value: 2.5
>    fe [-]: constant parameter, value: 5.0

The execution transfer parameter kc takes the influence of curing on the effective carbonation resistance into account.  It can be described by means of Equation 6, derived from Bayesian regression analysis.

$$k_c = \left(\frac{t_c}{7}\right)^{b_c}$$
(Equation 6)

>    $k_c$: execution transfer parameter [-]
>    $b_c$: exponent of regression [-], normally distributed variable
>    $t_c$: period of curing [d], constant parameter, value: period of curing

The inverse carbonation resistance of concrete $R_{ACC,0}^{-1}$ should be quantified using different direct and indirect testing methods.  If no test data is available, literature data can be used for orientation purposes [Table *B1-2*, FIB- CEB Task Group 5.6 (2006)].

The factors kt and $a_t$ have been introduced in order to transform the results gained under "accelerated carbonation" conditions $R_{ACC,0}^{-1}$ into an inverse carbonation resistance $R_{NAC,0}^{-1}$ under "natural carbonation" conditions.

$$R_{NAC,0}^{-1} = k_t \cdot R_{ACC,0}^{-1} + \dot{a}_t$$
(Equation 7)

> $R_{ACC,0}^{-1}$: inverse effective carbonation resistance of dry concrete, determined at a certain point of time $t_0$ on specimens with the accelerated carbonation test ACC [(mm$^2$/years)/(kg/m$^3$)], normally distributed variable.
>
> $R_{NAC,0}^{-1}$: inverse effective carbonation resistance of dry concrete (65%RH) determined at a certain point of time $t_0$ on specimens with the normal carbonation test NAC [(mm$^2$/years)/(kg/m$^3$)]
>
> kt:    regression parameter which considers the influence of test method on the ACC-test [-],normally distributed variable.
>
> $a_t$:    error term considering inaccuracies which occur conditionally when using the ACC test method [(mm$^2$/years)/(kg/m$^3$)], normally distributed variable.

The $CO_2$ concentration of the ambient air represents the direct impact on the concrete structure. The impact can be described by the following equation:

$$C_S = C_{S,atm} + C_{S,emi}$$
(Equation 8)

Where
>    $C_S$: $CO_2$ concentration [kg/m$^3$]
>    $C_{S,atm}$: $CO_2$ concentration of the atmosphere [kg/m$^3$]
>    $C_{S,emi}$: additional $CO_2$ concentration due to emission sources [kg/m$^3$]

For usual structures, Equation 6 can be reduced to Equation 9:

$$C_S = C_{S,atm} \qquad \textit{(Equation 9)}$$

The atmospheric concentration of $CO_2$ can be quantified as a normally distributed variable (mean= 0.00082, s=0.0001).

The weather function W takes the meso-climatic conditions due to wetting events of the concrete surface into account.

$$W = \left(\frac{t_0}{t}\right)^{\frac{(p_{SR}\cdot ToW)^{b_w}}{2}} = \left(\frac{t_0}{t}\right)^{w} \qquad \textit{(Equation 10)}$$

    $t_0$: time of reference [years]
    w: weather exponent [-]
    ToW: time of wetness [-], value: to be evaluated from weather station data

$$ToW = \frac{\textit{days with rainfall } h_{Nd} \geq 2.5 \textit{ mm per year}}{365} \qquad \textit{(Equation 11)}$$

    $p_{SR}$: probability of driving rain [-],value: depending on the type of structural elements
    $b_w$: exponent of regression [-],normally distributed variable
    $t_o$ [years]: constant parameter, value: 0.0767

The statistical quantification of the model parameters is provided in Table 46 based on the FIB- CEB Task Group 5.6 (2006) proposed model. For illustrational purposes, values for Portland Cement Concrete (PCC) and three different water/cement ratios (namely w/c=0.4,0.5 and 0.6) are given. Three different corrosion levels (low, medium, high) are considered (Table 46) based on recent available literature (Marques and Costa, 2010).

*Table 46 Statistical characteristics of parameters affecting the chloride induced corrosion deterioration of RC elements*

| Parameter | | water to cement ratio w/c | | | | | | Distribution | Reference |
|---|---|---|---|---|---|---|---|---|---|
| | | 0.4 | | 0.5 | | 0.6 | | | |
| | | Mean | cov | Mean | cov | Mean | cov | | |
| Cover Depth (mm) x | | 25 | 0.32 | 25 | 0.32 | 25 | 0.32 | Lognormal | FIB- CEB Task Group 5.6 (2006) |
| Regression variable be [K] | | 4800.00 | 0.15 | 4800.00 | 0.15 | 4800.00 | 0.15 | Normal | |
| Temperature of the structural element or the ambient air  (Treal) [K] | | 286 | 0.20 | 286 | 0.20 | 286 | 0.20 | Normal | |
| Chloride migration Coefficient ($D_{RCM,0}$) ($m^2$/s) | | 8.9E-12 | 0.2 | 1.58E-11 | 0.2 | 2.5E-11 | 0.2 | Normal | |
| Aging exponent n | | 0.3 | cov=0.4 , a=0.0, b=1.0 | 0.3 | cov=0.4 , a=0.0, b=1.0 | 0.3 | cov=0.4 , a=0.0, b=1.0 | Beta | |
| Critical Chloride Concentration (Ccr) wt % cement | | 0.6 | cov=0.25, a= 0.2, b=2.0 | 0.6 | cov=0.25, a= 0.2, b=2.0 | 0.6 | cov=0.25, a= 0.2, b=2.0 | Beta | |
| Surface Chloride Concentration (Cs) wt % cement | | 1.026 | 0.2 | 1.2825 | 0.2 | 1.539 | 0.2 | Normal | Choe et al. (2008) |
| Rate of Corrosion (icorr) mA/$cm^2$ | Low corrosion Level | 0.1 | 0.25 | 0.1 | 0.25 | 0.1 | 0.25 | Normal | Stewart (2004) |
| | Medium corrosion Level | 1 | | 1 | | 1 | | | |
| | High corrosion Level | 10 | | 10 | | 10 | | | |

### 5.1.3   Chloride-induced corrosion

#### 5.1.3.1 Mechanism

Chloride induced corrosion is reportedly the most serious and widespread deterioration mechanism of concrete structures, fib (2006). It can be attributed to the ingress of chloride ions from the concrete surface through the concrete cover to the reinforcing steel. Once the chlorides have penetrated the concrete cover and reached the surface of reinforcement, and their concentration exceeds a threshold value, corrosion is initiated (Figure 57 and Figure 58). According to DuraCrete (2000) two exposure environments are of main concern, namely marine and road environment. Within these, different zones are identified:

- the atmospheric

- the splash

- the tidal and

- the submerged zone

Chloride-induced corrosion causes extensive damage as the presence of salt and water creates the right conditions for rapid corrosion rates generating pits and expansive rust.
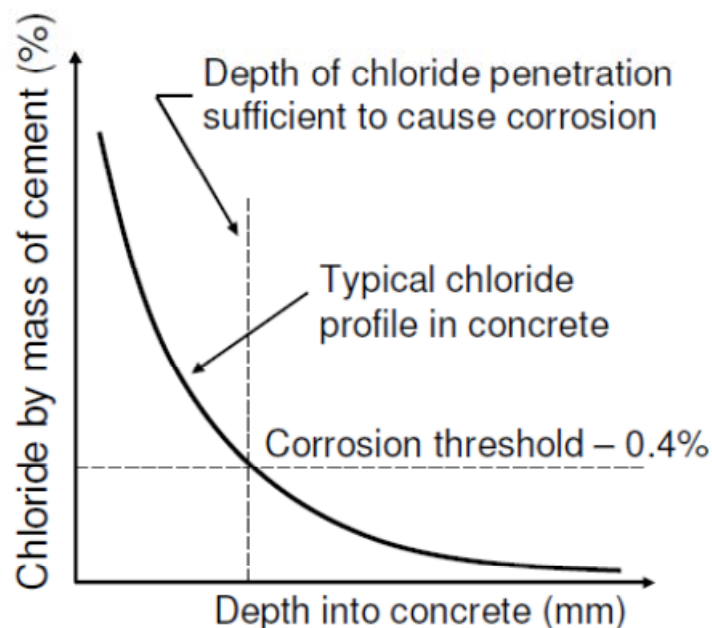


*Figure 57 Typical chloride profile in concrete (Beushausen and Alexander, 2010)*
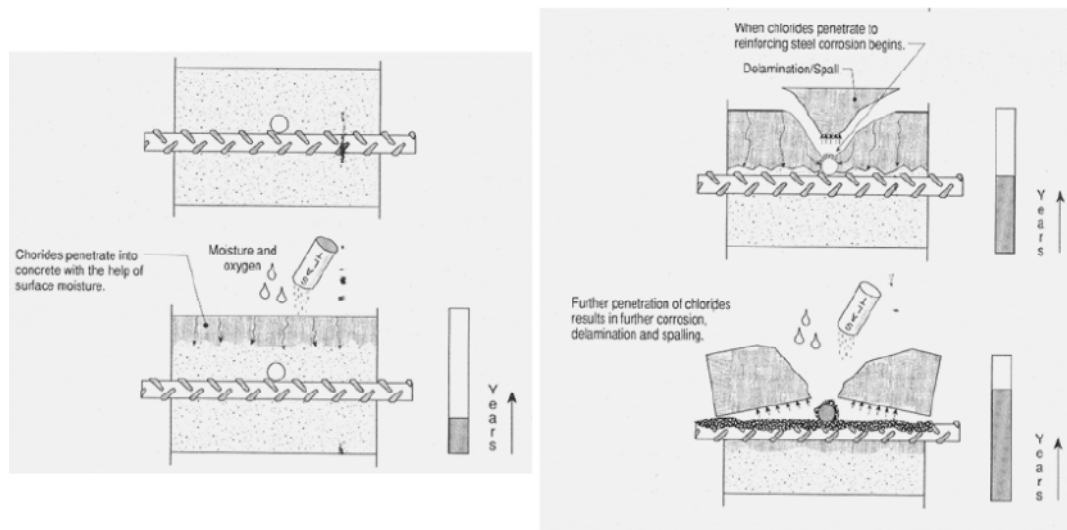
*Figure 58 Chloride induced corrosion of reinforcement (Beushausen and Alexander, 2010)*

### 5.1.3.2 Probabilistic modelling of chloride induced corrosion initiation

Several models have been proposed to quantify and account for corrosion in the design, construction, and maintenance of RC structures. A summary of these models can be found e.g. in DuraCrete (1998). Researchers tend to agree that corrosion phenomena are subject to severe uncertainties thus necessitating the use of probabilistic models. The probabilistic model proposed by FIB- CEB Task Group 5.6 (2006) for modelling corrosion initiation due to chloride ingress is adopted herein. It is based on the limit-state Equation 12, in which the critical chloride concentration $C_{crit}$ is compared to the actual chloride concentration at the depth of the reinforcing steel at a time t $C(x = a, t)$. The model has been developed within the research project DuraCrete and slightly revised in the research project DARTS, each project was funded by the European Union.

$$C_{crit.} = C(x = a,t) = C_0 + \left(C_{S,\Delta x} - C_0\right) \cdot \left(1 - erf \frac{a - \Delta x}{2 \cdot \sqrt{D_{app,C} \cdot t}}\right)$$

*Equation 12*

Where

  $C_{crit.}$: critical chloride content [wt.-%/c]
  $C(x,t)$: content of chlorides in the concrete at a depth x (structure surface: x = 0 m) and at time t [wt.-%/c]
  $C_0$: initial chloride content of the concrete [wt.-%/c]
  $C_{S,\Delta x}$: chloride content at a depth $\Delta x$ and a certain point of time t [wt.-%/c]
  x: depth with a corresponding content of chlorides $C(x,t)$ [mm]
  a: concrete cover [mm]
  $\Delta x$: depth of the convection zone (concrete layer, up to which the process of chloride penetration differs from Fick's 2nd law of diffusion) [mm]

$D_{app,C}$: apparent coefficient of chloride diffusion through concrete [mm2/years]
t: time [years]
erf: Gaussian error function

The apparent coefficient of chloride diffusion of concrete $D_{app,C}$ can be determined by means of $D_{app,C} = k_e \cdot D_{RCM,0} \cdot k_t \cdot A(t)$                        Equation 13

$$D_{app,C} = k_e \cdot D_{RCM,0} \cdot k_t \cdot A(t)$$                         *Equation 13*

Where

$k_e$: environmental transfer variable [-]
$D_{RCM,0}$: chloride migration coefficient [mm$^2$/a], normally distributed variable
kt: transfer parameter [-], constant parameter, value: 1
A(t): subfunction considering the 'ageing' [-]

The model is based on Fick's 2nd law of diffusion, taking into account that most observations indicate that transport of chlorides in concrete is diffusion controlled. However, in order to still describe the penetration of chlorides for an intermittent load using Fick's 2nd law of diffusion, the data of the convection zone Δx (e.g. zone exposed to frequent change of wetting and subsequent evaporation), is neglected and Fick's 2nd law of diffusion is applied starting at a depth Δx with a substitute surface concentration Cs, Δx. With this simplification, Fick's 2nd law of diffusion yields a good approximation of the chloride distribution at a depth x ≥Δx.

The environmental transfer variable ke has been introduced in order to take the influence of $T_{real}$ on the diffusion coefficient $D_{app,C}$ into account. It is described by the following equation:

$$k_e = exp\left( b_e \cdot \left( \frac{1}{T_{ref}} - \frac{1}{T_{real}} \right) \right)$$                        *Equation 14*

Where

$b_e$: regression variable [K], normally distributed variable
$T_{ref}$: standard test temperature [K], constant parameter, value: 293
$T_{real}$: temperature of the structural element or the ambient air [K], normally distributed variable, to be evaluated from nearby weather station data

The Chloride Migration Coefficient $D_{RCM,0}$ is one of the governing parameters for the description of the material properties in the chloride induced corrosion model. Suitable data for $D_{RCM,0}$ may be obtained from literature for different concrete mixtures to be used as starting variables in service life design or vulnerability assessment calculations [Table B2-1, FIB- CEB Task Group 5.6 (2006)].

The apparent diffusion coefficient $D_{app,C}$ is subject to considerable scatter and tends to reduce with increasing exposure time. In order to this take into account when modelling the initiation process, a transfer parameter $k_t$ in combination with a so-called ageing exponent n has been introduced.

$$A(t) = \left(\frac{t_0}{t}\right)^n$$

<div align="right">*Equation 15*</div>

n: ageing exponent [-], beta distributed variable, Table B2-2, FIB- CEB Task Group 5.6 (2006)
$t_0$: reference point of time [years], constant parameter, value: 0.0767

The chloride content in the concrete is not only caused by chloride ingress from the surface, but can also be due to chloride contaminated aggregates, cements or water used for the concrete production (initial chloride content $C_0$). In certain circumstances the chloride content of fine and coarse aggregates and water can be considerable.

The chloride content $C_S$ at the concrete surface as well as the substitute surface content $C_{S,\Delta x}$ at a depth $\Delta x$ are variables that depend on material properties (e.g. type of binder and the concrete composition) and on geometrical (e.g. geometry of the structural element and the distance to the chloride source) and environmental (e.g. equivalent chloride concentration of the ambient solution) conditions. The information needed to determine $C_S$ and $C_{S,\Delta x}$ is briefly summarized in the flowchart given in Figure 59.
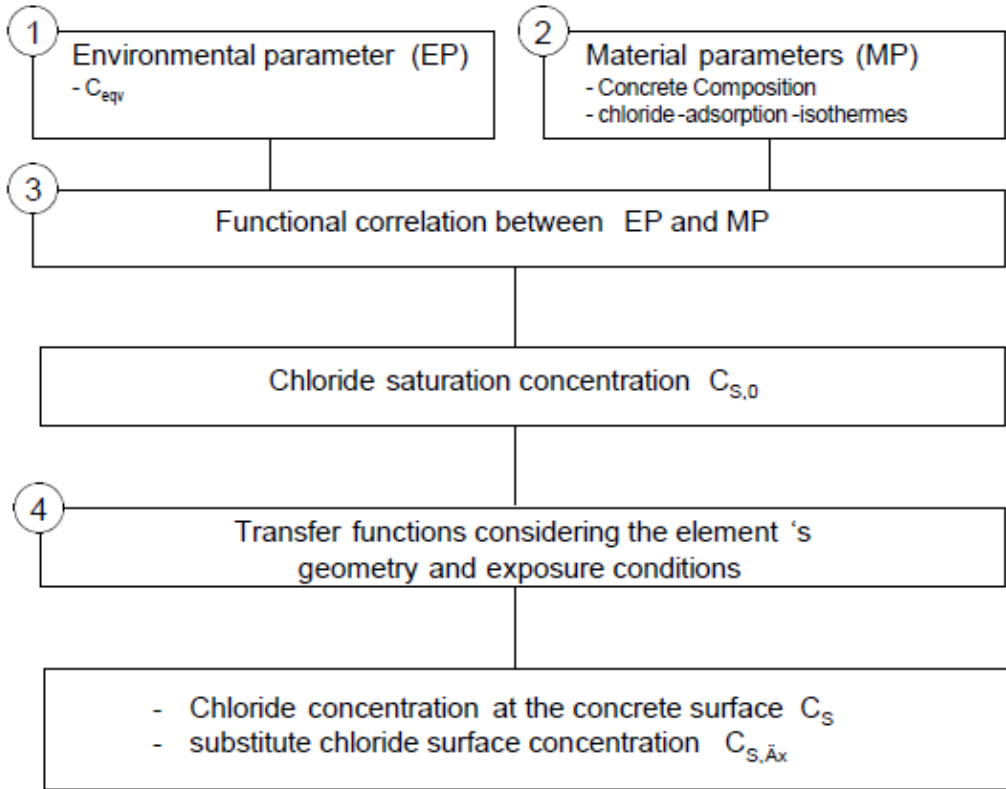


*Figure 59 Information needed to determine the variables CS and CS,Δx (FIB- CEB Task Group 5.6 , 2006)*

Under a continuous chloride impact of constant concentration, the chloride saturation concentration $C_{S,0}$ on the concrete surface is reached often in relative short time periods compared to the service life of the structure ($C_{S,0} = C_S$). Based on these results, the conservative simplification that the variable $C_S$ is from the beginning constant with time can

be concluded for certain exposure conditions (e. g. for concrete continuously exposed to sea water).

In order to quantify the substitute chloride surface concentration $C_{S,\Delta x}$, *the* transfer function $\Delta x$ needs to be determined. For the different types of exposure conditions (splash, submerged, spray, tidal and atmospheric) $\Delta x$ can be quantified based on the information provided in section B2.2.5.5 of FIB- CEB Task Group 5.6 (2006). Depending on the exposure condition $C_{S,\Delta x}$ may be defined as the maximum chloride content $C_{max}$. In cases when no $\Delta x$ develops (e.g. spray zone), $C_{max}$ represents the chloride content at the concrete surface $C_S$.

The critical chloride content $C_{crit}$ is the critical chloride concentration that causes dissolution of the protective passive film around the reinforcement and initiates corrosion. A beta-distribution with a lower boundary of 0.20 wt.-%/cement, mean value of 0.60 wt.-%/cement and upper boundary of 2 wt.-%/cement was found to yield a sufficiently good description of the test results.

Based                                                                              on

Equation 12 and assuming that the chloride ion concentration near the concrete surface is constant, the time till corrosion initiation can be determined as:

$$
T_{init} = \left( \frac{a^2}{4 \cdot k_e \cdot k_t \cdot D_{RCM,0} \cdot (t_0)^n} \cdot \left( erf^{-1}\left( 1 - \frac{C_{crit}}{C_s} \right) \right)^{-2} \right)^{\left(\frac{1}{1-n}\right)}
$$

*Equation 16*

Where

　　$T_{init}$: the corrosion initiation time (years) and
　　$C_s$: the equilibrium chloride concentration at the concrete surface

The statistical quantification of the model parameters describing the corrosion initiation of the reinforced concrete elements is provided in Table 47 based on the FIB- CEB Task Group 5.6 (2006) proposed model. For illustrational purposes, values for Portland Cement Concrete (PCC) and three different water/cement ratios (namely w/c=0.4,0.5 and 0.6) are given. The values of surface chloride concentration $C_S$ and of the temperature of the structural element or the ambient air $T_{real}$ presented in the table are applicable to structures exposed to atmospheric chloride condition (Choe et al. 2008). Three different corrosion levels (low, medium, high) are considered (Table 47) based on available literature (Stewart, 2004).

| Parameter | | water to cement ratio w/c | | | | | | Distribution | Reference |
|---|---|---|---|---|---|---|---|---|---|
| | | 0.4 | | 0.5 | | 0.6 | | | |
| | | Mean | cov | Mean | cov | Mean | cov | | |
| Cover Depth (mm) x | | 25 | 0.32 | 25 | 0.32 | 25 | 0.32 | Lognormal | FIB- CEB Task Group 5.6 (2006) |
| Regression variable be [K] | | 4800.00 | 0.15 | 4800.00 | 0.15 | 4800.00 | 0.15 | Normal | |
| Temperature of the structural element or the ambient air (Treal) [K] | | 286 | 0.20 | 286 | 0.20 | 286 | 0.20 | Normal | |
| Chloride migration Coefficient ($D_{RCM,0}$) ($m^2$/s) | | 8.9E-12 | 0.2 | 1.58E-11 | 0.2 | 2.5E-11 | 0.2 | Normal | |
| Aging exponent n | | 0.3 | cov=0.4 , a=0.0, b=1.0 | 0.3 | cov=0.4 , a=0.0, b=1.0 | 0.3 | cov=0.4 , a=0.0, b=1.0 | Beta | |
| Critical Chloride Concentration (Ccr) wt % cement | | 0.6 | cov=0.25, a= 0.2, b=2.0 | 0.6 | cov=0.25, a= 0.2, b=2.0 | 0.6 | cov=0.25, a= 0.2, b=2.0 | Beta | |
| Surface Chloride Concentration (Cs) wt % cement | | 1.026 | 0.2 | 1.2825 | 0.2 | 1.539 | 0.2 | Normal | Choe et al. (2008) |
| Rate of Corrosion (icorr) mA/$cm^2$ | Low corrosion Level | 0.1 | 0.25 | 0.1 | 0.25 | 0.1 | 0.25 | Normal | Stewart (2004) |
| | Medium corrosion Level | 1 | | 1 | | 1 | | | |
| | High corrosion Level | 10 | | 10 | | 10 | | | |

Table 47 Statistical characteristics of parameters affecting the chloride induced corrosion deterioration of RC elements

## 5.2    APPLICATION TO REFERENCE RC BUILDINGS

### 5.2.1    Numerical modelling of the buildings

The studied buildings (Figure 60) are single bay- single story RC bare frame structures with varying strength and stiffness characteristics of the foundation system (isolated footings, continuous foundation). They have been designed according to the provisions of the Greek Seismic Code (EAK 2000), for a design acceleration Ad = 0.36 g, and a behavior factor q = 3.5. The adopted dead and live loads (g = 1.3 kN/m$^2$ and q = 2 kN/m$^2$) are typical values for residential buildings. The beneficial contribution of masonry infill walls to the building capacity is not considered in this study. The reference buildings are assumed to be standing near the crest of a potentially precarious soil slope. Hence, for a certain earthquake scenario, the buildings may be subjected to a considerable amount of permanent differential displacement at the foundation level due to the effect of the earthquake triggered landslide hazard. The same methodology may be applied for other hazards (i.e. hydrogeological-intense precipitation). The analytical methodology for the vulnerability assessment of RC buildings exposed to earthquake induced slow moving soil slides as well as the proposition of adequate fragility functions for a variety of RC building typologies have been described and discussed in Pitilakis & Fotopoulou (2011).

The description of the numerical modelling of the typical RC buildings is briefly outlined herein. Note that these models need to be updated with deteriorated component models to take into account the effect of aging. The analyses of the reference RC buildings are conducted using the fibre-based finite element code SeismoStruct (Seismostruct, Seismosoft 2010). Non-linear static time-history analyses are performed for all numerical simulations. In this analysis type, the applied loads (displacements) at the foundation level vary in the pseudo-time domain, according to a load pattern prescribed as the differential permanent ground displacement (versus time) curves directly extracted from the seismic 2D dynamic analysis.
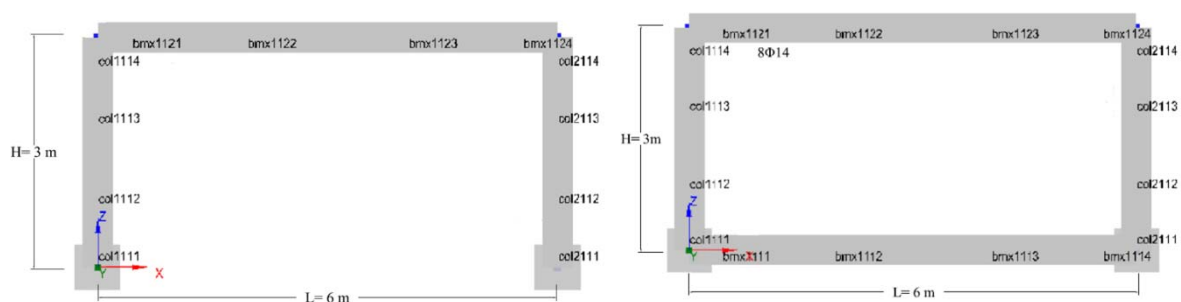


*Figure 60 Reference analysed RC frame buildings*

The material properties assumed for the members of the RC buildings are described below. A uni-axial nonlinear constant confinement model is used for the concrete material (fc=20MPa, ft=2.1MPa, strain at peak stress 0.002mm/mm, confinement factor 1.2), assuming a constant confining pressure throughout the entire stress-strain range (Mander et al., 1988). For the reinforcement, a uni-axial bilinear stress-strain model with kinematic strain hardening is utilized (fy=400MPa, E=200GPa, strain hardening parameter μ =0.005). All columns and beams have rectangular cross sections (beam: 0.30x 0.50 m, column: 0.40x 0.40m). The initial longitudinal section reinforcement degree used is 1% for the columns and 0.75% for the beams.

### 5.2.2  Quantification of aging probabilistic parameters

The present study considers the aging of the typical RC buildings by including probabilistic models of carbonation and chloride induced corrosion deterioration of the RC elements within the vulnerability modelling framework. The application of the fully probabilistic approach to the referred RC structures through a crude Monte Carlo simulation using the coefficient of variations proposed in FIB- CEB Task Group 5.6 (2006) was found to require large computational burden for practical problems and to yield to numerical errors and instability for usual sample sizes (e.g. 100000-500000). Hence, in an effort to equilibrate the computing efficiency and accuracy, for the probabilistic modelling of rebar corrosion of a specified RC building, it was decided to adopt the mean values of the parameters given in Table 46 and Table 47 and to consider lower variability for the random variables. Table 48 and

Table 49 present the statistical characteristics of the parameters finally adopted for an adverse carbonation and chloride induced corrosion scenario (w/c=0.6, High corrosion Level) respectively. It should be noted that for the chloride corrosion scenario, an atmospheric exposure environment is assumed (e.g. ke=0.67, Choe et al., 2008).

*Table 48 Characteristics of parameters affecting the carbonation induced corrosion deterioration of RC elements adopted in the present study*

| Parameter | Mean | COV | Distribution |
|---|---|---|---|
| Cover Depth (mm) a | 25.00 | 0.20 | Lognormal |
| $R_{real,k}$ (% rel. humidity) | 70.00 | cov=0.05 , a=40.0, b=100 | Beta |
| Exponent of regression bc | -0.567 | 0.035 | Normal |
| Inverse carbonation resistance ($R_{acc,0}^{-1}$) $(mm^2/year) / (kg/m^3)$ | 2.30E-10 | 0.10 | Normal |
| Influence of test method kt | 1.25 | 0.10 | Normal |
| Error term et $(mm^2/years)$ | 315.5 | 0.05 | Normal |
| Cs, atm $(kg/m^3)$ | 0.000820 | 0.10 | Normal |
| Exponent of regression bw | 0.446 | 0.10 | Normal |
| Rate of Corrosion (rcorr) $mA/cm^2$ | 2 | 0.20 | Normal |

*Table 49 Statistical characteristics of parameters affecting the chloride induced corrosion deterioration of RC elements adopted in the present study*

| Parameter | Mean | COV | Distribution |
|---|---|---|---|
| Cover Depth (mm) x | 25 | 0.2 | Lognormal |
| Environmental tranfer variable ke | 0.67 | 0.1 | Normal |
| Chloride migration Coefficient ($D_{RCM,0}$) ($m^2/s$) | 2.5E-11 | 0.1 | Normal |
| Aging exponent n | 0.3 | cov=0.05 , a=0.0, b=1.0 | Beta |
| Critical Chloride Concentration (Ccr) wt % cement | 0.6 | cov=0.05, a= 0.2, b=2.0 | Beta |
| Surface Chloride Concentration (Cs) wt % cement | 1.539 | 0.1 | Normal |
| Rate of Corrosion (icorr) $mA/cm^2$ | 10 | 0.20 | Normal |

### 5.2.2.1 Corrosion initiation time

The distribution for the corrosion initiation time is assessed through Monte Carlo simulation having a sample size of 100000. A lognormal distribution with mean 36.40 years and standard deviation of 20.85 years is found to be a good fit to the simulated data for carbonation induced corrosion initiation time (Figure 61). Similarly, a lognormal fit with mean 2.96 years and standard deviation of 2.16 years is adopted for chloride induced corrosion initiation time (Figure 62). These distributions will subsequently be used as key inputs for probabilistic modelling of rebar corrosion due to presence of carbonation and chloride concentration.
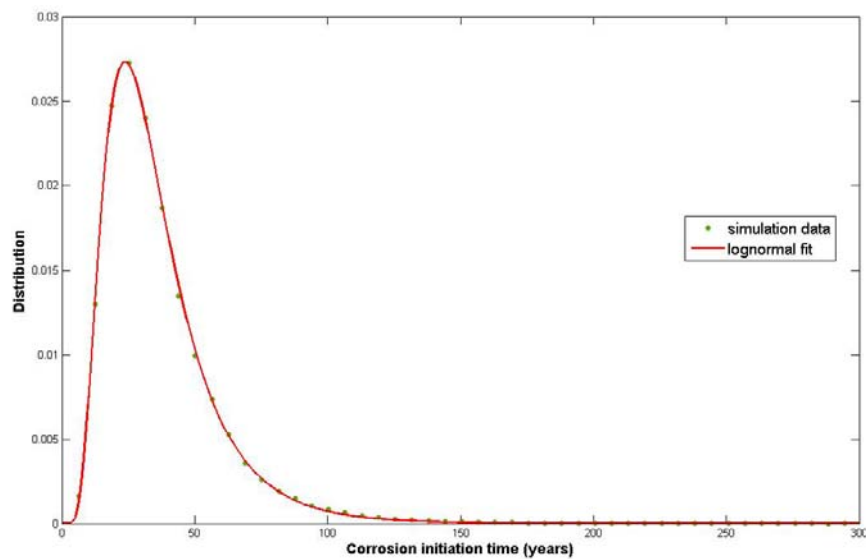
*Figure 61 Distribution of carbonation induced corrosion initiation time Tini (mean = 36.40years, Standard Deviation = 20.85 years)*
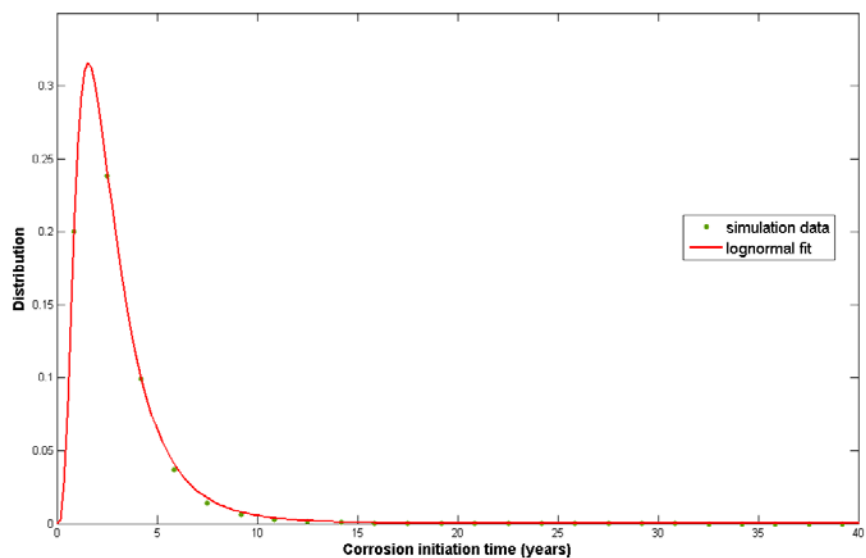


*Figure 62 Distribution of chloride corrosion initiation time Tini (mean = 2.96 years, Standard Deviation = 2.16 years)*

### 5.2.2.2 Corrosion of reinforcement

The corrosion initiation time depends on a number of parameters that can vary considerably for different structures depending on the deterioration mechanism, the structure location and environmental exposure condition. Once the protective passive film around the reinforcement dissolves due to continued chloride ingress or carbonation, corrosion initiates and the time dependent loss of reinforcement cross-sectional area can be expressed as (e.g. Ghosh and Padgett, 2010):

$$A(t) = \begin{cases} n \cdot D_i^2 \cdot \dfrac{\pi}{4} & if \ \ t \leq T_{init} \\ max\left[ n \cdot (D(t))^2 \cdot \dfrac{\pi}{4} \ , 0 \right] & if \ \ t \geq T_{init} \end{cases}$$   (Equation 17)

where, $n$ is the number of reinforcement bars, $D_i$ is the initial diameter of steel reinforcement, $t$ is the elapsed time in years and $D(t)$ is the reinforcement diameter at the end of (t-Ti) years , which can be represented as:

$$D(t) = \begin{cases} D_i & if \ \ t \leq T_{init} \\ max[\, D_i - i_{corr} \cdot \kappa \cdot (t - T_{init}), 0] & if \ \ t \geq T_{init} \end{cases}$$   (Equation 18)

If generalized corrosion is considered, the loss of metal due to corrosion is approximately uniform over the whole surface. In this case, Faraday's law indicates that a corrosion current density corresponds to a uniform corrosion penetration of $\kappa = 11$, 6µm/year. The rate of corrosion $i_{corr}$ in this study is considered to be constant on average along the service life of the structure. Generally, the rate of corrosion due to carbonated concrete cover is slower compared to chloride-induced corrosion.

The loss of area of steel due to corrosion of the RC elements is modelled as a reduction in longitudinal reinforcing bar cross sectional area as compared to the elements in the initial nondegraded state. It is assumed that the corrosion will not affect the mechanical and material properties of the steel reinforcing bars. Figure 63 (a) and (b) shows the probabilistic assessment of the time-dependent area reduction ratio, which is the area of reinforcing steel at time t, A(t), normalized by the initial area of reinforcement, A(t₀). As expected, the variability in the loss of area of reinforcing steel tends to increase with time due to the combined effect of the variability of reinforcement diameter, rate of corrosion and corrosion initiation time.
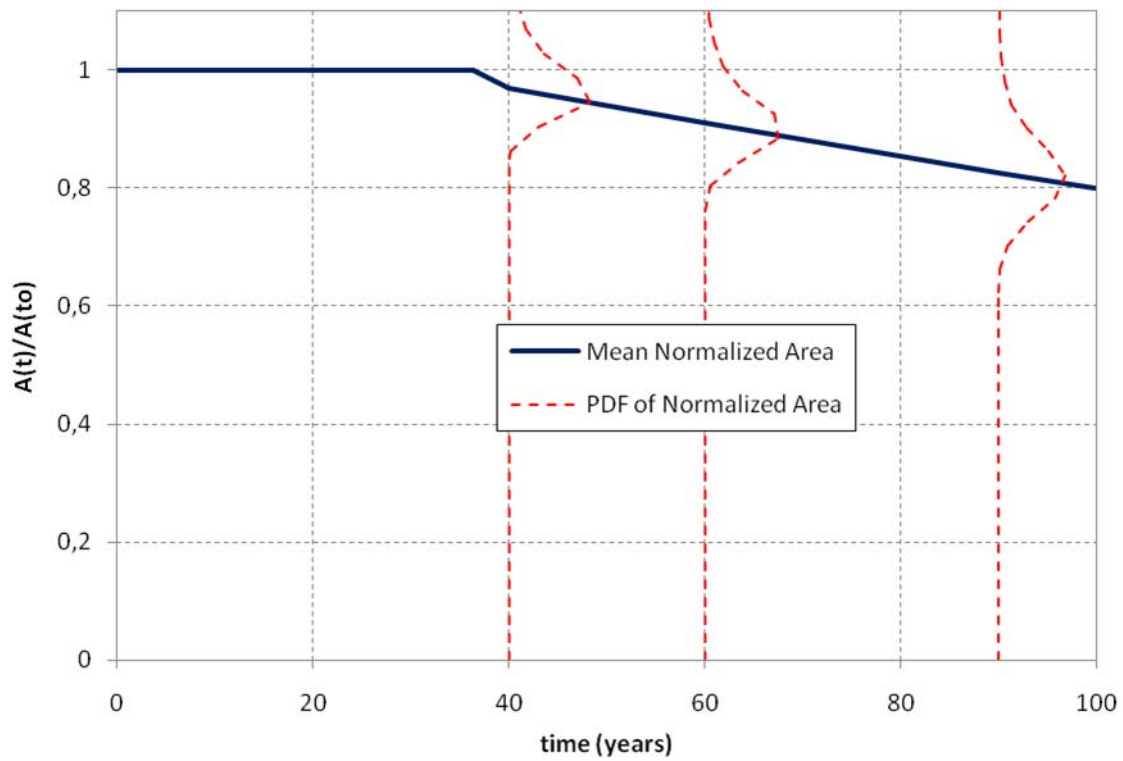
*Figure 63 Distribution of normalized time variant area of the reinforcement (a) for carbonation and (b) chloride induced deterioration*
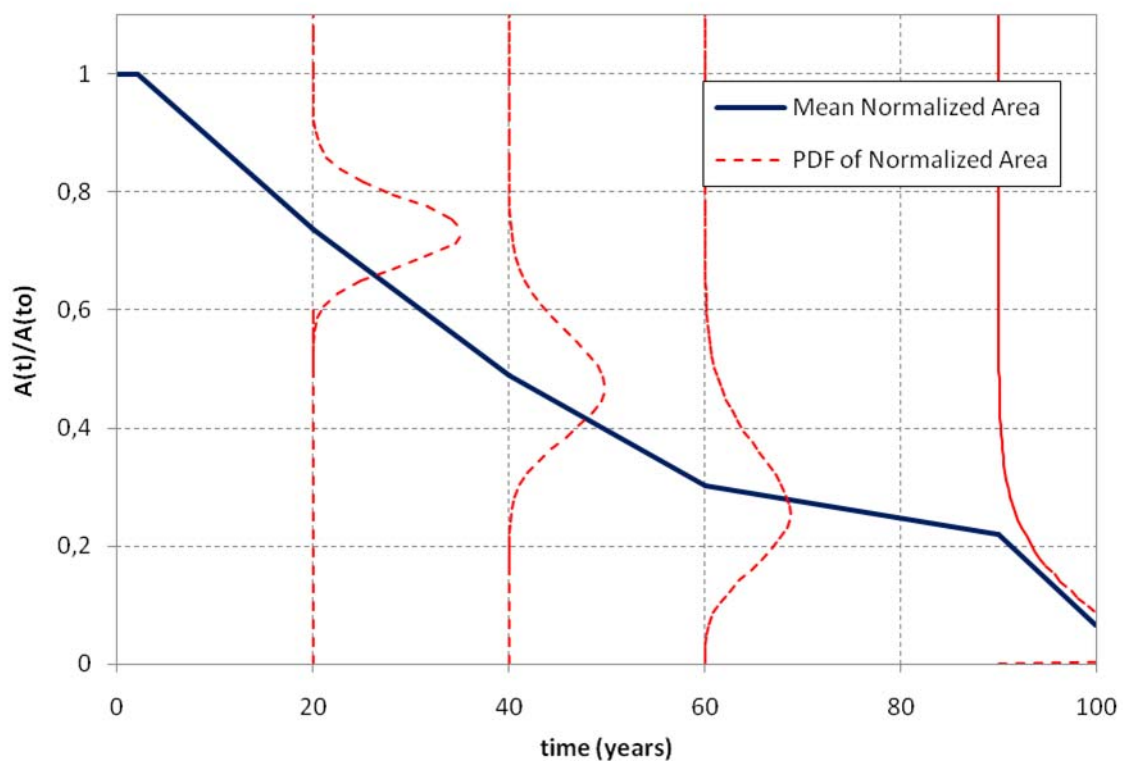
### 5.2.3   Evolution of vulnerability

#### *5.2.3.1 Fragility functions*

In order to identify the building performance at different points in time and to construct the corresponding time-dependent fragility curves, a damage index (DI) is introduced, describing the steel and concrete material strains. Within the context of a fibre-based modelling approach, as implemented in SeismoStruct, material strains usually constitute the best parameter for identification of the performance state of a given structure (Seismosoft 2010). In all cases analysed the steel strain ($\varepsilon_s$) yields more critical results. Thus, it was decided to adopt hereafter only this parameter as a damage index. In this way it is possible to establish a relationship between the damage index ($\varepsilon_s$) and the input motion intensity in terms of the peak horizontal ground acceleration (PHGA)  values at the seismic bedrock or permanent ground displacement (PGD) values at the slope area, for different building typologies and consequently to assign a median value of PHGA/PGD to each limit state. The use of PHGA or PGD is associated to the data availability on the site.

*The next step is the definition of the damage or limit states. For RC corroded buildings characterized by a low level of confinement, the limit steel strains needed to exceed post yield limit states should have lower values compared to adequately and properly confined structures (Crowley et al. 2004; Bird et al. 2005). As a consequence, we decided to adopt lower limit state values to derive exceedance of moderate, extensive and complete damage for the corroded poorly confined buildings. The time-dependent limit state values finally adopted for different damage states for the carbonation and chloride induced deterioration scenario are presented in Table 50 and*

*Table 51 respectively. Note that for carbonation induced corrosion the reduction in longitudinal reinforcing bar cross sectional area is less than 20% in time t=90 years (see Figure 63a). Thus a minor reduction on the limit strain values for the corroded structures is assigned as shown in*

Table 51. On the contrary, larger reduction in the longitudinal reinforcing bar cross sectional area is expected for the chloride induced corrosion (see Figure 63b) resulting in significantly reduced values over time for the corresponding limit states.

*Table 50 Definition of Limit states for the building for the carbonation induced deterioration scenario*

| Time (years) | Limit state | | | |
|---|---|---|---|---|
| | Limit State 1 | Limit State 2 | Limit State 3 | Limit State 4 |
| 0 | | 0.0125 | 0.040 | 0.060 |
| 40 | Steel bar yielding | 0.0125 | 0.039 | 0.059 |
| 60 | | 0.0117 | 0.037 | 0.057 |
| 90 | | 0.0115 | 0.035 | 0.055 |

Table 51 Definition of Limit states for the buildings in different points in time for the chloride induced deterioration scenario

| Time (years) | Limit state | | | |
| :---: | :---: | :---: | :---: | :---: |
| | Limit State 1 | Limit State 2 | Limit State 3 | Limit State 4 |
| 0 | | 0.0125 | 0.040 | 0.060 |
| 20 | | 0.0115 | 0.035 | 0.055 |
| 40 | Steel bar yielding | 0.010 | 0.025 | 0.045 |
| 60 | | 0.006 | 0.015 | 0.030 |
| 90 | | 0.006 | 0.015 | 0.025 |

The overall fragility function of the buildings can be mathematically expressed as:

$$P[LS / IM] = \Phi\left(\frac{In(IM) - In(m(t))}{\beta(t)}\right)$$

<div align="right">*Equation 19*</div>

where, IM is the intensity measure of the earthquake induced landslide expressed in terms of PHGA at the "seismic bedrock" or PGD at the slope area, m(t) and β(t) are the median values (in units of *g* or m depending on the selected intensity measure PHGA or PGD respectively) and logarithmic standard deviations of the system fragilities at different points in time along the service life and LS is the limit state.

The median values of PHGA (t) and PGD (t) that correspond to each limit state can be defined for the threshold values of the aforementioned damage indexes as the values that correspond to the 50% probability of exceeding each limit state. The time-dependent median of the buildings fragilities at each limit state can be adequately represented by a quadratic fit for both deterioration scenarios as will be shown in the followings subsections. The standard deviation values (β) describe the total variability associated with each fragility curve. Three primary sources contribute to the total variability for any given damage state (NIBS 2004), namely the variability associated with the definition of the limit state value, the capacity of each structural type (including the time-dependent variability within the estimation of the corrosion of the reinforcement) and the demand (seismic demand, landslide type, relative position of the structure to the landslide). The median and standard deviation values (β) adopted are presented in Table 52 and Table 54 for the carbonation induced corrosion for buildings with flexible and stiff foundations respectively and in Table 56 and Table 58 for the chloride induced corrosion of the reinforcement for buildings with flexible and stiff foundations respectively. Table 53 and Table 55 provide the percent (%) changes in fragility (in terms of median PHGA/PGD and dispersion β) with aging for the carbonation induced corroded buildings with flexible and stiff foundation system respectively while

Table 57 and Table 59 present the corresponding changes for the chloride induced corroded buildings.  Fragility curves in terms of PHGA (outcrop conditions) and PGD for different damage states are analytically evaluated at different points in time along the service life of the studied buildings to assess the time-dependent effect of corrosion on their vulnerability for the given carbonation (§5.2.3.2) or chloride induced (§5.2.3.3) deterioration scenario. It is observed that the fragility of the structure generally increases over time due to corrosion. Greater increase in vulnerability is expected for the chloride induced corroded building with flexible foundation system (Table 59).

A 3D illustration of the fragility estimates over time (fragility surface) is also shown in order to obtain a better view of the evolution of vulnerability with time.

### 5.2.3.2 Fragility functions for carbonation induced corrosion of reinforcement

_Building with flexible foundation system_

_Table 52 Parameters of fragility functions for buildings with flexible foundation system_

| Time (years) | Median PGA (g) | | | | Median PGD (m) | | | | Dispersion β |
|:---:|:---:|:---:|:---:|:---:|:---:|:---:|:---:|:---:|:---:|
| | LS1 | LS2 | LS3 | LS4 | LS1 | LS2 | LS3 | LS4 | |
| 0 | 0.32 | 0.40 | 0.63 | 0.80 | 0.205 | 0.474 | 1.179 | 1.692 | 0.82 |
| 40 | 0.31 | 0.40 | 0.61 | 0.77 | 0.205 | 0.474 | 1.154 | 1.667 | 0.82 |
| 60 | 0.32 | 0.39 | 0.60 | 0.75 | 0.200 | 0.443 | 1.075 | 1.575 | 0.81 |
| 90 | 0.30 | 0.38 | 0.56 | 0.72 | 0.155 | 0.428 | 1.000 | 1.450 | 0.75 |

_Table 53 Percent (%) Changes in Median PGA/PGD and dispersion β values with aging for buildings with flexible foundation system_

| | Change (%) with aging | | | | | | | | |
|:---:|:---:|:---:|:---:|:---:|:---:|:---:|:---:|:---:|:---:|
| Time (years) | Median PGA | | | | Median PGD | | | | Dispersion β |
| | LS1 | LS2 | LS3 | LS4 | LS1 | LS2 | LS3 | LS4 | |
| 0.00 | 0.00 | 0.00 | 0.00 | 0.00 | 0.00 | 0.00 | 0.00 | 0.00 | 0.00 |
| 40.00 | 3.13 | 0.00 | 3.17 | 3.75 | 0.00 | 0.00 | 2.12 | 1.48 | 0.00 |
| 60.00 | 0.00 | 2.50 | 4.76 | 6.25 | 2.44 | 6.54 | 8.82 | 6.91 | 1.22 |
| 90.00 | 6.25 | 5.00 | 11.11 | 10.00 | 24.39 | 9.70 | 15.18 | 14.30 | 8.54 |

*Fragility curves in terms of PGA*



*Figure 64 Fragility curves in terms of PGA for Slight Damage*



*Figure 65 Fragility curves in terms of PGA for Moderate Damage*



*Figure 66 Fragility curves in terms of PGA for Extensive Damage*
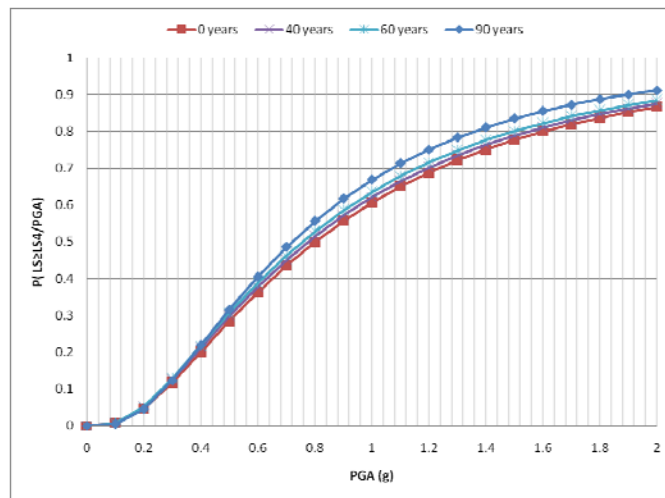
*Figure 67 Fragility curves in terms of PGA for Complete Damage*

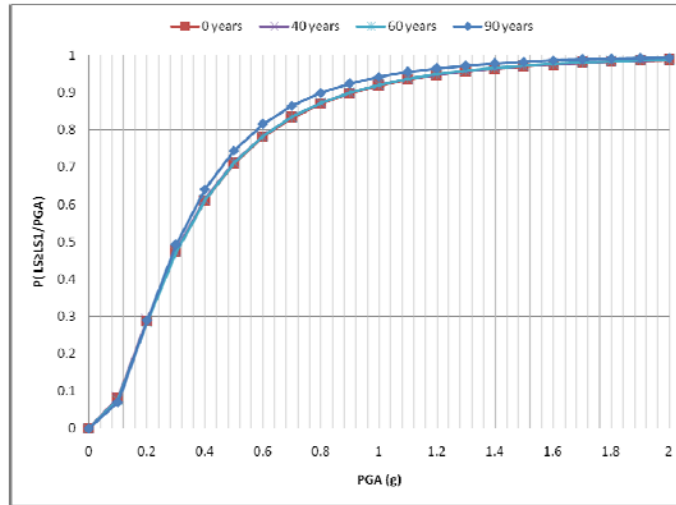*Fragility curves in terms of PGD*
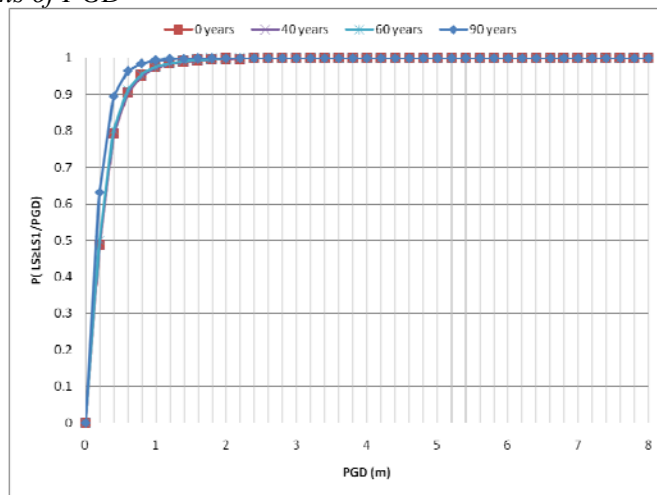


*Figure 68 Fragility curves in terms of PGD for Slight Damage*
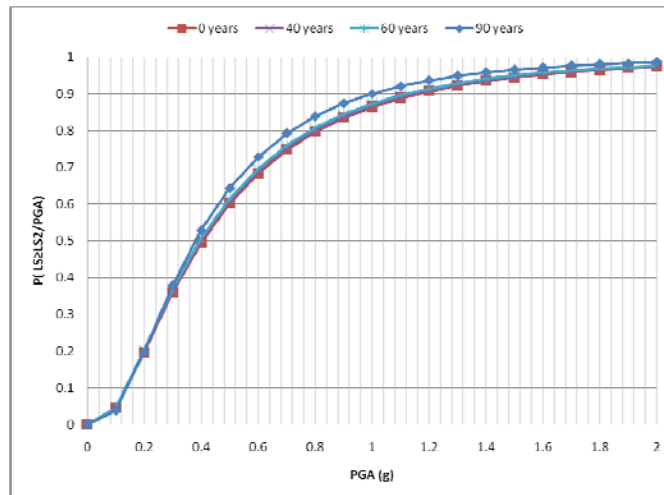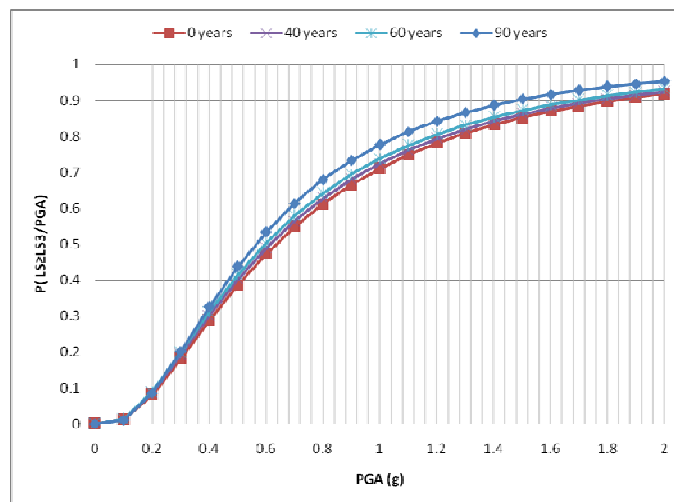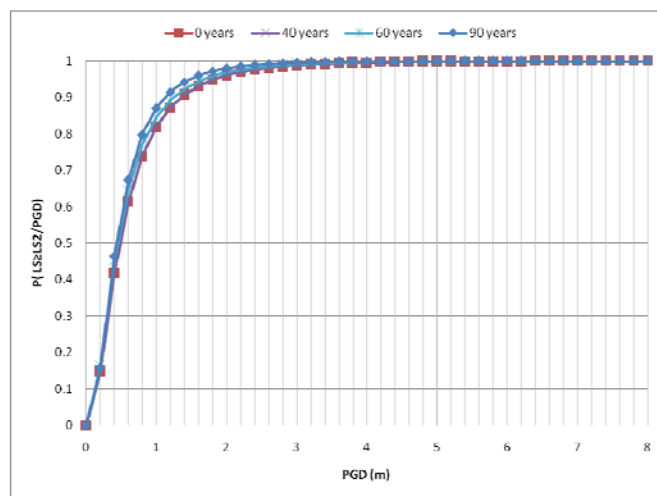


*Figure 69 Fragility curves in terms of PGD for Moderate Damage*
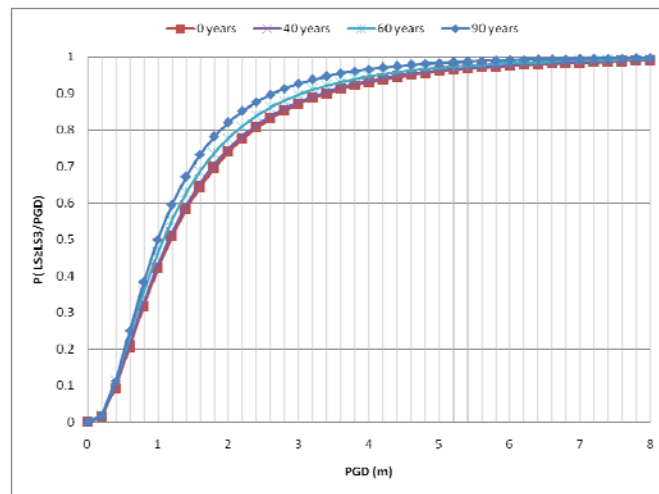
*Figure 70 Fragility curves in terms of PGD for Extensive Damage*
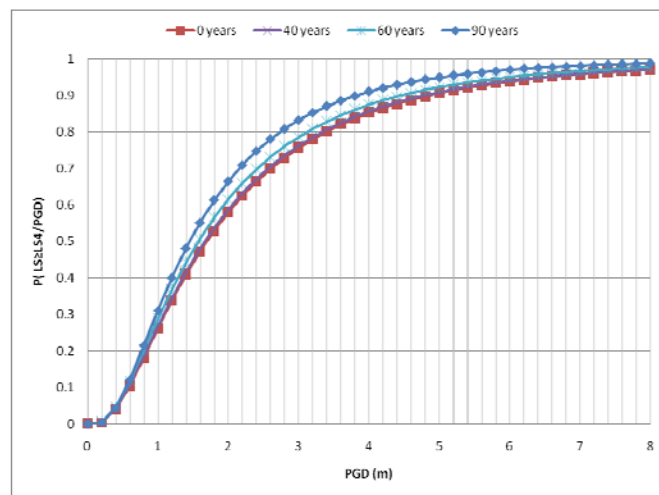


*Figure 71 Fragility curves in terms of PGD for Complete Damage*

**2$^{nd}$ order polynomial regression of median values of PGA vs time for each limit state**
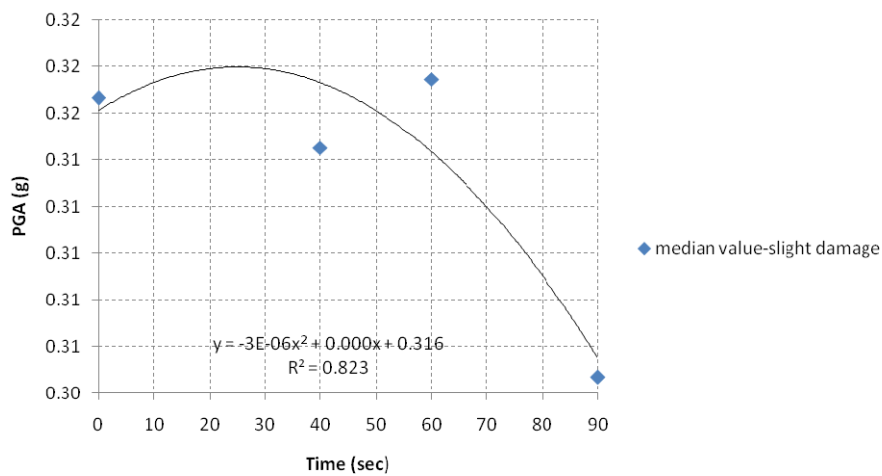


*Figure 72 Time-dependent quadratic fit of median values of PGA for the slight damage state*
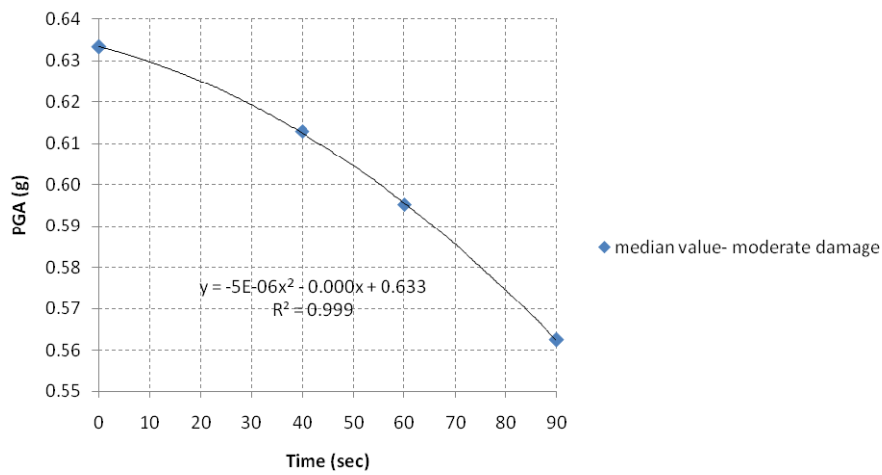
*Figure 73 Time-dependent quadratic fit of median values of PGA for the moderate damage state*
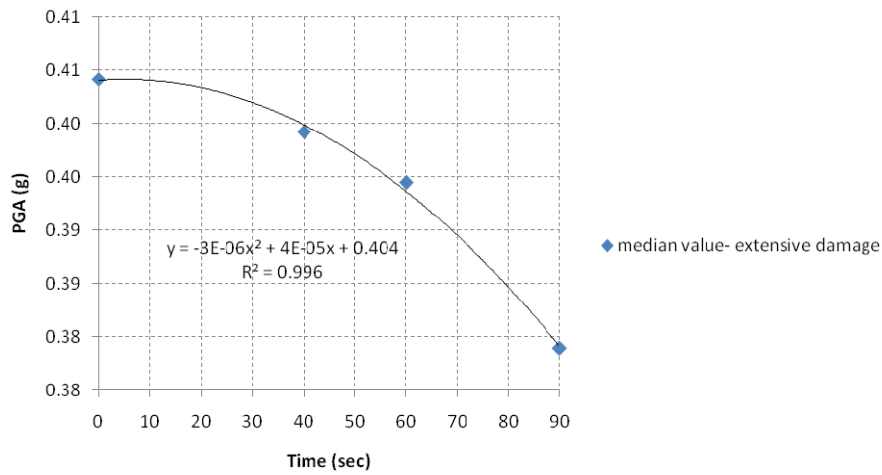


*Figure 74 Time-dependent quadratic fit of median values of PGA for the extensive damage state*
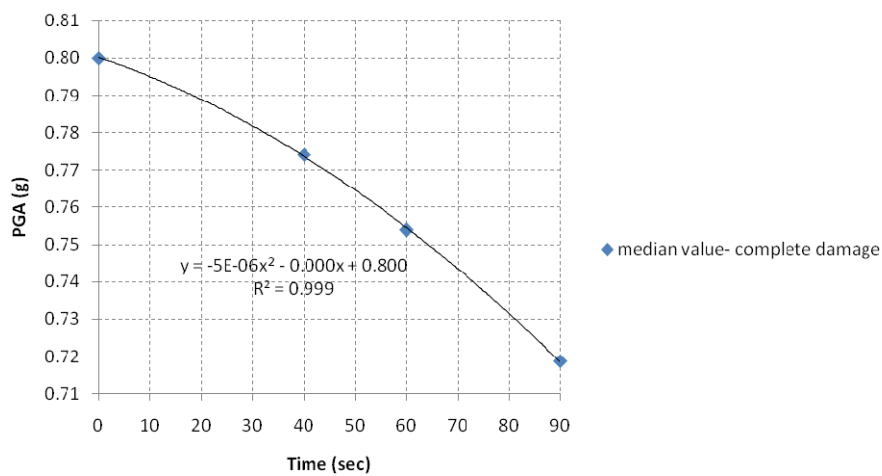


*Figure 75 Time-dependent quadratic fit of median values of PGA for the complete damage state*

*2^(nd) order polynomial regression of median values of PGD vs time for each limit state*
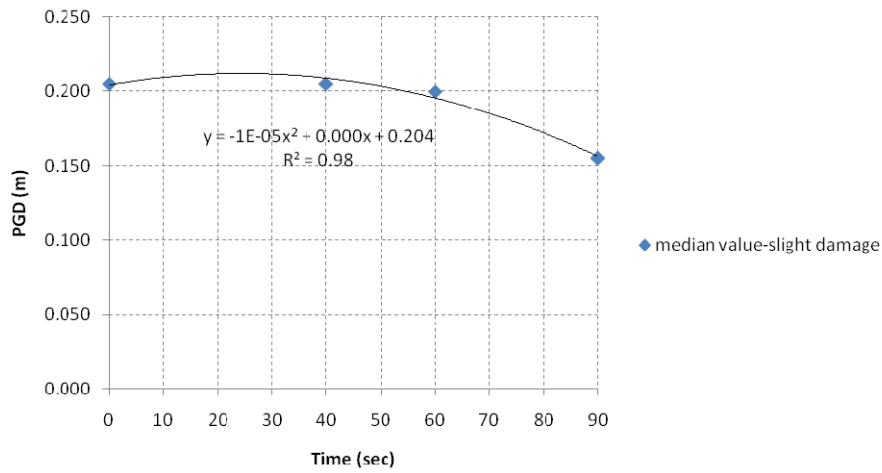


*Figure 76 Time-dependent quadratic fit of median values of PGD for the slight damage state*
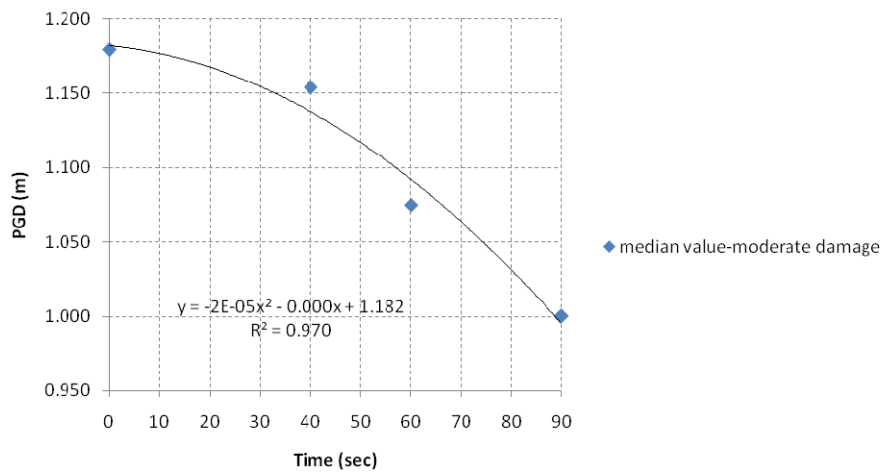


*Figure 77 Time-dependent quadratic fit of median values of PGD for the moderate damage state*
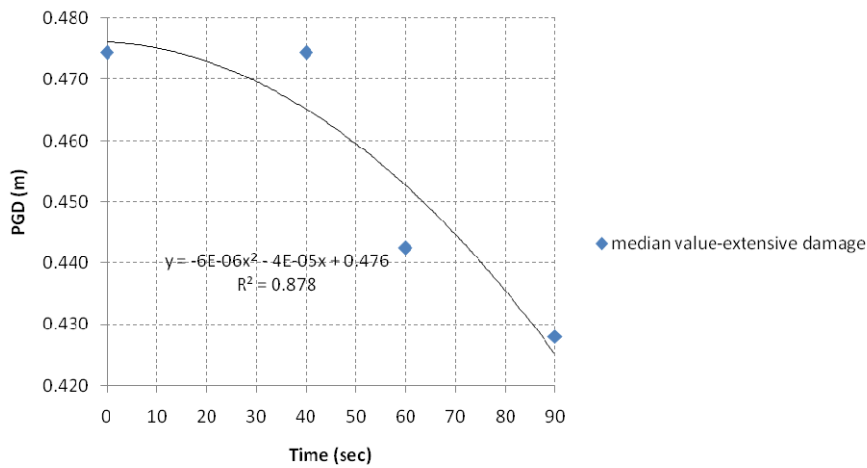
*Figure 78 Time-dependent quadratic fit of median values of PGD for the extensive damage state*
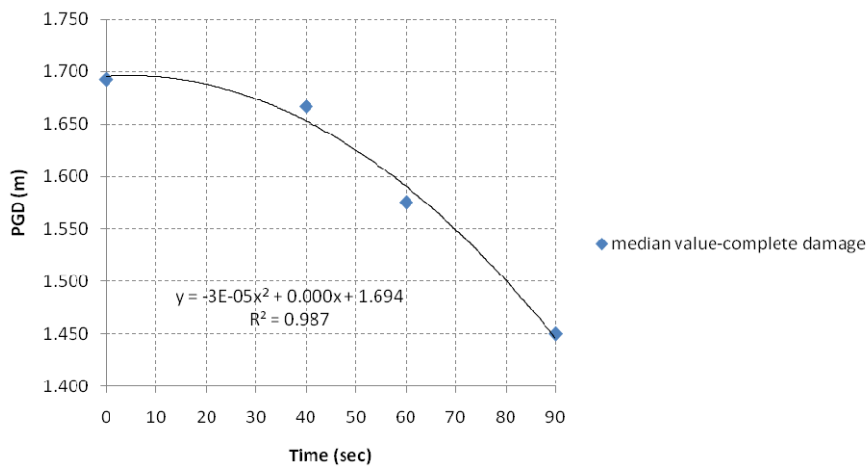


*Figure 79 Time-dependent quadratic fit of median values of PGD for the complete damage state*

## Fragility surfaces as a function of PGA
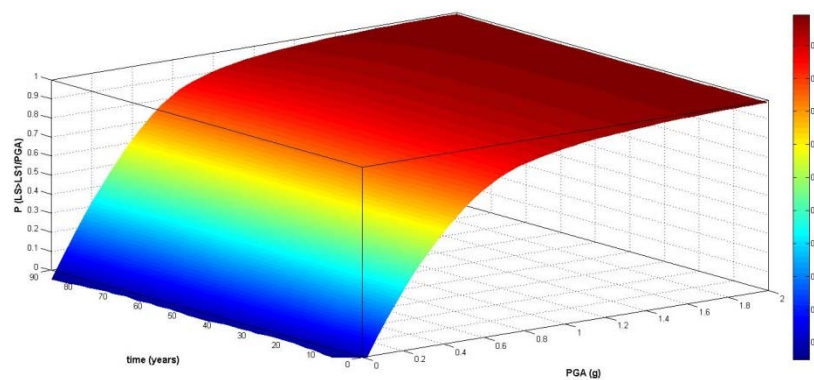


*Figure 80 Fragility surface as a function of PGA for Slight Damage (fit: Locally weighted smoothing quadratic regression)*
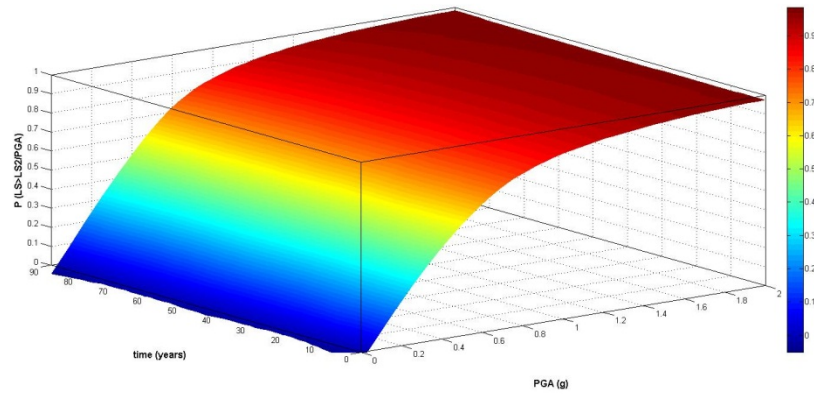
*Figure 81 Fragility surface as a function of PGA for Moderate Damage (fit: Locally weighted smoothing quadratic regression)*
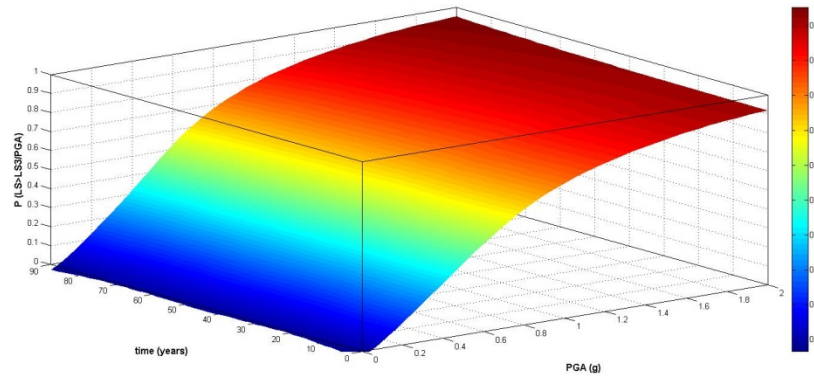


*Figure 82 Fragility surface as a function of PGA for Extensive Damage (fit: Locally weighted smoothing quadratic regression)*
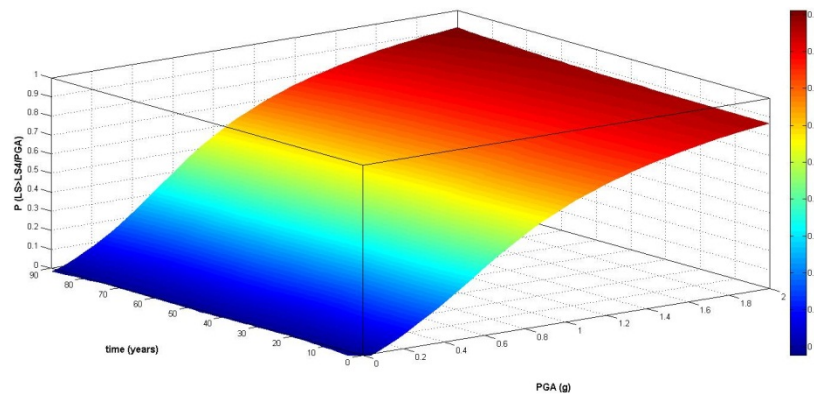


*Figure 83 Fragility surface as a function of PGA for Complete Damage (fit: Locally weighted smoothing quadratic regression)*

*Fragility surfaces as a function of PGD*
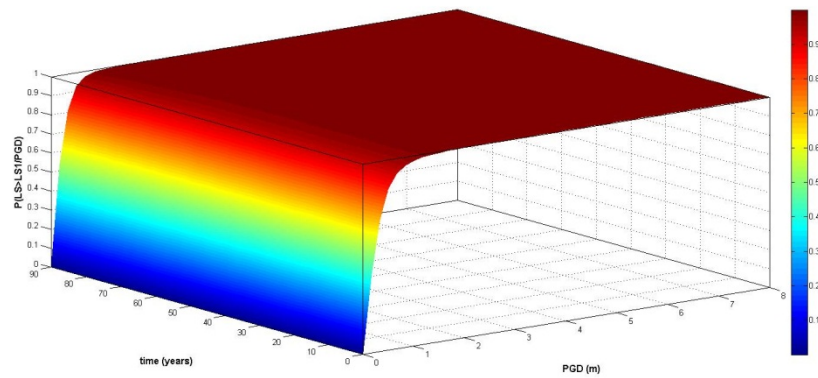


*Figure 84 Fragility surface as a function of PGD for Slight Damage (fit: Interpolant)*
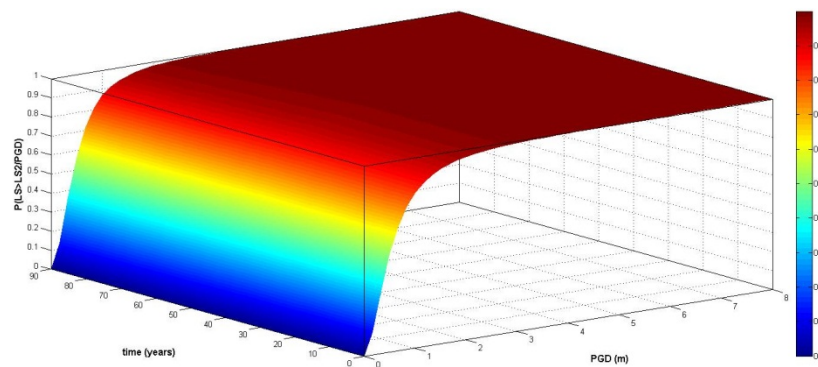


*Figure 85 Fragility surface as a function of PGD for Moderate Damage (fit: Interpolant)*
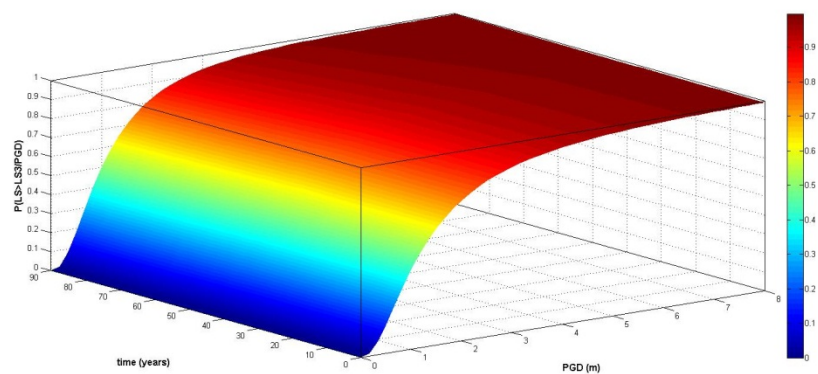


*Figure 86 Fragility surface as a function of PGD for Extensive Damage (fit: Interpolant)*
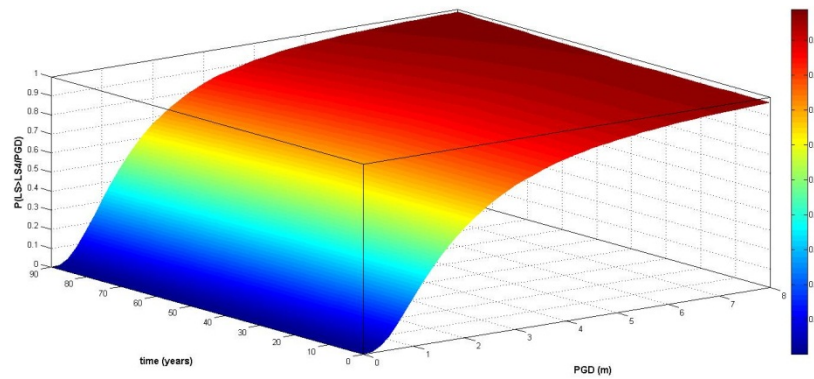
*Figure 87 Fragility surface as a function of PGD for Complete Damage (fit: Interpolant)*

### *Building with stiff foundation system*

*Table 54 Parameters of fragility functions for buildings with stiff foundation system*

| time (years) | Median PGA (g) | | | | Median PGD (m) | | | | Dispersion β |
|---|---|---|---|---|---|---|---|---|---|
| | LS1 | LS2 | LS3 | LS4 | LS1 | LS2 | LS3 | LS4 | |
| 0 | 0.35 | 0.59 | 1.23 | 1.70 | 0.205 | 0.474 | 1.179 | 1.692 | 0.74 |
| 40 | 0.36 | 0.59 | 1.18 | 1.62 | 0.205 | 0.270 | 1.120 | 1.622 | 0.76 |
| 60 | 0.33 | 0.55 | 1.11 | 1.33 | 0.200 | 0.245 | 0.980 | 1.333 | 0.76 |
| 90 | 0.33 | 0.53 | 1.04 | 1.48 | 0.155 | 0.265 | 1.040 | 1.478 | 0.74 |

*Table 55 Percent (%) Changes in Median PGA/PGD and dispersion β values with aging for buildings with stiff foundation system*

| | Difference(%) | | | | | | | | |
|---|---|---|---|---|---|---|---|---|---|
| Time (years) | Median PGA | | | | Median PGD | | | | Dispersion β |
| | LS1 | LS2 | LS3 | LS4 | LS1 | LS2 | LS3 | LS4 | |
| 0 | 0.00 | 0.00 | 0.00 | 0.00 | 0.00 | 0.00 | 0.00 | 0.00 | 0.00 |
| 40 | -2.86 | 0.00 | 4.07 | 4.71 | 0.00 | 43.04 | 5.00 | 4.14 | -2.70 |
| 60 | 5.71 | 6.78 | 9.76 | 21.76 | 2.44 | 48.31 | 16.88 | 21.22 | -2.70 |

| | | | | | | | | | |
|---|---|---|---|---|---|---|---|---|---|
| 90 | 5.71 | 10.17 | 15.45 | 12.94 | 24.39 | 44.09 | 11.79 | 12.65 | 0.00 |

*Fragility curves in terms of PGA*
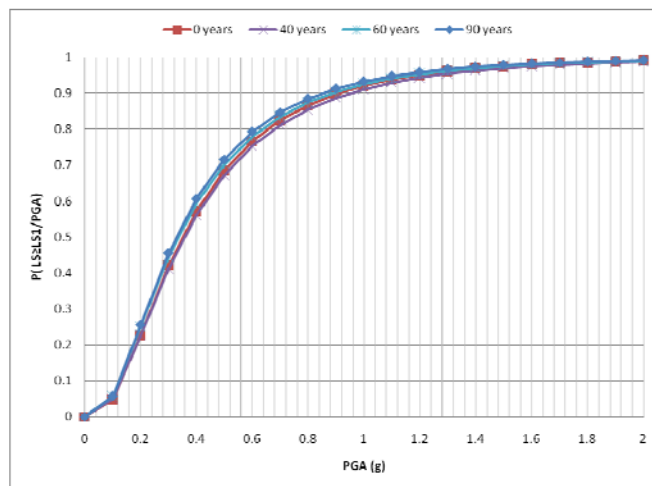


*Figure 88 Fragility curves in terms of PGA for Slight Damage*
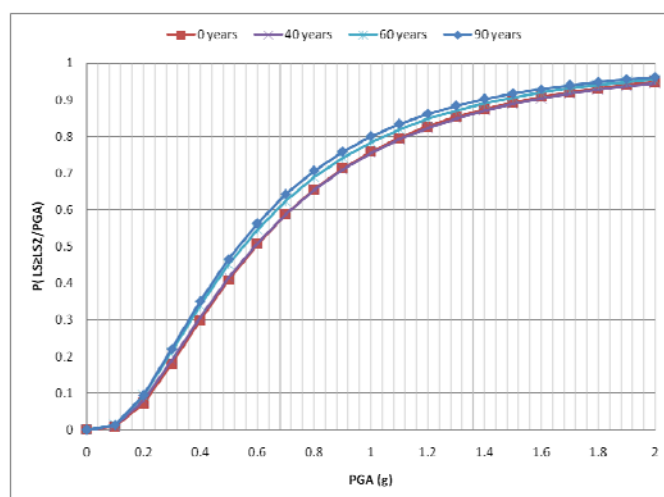


*Figure 89 Fragility curves in terms of PGA for Moderate Damage*
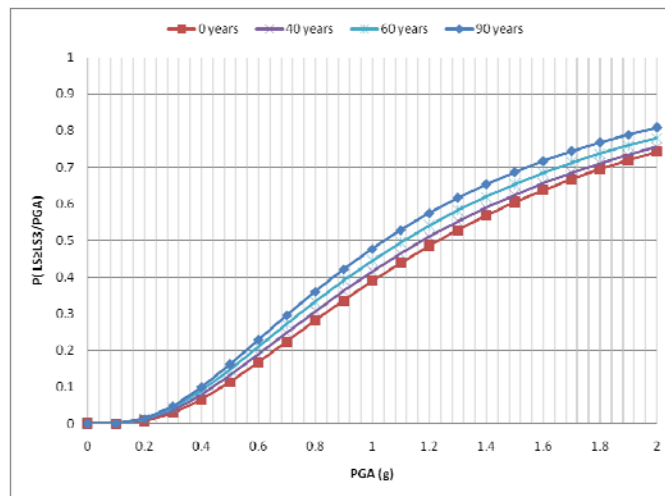
*Figure 90 Fragility curves in terms of PGA for Extensive Damage*
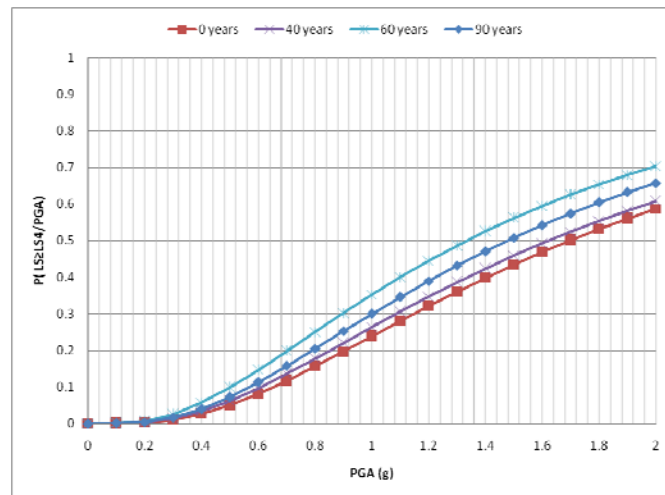


*Figure 91 Fragility curves in terms of PGA for Complete Damage*

*Fragility curves in terms of PGD*
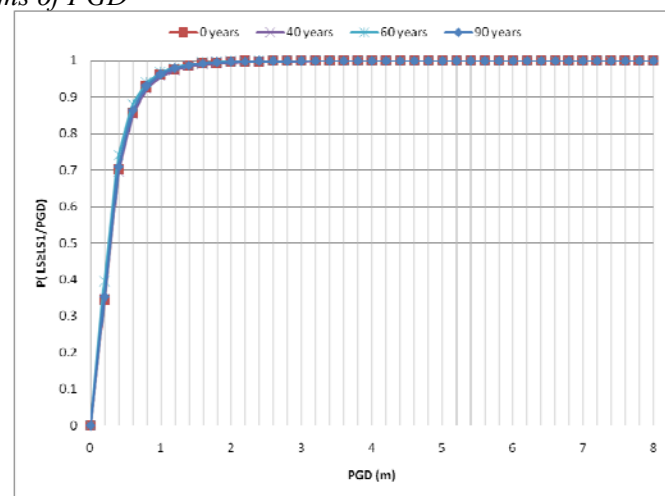


*Figure 92 Fragility curves in terms of PGD for Slight Damage*
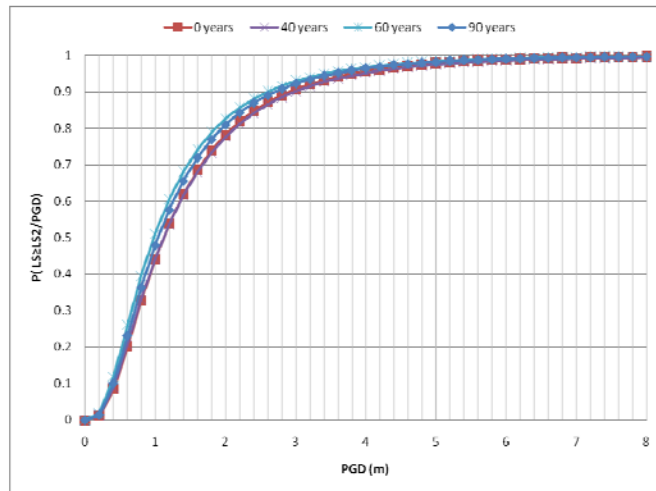
*Figure 93 Fragility curves in terms of PGD for Moderate Damage*



*Figure 94 Fragility curves in terms of PGD for Extensive Damage*



*Figure 95 Fragility curves in terms of PGD for Complete Damage*

*2$^{nd}$ order polynomial regression of median values of PGA vs time for each limit state*
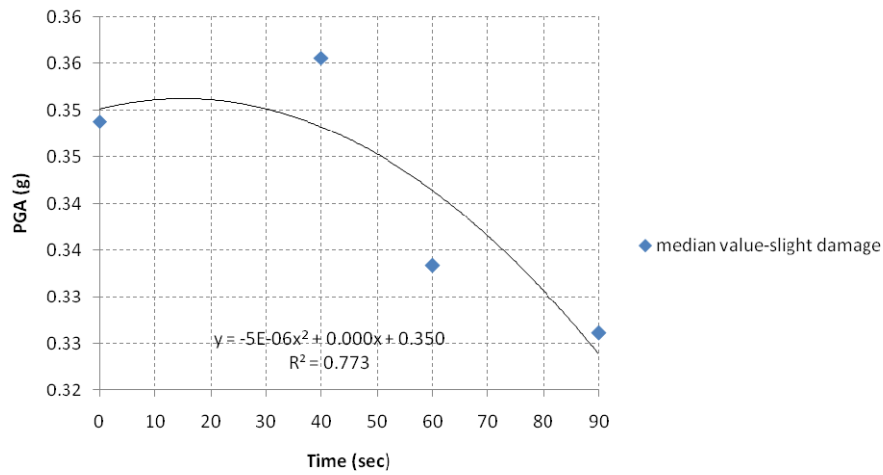


*Figure 96 Time-dependent quadratic fit of median values of PGA for the slight damage state*
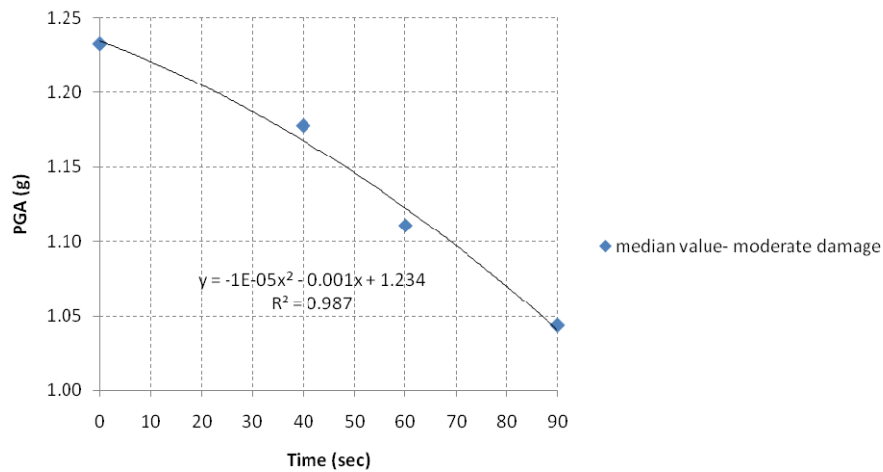


*Figure 97 Time-dependent quadratic fit of median values of PGA for the moderate damage state*
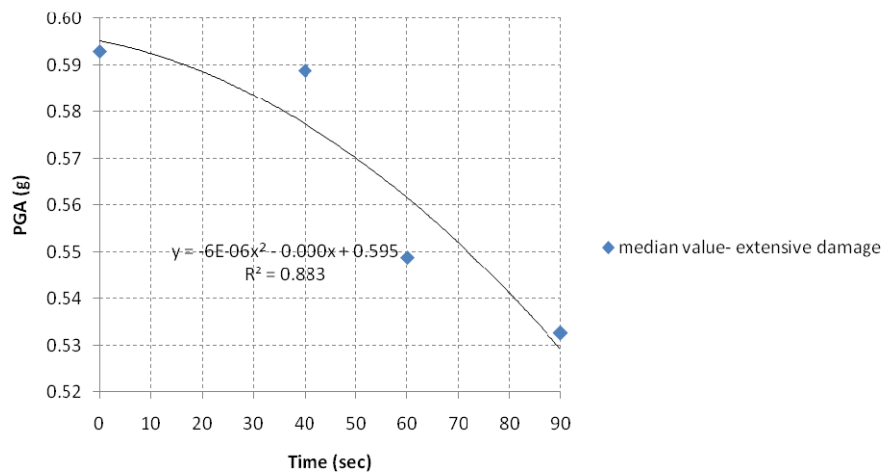
*Figure 98 Time-dependent quadratic fit of median values of PGA for the extensive damage state*
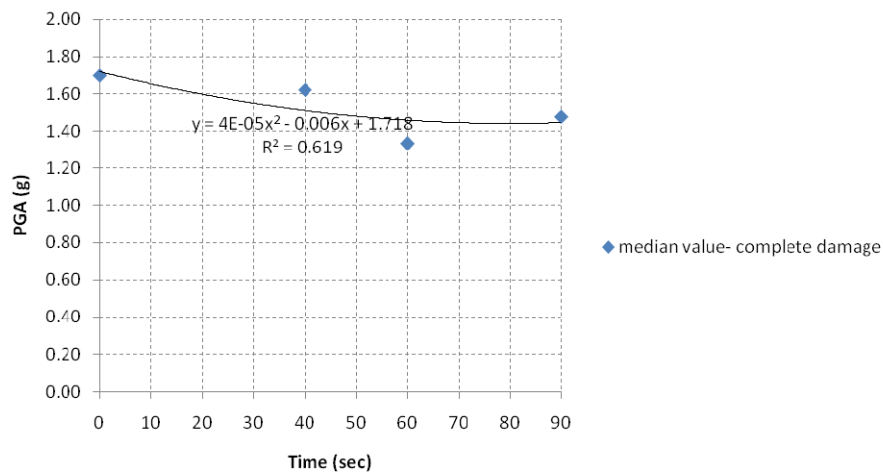


*Figure 99 Time-dependent quadratic fit of median values of PGA for the complete damage state*

**2$^{nd}$ order polynomial regression of median values of PGD vs time for each limit state**

*Figure 100 Time-dependent quadratic fit of median values of PGD for the slight damage state*



The equation shown: $y = 1E-05x^2 - 0.004x + 2.958$, $R^2 = 0.743$

*Figure 101 Time-dependent quadratic fit of median values of PGD for the moderate damage state*



The equation shown: $y = 9E-06x^2 - 0.002x + 1.130$, $R^2 = 0.469$

*Figure 102 Time-dependent quadratic fit of median values of PGD for the extensive damage state*



The equation shown: $y = 0.000x^2 - 0.017x + 4.116$, $R^2 = 0.373$
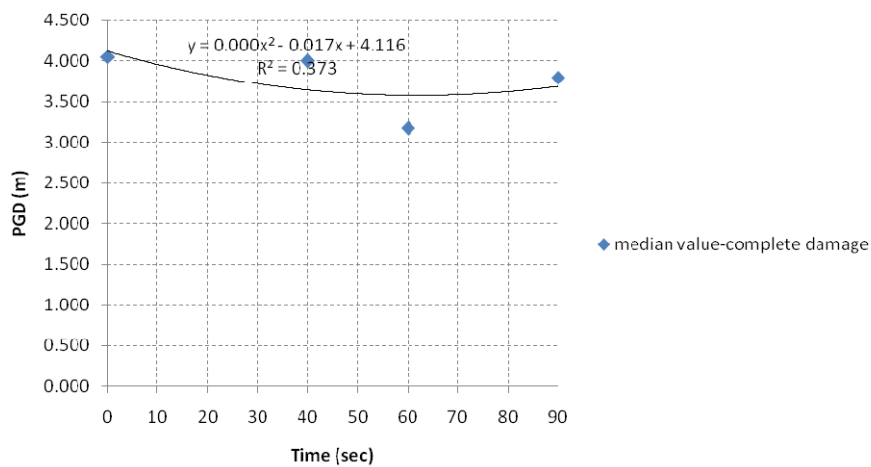
*Figure 103 Time-dependent quadratic fit of median values of PGD for the complete damage state*

*Fragility surfaces in terms of PGA*



Figure 104 Fragility surface as a function of PGA for Slight Damage (fit: Locally weighted smoothing quadratic regression)



Figure 105 Fragility surface as a function of PGA for Moderate Damage (fit: Locally weighted smoothing quadratic regression)



Figure 106 Fragility surface as a function of PGA for Extensive Damage (fit: Locally weighted smoothing quadratic regression)

*Figure 107 Fragility surface as a function of PGA for Complete Damage (fit: Locally weighted smoothing quadratic regression)*

*Fragility surfaces in terms of PGD*



*Figure 108 Fragility surface as a function of PGD for Slight Damage (fit: Interpolant)*



*Figure 109 Fragility surface as a function of PGD for Moderate Damage (fit: Interpolant)*

*Figure 110 Fragility surface as a function of PGD for Extensive Damage (fit: Interpolant)*



*Figure 111 Fragility surface as a function of PGD for Complete Damage (fit: Interpolant)*

### 5.2.3.3 Fragility functions for chloride induced corrosion of reinforcement

<u>Building with flexible foundation system</u>

*Table 56 Parameters of fragility functions for buildings with flexible foundation system*

| time | Median PGA (g) | | | | Median PGD (m) | | | | Dispersion |
|------|------|------|------|------|------|------|------|------|------|
| (years) | LS1 | LS2 | LS3 | LS4 | LS1 | LS2 | LS3 | LS4 | β |
| 0 | 0.32 | 0.40 | 0.63 | 0.80 | 0.21 | 0.47 | 1.18 | 1.69 | 0.82 |
| 20 | 0.31 | 0.38 | 0.55 | 0.70 | 0.13 | 0.36 | 0.95 | 1.45 | 0.79 |
| 40 | 0.25 | 0.36 | 0.46 | 0.61 | 0.12 | 0.32 | 0.68 | 1.17 | 0.79 |
| 60 | 0.18 | 0.32 | 0.44 | 0.63 | 0.17 | 0.31 | 0.62 | 1.14 | 0.74 |
| 90 | 0.14 | 0.30 | 0.35 | 0.41 | 0.04 | 0.13 | 0.32 | 0.54 | 0.73 |

*Table 57 Percent (%) Changes in Median PGA/PGD and dispersion β values with aging for buildings with flexible foundation system*

| Time | Median PGA | | | | Median PGD | | | | Dispersion |
|---|---|---|---|---|---|---|---|---|---|
| (years) | LS1 | LS2 | LS3 | LS4 | LS1 | LS2 | LS3 | LS4 | β |
| 0.00 | 0.00 | 0.00 | 0.00 | 0.00 | 0.00 | 0.00 | 0.00 | 0.00 | 0.00 |
| 20.00 | 3.13 | 5.00 | 12.70 | 12.50 | 38.10 | 23.40 | 19.49 | 14.20 | 3.66 |
| 40.00 | 21.88 | 10.00 | 26.98 | 23.75 | 42.86 | 31.91 | 42.37 | 30.77 | 3.66 |
| 60.00 | 43.75 | 20.00 | 30.16 | 21.25 | 19.05 | 34.04 | 47.46 | 32.54 | 9.76 |
| 90.00 | 56.25 | 25.00 | 44.44 | 48.75 | 80.95 | 72.34 | 72.88 | 68.05 | 10.98 |

*Fragility curves in terms of PGA*



*Figure 112 Fragility curves in terms of PGA for Slight Damage*

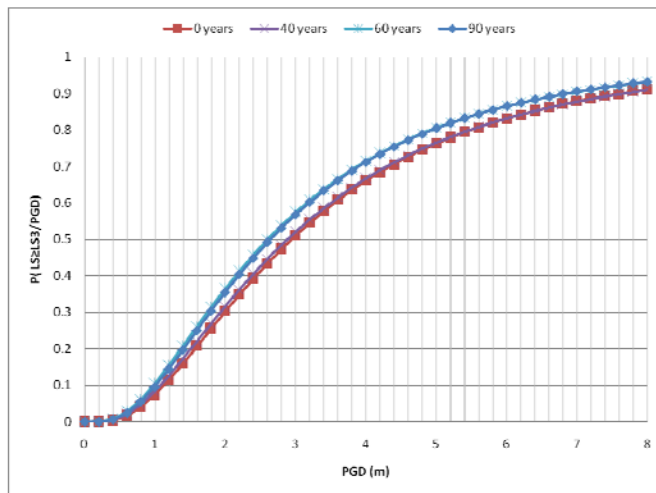*Figure 113 Fragility curves in terms of PGA for Moderate Damage*



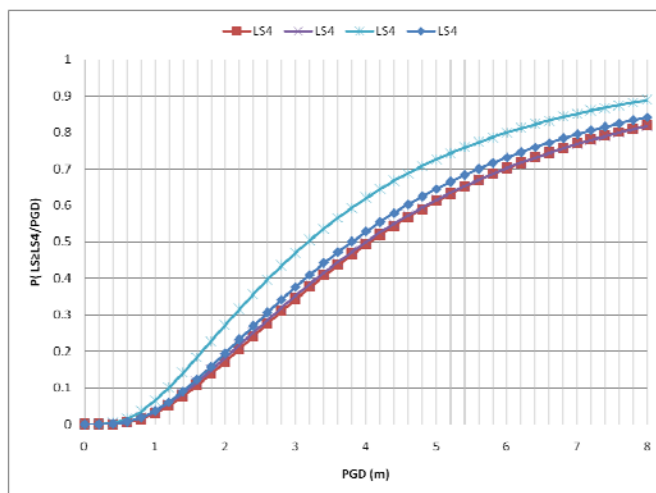*Figure 114 Fragility curves in terms of PGA for Extensive Damage*



*Figure 115 Fragility curves in terms of PGA for Complete Damage*

*Fragility curves in terms of PGD*
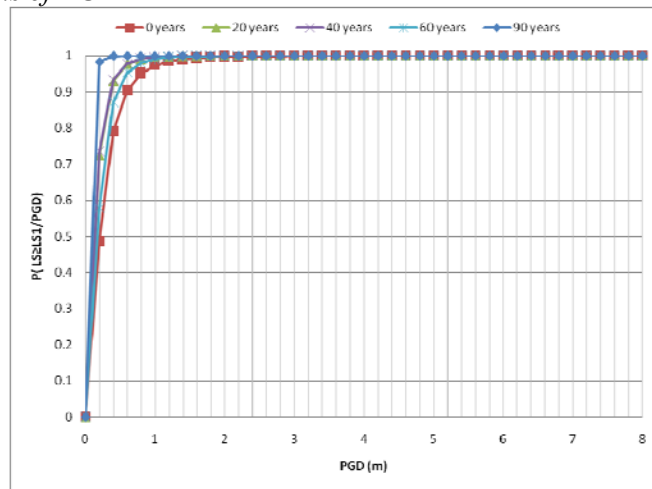


*Figure 116 Fragility curves in terms of PGD for Slight Damage*
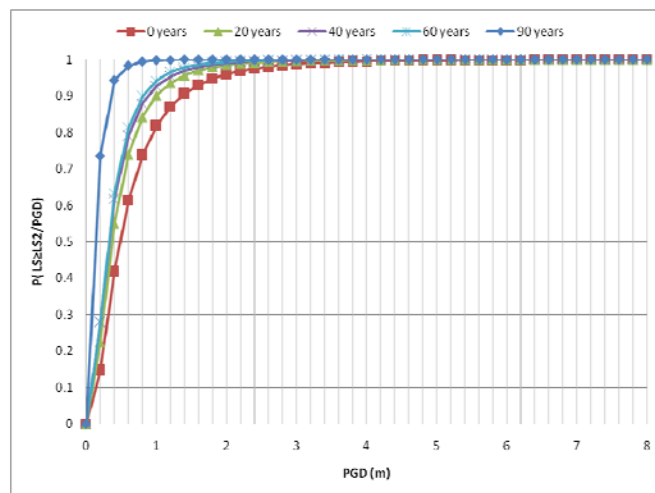


*Figure 117 Fragility curves in terms of PGD for Moderate Damage*
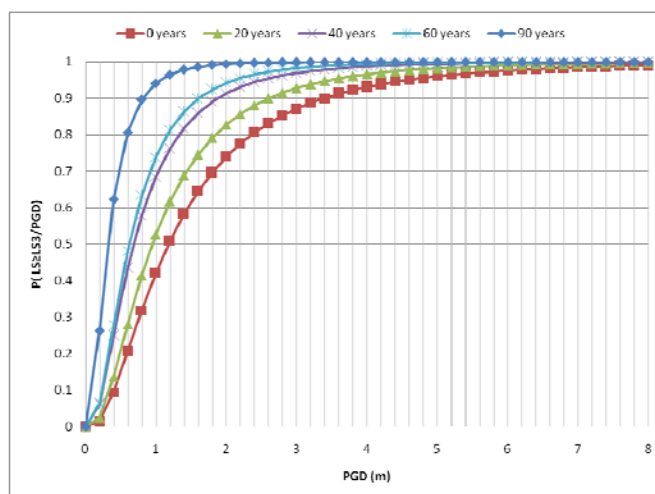
*Figure 118 Fragility curves in terms of PGD for Extensive Damage*
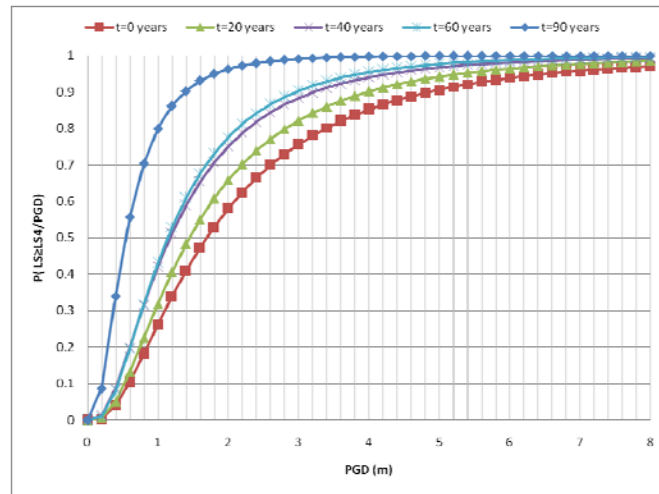


*Figure 119 Fragility curves in terms of PGD for Complete Damage*

**$2^{nd}$ order polynomial regression of median values of PGA vs time for each limit state**



$$y = -2E-06x^2 - 0.002x + 0.328$$
$$R^2 = 0.953$$
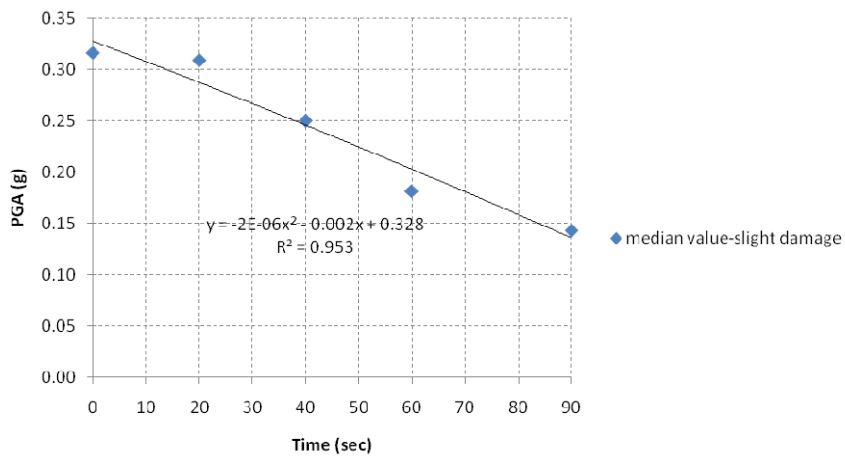
*Figure 120 Time-dependent quadratic fit of median values of PGA for the slight damage state*



$$y = 1E-05x^2 - 0.004x + 0.631$$
$$R^2 = 0.990$$
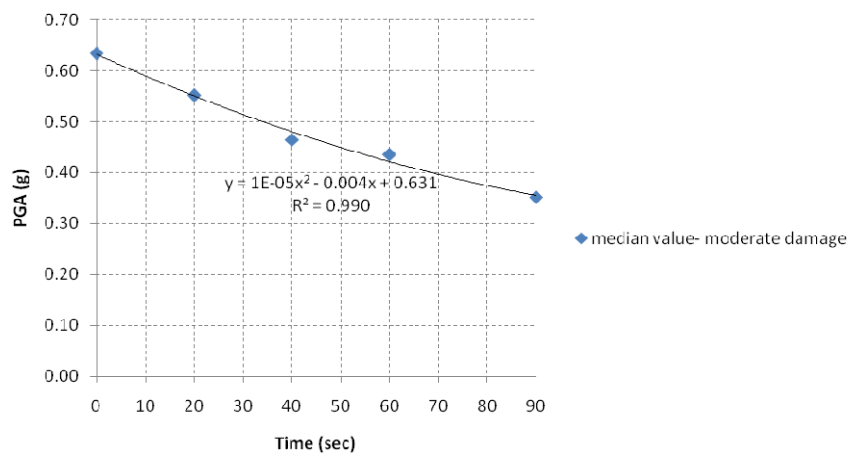
*Figure 121 Time-dependent quadratic fit of median values of PGA for the moderate damage state*
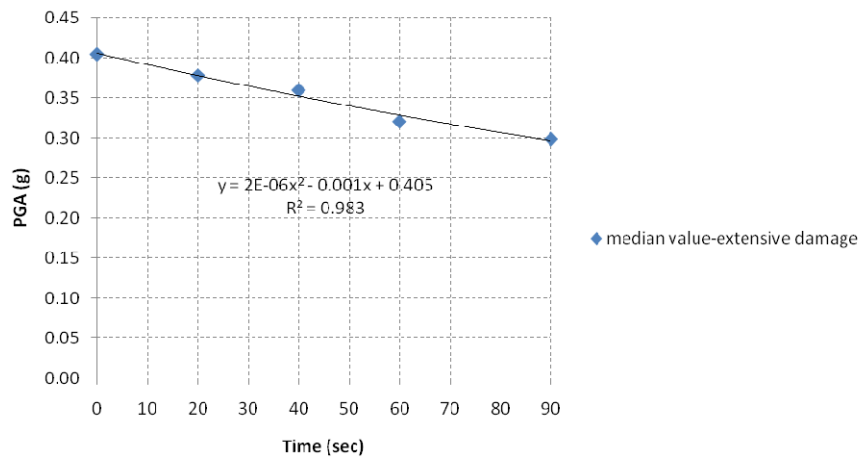
*Figure 122 Time-dependent quadratic fit of median values of PGA for the extensive damage state*
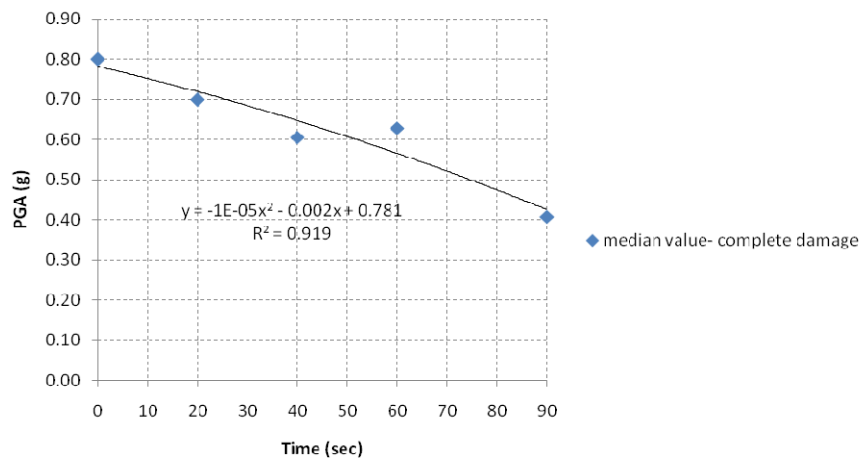


*Figure 123 Time-dependent quadratic fit of median values of PGA for the complete damage state*

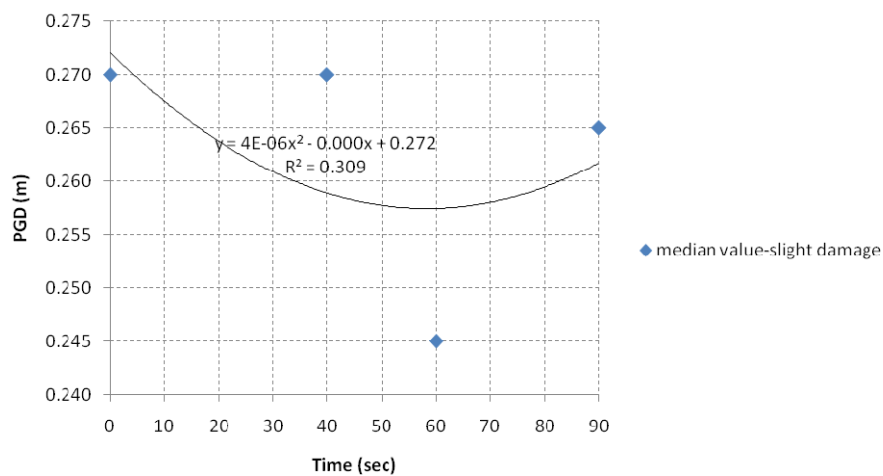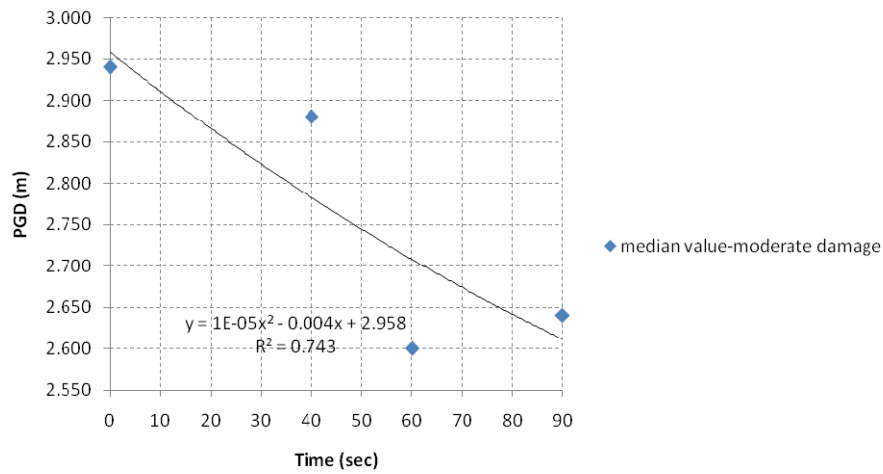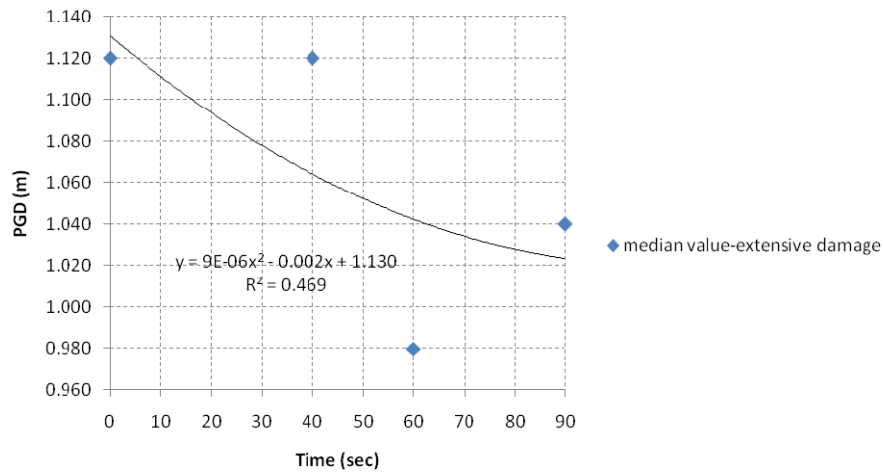*2$^{nd}$ order polynomial regression of median values of PGA vs time for each limit state*
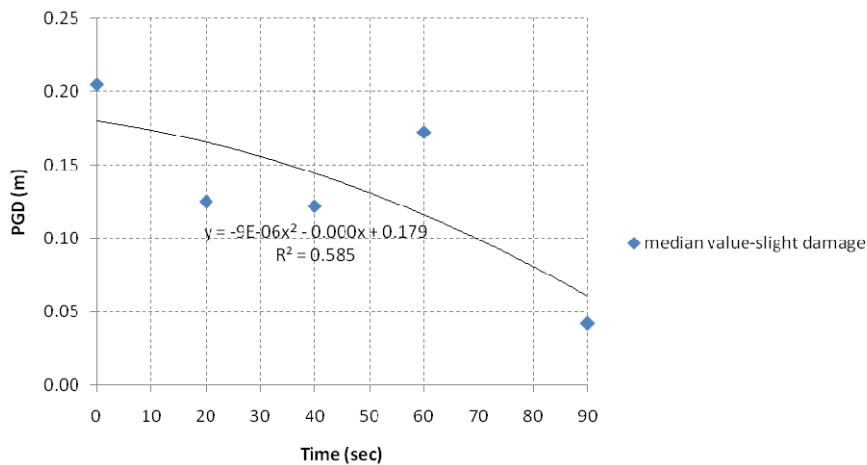


*Figure 124 Time-dependent quadratic fit of median values of PGD for the slight damage state*
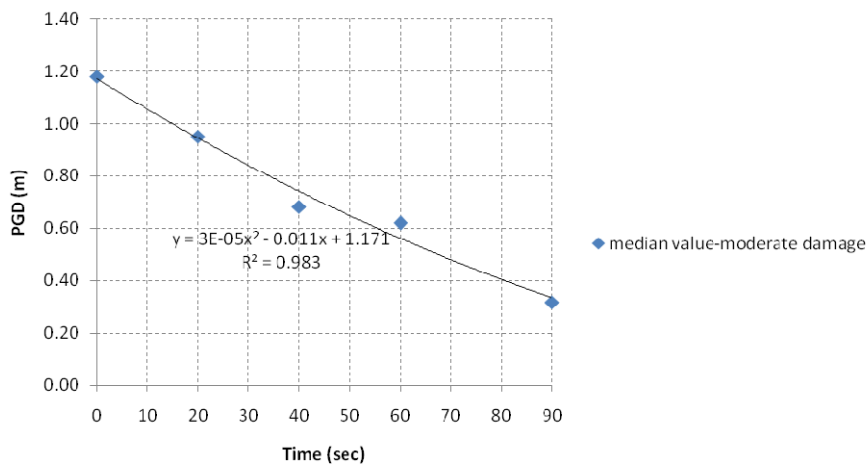
*Figure 125 Time-dependent quadratic fit of median values of PGD for the moderate damage state*
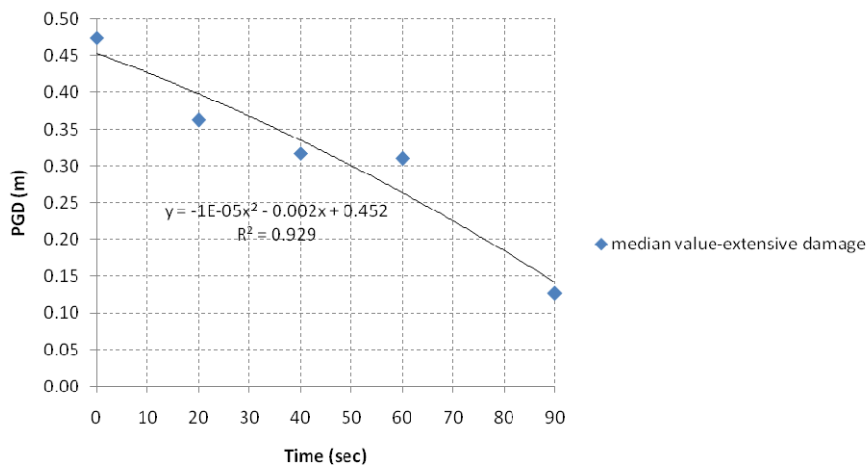


*Figure 126 Time-dependent quadratic fit of median values of PGD for the extensive damage state*
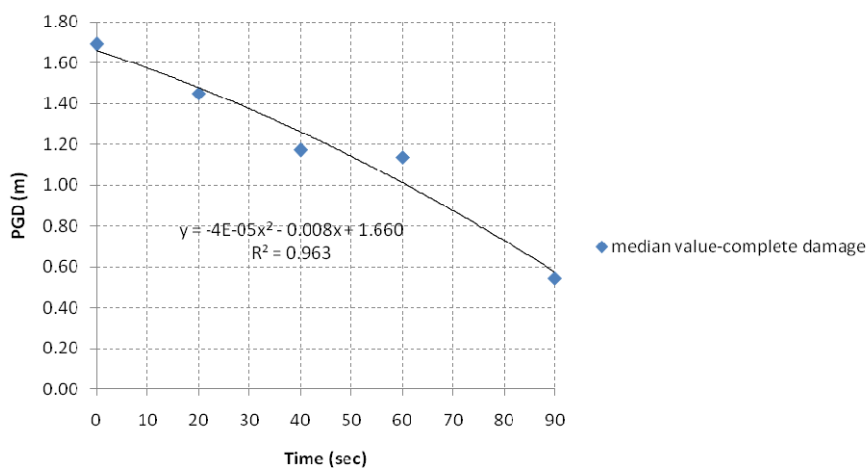


*Figure 127 Time-dependent quadratic fit of median values of PGD for the complete damage state*
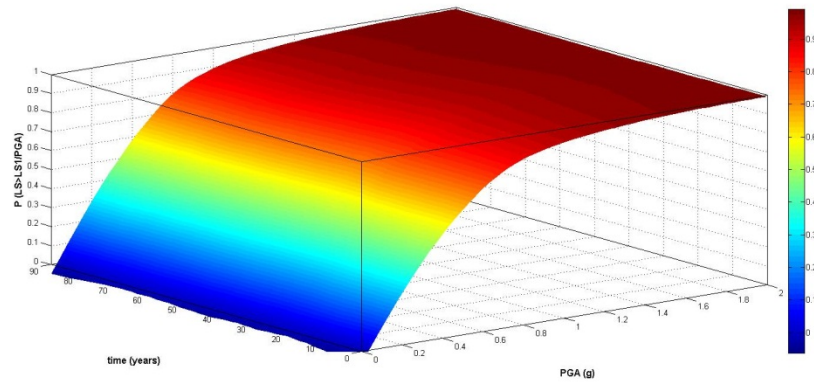
*Fragility surfaces in terms of PGA*
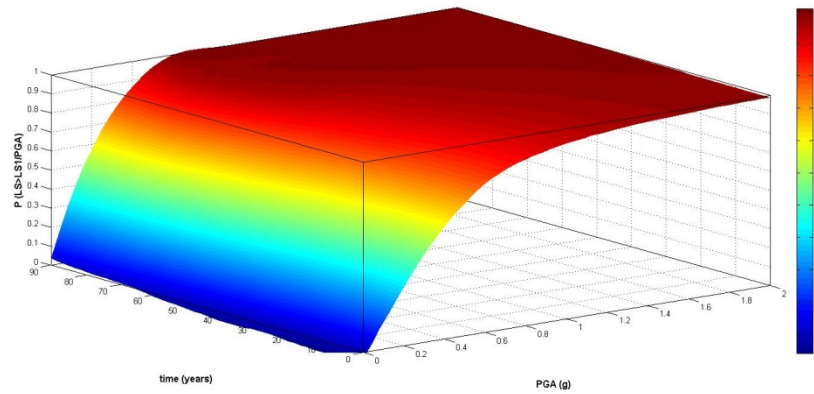


*Figure 128 Fragility surface as a function of PGA for Slight Damage (fit: Locally weighted smoothing quadratic regression)*
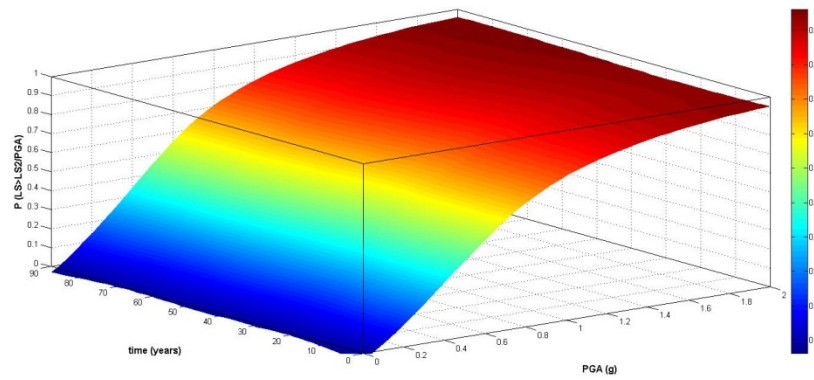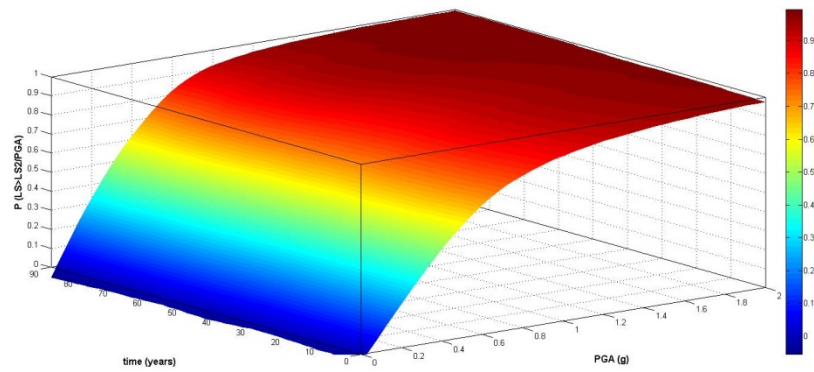


*Figure 129 Fragility surface as a function of PGA for Moderate Damage (fit: Locally weighted smoothing quadratic regression)*
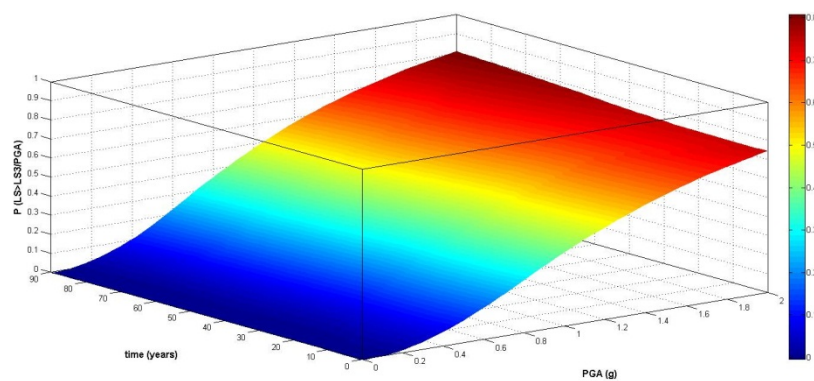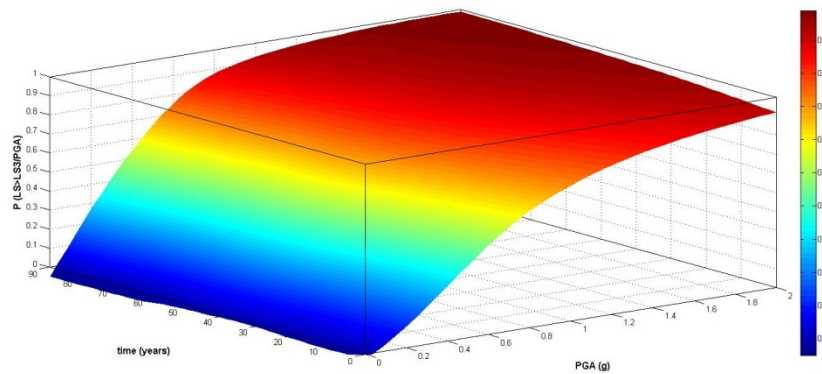


*Figure 130 Fragility surface as a function of PGA for Extensive Damage (fit: Locally weighted smoothing quadratic regression)*
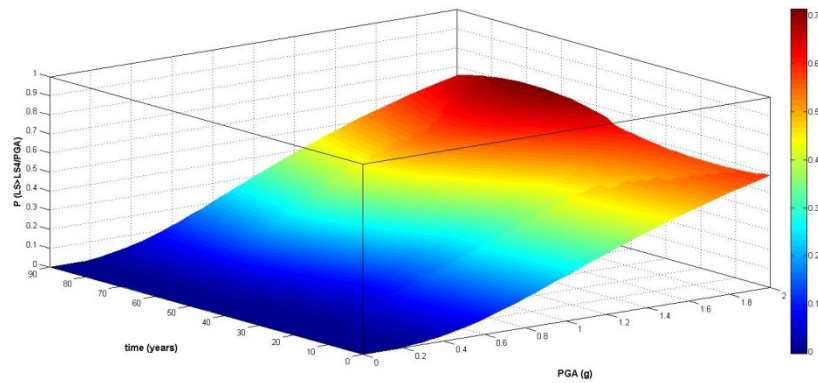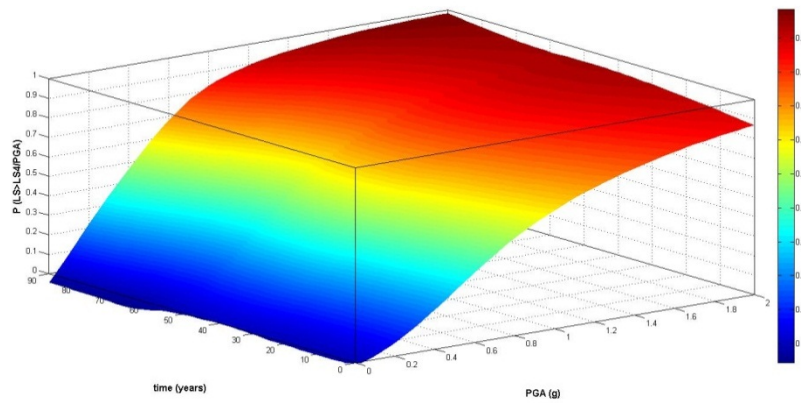
*Figure 131 Fragility surface as a function of PGA for Complete Damage (fit: Locally weighted smoothing quadratic regression)*
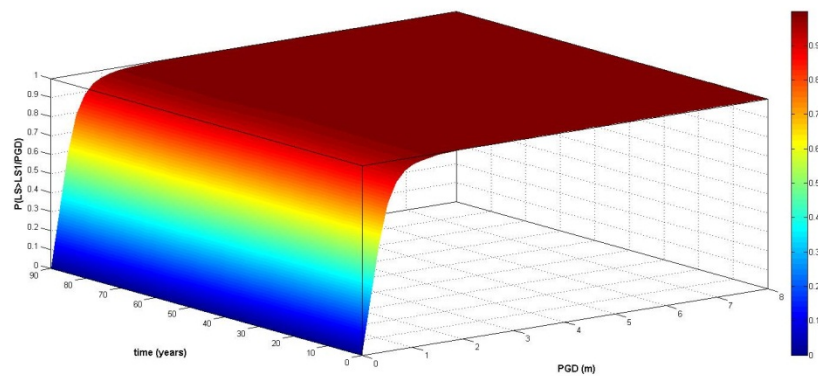
*Fragility surfaces in terms of PGD*
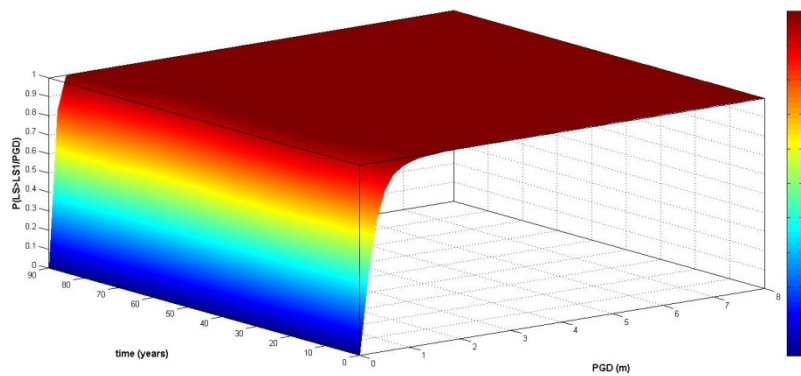


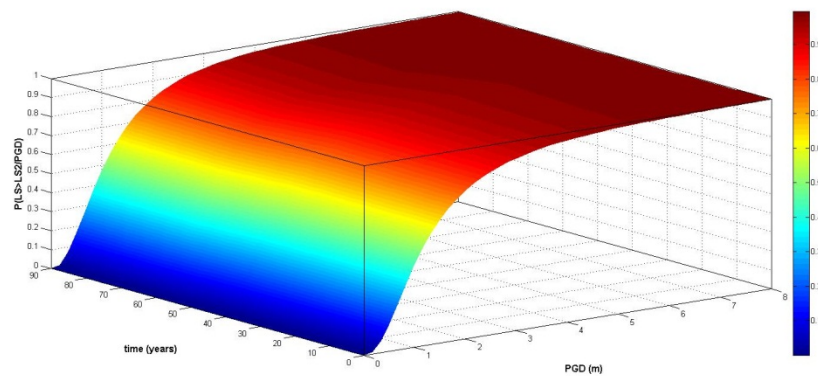*Figure 132 Fragility surface as a function of PGD for Slight Damage (fit: Interpolant)*
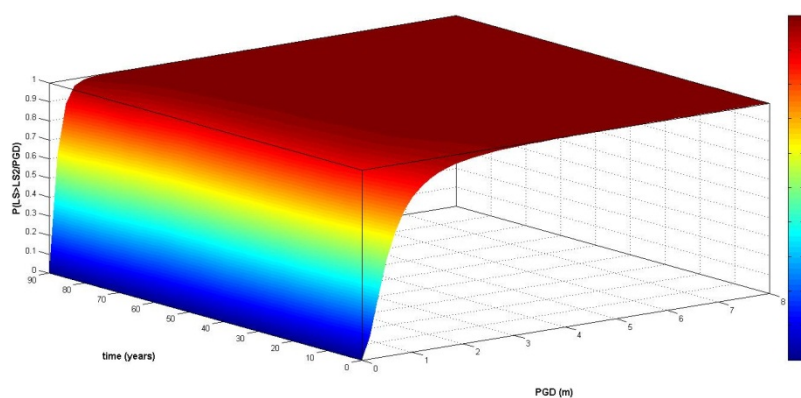


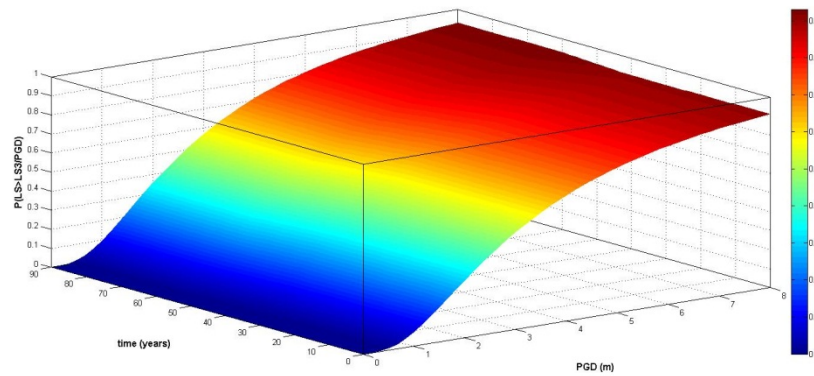*Figure 133 Fragility surface as a function of PGD for Moderate Damage (fit: Interpolant)*
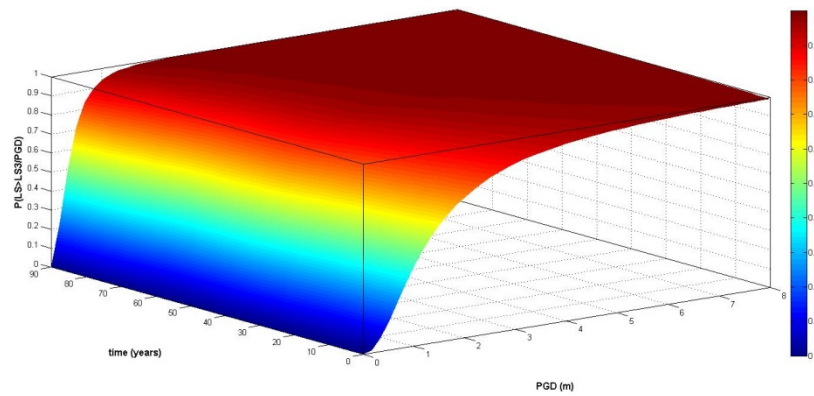
*Figure 134 Fragility surface as a function of PGD for Extensive Damage (fit: Interpolant)*
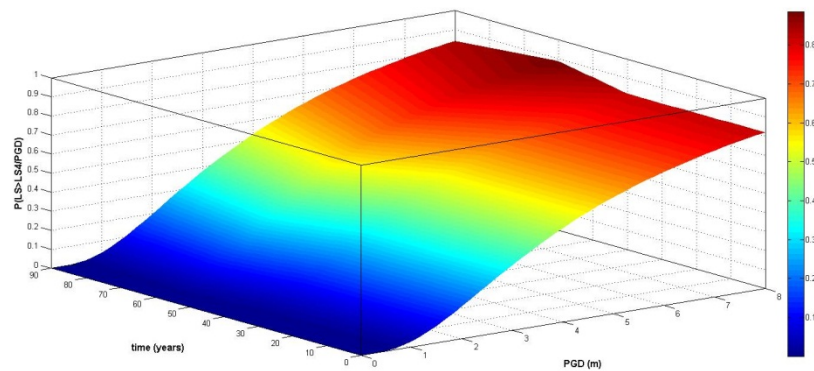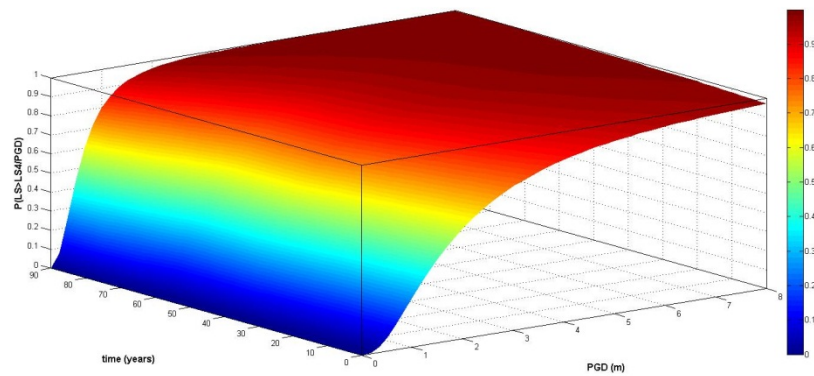


*Figure 135 Fragility surface as a function of PGD for Complete Damage (fit: Interpolant)*

### Building with stiff foundation system

*Table 58 Parameters of fragility functions for buildings with stiff foundation system*

| Time (years) | Median PGA (g) | | | | Median PGD (m) | | | | Dispersion β |
|---|---|---|---|---|---|---|---|---|---|
| | LS1 | LS2 | LS3 | LS4 | LS1 | LS2 | LS3 | LS4 | |
| 0 | 0.35 | 0.59 | 1.23 | 1.70 | 0.27 | 1.12 | 2.94 | 4.06 | 0.74 |
| 20 | 0.33 | 0.54 | 1.07 | 1.51 | 0.27 | 1.02 | 2.64 | 3.79 | 0.77 |
| 40 | 0.33 | 0.51 | 0.86 | 1.33 | 0.22 | 1.10 | 2.23 | 3.58 | 0.80 |
| 60 | 0.33 | 0.43 | 0.65 | 1.03 | 0.29 | 0.66 | 1.41 | 2.49 | 0.82 |
| 90 | 0.31 | 0.41 | 0.64 | 0.90 | 0.21 | 0.73 | 1.44 | 2.00 | 0.82 |

*Table 59 Percent (%) Changes in Median PGA/PGD and dispersion β values with aging for buildings with stiff foundation system*

| Time (years) | Change (%) with aging | | | | | | | | Dispersion β |
| | Median PGA | | | | Median PGD | | | | |
| | LS1 | LS2 | LS3 | LS4 | LS1 | LS2 | LS3 | LS4 | |
|---|---|---|---|---|---|---|---|---|---|
| 0 | 0.00 | 0.00 | 0.00 | 0.00 | 0.00 | 0.00 | 0.00 | 0.00 | 0.00 |
| 20 | 5.71 | 8.47 | 13.01 | 11.18 | 0.00 | 8.93 | 10.20 | 6.65 | -4.05 |
| 40 | 5.71 | 13.56 | 30.08 | 21.76 | 18.52 | 1.79 | 24.15 | 11.82 | -8.11 |
| 60 | 5.71 | 27.12 | 47.15 | 39.41 | -7.41 | 41.07 | 52.04 | 38.67 | -10.81 |
| 90 | 11.43 | 30.51 | 47.97 | 47.06 | 22.22 | 34.82 | 51.02 | 50.74 | -10.81 |

*Fragility curves in terms of PGA*
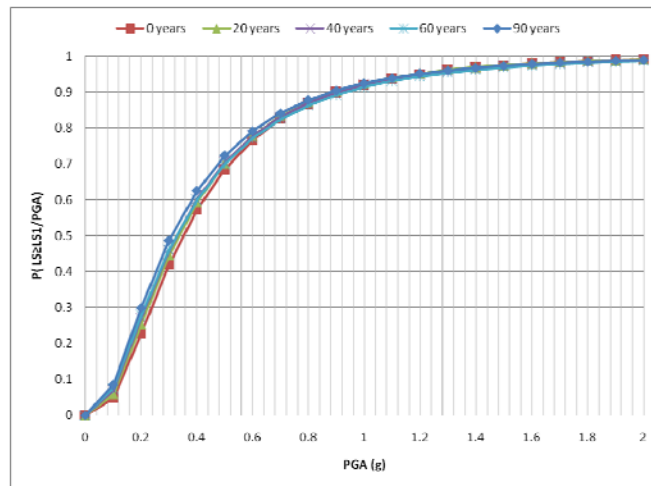


*Figure 136 Fragility curves in terms of PGA for Slight Damage*
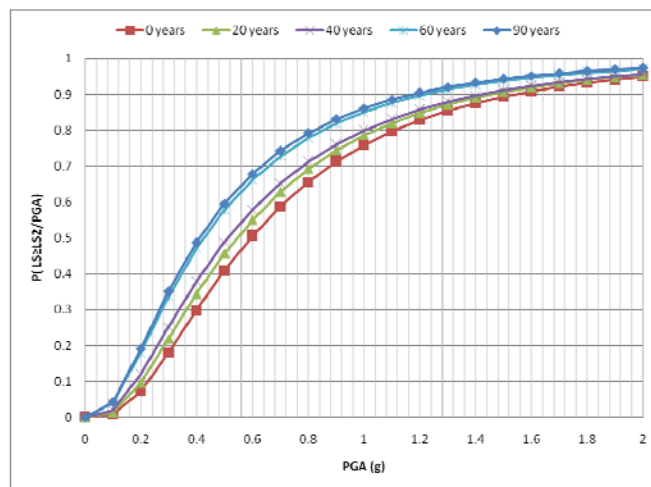


*Figure 137 Fragility curves in terms of PGA for Moderate Damage*
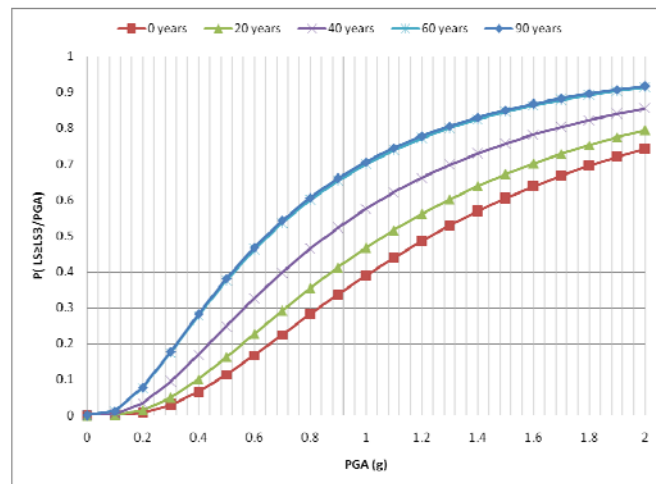
*Figure 138 Fragility curves in terms of PGA for Extensive Damage*
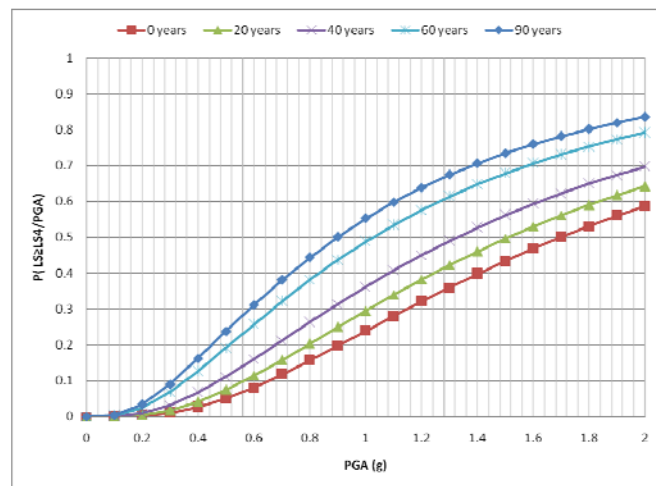


*Figure 139 Fragility curves in terms of PGA for Complete Damage*

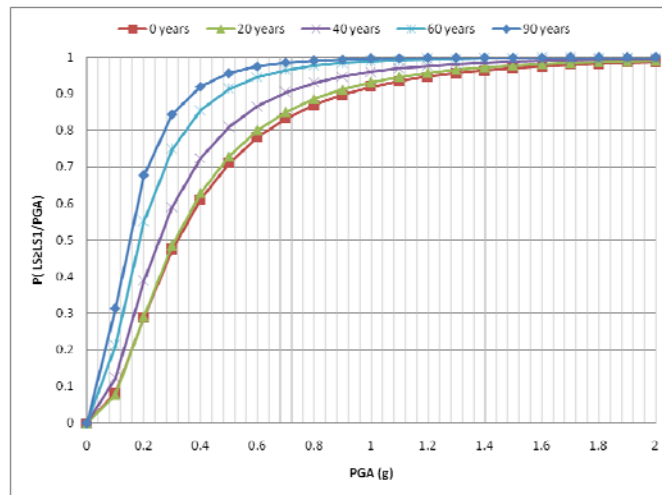*Fragility curves in terms of PGD*
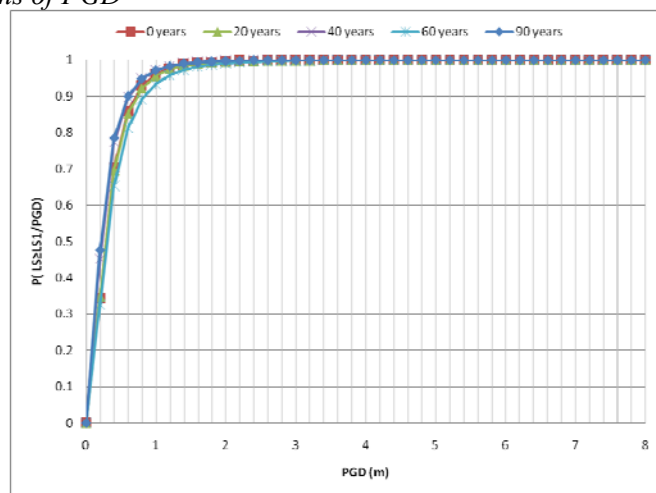


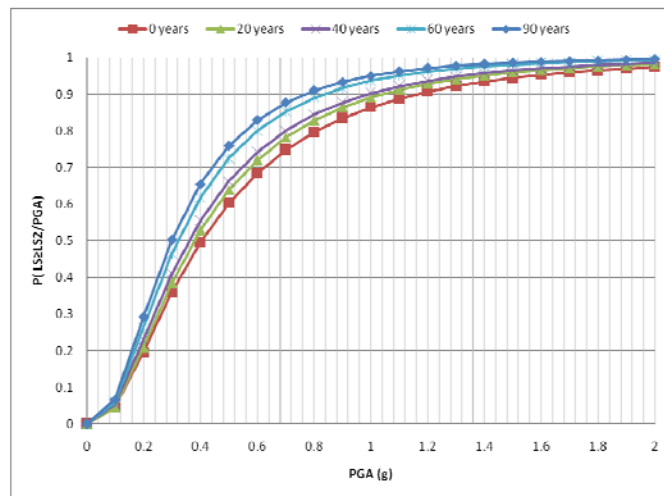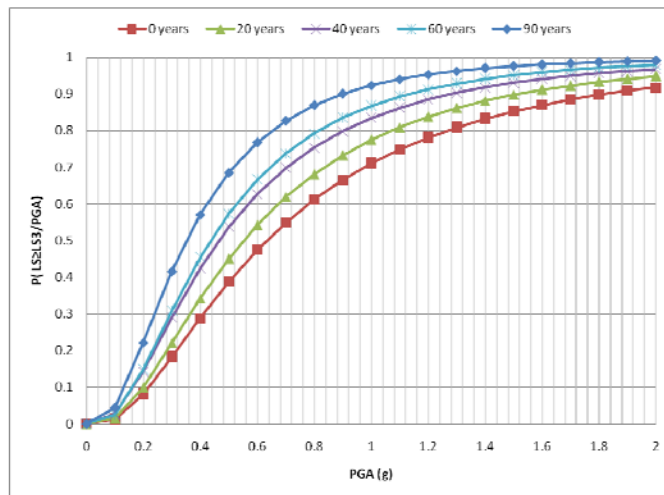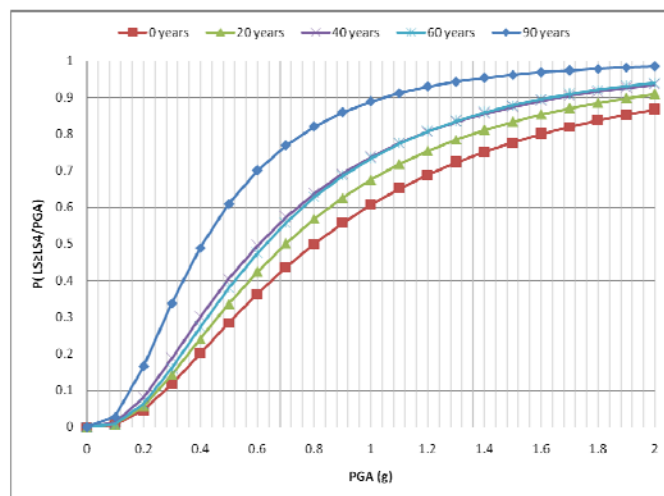*Figure 140 Fragility curves in terms of PGD for Slight Damage*
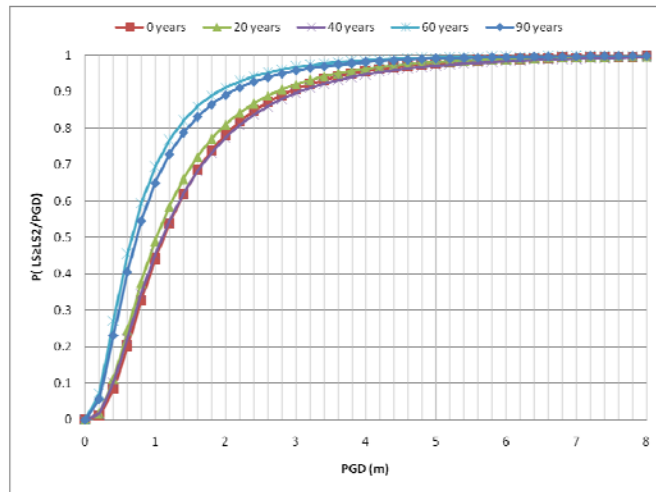
*Figure 141 Fragility curves in terms of PGD for Moderate Damage*
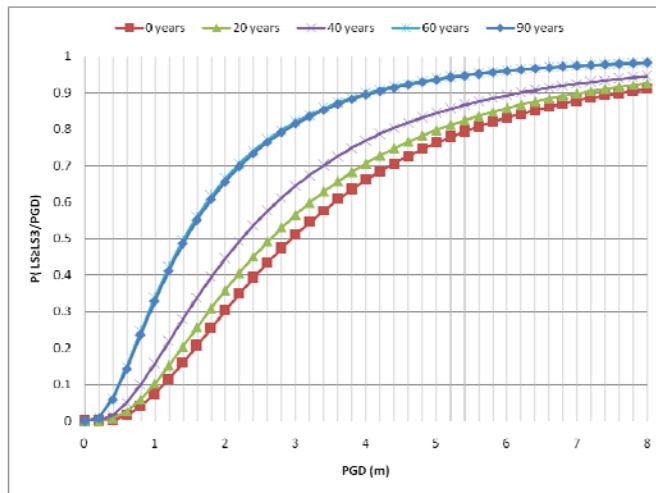


*Figure 142 Fragility curves in terms of PGD for Extensive Damage*
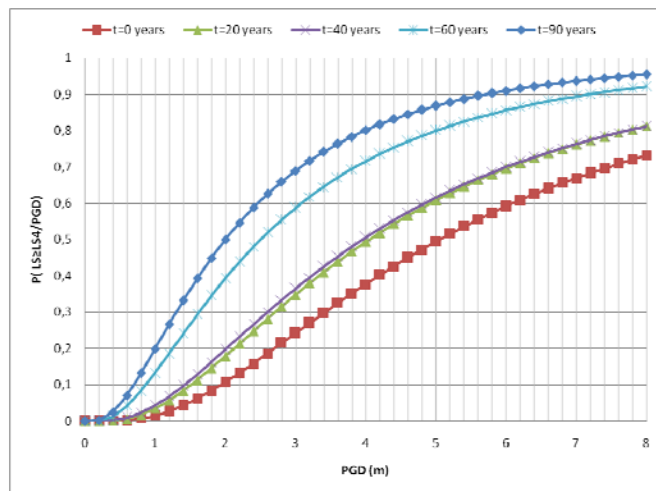


*Figure 143 Fragility curves in terms of PGD for Complete Damage*

*2$^{nd}$ order polynomial regression of median values of PGA vs time for each limit state*
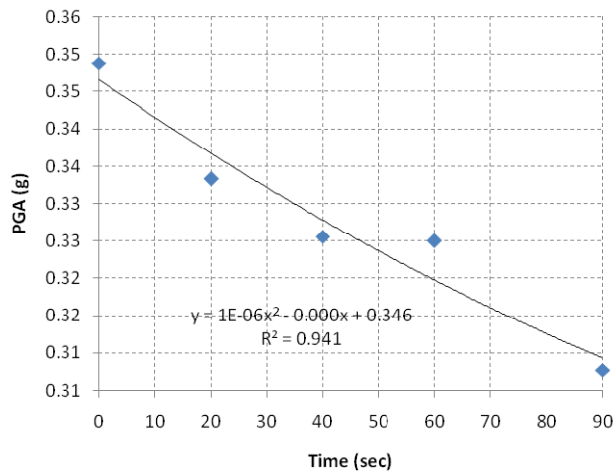


*Figure 144 Time-dependent quadratic fit of median values of PGA for the slight damage state*
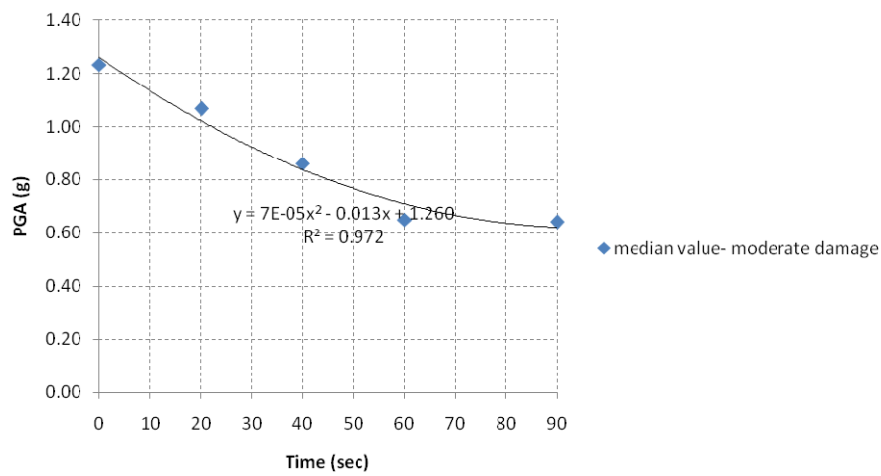


*Figure 145 Time-dependent quadratic fit of median values of PGA for the moderate damage state*
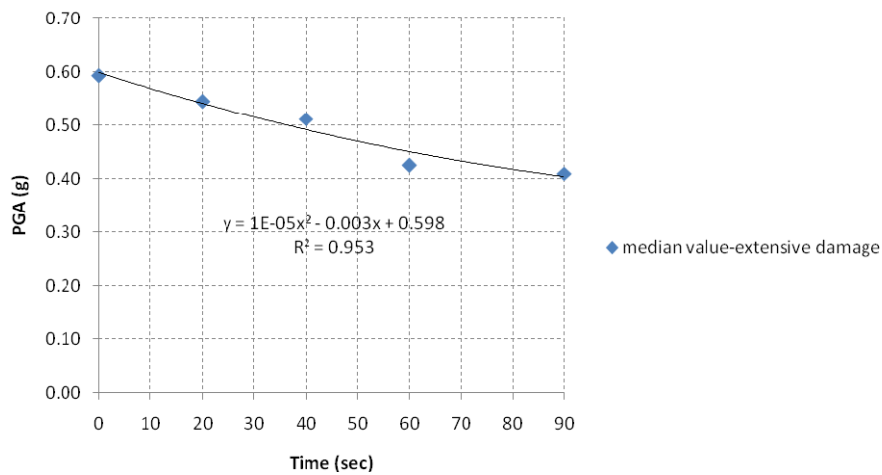
*Figure 146 Time-dependent quadratic fit of median values of PGA for the extensive damage state*
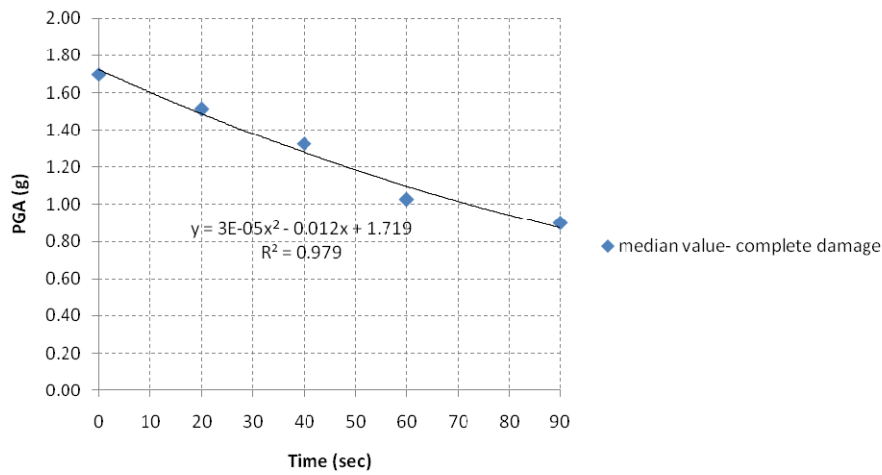


*Figure 147 Time-dependent quadratic fit of median values of PGA for the complete damage state*

*2nd order polynomial regression of median values of PGD vs time for each limit state*
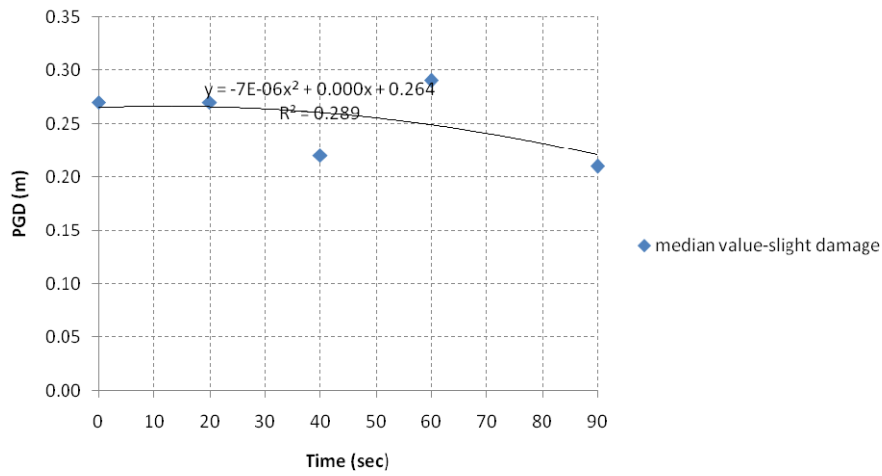


*Figure 148 Time-dependent quadratic fit of median values of PGD for the slight damage state*
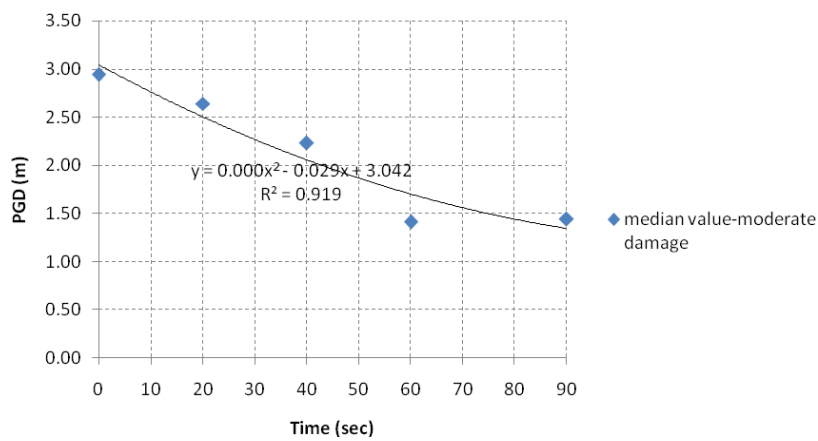


*Figure 149 Time-dependent quadratic fit of median values of PGD for the moderate damage state*
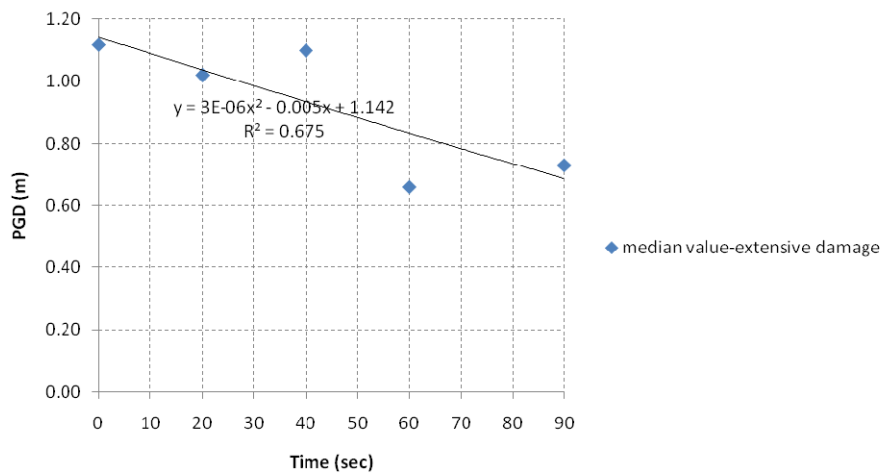


*Figure 150 Time-dependent quadratic fit of median values of PGD for the extensive damage state*
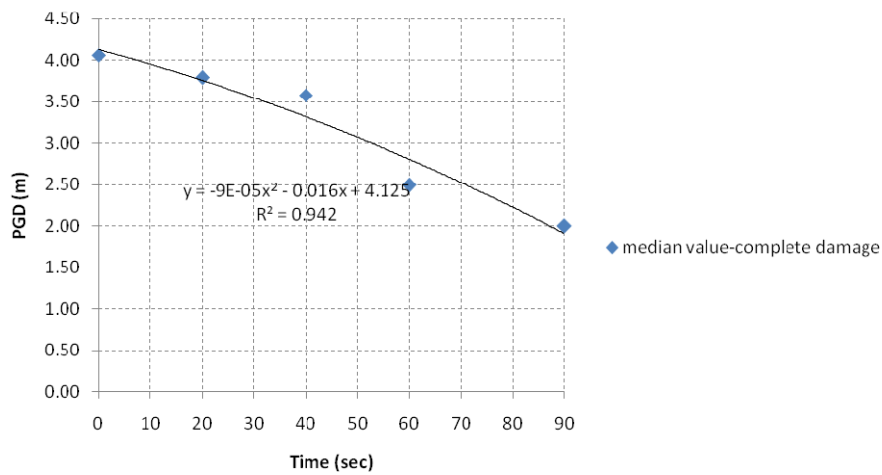
*Figure 151 Time-dependent quadratic fit of median values of PGD for the complete damage state*

*Fragility surfaces in terms of PGA*
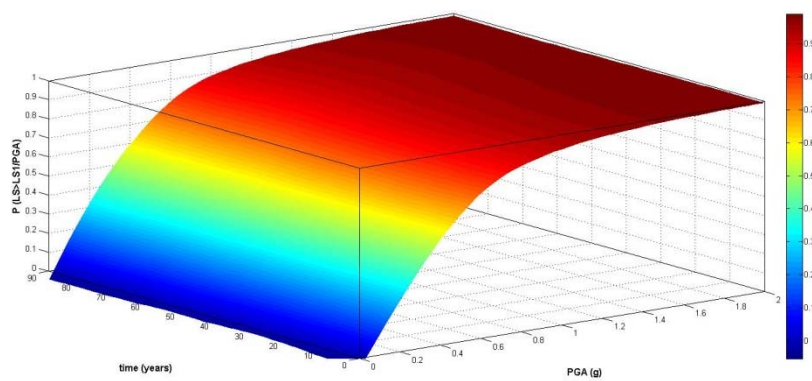


*Figure 152 Fragility surface as a function of PGA for Slight Damage (fit: Locally weighted smoothing quadratic regression)*
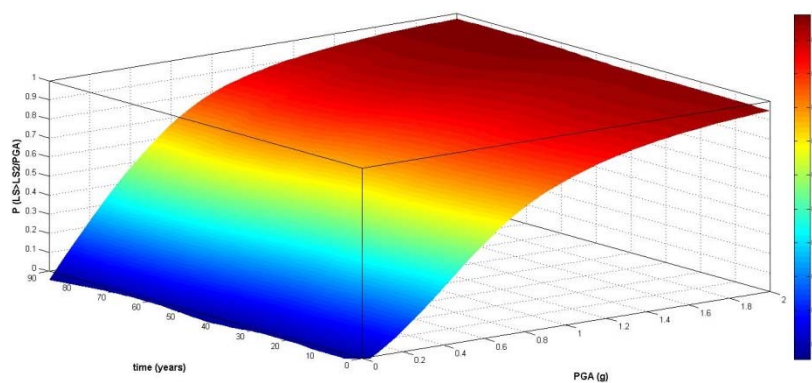


*Figure 153 Fragility surface as a function of PGA for Moderate Damage (fit: Locally weighted smoothing quadratic regression)*
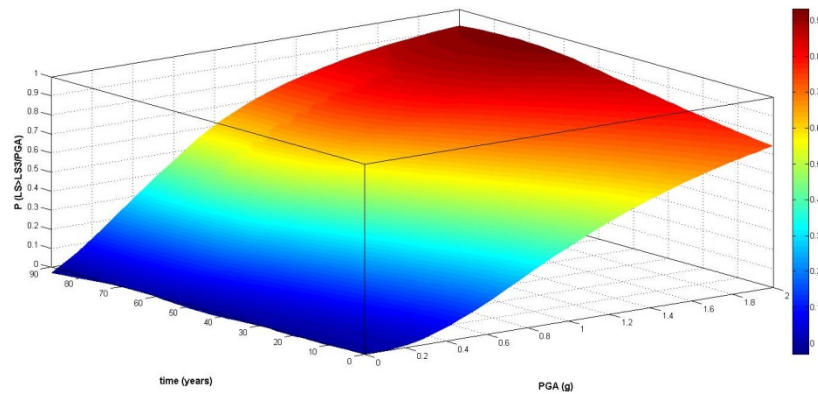
*Figure 154 Fragility surface as a function of PGA for Extensive Damage (fit: Locally weighted smoothing quadratic regression)*
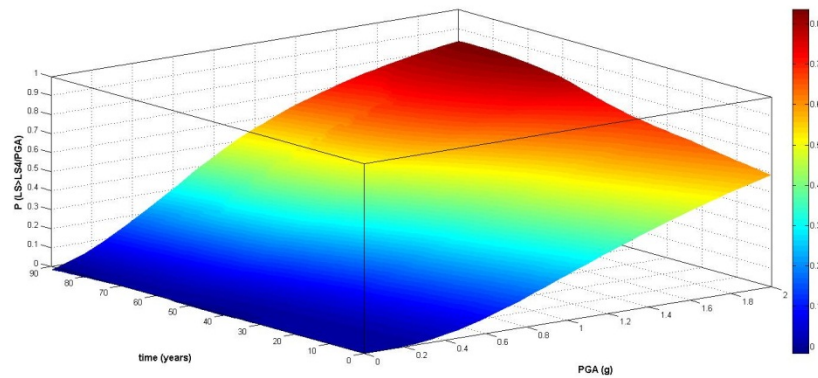


*Figure 155 Fragility surface as a function of PGA for Complete Damage (fit: Locally weighted smoothing quadratic regression)*

*Fragility surfaces in terms of PGD*
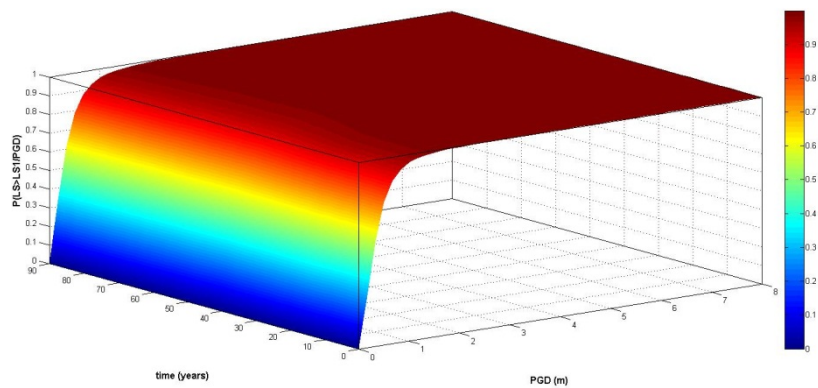


*Figure 156 Fragility surface as a function of PGD for Slight Damage (fit: Interpolant)*
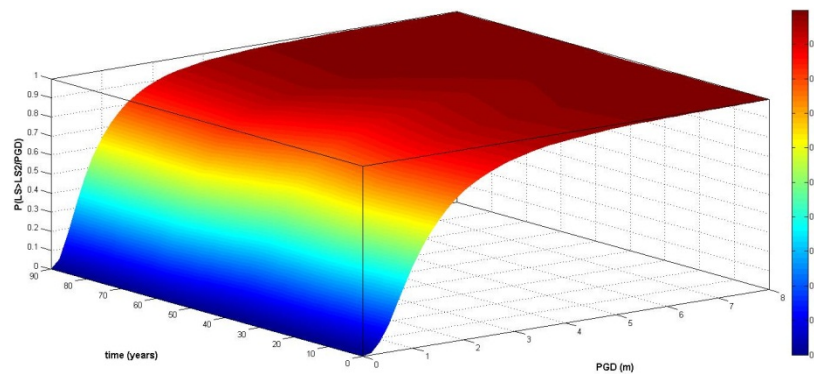
*Figure 157 Fragility surface as a function of PGD for Moderate Damage (fit: Interpolant)*
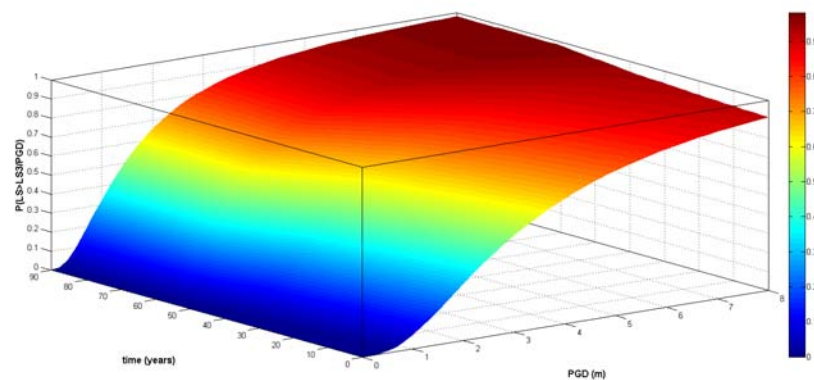


*Figure 158 Fragility surface as a function of PGD for Extensive Damage (fit: Interpolant)*
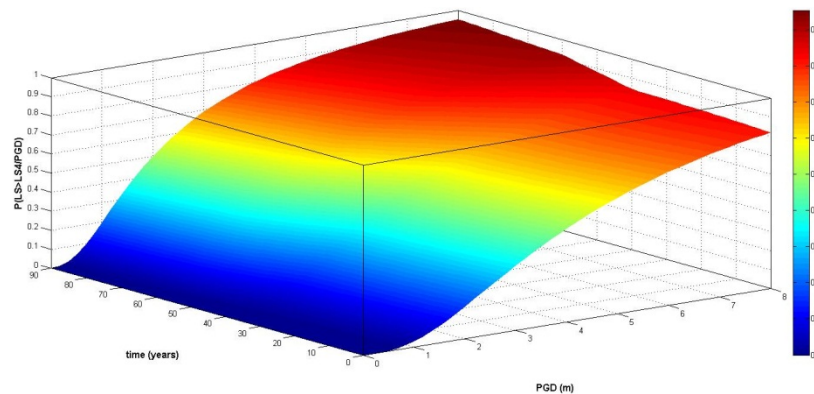


*Figure 159 Fragility surface as a function of PGD for Complete Damage (fit: Interpolant)*

## 5.3    CONCLUSIONS

A framework for time-dependent fragility analysis of corroded RC buildings impacted by co-seismic permanent landslide displacements based on numerical analysis and analytical simulations has been presented. Two potential adverse corrosion scenarios are examined: chloride and carbonation induced corrosion of the steel reinforcement. The methodology is applied to reference low rise RC frame buildings with varying strength and stiffness of the

foundation system that are subjected to the combined effects of reinforcement corrosion and earthquake triggered landslide displacements. Fragility curves in terms of PGA (outcrop conditions) and PGD for different damage states are analytically evaluated at different points in time  (0, 20, 40, 60, 90 years) to assess the time-dependent effect of corrosion on their vulnerability for the given carbonation or chloride induced deterioration scenario. It is observed that the fragility of the structures generally increases over time due to corrosion. This increase is more pronounced for the chloride induced corroded RC buildings founded on isolated footings.

Future work should aim at the validation of the proposed model by comparison of the computed damages to experimental results and/or empirical data. Significant effort should also be devoted in the more refined definition of the time-dependent limit states. Moreover, further research is needed to address time-dependent fragility of additional building types and geometries, different triggering mechanisms of the potential landslide mass (e.g. intense precipitation) and different hazard (e.g. earthquakes) as well as deterioration mechanisms.

# 6 CONCLUSION AND DISCUSSION

This work presented means of assessing landslide risk evolution with climate change scenarios. Those methods depend from the data available as inputs and we have seen that if climate change scenarios and land cover evolution scenarios can be developed quite accurately; the scenarios of population and human activity evolution are rougher and especially at site scales.

Even though, the three studies of landslide risk assessment on the French, Norwegian and Scottish sites seem to tend to a similar trend: an increase of landslide risk. This increase in risk is more or less important depending on the considered sites and parameters (see sections 1.3, 2.3 and 3.5). Due to a high level of uncertainties on population and traffic evolution scenarios, precautions need to be taken with the figures.

Regarding the influence of suction change due to vegetation/canopy on the factor of safety, a methodology has been developed to obtain simplified and rapid estimations of possible unstable slopes. The approach considers only the influence of the root water uptake caused by evapotranspiration and other phenomenon due to the presence of vegetation is not taken into account. Further development would be the production of abacus for a wide range of vegetation and then the analysis of the impact of climate change through the vegetation change.

In parallel, time-dependent fragility analysis of corroded RC buildings impacted by co-seismic permanent landslide displacements has been developed. In order to be integrated in risk evolution assessment of the studies of part one, this methodology needs to be adapted to rainfall triggered landslides. The risk evolution would be thus a combination of hazard changes, exposure changes and vulnerability changes.

# REFERENCES

Ahmad, R. 2003. Developing early warning systems in Jamaica: rainfall thresholds for hydrogeological hazards. Proceedings, National Disaster Management Conference. Ocho Rios (St Ann), Jamaica: Office of Disaster Preparedness and Emergency Management. (Sourced from http://www.mona.uwi.edu/uds/ June 2006.)

Aleotti, P. 2004. A warning system for rainfall-induced shallow failures. Engineering Geology, 73, 247-265.

Anon. 1989. The climate of Scotland – some facts and figures. London: The Stationery Office.

Anon. 2006. Scottish transport statistics, No 25, 2006 Edition. National Statistics Publication. Edinburgh: Scottish Executive.

Anon. 2007. Rainfall thresholds for the initiation of landslides. Istituto di Ricerca per la Protozione Idrogelogica, Italy. http://rainfallthresholds.irpi.cnr.it/ accessed June 2007.

Anon. 2011a. Scottish road network climate change study: UKCP09 update. Report by Jacobs for Transport Scotland: http://www.transportscotland.gov.uk/strategy-and-research/publications-and-consultations/j209391-00.htm  accessed December 2011.

Anon. 2011b. Scottish transport statistics, No 30, 2011 Edition. National Statistics Publication. Edinburgh: Transport Scotland.

Barnett, C., Perry, M., Hossell, J., Hughes, G. & Procter, C. 2006a. A handbook of climate trends across Scotland; presenting changes in the climate across Scotland over the last century. 58p. SNIFFER Project CC03. Edinburgh: Scotland and Northern Ireland Forum for Environmental Research.

Barnett, C., Perry, M., Hossell, J., Hughes, G. & Procter, C. 2006b. Patterns of climate change across Scotland: technical report, 102p. SNIFFER Project CC03. Edinburgh: Scotland and Northern Ireland Forum for Environmental Research.

Bellamy, D. & Barrett, J. 2007. Climate stability: an inconvenient proof. Proceedings of the Institution of Civil Engineers: Civil Engineering, 160(2), 66-72.

Beushausen, H.,  Alexander, M. (2010). Concrete deterioration: causes, mechanisms, prevention. Concrete Technology for Structural Engineers, Workshop, May 2010.

Biarez J., Fleureau J.M. and Taibi S. Mechanical constitutive model for unsaturated granular media. In C. Thornton, ed, The Second International Conference on Micromechanics of granular Media, Birmingham, pages 51–58. Balkema, Rotterdam, 1993.

Biot M. General theory of three-dimensional consolidation. Journal of Applied Physics, 12:155–164, 1941.

Biot M. and Willis P.G. The elastic coefficients of the theory of consolidation. Journal o f Applied Mechanics, 24:594–601, 1957.

Bird J.F, Crowley H., Pinho R., Bommer J.J. (2005). Assessment of building response to liquefaction induced differential ground deformation. Bul of the New Zealand Society for Earthquake Engineering 38(4):215-234.

Boylan, N., Jennings, P. & Long, M. 2008. Peat slope failures in Ireland. Quarterly Journal of Engineering & Hydrogeology, 41, 93-108.

Bromhead, E. N., Winter, M. G., Floyd-Walker, H. & Hosseyni, M. 2012. The contribution of QJEGH to landslide knowledge: there and back in 45 volumes. Proceedings, 11th International Symposium on landslides / 2nd North American Symposium on Landslides. Banff.

Brooks R.N. and Corey A.T. Properties of porous media affecting fluid flow. J. Irrig.Drain. Div. Am. Soc. Civ. Engrg., (92):61–88, 1966.

Caine, N. 1980. The rainfall intensity-duration control of shallow landslides and debris flows. Geografiska Annaler, 62 A, 23-27.

Campbell, R. H. 1975. Soil slips, debris flows, and rainstorms in the Santa Monica Mountains and vicinity, southern California. US Geological Survey Professional Paper 851, 51p.

Cannon, S. H., Gartner, J. E., Wilson, R. C., Bowers, J. C. & Laber, J. L. 2008. Storm rainfall conditions for floods and debris flows from recently burned area in southwestern Colorado and southern California. Geomorphology, 96, 250-269.

CEB-FIB Task Group 5.6 (2006), Model Code for Service Life Design. Bulletin 31, fédération internationale du béton (fib), 2006.

Clarke, D. & Smethurst, J. A. 2010. Effects of climate change on cycles of wetting and drying in engineered clay slopes in England. Quarterly Journal of Engineering Geology & Hydrogeology, 43(4), 461-472.

Crowley H., Pinho R., Bommer J.J. (2004). A probabilistic displacement-based vulnerability assessment procedure for earthquake loss estimation. Bulletin of Earthquake Engineering 2(2):173-219.

DARTS – Durable and Reliable Tunnel Structures: Deterioration Modelling, European Commission, Growths 2000, Contract G1RD-CT-2000-00467, Project GrD1-25633, 2004.

Dijkstra, T. & Dixon, N. 2010.Climate change and slope stability in the UK: challenges and approaches. Quarterly Journal of Engineering Geology & Hydrogeology, 43(4), 371-385.

Dixon, N., Dijkstra, T., Forster, A. & Connell, R. 2006. Climate change impact forecasting for slopes (CLIFFS) in the built environment. Engineering Geology for Tomorrow's Cities: Proceedings, 10th International Association of Engineering Geology Congress, p. 43 and DVD-Rom. London: The Geological Society.

DuraCrete – Probabilistic Performance Based Durability Design of Concrete Structures: Statistical Quantification of the Variables in the Limit State Functions. Report No.: BE 95-1347, pp. 62-63, 2000.

Dykes, A. P. & Jennings, P. 2010. Peat slope failures and other mass movements in western Ireland, August 2008. Quarterly Journal of Engineering Geology and Hydrogeology, 44, 5-15.

Dykes, A. P. & Jennings, P. 2011. Reply to discussion on Peat slope failures and other mass movements in western Ireland, August 2008. Quarterly Journal of Engineering Geology and Hydrogeology, 44, 492-494.

Dykes, A. P. & Jennings, P. 2011. Peat slope failures and other mass movements in western Ireland, August 2008. Quarterly Journal of Engineering Geology and Hydrogeology, 44, 5-15.

Dykes, A. P., Wharburton, J., Nichol, D., Doherty, G. K. & Scott, M. J. 2008. Discussion on A5 Llyn Ogwen peatslide, Capel Curig, North Wales, 40, 293-299. Quarterly Journal of Engineering Geology and Hydrogeology, 41, 123-126.

Eyles, R. J. 1979. Slip-triggering rainfalls in Wellington City, New Zealand. New Zealand Journal of Science, 22(2), 117-122.Feddes, R. A., Kowalik, P. J., Zaradny, H., Simulation of field water use and crop yield, Wiley, New York, 1978, ISBN 0470264632

Flentje, P. & Chowdury, R. 2006. Observational approach for urban landslide management. Engineering Geology for Tomorrow's Cities, p. 56, Paper No 522. London: The Geological Society.

Foster, M., Werrity, A. & Smith, K. 1997. The nature, causes and impacts of recent hydroclimatic variability in Scvotland and Northern Ireland. Proceedings, Sixth national Hydrology Symposium, 8.9-8.17. British Hydrology Society, Salford.

Fukuoka, M. 1980. Landslides associated with rainfall. Geotechnical Engineering, 11, 1-29.

Galbraith, R. M., Price, D. J. & Shackman, L. (Eds.) 2005. Scottish road network climate change study. 100p. Scottish Executive, Edinburgh.

Geoslope 2005. Why do slopes become unstable after rainfall events? http://www.geo-slope.com. Direct Contact, April 2005.

Ghosh J., Padgett J. E., (2010). Aging Considerations in the Development of Time-Dependent Seismic Fragility Curves, Journal of Structural Engineering.

Gibson, A. D., Culshaw, M. G., Foster, C. & Pennington, C. V. L. In Press. Landslide management in the UK – the problem of managing hazards in a 'low risk' environment. Landslides.

Greenwood, J.R., Norris, J.E. & Wint, J. 2004. Assessing the contribution of vegetation to slope stability. Geotechnical Engineering, 157, GE4, 199–208.

Guthrie, R. H., Mitchell, S. J., Lanquate-Opoku, N. & Evans, S. G. 2010. Extreme weather and landslide initiation in coastal British Columbia. Quarterly Journal of Engineering Geology and Hydrogeology, 43(4), 417-428.

Hemmati S., Etude de l'Interaction Sol-Végétation- Atmosphère avec une approche couplée Thermo-Hydro-Mécanique, PhD Thesis, ENPC, 2009

Hill, D., Winter, M. G. & McCrae, I. S. 2007. Opportunities for offsetting carbon emissions on the Scottish trunk road network: overview report. Edinburgh: Transport Scotland.

Hulme, M., Jenkins, G. J., Lu, X., Turnpenny, J. R., Mitchell, T. D., Jones, R. G., Lowe, J., Murphy, J. M., Hassell, D, Boorman, P., MacDonald, R., & Hill, S. 2002. Climate changes scenarios for the United Kingdom: the UKCIP02 scientific report. Tyndall Centre for Climate Change research, 120p. Norwich: University of East Anglia.

Hurlimann, M., Rickenmann, D. & Graf, C. 2003. Field and monitoring data of debris flow events in The Swiss Alps. Canadian Geotechnical Journal, 40, 161-175.

Indaratna B., Fatahi B., Khabbaz H. (2006). "Numerical analysis of matric suction effects of tree roots, Geotechnical Engineering, 159 (GE2), 77-90.

Institute of Hydrology. 1999. Flood estimation handbook. Wallingford (UK): Natural Environment Research Council.

Jaedicke, C. and A. Kleven (2008) Long-term precipitation and slide activity in south-eastern Norway, autumn 2000. Hydrol.Process. 22 (4).

Jenkins, G. J., Perry, M. C. & Prior, M. J. O. 2007. The climate of the United Kingdom and recent trends. Exeter: Met Office Hadley Centre.

Jenkins, G. J., Murphy, J. M., Sexton, D. S., Lowe, J. A., Jones, P. & Kilsby, C.G. 2009. UK Climate projections: briefing report. Exeter: Met Office Hadley Centre.

Jones, F. O. 1973. Landslides of Rio de Janeiro and the Serra das Araras Escarpment, Brazil. US Geological Survey Professional Paper 697, 42p.

Ko, F. W. Y. 2005. Correlation between rainfall and natural terrain landslide occurrence in Hong Kong. GEO Report No. 168. Hong Kong SAR: Geotechnical Engineering Office.

Landsberg, J.J. (1999) The Way Trees Use Water. Water and Salinity Issues in Agroforestry No. 5, RIRDC Publication No. 99/37, Australia, 1-24.

Lee Min Lee, Nurly Gofar, Harianto Rahardjo, A simple model for preliminary evaluation of rainfall-induced slope instability, Engineering Geology, Volume 108, Issues 3–4, 8 October 2009, Pages 272-285

Long, M. & Boylan, N. 2008. Discussion on A5 Llyn Ogwen peatslide, Capel Curig, North Wales, 40, 293-299. Quarterly Journal of Engineering Geology and Hydrogeology, 41, 487-489.

Long, M. & Boylan, N. 2011. Discussion on Peat slope failures and other mass movements in western Ireland, August 2008. Quarterly Journal of Engineering Geology and Hydrogeology, 44, 491-492.

Loveridge, F. A., Spink, T. W., O'Brien, A. S., Briggs, K. M. & Butcher, D. 2010. The impact of climate change on infrastructure slopes, with particular reference to southern England. Quarterly Journal of Engineering Geology & Hydrogeology, 43(4), 461-472.

Mander, J. B., Priestley, M. J. N., and Park, R.: Theoretical stress-strain model for confined concrete, Journal of Structural Engineering, 114(8), 1804-1826, 1988.

Marques, P.F., Costa, A. (2010). Service life of RC structures: Carbonation induced corrosion. Prescriptive vs. performance-based methodologies, Construction and Building Materials, vol. 24, pp.258–265.

Marsh, T. J. 1996. The 1995 UK drought – signal of climatic stability? Proceedings, Institution of Civil Engineers (Water, Maritime and Energy), 118, 189-195.

McAdam, D. 1993. Edinburgh – a landscape fashioned by geology. Edinburgh: Scottish Natural Heritage and British Geological Survey.

McGregor, P. & MacDougall, K. 2009. A review of the Scottish rain-gauge network. Proceedings, Institution of Civil Engineers (Water Management), 162(2), 137-146.

McMillan, P., Brown, D. J., Forster, A. & Winter, M. G. 2005. Debris flow information sources. In: Scottish Road Network Landslides Study (Eds: Winter, M. G., Macgregor, F. & Shackman, L.), 25-44. Edinburgh: The Scottish Executive.

Milne, F. D., Werritty, A., Davies, M. C. R. & Browne, M. J. 2009. A recent debris flow event and implications for hazard management. Quarterly Journal of Engineering Geology and Hydrogeology, 42(1), 51-60.

Modaressi-Farahmand-Razavi A., Numerical Modeling: An Efficient Tool for Analyzing the Behavior of Constructions, Multiscale Geomechanics, From Soil to Engineering Projects, Multiscale Geomechanics, From Soil to Engineering Projects, Edited by Pierre-Yves Hicher, ISTE, October 2011.

Modaressi-Farahmand-Razavi A., Modélisation numérique: un outil efficace pour analyser le comportement des ouvrages, Chap. 9, Du sol à l'ouvrage, Une vision multi-échelles de la méomécanique, ed. P-Y Hicher and E. Flavigny, Hermès, 2010.

Modaressi A., Fry J-J., Barrages et Remblai , Mécanique des sols non saturés , Coussy et Fleureau (eds) , Collection MIM (Mécanique et Ingéniérie des Matériaux), Hermès, 2002.

Moore, R., Carey, J. M. & McInnes, R. G. 2010. Landslide behaviour and climate change: predictable consequences for the Ventnor Undercliff, Isle of Wight. Quarterly Journal of Engineering Geology & Hydrogeology, 43(4), 447-460.

Moravek, A. (2011). Modelling of land cover changes in the Barcelonnette basin, Alpes-de-Haute-Provence (France).

Nadim, F., O. Kjekstad, P. Peduzzi, C. Herold, and C. Jaedicke (2006) Global landslide and avalanche hotspots. Landslides 3 (2).

Nichol, D., Doherty, G. K. & Scott, M. J. 2007. A5 Llyn Ogwen peatslide, Capel Curig, North Wales. Quarterly Journal of Engineering Geology and Hydrogeology, 40, 293-299.

Nichol, D., Doherty, G. K. & Scott, M. J. 2008. Reply to discussion on A5 Llyn Ogwen peatslide, Capel Curig, North Wales, 40, 293-299. Quarterly Journal of Engineering Geology and Hydrogeology, 41, 489.

Nimah, M.N., Hanks, R.J. (1973) Model for estimating soil water, plant, and atmospheric interrelations. I. Description and sensitivity. Soil Sci. Soc. Am. Proc., 37, 522–527. 116. Olhoeft, G.R.

NCHRP 1-37A (2004). Mechanistic-Empirical Design of New and Rehabilitated Pavement Structures, Final Report, NCHRP Project 1-37A, Transportation Research Board, National Research Council, Washington, D.C.

Norris E. & J.R. Greenwood Joanne, Assessing the role of vegetation on soil slopes in urban areas, IAEG2006 Paper number 744, The Geological Society of London 2006

Norwegian Geotechnical Institute (2004) Global Landslide and Avalanche Hotspots. First-order identification of global slide and avalanche hotspots, NGI report 20021613-1.

Norwegian Geotechnical Institute (2009) Natural and Conflict Related Hazards in Asia-Pacific. Risk assessment and mitigation measures for natural and conflict related hazards in Asia-Pacific., NGI report 20071600-1.

Osbourn, T. J., Hulme, M., Jones, P. D., & Basnett, T. A. 2000. Observed trends in daily intensity of United Kingdom precipitation. International Journal of Climatology, 20(4), 347-364.

Peng J., Stewart M.G. ,Carbonation-Induced Corrosion Damage and Structural Safety for Concrete Structures under Enhanced Greenhouse Conditions, Research Report No. 270.11.2008

Petley, D. 2010. On the impact of climate change and population growth on the occurrence of fatal landslides in South, East and Southeast Asia. *Quarterly Journal of Engineering Geology and Hydrogeology*, **43**(4), 487-496.

Pitilakis. K. & Fotopolou, S. (Eds.) 2011. Physical vulnerability of elements at risk to landslides: methodology for evaluation, fragility curves and damage states for buildings and lifelines. SafeLand Deliverable 2.5. Unpublished Report.

Polemio, M. & Petrucci, O. 2010. Occurrence of landslide events and the role of climate in the twentieth century in Calabria, southern Italy. Quarterly Journal of Engineering Geology and Hydrogeology, 43(4), 403-415.

SafeLand D2.10.

SafeLand D3.6 (2010). Database of human activity factors affecting the local landslide risk at selected sites (including maps of controlling factors and changes in these factors; land cover, demographic and economic scenarios; trajectory of key indicator of changes).

SafeLand D3.7.

SafeLand D3.8 (2012). Changing pattern in climate-driven landslide hazard at selected sites in Europe (focus on Southern Italy, the Alps and Southern Norway) in the next 50 yearsDeliverable D3.2 report, SafeLand: Seventh Framework Programme for research and technological development (FP7) of the European Commission.

Sedan, O., Mirgon, C. and Bes de Berc, S. (2006). Cartographie de l'aléa mouvements de terrain – Prise en compte de la propagation – Programme BORA – Rapport final. BRGM/RP-54650-FR, 166p, 6 appendices [In French]

SeismoSoft, SeismoStruct – A computer program for static and dynamic nonlinear analysis of framed structures, 2010, (online): Available from URL: www.seismosoft.com

Selby, M. J. 1976. Slope erosion due to extreme rainfall: a case study from New Zealand. Geografiska Annaler, 58 A, 131-138.

Sidle, R. C. & Swanson, D. N. 1982. Analysis of a small debris slide in coastal Alaska. Canadian Geotechnical Journal, 19(2), 167-174.

Skempton A.W. The colloidal activity of clays. In Proceedings of 3rd International Conference in Soil Mechanics and Foundation Engineering, Switzerland, volume I, pages 57–, 1953.

Springman, S. M., Jommi, C. & Teysseire, P. 2003. Instabilities on moraine slopes induced by loss of suction: a case history. Géotechnique, 53(1), 3-10.

Sudret B., Defaux, G., Pendola, M. (2007). Stochastic evaluation of the damage length in RC beams submitted to corrosion of reinforcing steel. Civil Engineering and Environmental Systems, Vol. 24, No. 2, pp.165–178.

Terzaghi K. and Peck R.B. Soil Mechanics in engineering practice. John Wiley and Sons, New York, 2nd edition, 1967.

Toll, D. G. 2001. Rainfall-induced landslides in Singapore. Proceedings of the Institution of Civil Engineers (Geotechnical Engineering), 149(4): 211-216.

Van Genuchten M.T. A closed form for predicting the hydraulic conductivity of unsaturated soils. Soils Sci. Am. Soc., (44):892–898, 1980.

Walking the-Talk 2011. Paths and climate change – an investigation into the potential impacts of climate change on the planning, design, construction and management of paths in Scotland. Scottish Natural Heritage Commissioned Report No 436. Inverness: Scottish Natural Heritage.

Wasowski, J., Lamanna, C. & Casarano, D. 2010. Influence of land-use change and precipitation patterns on landslide activity in the Daunia Apennines, Italy. Quarterly Journal of Engineering Geology and Hydrogeology, 43(4), 387-401.

Wheeler, S. J., Sharma, R. S. & Buisson, M. S. R. 2003. Coupling of hydraulic hysteresis and stress-strain behaviour in unsaturated soils. Géotechnique, 53(1), 41-54.

Winter, M. G. (In Press). DS 4.4 Lead Discussion: Landslides. Geotechnics of Hard Soils – Weak Rocks: Proceedings, XV European Conference on Soil Mechanics and Geotechnical Engineering, (Eds: Anagnostopoulos, A, Pachakis, M. & Tsatsanifos, C.) 4, ####-####. Amsterdam: IOS Press.

Winter, M G, Macgregor, F. & Shackman, L. (Editors) 2005. Scottish Road Network Landslides Study, 119p. Trunk Roads: Network Management Division Published Report Series. Edinburgh: The Scottish Executive.

Winter, M. G., Heald, A., Parsons, J., Shackman, L. & Macgregor, F. 2006. Scottish debris flow events of August 2004. Quarterly Journal of Engineering Geology and Hydrogeology, 39(1), 73-78.

Winter, M. G., Shackman, L. & Macgregor, F. 2007. Landslide management and mitigation on the Scottish road network. Landslides and Climate Change: Challenges and Solutions (Eds: McInnes, R, Jakeways, J, Fairbank, H and Mathie, E), 249-258. London: Taylor & Francis.

Winter, M G, Macgregor, F. & Shackman, L. 2008. Climate change impacts on debris flow in Scotland. Proceedings, First World Landslide Forum, Parallel Session Volume, 677-680. Tokyo, Japan: United Nations University.

Winter, M G, Macgregor, F. & Shackman, L. (Editors) 2009a. Scottish road network landslides study: implementation, 278p. Transport Scotland Published Report Series. Edinburgh: Transport Scotland.

Winter, M. G., Barker. K., Reid, J. M., Boylan, N., Jennings, P. & Long, M. 2009b. Discussion on Peat slope failures in Ireland, 41, 93-108. Quarterly Journal of Engineering & Hydrogeology, 42, 129-132.

Winter, M. G., Dixon, N., Wasowski, J. & Dijkstra, T. 2010a. Introduction to land use and climate change impacts on landslides. Quarterly Journal of Engineering Geology & Hydrogeology, 43(4), 367-370.

Winter, M. G., J Dent, J., Macgregor, F., Dempsey, P., Motion, A. & Shackman, L. 2010b. Debris flow, rainfall and climate change in Scotland. Quarterly Journal of Engineering Geology & Hydrogeology, 43(4), 429-446.

Winter, M. G. & Bromhead, E. N. 2011. Landslide risk – some issues that determine societal acceptance. Natural Hazards, DOI 10.1007/s11069-011-9987-1.

Wieczorek, G. F. 1987. Effect of rainfall intensity and duration on debris flows in central Santa Cruz Mountains, California. Debris Flow/Avalanches: Process, Recognition and Mitigation (Eds: Costa, J.E. & Wieczorek, G.F.). Reviews in Engineering Geology, VII, 93-104. Boulder, CO: Geological Society of America.